

ACTA DE EVALUACIÓN DE LA TESIS DOCTORAL
(FOR EVALUATION OF THE ACT DOCTORAL THESIS)

Año académico (academic year): 2019/20

DOCTORANDO (candidate PHD): **BOUSDAR AHMED, DINA**

D.N.I./PASAPORTE (Id.Passport): ******8801X**

PROGRAMA DE DOCTORADO (Academic Committee of the Programme): **D441-ELECTRÓNICA: SISTEMAS ELECTRÓNICAS AVANZADOS. SISTEMAS INTELIGENTES**

DPTO. COORDINADOR DEL PROGRAMA (Department): **ELECTRÓNICA**

TITULACIÓN DE DOCTOR EN (Phd title): **DOCTOR/A POR LA UNIVERSIDAD DE ALCALÁ**

En el día de hoy 12/12/19, reunido el tribunal de evaluación, constituido por los miembros que suscriben el presente Acta, el aspirante defendió su Tesis Doctoral **con Mención Internacional** (In today assessment met the court, consisting of the members who signed this Act, the candidate defended his doctoral thesis with mention as International Doctorate), elaborada bajo la dirección de (prepared under the direction of) **JUAN JESÚS GARCÍA DOMÍNGUEZ // ESTEFANÍA MUÑOZ DÍAZ-ROPERO**.

Sobre el siguiente tema (Title of the doctoral thesis): **WEARABLE-BASED PEDESTRIAN LOCALIZATION THROUGH FUSION OF INERTIAL SENSOR MEASUREMENTS**

Finalizada la defensa y discusión de la tesis, el tribunal acordó otorgar la CALIFICACIÓN GLOBAL¹ de (**no apto, aprobado, notable y sobresaliente**) (After the defense and defense of the thesis, the court agreed to grant the GLOBAL RATING (fail, pass, good and excellent): **SOBRESALIENTE**

Alcalá de Henares, a 12 de 12 de 2019

Fdo. (Signed):

Fdo. (Signed):

Fdo. (Signed):

FIRMA DEL ALUMNO (candidate's signature),

Con fecha 16 de diciembre de 2019 la Comisión Delegada de la Comisión de Estudios Oficiales de Posgrado, a la vista de los votos emitidos de manera anónima por el tribunal que ha juzgado la tesis, resuelve:

- ☒ Conceder la Mención de "Cum Laude"
☐ No conceder la Mención de "Cum Laude"

La Secretaria de la Comisión Delegada

¹ La calificación podrá ser "no apto" "aprobado" "notable" y "sobresaliente". El tribunal podrá otorgar la mención de "cum laude" si la calificación global es de sobresaliente y se emite en tal sentido el voto secreto positivo por unanimidad. (The grade may be "fail" "pass" "good" or "excellent". The panel may confer the distinction of "cum laude" if the overall grade is "Excellent" and has been awarded unanimously as such after secret voting.).

Fdo. (Signed):

INCIDENCIAS / OBSERVACIONES:
(Incidents / Comments)

DILIGENCIA DE DEPÓSITO DE TESIS.

Comprobado que el expediente académico de D./D^a _____
reúne los requisitos exigidos para la presentación de la Tesis, de acuerdo a la normativa vigente, se
procede, con fecha de hoy a registrar el depósito de la tesis en el Servicio de Estudios Oficiales de
Posgrado, con número de páginas: _____.

Alcalá de Henares a _____ de _____ de 20____



Pilar de la Vega Gallego
Fdo. El Funcionario



Universidad
de Alcalá

DEPARTAMENTO DE ELECTRÓNICA
Escuela Politécnica Superior
28805 Alcalá de Henares (Madrid)
Teléfonos: 91 885 65 40 Fax: 91 885 65 91
eldep@depeca.uah.es

Dr. Juan Jesús García Domínguez

Dra. Estefanía Muñoz Díaz-Ropero

INFORMAN:

Que la Tesis Doctoral titulada "Wearable-based pedestrian localization through fusion of inertial sensor measurements", presentada por Dña. Dina Bousdar Ahmed y realizada bajo nuestra dirección, dentro del campo de **Sistemas de Percepción y Localización**, reúne los méritos de calidad y originalidad para optar al Grado de Doctor.

Alcalá de Henares, a 14 de octubre de 2019

Fdo.: Juan Jesús García Domínguez

Fdo.: Estefanía Muñoz Díaz-Ropero

D. Miguel González Herráez, Coordinador de la Comisión Académica del Programa de Doctorado en: Sistemas Electrónicos Avanzados. Sistemas Inteligentes

INFORMA que la Tesis Doctoral titulada: **Wearable-based pedestrian localization through fusion of inertial sensor measurements** presentada por el D^a Dina Bousdar Ahmed, bajo la dirección del Dr. D. Juan Jesús García Domínguez y la Dra. D^a Estefanía Muñoz-Díaz Roperó, reúne los requisitos científicos de originalidad y rigor metodológicos para ser defendida ante un tribunal. Esta Comisión ha tenido también en cuenta la evaluación positiva anual del doctorando, habiendo obtenido las correspondientes competencias establecidas en el Programa.

Para que así conste y surta los efectos oportunos, se firma el presente informe en Alcalá de Henares a 15 de octubre de 2019



Fdo.: D. Miguel González Herráez



PhD. Program in Electronics: Advanced Electronic Systems.
Intelligent Systems

Wearable-based pedestrian localization through fusion of inertial sensor measurements

PhD Thesis Presented by
Dina Bousdar Ahmed

Advisors

Dr. Juan Jesús García Domínguez
Dr. Estefanía Muñoz-Díaz Roperó

Alcalá de Henares, 2019

*To my mom,
you are part of every step of our lives.*

*A mi madre,
eres parte de cada paso de nuestras vidas.*

Acknowledgements

Whoever that has got to know me during my phase as a PhD candidate knows one thing about me: Estefanía Muñoz Díaz is my PhD supervisor at DLR. However, calling her only my PhD supervisor is an understatement. She has been a supportive colleague when I needed someone to have technical discussions with. I think we should patent the idea of “hot chocolate and coloured diagrams” as a problem-solving technique. She has been an attentive friend when everything went south, and to this day, I can say with confidence that she has become one of my role models. Thank you for giving me the opportunity of learning from you.

I would like to thank Juan Jesús García for accepting to supervise me, with all that entailed. I enjoyed my time discussing with you, and I especially enjoyed getting a different point of view when I thought there was only one way of doing things.

There are two people who I believe were key for the kick-start of this PhD thesis: Stephan Sand and Uwe-Carsten Fiebig. I still remember the discussions a few years ago on what I could focus my research on. I can say now that those discussions were the push I needed to start this journey. And talking about the journey, I need to thank my group: Fabian, Oliver, Ibrahim, Susanna, Benjamin, Paul, Martin and Mohammad for making it enjoyable both in the professional and personal level. You are all extraordinary scientists and even better people.

Jutta and Christina are, to my opinion, the heart and soul of the Communication Systems Department. In these acknowledgements, I want to thank you for paving the way to help me do my job. The feeling that we can count on you is truly priceless.

In these acknowledgements, I cannot forget the role that my mom and my sisters played. They are not only my rock but also my inspiration to be my best self. For everything you do, for being you, simply thank you.

Last, but not least, I would like to thank Mohammad. I want to thank him for his unconditional support during these years. I want to thank him for staying around when it was not fun to be around. Someday, I want to see the world in the way that you do.

Abstract

In pedestrian localization, fusion techniques have been exploited to address the weaknesses of different types of localization systems. Inertial localization is a particular case where the community has attempted to combine inertial technology with other technologies like satellite-based navigation or WiFi.

Less explored are the approaches that combine multiple inertial sensors mounted on the human body. We refer to these approaches as multi-inertial measurement unit (IMU) localization systems. In this work, we want to study multi-IMU localization systems for pedestrian localization.

The overall research objective of this thesis is pedestrian localization by means of inertial sensor fusion. We aim to determine the benefits, in distance accuracy, heading accuracy and height accuracy, of combining two inertial sensors. They will be mounted on the pocket and the foot of the same leg, respectively. The reason for choosing these body locations is that they have characteristic features during walking. Moreover, the fact that we consider the same leg will allow us to observe possible correlations between the measurements of the foot IMU and the pocket IMU during the walk.

Our first step is the design of the evaluation methodology, which is inspired by the methodologies implemented in indoor localization competitions. The evaluation methodology allows us to quantitatively assess the performance of the two inertial localization systems based on a pocket IMU and a foot IMU. With our study, we identify the strengths and weaknesses of each of these systems, which helps us proposing the multi-IMU localization systems that we develop later on.

Our proposed multi-IMU localization systems focus on three main challenges of inertial localization. The first challenge is related to the need for calibration of the parameters of step length models, which are used in non-foot-mounted inertial localization systems. The second challenge is the height drift that affects foot-mounted inertial systems. Finally, the last challenge is the heading drift, which is a challenge common to all inertial localization systems.

The proposed calibration method automatically estimates the parameters of a step length model of the pocket inertial navigation system (INS). We explain how the optimal value of the parameters of the step length model are estimated, given the step length from the foot INS and the pitch amplitude of the pocket INS. We make two proposals: the first one calibrates only one parameter of the step length model

and the second one calibrates both parameters.

The proposed calibration method has the advantage of the automatization. That is, there is no need for an external operator to manually calibrate the step length model of the pocket INS. In addition, the automatic calibration can be carried out in real time, which is not possible with either of the state of the art calibration methods.

Next, we address the challenges related to the height drift and the heading drift. We study two different alternatives: a loose coupling system and a tight coupling system.

The proposed loose coupling system combines the outputs of the foot INS and the pocket INS. The goal is to obtain an improved position estimation with respect to the single-IMU localization systems. The first contribution of this system is the development of an algorithm to determine how accurate the heading of the foot INS is with respect to the heading of the pocket INS. The second contribution of the loose coupling system is that it leverages the complementary strengths of the single-IMU localization systems regarding the height estimation. The height error of the loose coupling system outperforms the height error of the foot INS and the pocket INS in 75% and 87%, respectively.

The last multi-IMU localization system we develop is the tight coupling system, which combines the raw measurements of the pocket IMU and the foot IMU. We develop a biomechanical model of the human leg which is used to analyze the typical motion, in terms of the roll and pitch, of the leg limbs. We compare the typical motion of the leg limbs to the one derived from the inertial roll and inertial pitch. In this way, we are able to observe the errors of an inertial localization system without the need of a reference trajectory.

In order to characterize the heading from the biomechanical point of view, we compare the heading of the thigh to the heading of the foot. The advantage of this analysis is that we can observe incoherences in the relative heading between the two body limbs, which is equivalent to the relative heading between the pocket IMU and the foot IMU, respectively.

The findings of the biomechanical study are then integrated in a tight coupling system. A highlight is that we avoid the use of hard constraints by modelling the roll and pitch angles of the pocket IMU and foot IMU as Gaussian distributions. With our proposal, it is possible to keep the behaviour of these angles coherent with respect to human motion. Regarding the relative heading, we introduce a pseudo-measurement update on the slope of the relative heading. The tight coupling system reduces its heading error in 70% and 72% with respect to the heading error of the pocket INS and the foot INS, respectively. Moreover, the height error of the tight coupling system is reduced in 87% and 75% with respect to the height error of the pocket INS and the foot INS, respectively.

The evaluation of the proposed methods leads to interesting observations. For instance, all the inertial localization systems have approximately the same average distance error. In contrast, the tight coupling system outperforms all the other inertial localization systems regarding the heading estimation. One of the highlights

of the loose coupling system is the reduction of the height error. This decrease is the result of sampling the height of the foot INS only when the user is walking the stairs.

We close our work by stating that multi-IMU localization systems are more accurate than single-IMU localization systems. This accuracy is reflected in a considerable improvement of the heading error and the height error. Therefore, we recommend the use of multiple IMUs placed on different parts of the body to improve the accuracy of an inertial localization system.

Resumen

Los sistemas de posicionamiento para peatones se han beneficiado de diferentes técnicas de fusión con el objeto de abordar las desventajas de dichos sistemas. En el caso particular de los sistemas inerciales, las técnicas de fusión más explotadas se centran en combinar la tecnología inercial con otras tecnologías como la navegación por satélite o el posicionamiento WiFi. Los sistemas de posicionamiento que combinan varios sensores inerciales montados en el cuerpo constituyen un campo menos estudiado que la fusión de sensores inerciales con otras tecnologías.

El objetivo de este trabajo es desarrollar sistemas de posicionamiento para peatones basados en la fusión de sensores inerciales. En concreto, se pretende determinar si es posible mejorar, a través de dicha fusión, la precisión en la estimación de la distancia, de la dirección de la marcha y de la altura. Los sensores inerciales se colocarán en el bolsillo delantero de los pantalones y en el pie de la misma pierna. Estas dos posiciones se han elegido por su movimiento característico durante la marcha. Además, el hecho de utilizar la misma pierna nos permitirá observar posibles correlaciones entre las medidas de los sensores inerciales del bolsillo y del pie.

El primer paso de nuestro trabajo es el diseño de la metodología de evaluación. Para ello nos hemos basado en las metodologías de evaluación implementadas en diferentes competiciones de sistemas de posicionamiento. Gracias a dicha metodología, hemos evaluado cuantitativamente los sistemas de posicionamiento inerciales basados en el pie y en el bolsillo. A continuación, hemos identificado las ventajas e inconvenientes de cada uno de dichos sistemas.

De acuerdo a los resultados del estudio previo, hemos elegido desarrollar sistemas de posicionamiento cuyo objetivo es abordar los tres inconvenientes principales de los sistemas inerciales. El primer inconveniente está relacionado con la necesidad de calibrar los parámetros de los modelos que estiman la longitud del paso. Dichos modelos son necesarios siempre que el sensor inercial se coloque por encima del tobillo, e.g. en el bolsillo. El segundo inconveniente de los sistemas inerciales es la acumulación del error en altura. Este error afecta principalmente a aquellos sistemas basados en un sensor inercial colocado en el pie. El último inconveniente que vamos a abordar es la acumulación de error en la dirección de la marcha o *yaw*. Este ángulo indica la dirección en la que el peatón se está moviendo. Dicho inconveniente es común a todos los sistemas inerciales y es la principal fuente de error en la estimación de la posición.

El sistema de calibración que proponemos estima, automáticamente, los parámetros

del modelo que calcula la longitud del paso. Para dicha automatización, utilizamos la posición estimada por el sistema inercial del pie. Demostramos la viabilidad del proceso tomando como el ejemplo el modelo del sistema inercial del bolsillo. En nuestro método, estimamos los parámetros óptimos del modelo a través de dos variables: la longitud del paso y la amplitud del cabeceo de la pierna. El primer parámetro lo estima el sistema inercial del pie mientras que el segundo se obtiene gracias al sistema inercial del bolsillo.

La principal ventaja de la calibración que proponemos es la automatización del proceso de calibración. Además, nuestra propuesta estima los parámetros del modelo en tiempo real, lo cual no es posible con las técnicas de calibración del estado del arte.

El siguiente objeto de estudio es la acumulación de error en altura y en *yaw*. Para abordar ambos inconvenientes proponemos dos sistemas de posicionamiento: un sistema modular y un sistema integrado.

El sistema modular combina la salida; es decir, la posición, de los sistemas inerciales del pie y del bolsillo. La primera contribución del sistema modular es el desarrollo de un método para comparar la precisión dos ángulos, *yaw*, y determinar de manera objetiva cuanto más preciso es un ángulo con respecto al otro. La segunda contribución del sistema modular es su método de estimación de la altura, mediante el cual se explotan las ventajas tanto del sistema inercial del pie como del sistema inercial bolsillo. Mediante la combinación de estos dos aspectos, el sistema modular consigue reducir el error en altura en un 75% y un 87% con respecto al error en altura de los sistemas inerciales del pie y el bolsillo, respectivamente.

El sistema integrado combina las medidas; es decir, la aceleración y la velocidad angular, de los sensores inerciales del pie y del bolsillo. El objetivo del sistema integrado es explotar aspectos biomecánicos relacionados con la marcha. Para ello, desarrollamos un modelo biomecánico de la pierna. Este modelo analiza cómo una persona camina desde el punto de vista de los ángulos inerciales: alabeo y cabeceo. Gracias al modelo biomecánico, podemos observar los errores en los ángulos de un sistema inercial sin necesidad de disponer de una trayectoria de referencia.

Para analizar el *yaw* de una extremidad desde el punto de vista biomecánico, es necesario comparar dicho ángulo al *yaw* de otra extremidad. Esta comparación nos lleva a la estimación del *yaw* relativo, que en nuestro caso compara el *yaw* del sensor inercial bolsillo con el del sensor inercial la pierna. Gracias a este análisis, podemos observar incoherencias biomecánicas en el *yaw* de los sistemas inerciales.

El sistema integrado incorpora los resultados del estudio biomecánico. En dicho sistema integrado, los ángulos tanto del pie como del bolsillo se estiman en el mismo filtro probabilístico de manera que los conceptos anteriores se pueden implementar de manera óptima. El sistema integrado reduce el error en la dirección de la marcha en un 70% y un 72% con respecto al error de los sistemas inerciales del bolsillo y del pie, respectivamente. Además, el error en altura del sistema integrado es un 87% y un 75% menor que el mismo error de los sistemas inerciales del bolsillo y del pie, respectivamente.

Todos los sistemas que hemos desarrollado se han evaluado con el mismo sistema de evaluación presentado anteriormente. Hemos podido observar varios aspectos interesantes durante dicha evaluación. Por ejemplo, todos los sistemas tienen aproximadamente el mismo error en distancia. En cuanto al error en el *yaw*, el sistema integrado es el más preciso. Tal y como indicamos antes, el elemento más destacado del sistema modular es la reducción del error en altura a través de la combinación de las características de los sistemas inerciales del bolsillo y del pie.

Con nuestro trabajo, podemos concluir que los sistemas de posicionamiento inerciales basados en dos sensores inerciales son más precisos que los sistemas de posicionamiento inerciales basados en un único sensor. La mejora en la precisión se refleja tanto en la precisión de la estimación de la dirección de la marcha como en la precisión de la estimación de la altura. Por lo tanto, recomendamos el uso de varios sensores inerciales distribuidos por el cuerpo con el fin de conseguir un sistema de posicionamiento más preciso.

Contents

1	Introduction	9
1.1	Challenges of Location-Based Services	10
1.2	Objectives and Research Questions	13
1.3	Thesis Contributions	13
1.4	Thesis Structure	15
2	State of the Art	17
2.1	Single-IMU Localization	18
2.2	Calibration of Non-Foot-Mounted Systems	21
2.3	Drift Compensation Techniques	22
2.3.1	Drift Compensation Based on Sensor Fusion	22
2.3.2	Drift Compensation Based on Algorithms	24
2.4	Summary of Unsolved Challenges of Inertial Pedestrian Localization .	26
3	Fundamentals	27
3.1	Attitude Vector	27
3.1.1	Attitude Vector Propagation	28
3.1.2	Implementation Through UKF	30
3.2	Pedestrian Dead Reckoning	32
3.2.1	Strapdown Algorithm	32
3.2.2	Step & Heading Algorithm	35
3.3	Robotics Fundamentals	38
3.3.1	Denavit-Hartenberg Parameters	38
3.3.2	Homogenous Matrix	39
4	T&E Methodology of Inertial Localization Systems	41
4.1	Challenges of Test & Evaluation	41
4.2	Proposed T&E Methodology	43
4.2.1	Ground Truth System	43
4.2.2	Performance Metrics	43
4.2.3	Data Set	44
4.3	Boundary Conditions	46
4.4	Characterisation of the Pocket INS and the Foot INS	46
4.5	Outline of Proposed Multi-IMU Approaches	51
4.6	Summary and Conclusions	53

5	Calibration of Step Length Models	55
5.1	Step Length Model of the Pocket INS	55
5.2	Calibration Overview	56
5.3	Calibration of the Offset	57
5.4	Full Calibration	62
5.5	Summary and Conclusions	69
6	Loose Coupling System	71
6.1	System Overview	72
6.2	Smart Fusion	73
6.2.1	Fusion for 2D	74
6.2.2	Fusion for 3D	76
6.3	Estimation of the Heading Quality	78
6.3.1	Proposed Method	79
6.3.2	Simulative Proof	80
6.4	Summary and Conclusions	84
7	Biomechanical Study of the Human Leg	87
7.1	Proposed Leg Model	87
7.2	Motion Tracking Experiment	90
7.3	Tilt Angles	93
7.3.1	Analysis with Ground Truth	94
7.3.2	Analysis with Inertial Data	97
7.3.3	Probabilistic Model	98
7.4	Relative Heading	102
7.5	Summary and Conclusions	105
8	Tight Coupling System	107
8.1	System Overview	107
8.2	Attitude Tracker	108
8.3	Comfort Zone Update	108
8.4	Relative-Heading Update	110
8.5	Distance Estimation	112
8.6	Summary and Conclusions	113
9	Evaluation	115
9.1	Evaluation of the Calibration	116
9.2	Evaluation of the Loose Coupling System	119
9.3	Evaluation of the Biomechanical Constraints	124
9.4	Evaluation of the Tight Coupling System	129
9.5	Summary and Conclusions	134
10	Conclusions and Future Work	141
10.1	Summary of the Main Contributions	141
10.2	Conclusions	143
10.3	Future Work	143
10.4	List of Publications	144

A	Human Gait	147
B	Attitude Representation	149
C	Unscented Kalman Filter	151
D	Simulative Proof Results (Extension)	155
E	Derivation of the Denavit-Hartenberg Parameters	159
F	Derivation of the Turn Rate Equations	163
G	Noise Parameters of the Inertial Sensors	169

List of Figures

1.1	Thesis contributions.	14
2.1	Elements of an inertial localization system.	17
2.2	Classification of inertial localization systems depending on the location of the sensor. The PDR algorithm depends on the body location of the IMU.	18
3.1	Representation of the relevant coordinate frames in inertial localization.	28
3.2	Block diagram of the UKF that iteratively tracks the attitude of an IMU.	31
3.3	Block diagram of the strapdown algorithm.	33
3.4	Block diagram of the UKF that iteratively tracks the position, velocity and attitude of an IMU.	33
3.5	Block diagram of the step&heading algorithm.	35
3.6	Step detector for a pocket IMU.	36
3.7	Pitch of the pocket IMU while walking horizontally and stairs walking.	36
3.8	Step length model exemplification for three different users.	37
3.9	Robotic structure that consists with three joints and two links.	38
4.1	Evaluation sequence followed to generate the performance figures. . .	43
4.2	Institute of Communications and Navigation of the German Aerospace Centre (DLR).	45
4.3	Approximate 2D trajectory and height profile followed by the users. .	45
4.4	Identification of the stop at the ground truth points.	46
4.5	Absolute value of the heading error for the pocket INS and the foot INS.	47
4.6	Pitch of the pocket INS with and without bias perturbation.	48
4.7	Simultaneous gait analysis of the pocket INS and the foot INS.	49
4.8	Pitch of the pocket INS while walking horizontally and while walking the stairs.	50
4.9	Height estimation of the foot INS.	50
4.10	Summary of multi-IMU approaches	51
5.1	Overview of the calibration method.	57
5.2	Thigh and foot behaviour during a step.	57
5.3	First-order linear regression models fitted to the step length and the pitch amplitude of the pocket INS of three different users.	58

5.4	Local minima of the error in the step length model.	59
5.5	Recursive estimation of the offset with approach 1 and 10 steps. . . .	60
5.6	Recursive estimation of the offset with approach 1 and 120 steps. . .	61
5.7	Comparison of the step length model adapted to the same user with two different set of parameters.	62
5.8	Effect of calibrating only the offset when the universal slope differs from the user's optimal slope.	63
5.9	Comparison of the different step length models of a user whose opti- mal slope differs from the universal one.	64
5.10	Comparison of the different step length models of a user whose opti- mal slope is approximately the same as the universal one.	65
5.11	Heat map with the offset values as a function of the change in walking speed.	66
5.12	Trend of the offset difference with respect to the increase in walking speed.	67
5.13	Offset variance for two different users.	68
5.14	Trend of the offset variance when the window length increases. . . .	68
5.15	Block diagram of the <i>Parameter calibration</i> block in Figure 5.1. . . .	69
6.1	Loose coupling representation.	71
6.2	Block diagram of the 3D loose coupling.	72
6.3	Behaviour of the pocket Inertial Measurement Unit (IMU) and the foot IMU during the stance phase.	73
6.4	Example of the heading weights during the automatic quality estima- tion.	76
6.5	Legs behaviour while walking upstairs.	77
6.6	Example of the height estimation of the foot-mounted INS.	78
6.7	Vertical displacement estimation in the loose coupling.	78
6.8	Example of unknown heading quality.	79
6.9	Block diagram for the estimation of the quality factor.	80
6.10	Reference walk of the example.	81
6.11	Set up of the simulative proof to validate the method to estimate the heading quality.	81
6.12	Case study 1	83
6.13	Case study 2	83
6.14	Case study 4	84
6.15	Case study 8	84
7.1	Simplification of the human leg as a robotic structure.	88
7.2	Setup of the IMUs and the reflectors during the motion tracking ex- periments.	91
7.3	Process to validate the leg model.	93
7.4	Analysis of human motion using the leg model.	94
7.5	Effect of a heading rotation with errors on the joint positions. . . .	94
7.6	Knee positions of User 1 estimated with the leg model.	95
7.7	Top view of the ankle and metatarsal positions of User 1 estimated with the leg model.	95

7.8	Most frequent knee positions.	96
7.9	Most frequent ankle positions.	96
7.10	Most frequent metatarsal positions.	96
7.11	Knee positions estimated with the inertial attitude.	97
7.12	Ankle and metatarsal position estimated with the inertial attitude.	98
7.13	Heat map of the tilt angles of the pocket IMU and the foot IMU.	99
7.14	Experimental PDF of the tilt angles of the thigh.	99
7.15	Experimental PDF of the tilt angles of the foot.	100
7.16	Tilt angles of the pocket IMU and foot IMU over time.	100
7.17	PDF of the tilt angles of the pocket IMU during the stance phase.	101
7.18	PDF of the tilt angles of the foot IMU during the stance phase.	101
7.19	Comparison of the relative heading estimated through the long and the short way.	103
7.20	Relative heading between the thigh and the foot of a user.	103
7.21	Generalization of the relative heading between the thigh and the foot.	104
7.22	Relative heading of the thigh and foot estimated with the inertial attitude.	104
7.23	Model of the inertial relative heading.	105
8.1	Block diagram of the tight coupling.	108
8.2	Example of the tilt angles of the pocket Inertial Navigation System (INS).	109
8.3	Example before and after the comfort zone update on the tilt angles of the pocket.	109
8.4	Example of the relative heading between the heading of the pocket INS and the heading of the foot INS.	110
8.5	Exemplification of the relative heading update.	111
8.6	Comparison of the relative heading before and after the relative heading update.	112
9.1	Approximate true trajectory.	116
9.2	CDF of the distance error of the pocket INS with different configurations.	117
9.3	Comparison of the model parameters estimated by the full calibration method and the offset calibration method.	118
9.4	Example odometry of the pocket INS with different calibration options.	119
9.5	CDF of the distance error of the single-IMU systems and the loose coupling system.	120
9.6	CDF of the heading error of the single-sensor systems and the loose coupling.	120
9.7	Example odometry of the loose coupling system.	121
9.8	Heading weights of the foot INS and the pocket INS of Figure 9.7.	122
9.9	Heading error of the odometries shown in Figure 9.7.	122
9.10	CDF of the height error of the single-IMU localization systems, the loose coupling system and the tight coupling system.	123
9.11	Height estimation of the inertial localization systems in Figure 9.7.	124

9.12	CDF of the distance error of the single-IMU localization systems with- out and with the comfort zone update.	125
9.13	CDF of the height error of the single-IMU localization systems with- out and with the comfort zone update.	126
9.14	CDF of the tilt angles of the pocket IMU during the stance phase. . .	127
9.15	CDF of the tilt angles of the foot IMU during the stance phase. . . .	127
9.16	CDF of the distance error of the single-IMU localization systems and the tight coupling system.	130
9.17	CDF of the heading error of the single-IMU localization systems and the tight coupling system.	130
9.18	Example odometry of the tight coupling system.	131
9.19	Heading error of the odometries shown in Figure 9.18.	132
9.20	Height estimation of the inertial localization systems in Figure 9.18. .	132
9.21	Pitch of the pocket IMU estimated by the tight coupling system and the pocket INS.	133
9.22	First-order linear regressions that model the relative heading.	134
9.23	Error bar of the distance error of all the inertial localization systems studied in this work.	135
9.24	Error bar of the heading error of all the inertial localization systems studied in this work.	136
9.25	Error bar of the height error of all the inertial localization systems studied in this work.	137
A.1	Phases of the gait cycle. The right leg is depicted in grey whereas the left leg is depicted in black.	147
A.2	Stride and step length during the gait cycle.	148
B.1	Navigation frame (n) and body frame (b). Each axis of the body frame can be presented in the navigation frame through the attitude of the body frame.	149
C.1	Block diagram of the states prediction of an UKF.	152
D.1	Case study 3	156
D.2	Case study 5	156
D.3	Case study 6	156
D.4	Case study 7	156
D.5	Case study 9	157
E.1	Representation of a robotic structure with three joints. Each joint has only one rotation axis, z_i . The base frame is represented by the triad $\{x_0, y_0, z_0\}$	159
F.1	Three successive rotations represented by the Euler angles. (a) Ro- tation around the x-axis. (b) Rotation around the resulting y-axis, namely y' . (c) Rotation around the resulting z-axis, namely z''	165

List of Tables

3.1	Example of a set of Denavit-Hartenberg parameters.	39
4.1	Summary of the experiments.	45
4.2	Performance figures of the single-IMU localization systems.	47
4.3	Strengths and weaknesses of the pocket INS and the foot INS.	49
4.4	Advantages and disadvantages of the two fusion approaches proposed.	52
6.1	Configuration of the gyroscope errors of the <i>IMU simulator</i>	82
6.2	Error configuration of each case study.	82
6.3	Summary of the quality factors of each case study.	85
7.1	Denavit-Hartenberg parameters of the leg model.	89
7.2	Set of joint positions of a straight leg.	90
7.3	Set of joint positions of a bent leg.	90
7.4	Summary table of the experiments to evaluate the biomechanical motion of the leg.	91
7.5	Results of the validation of the leg model.	93
7.6	Heuristic limits of the comfort zone of each joint given in terms of the joint position.	97
7.7	Parameters of the MLE Gaussian distributions of each tilt angle of the thigh and the foot.	102
9.1	Evaluation of the pocket INS with different calibration configurations.	117
9.2	Evaluation of the loose coupling system.	119
9.3	Evaluation of the pocket INS and the foot INS with the comfort zone update.	125
9.4	Residual sum of squares of the tilt angles distribution of the pocket IMU and the foot IMU.	128
9.5	Residual sum of squares of the tilt angles distribution of the pocket IMU and the foot IMU.	128
9.6	Evaluation of the tight coupling system.	129
9.7	Third quartile of the distance error, the heading error and the height error.	135
9.8	Summary of the strengths and weaknesses of all the inertial localization systems considered in this work.	138
10.1	List of publications.	144

D.1	Error configuration of each case study.	155
E.1	(Left) Definition of the new x -axis, i.e. x_1 . (Right) Denavit-Hartenberg parameters associated to the axis z_1	160
E.2	(Left) Definition of the new x -axis, i.e. x_2 . (Right) Denavit-Hartenberg parameters associated to the axis z_2	161
E.3	(Left) Definition of the new x -axis, i.e. x_3 . (Right) Denavit-Hartenberg parameters associated to the axis z_3	161
G.1	Random walk and bias stability of the accelerometers.	169
G.2	Random walk and bias stability of the gyroscopes.	169

Glossary

AAL Ambient Assisted Living. 11

CDF Cumulative Distribution Function. 44, 117, 120, 123, 125–127, 129, 131, 136

DCM Direction Cosine Matrix. 27–29, 34, 102, 150

DoF Degree-of-Freedom. 88

EKF Extended Kalman Filter. 30

GNSS Global Navigation Satellite System. 9, 22, 23

IMU Inertial Measurement Unit. 2, 13, 15, 17–24, 26–32, 34–37, 41, 45–48, 51–53, 55, 56, 60, 72–74, 76–82, 88, 90, 91, 94, 98–101, 106–113, 115, 119, 120, 122–131, 133–135, 137, 139, 141–144, 148, 169

INS Inertial Navigation System. 3, 13–15, 20, 25, 35, 37, 41, 43, 46–53, 55–59, 61, 63, 65, 69, 70, 72–85, 97, 106, 109, 110, 116–127, 129–139, 142, 143, 145, 155

ISO International Organization for Standardization. 41

LBS Location-Based Services. 10, 11

MEMS Micro-Electro Mechanical Systems. 18

MLE Maximum Likelihood Estimation. 100, 101

MVN MultiVariate Normal Distribution. 99, 100

OSM Open Street Map. 25

PDF Probability Density Function. 98–101, 106

PDR Pedestrian Dead Reckoning. 18, 19, 32, 46

PVC PoliVinyl Chloride. 90

RFID Radio Frequency IDentification. 23

SLAM Simultaneous Localization And Mapping. 24, 25, 122, 144

T&E Test and Evaluation. 13, 15, 41, 42, 53, 115, 141, 143–145

UKF Unscented Kalman Filter. 15, 20, 30–34, 82, 108, 112, 113, 131, 151–153

UWB Ultra-Wide Band. 23

ZUPT Zero-Velocity UPdaTe. 19, 34, 56, 74, 110, 147

Chapter 1

Introduction

*The future belongs to those
who believe in the beauty of their dreams*
—Eleanor Roosevelt

The survival and evolution of mankind has been tightly coupled to the evolution of navigation. One might consider this sentence an overstatement, but the fact is that by simply observing the sunrise and sunset, hunters and gatherers profited from a sense of time and orientation that increased their chances of survival. Tribes would migrate seasonally depending on the sun location, thus, going from poorly supplied areas to richly supplied ones.

Whereas sun-based navigation is limited to daylight use, the development of celestial navigation was crucial to promote seamanship. The Arabs' ambition to maintain and extend their trading routes propelled seamanship, not only in naval technology but also in navigation [1]. And so, the progress continues.

The 15th century, which could be labelled as the *Age of Discovery*, is a landmark in the history of exploration. Castile, nowadays Spain, and Portugal were at the cutting-edge of navigation, which allowed for the discovery of America. This achievement led to numerous economical benefits, and most importantly it paved the way to globalization.

With the promise of new lands and riches, it was only natural that efforts were dedicated to improve the contemporary navigation techniques. Since then until nowadays, technology has evolved all the way from celestial navigation to the Global Navigation Satellite System (GNSS).

As remarkable as the evolution in localization technologies has been, the applications derived from localization also deserve a special mentioning. Mankind has found a way to apply localization not only to guide vessels and aircraft but also to navigate pedestrians. In fact, pedestrian navigation systems have become necessary in a variety of applications.

Pedestrian navigation is used not only to guide a pedestrian from a starting point to an end one but also to save lives. For instance, pedestrian localization systems

can track the position of the firefighters that go into a collapsing building. In that way, should a firefighter need help, the chief who supervises the operation can send assistance to the exact point where the firefighter in need is.

In modern metropolises, the existence of blind spots puts pedestrians at risk when they interact with vehicles. Due to these blind spots, a driver cannot be aware of the presence of a pedestrian who is about to cross the street. Such unawareness increases the collision risk between the pedestrian and the vehicle. An option to address this challenge is to predict the collision risk between a pedestrian and a vehicle based on their respective locations and trajectories.

Nowadays, it is possible to localize a pedestrian using two types of devices, namely smartphones and wearable devices. A wearable device, or wearable, is carried by a user either by attaching it to her body, e.g. a smart watch, or embedding it in the clothes. The purpose of these devices is varied, and it ranges from duplicating the functionality of a smartphone¹ to health monitoring [2] and activity tracking [3].

Generally, smartphones have been widely used in the last decade, which makes them attractive to implement mass market applications. In contrast, wearables have become popular in the last five years [4] and their presence in the market is expected to grow to 411 million devices by 2020 [5].

Wearables are discreet and comfortable and they can operate during multiple hours. Moreover, they are attached to the body, and thus, they are able to measure kinematic information of the body limb the wearable is attached to. An advantage of wearables is that they can be attached to any body limb, whereas it is hard to carry a smartphone on certain body limbs, e.g. the foot. Furthermore, wearables have sensing and processing capabilities that are expected to be similar to those of a smartphone [4]. Finally, wearables are unobtrusive, which is an important factor for the success of wearable devices. These advantages make wearable devices the ideal ally to develop pedestrian localization systems.

In order to develop a localization system, it is necessary to understand the requirements and challenges of the localization-based application. These requirements and challenges are reviewed in the next section.

1.1 Challenges of Location-Based Services

This section presents a review of Location-Based Services (LBS). A LBS is the one that provides or customizes a service based on the user's location. The market of LBS is classified in two categories according to Basiri et al [6]: services for location-based information retrieval and services for safety and security. The last category is the focus of this section. More specifically, we focus on emergency services, healthcare services and transportation services.

¹<https://www.apple.com/de/apple-watch-series-3/>

Emergency services are those provided by the professional market, namely firefighters, policemen and emergency first responders. In this category, the potential users of location-based services are often dragged into life-threatening situations that can be either indoors or outdoors. For instance, firefighters entering a building on fire or policeman brigades coming to the location of a terrorist attack.

LBS for the professional market focus on tracking the user's position to ensure that they are safe. For instance, the chief of a fire brigade needs to know, at least with room-level accuracy, where the firefighters are. More importantly, the chief of the fire brigade needs to know the floor on which the firefighters are. In this use case, the pedestrian localization system should not interfere with the firefighter's activity. For instance, a firefighter will not have time to install any infrastructure in a collapsing building only to have her position tracked. Thus, possible solutions should be integrable within the clothes, e.g. through wearable devices.

The second market we analyze is the healthcare sector. An example of application is the Ambient Assisted Living (AAL) framework sponsored by the European Union². AAL aims at using information and communication technologies to favour the elderly to live independently at their homes. In this use case, healthcare professionals monitor remotely the user's activity levels. To that end, users may be equipped with a pedestrian localization system, which estimates how long a user has been active, i.e. walking. The accuracy requirement may be dictated by the minimum time, e.g. 1 min, that a user should be walking.

One of the syndromes that affect the elderly population is frailty: a decline in the physiological systems due to aging [7]. An option to monitor this syndrome is by assessing the degradation in the physical activity of the patient. To this date, monitoring the patients activity is done by visual inspection and with the patient's feedback. This method has two shortcomings. First, the visual inspection can only be carried out during a short period of time, e.g. 10 min to 30 min. Second, the patient may forget what she has done and provide incorrect or incomplete feedback.

Pedestrian localization systems could be used to track the patient's activity, e.g. how long a patient has been walking. This information can help doctors and nurses to objectively assess a degradation in the daily activity levels and take measures to cope with this syndrome. Another option is to monitor the patient's walking pace over a long period of time, e.g. six months or even a year. In this case, the pedestrian localization system should have an accuracy such that a doctor can detect a meaningful change in the patient's activity levels. An example is to be able to detect that the patient's walking pace reduces from 1 m/s to 0.5 m/s.

The pedestrian localization systems for AAL and frailty monitoring should be unobtrusive and comfortable to wear in order to favour the patients' willingness to use the system. Also, the devices need to have a long battery lifetime because they will have to be operating during several hours or even days.

The last market we review is transportation systems in urban environments. The number of accidents between pedestrians and vehicles in urban environments [8]

²<http://www.aal-europe.eu/>

has promoted the development of technologies that should guarantee the safety of a pedestrian. An example is a system which predicts the collision risk between a vehicle and a pedestrian. Such a system would require the position of both the vehicle and the pedestrian with an accuracy of at least the length of the vehicle.

An important requirement of the pedestrian localization system is that it should be implemented with a device that the user is already carrying, e.g. a smartphone or a wearable device. Otherwise, pedestrians may be reluctant to wear an additional device only for the purpose of localization. This requirement is a difference with respect to the professional market or healthcare sector. In these markets, the users are expected to wear additional devices for the purpose of localization.

Another use of pedestrian localization in urban scenarios is urban mobility. The latter is a topic that has also gained attention in the last years [9]. Urban mobility³ refers to the infrastructures that citizens have at their disposal to move in urban spaces. The goal is to achieve efficient and effective urban transport to satisfy the requirements regarding the policies for transportation systems or pollution in cities.

In order to effectively design and adapt the transportation options to the citizens' needs, we need to know how citizens move. This knowledge can be extracted from personal navigation devices which should work seamlessly over multiple modes of transportation, for instance walking, biking, travelling in a bus or in the subway. The pedestrian localization device should be able to estimate the pedestrian's position with an accuracy lower than the width of the sidewalk.

One of the challenges of this niche is to guarantee the user's privacy and security, which are a sensitive topic nowadays [10], as well as an unsolved challenge. For a successful realization of the use cases mentioned above, it will be necessary for governmental bodies to appropriately regulate these applications in order to ensure the privacy and safety standards.

All in all, we observe two common requirements of the different markets explored above. Firstly, all markets require the users to wear or carry the devices that contain the pedestrian localization system. Secondly, the devices for pedestrian localization system should be unobtrusive and comfortable to wear. These requirements are satisfied by wearable devices because not only they are carried or integrated in the clothes but they also unobtrusive.

In this thesis, we pay special attention to wearable devices due to the expected growth for their use [5]. We expect that a pedestrian will carry multiple wearable devices in the future. In such a case, it will be possible to implement localization systems that combine technologies and information from wearables worn on different body parts.

The advantage of using wearables worn on different body parts is that the fusion can be done with different approaches. For instance, we could combine the different technologies embedded in one wearable. Another option would be to combine the same technology from wearables worn on different body locations.

³https://ec.europa.eu/transport/themes/urban/urban_mobility_en

Due to its potential, the main focus of this work is the combination of wearable devices for pedestrian localization. The next section introduces the objectives of this work.

1.2 Objectives and Research Questions

The overall research objective of this thesis is pedestrian localization by means of inertial sensor fusion. We aim to determine the benefits in distance accuracy, heading accuracy and height accuracy of combining two IMUs in an inertial localization system. The IMUs will be mounted on the pocket and the foot of the same leg, respectively. The reason for choosing these body locations is that they have characteristic features during walking [11, 12]. Moreover, the fact that we consider the same leg will allow us to observe possible correlations between the measurements of the foot IMU and the pocket IMU during the walk.

In particular, we do have the following objectives:

- Research goal 1: determine the strengths and weaknesses, as well as the open challenges, of the inertial localization systems based on a foot-mounted IMU and a pocket-mounted IMU. We refer to these inertial localization systems as the foot INS and the pocket INS, respectively. An evaluation of the inertial localization systems will be carried out to generate benchmark figures for the next research goal.
- Research goal 2: investigate, develop and implement fusion methods with a foot-mounted IMU and a pocket-mounted IMU. For simplicity we refer to these sensors as the foot IMU and the pocket IMU, respectively. The proposed fusion methods should address the challenges identified during research goal 1. For each fusion method, the distance accuracy, heading accuracy and height accuracy will be estimated and compared to the performance figures of the foot INS and the pocket INS.

1.3 Thesis Contributions

An inertial localization system processes acceleration and turn rate vectors to iteratively estimate the pedestrian's position. Throughout this work, we refer to the pedestrian as the user of inertial localization systems. Finally, inertial localization systems may also be referred to as INS.

The first contribution of our work is the proposal of a Test and Evaluation (T&E) methodology to quantify the performance of an inertial localization system. In the design process of our T&E methodology, we have reviewed the state of the art of T&E methodologies of pedestrian localization systems. Our main finding is that the community has not adopted a standardized T&E methodology. Thanks to our T&E methodology, we have been able to assess the challenges of inertial localization

systems. In order to address them, we have developed three inertial localization systems which are summarized in Figure 1.1.

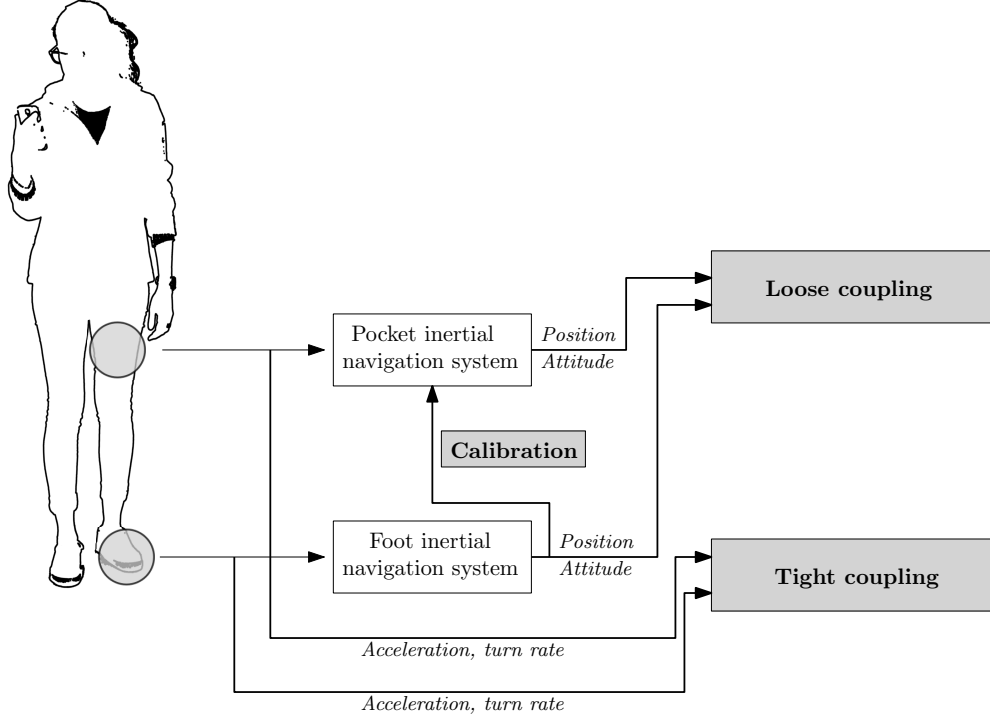


Figure 1.1: Block diagram of the contributions of this thesis. The contributions are indicated by the shadowed boxes.

The second contribution of this work is the development of an automatic calibration method of step length models. The calibration method uses the output of the foot INS to automatically estimate the user-dependent parameters of a step length model. In this work, the automatic calibration method is exemplified with a step length model developed for a pocket INS [13].

The third contribution is the development of a loose coupling system. The loose coupling system processes the output of independent systems, in our case these systems are the pocket INS and the foot INS. The output of these independent systems are the respective estimations of the user's position. The loose coupling system combines the step length and the heading of the pocket INS and the foot INS by weighting them. The associated weights reflect how accurate the step length and the heading are. In order to estimate the vertical displacement, the loose coupling system exploits the complementary 3D features of the pocket INS and the foot INS. The output of the loose coupling system system is a single estimation of the user's position.

The fourth contribution is the integration of biomechanical constraints of the human walk in inertial localization systems. We have analyzed the leg motion while walking and characterized the expected leg motion. This characterization is integrated in

a tight coupling system in two ways. Firstly, the tight coupling system imposes soft constraints on the roll and pitch of both the pocket IMU and the foot IMU. Secondly, the tight coupling system integrates a constraint on the difference between the heading of the pocket INS and the heading of the foot INS.

1.4 Thesis Structure

This thesis is structured as follows:

- in Chapter 2, we review the state of the art of inertial localization systems as well as the most relevant techniques to address the challenges of inertial localization. This chapter is supported by Appendix A and Appendix B.
- in Chapter 3, we introduce the fundamental concepts that are the basis of this thesis, namely the Unscented Kalman Filter (UKF), the two basic dead reckoning algorithms and the mathematical tool to model robotic structures. This chapter is supported by Appendix B, Appendix C and Appendix E.
- in Chapter 4, we describe the proposed T&E methodology to evaluate inertial localization systems. We also present the evaluation results of the foot INS and the pocket INS. We finalize the chapter with a summary of the identified challenges as well as an overview of the fusion methods implemented in this thesis.
- in Chapter 5, we develop the concept to automatically calibrate the step length models of non-foot-mounted inertial localization systems with a foot INS.
- in Chapter 6, we describe the loose coupling system for the estimation of a user's position. This chapter is supported by Appendix D, Appendix F and Appendix G.
- in Chapter 7, we present the biomechanical study of the human leg. In the study, we analyze the attitude vectors of the pocket INS and the foot INS.
- in Chapter 8, we describe the tight coupling system, which is based on the study of Chapter 7.
- in Chapter 9, we present the evaluation of all the proposed inertial localization systems. We finalize with the discussion of the results and a comparison of all the systems. This chapter is supported by Appendix G.
- in Chapter 10, we close our work by summarizing the main contributions and drawing the conclusions of this work. We also outline possible lines of research for future work.

Chapter 2

State of the Art

*A person who never made a mistake,
never tried anything new*
—Albert Einstein

This chapter reviews the state of the art of pedestrian inertial localization systems. As Figure 2.1 indicates, there are two main elements in an inertial localization system: the sensing unit and the processing unit. The sensing unit may be comprised by one or more IMUs. It generates the measurements that are processed in the processing unit by an algorithm which estimates the position of a user.

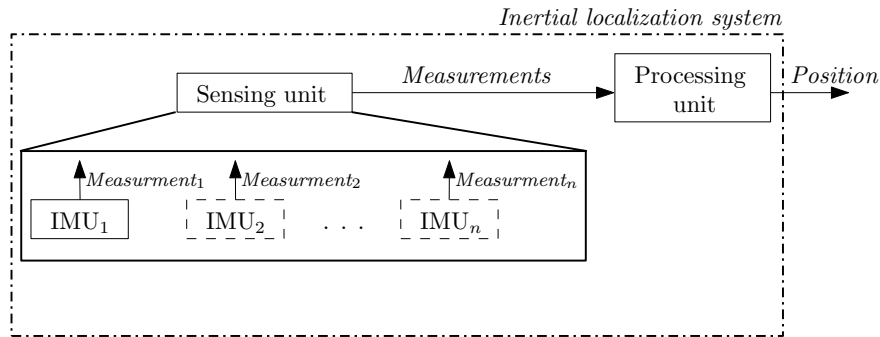


Figure 2.1: Elements of an inertial localization system.

The block diagram in Figure 2.1 is applicable to inertial localization systems for pedestrians, robots and objects. Since this work focuses on pedestrian localization systems, in further references, we will refer to the systems in Figure 2.1 as inertial localization systems instead of pedestrian inertial localization systems. Alternatively, we use the term single-IMU localization system to refer to the systems based on only an IMU.

In the following, we review the state of the art of inertial localization systems to identify the opportunities for innovation. Firstly, we review single-IMU localization systems and identify the two main challenges of these systems. Secondly, we review the techniques that address these challenges.

2.1 Single-IMU Localization

IMUs are based on Micro-Electro Mechanical Systems (MEMS) technology, which makes them small, light-weight and low-cost [14]. These properties of MEMS-based IMUs have favoured their use such that, nowadays, they can be found in all smartphones and the majority of wearable devices.

Pedestrian localization with IMUs implements the dead reckoning algorithm or Pedestrian Dead Reckoning (PDR). The user's position is computed iteratively, such that the new position estimate is the sum of the previous estimate and the increment in distance in each of the cartesian axes. There are two main types of PDR algorithms: the strapdown algorithm and the step&heading algorithm.

As Figure 2.2 depicts, Inertial localization systems can be classified in two main types depending on the body location of the IMU: foot-mounted and non-foot-mounted inertial localization systems. The body location of the IMU conditions not only the type of PDR algorithm to be used, but also the event of the gait cycle that is observed through the IMU. Figure 2.2 points out both the PDR algorithm and the events of the gait cycle associated to each body location.

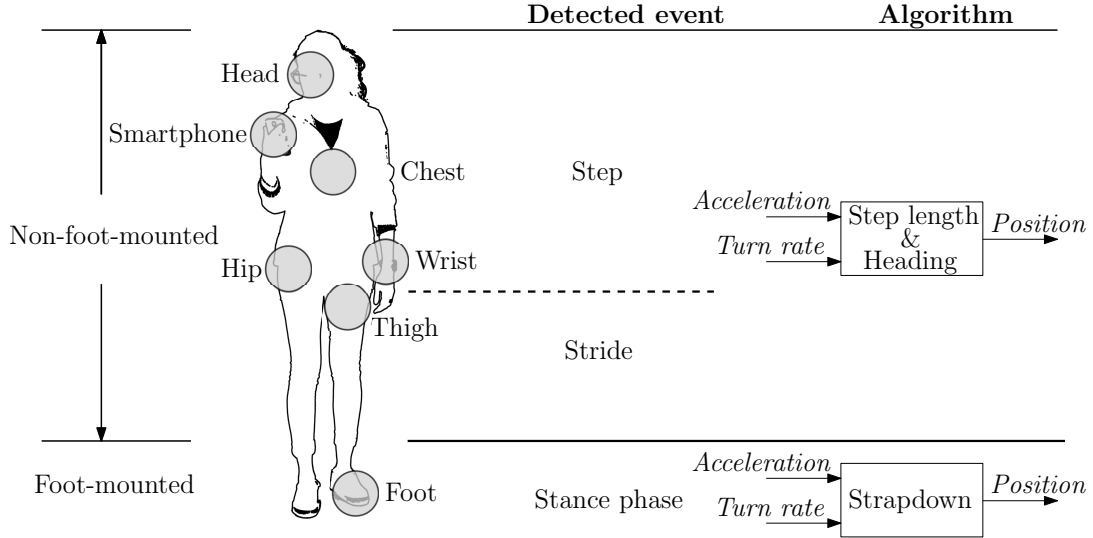


Figure 2.2: Classification of inertial localization systems depending on the location of the sensor. The PDR algorithm depends on the body location of the IMU.

There are two main events of the gait cycle that are exploited in nowadays PDR algorithms: the stance phase and the step or stride. The stance phase refers to the phase of the gait cycle when the foot is in contact with the ground. The stance phase is observable by placing the IMU on either foot. The step or stride represents the length walked by a user. A stride is defined by the distance between two consecutive stance phases of the same leg. A step is defined by the distance between consecutive stance phases of alternating legs, e.g. between the stance phase of the right foot

and the stance of the left foot. For further details on the events of the gait cycle, the reader is referred to Appendix A.

Single-IMU localization systems began by placing the sensor on the foot. In this case, the PDR algorithm applied to estimate the user’s position is the strapdown, see Figure 2.2. This approach integrates the turn rate vector to estimate the attitude of the IMU [11]. Then, the attitude is used to project the acceleration vector onto the localization frame. After correcting the gravity effect, the acceleration vector is double-integrated to estimate the user’s position.

The challenge of position tracking with the strapdown algorithm is the error accumulation in the position estimation. The error accumulation occurs due to the integration of the bias and bias stability that disturb the inertial measurements [11]. In fact, the position error grows cubic over time due to the integration of the bias and bias stability. Such a degradation of the position error makes it infeasible to implement the strapdown algorithm with IMUs.

Foxlin [15] presented the first low-cost inertial localization system based on a foot IMU. He implemented a novel concept, known as Zero-Velocity UPdaTe (ZUPT). The ZUPT corrects the velocity estimated by the inertial localization system during the stance phase of the foot by setting the estimated velocity to zero. The main advantage of the ZUPT is that the error growth in the position estimation is reduced to linear instead of cubic. Nevertheless, the position error still accumulates over time.

The key to an effective ZUPT is the correct detection of the stance phase. In [15], Foxlin proposed the use of thresholds on the acceleration vector and turn rate vector to detect the stance phase. Other approaches have arisen over time, e.g. detectors based on the energy of the turn rate vector or the variance of the acceleration vector [16]. Ruppelt *et al.* proposed a stance phase detection method based on a finite-state machine [17].

Figure 2.2 indicates that there are inertial localization systems based on non-foot-mounted IMUs. The goal of these systems is to profit from widespread devices with integrated IMUs, e.g. smartphones, smart watches or smart glasses. Inertial systems based on non-foot-mounted IMUs follow the step&heading algorithm. That is, the user’s position is estimated by computing the user’s step length and heading. These two variables are used to estimate the displacement in each cartesian axis, which are then added to the previously estimated position.

The step&heading algorithm requires a step length model, which is a function that relates observable parameters, e.g. the time-difference between the maxima of the acceleration norm [18], with the step length. The observable parameters are weighted by scaling factors which have to be adapted to each user for an optimal performance of the step length model.

The step&heading algorithm suffers from two types of cumulative errors. The first one is the error accumulation due to the estimation of the user’s step length through a model. The second one is the error accumulation due to the heading drift.

In contrast to the strapdown approach, the step&heading algorithm is limited to 2D localization. There are, nevertheless, certain body locations that allow for 3D position estimation. Munoz presents in [19] a pocket INS with 3D position estimation. The author is able to identify stairs by analyzing the pitch of the leg. In such a case, a model to estimate vertical displacement is developed in order to track the user's 3D position using only a pocket IMU.

Smartphones can be carried in the front pocket of the trousers. In this case, an inertial localization system as the one in [12] can track the user's position with the step&heading algorithm. The authors present a novel approach to estimate the step length using the opening angle of the leg. The heading is estimated through the attitude tracking algorithm implemented in an UKF. Dent *et al.* [20] focus on the estimation of the heading with a pocket IMU, where the principal component analysis is used to extract the user's heading.

Smartphones can also be held in the hand. In this case, the step&heading algorithm assumes a specific carrying mode. The carrying mode defines how the user is holding the smartphone, e.g. holding the phone while the hand is swinging or holding the phone while staring at it. The disadvantage of assuming a carrying mode is that the assumption may not hold because the motion of the hand is decoupled from the motion of the body. For instance, a user can be walking and moving his hand randomly instead of swinging it. Therefore, hand-held inertial localization is more challenging than, for instance, inertial localization system based on a pocket IMU or a foot IMU.

To address the previous challenge, it is necessary to account for the carrying mode of the smartphone while the user is walking. Some approaches have been proposed by Renaudin *et al.* [21] and Deng *et al.* [22] to detect the carrying mode of a smartphone. Then, the step&heading algorithm is adapted depending on the detected carrying mode.

Elhoushi *et al.* stress that recognising the motion mode is important to improve the accuracy of the position estimation with smartphones, smart watches and smart glasses [23]. The motion mode refers to the user's activity, which could be walking, standing, sitting, running, etc. They show that it is possible to enhance the position accuracy by recognising the user's activity. The system developed in [24] not only considers different motion modes but also different carrying modes.

Inertial localization with smart watches and smart glasses face similar challenges as hand-held localization. That is, the devices are attached to body parts, wrist and head respectively, whose motion might be different from that of the body during walking. For instance, a user might be walking and scratching his head or walking straight while looking to the right. These behaviours are normal during natural walking but they difficult the tracking of a user's position with wrist-mounted or glass-mounted sensors.

In [25], Diez *et al.* direct their efforts to improve the heading estimation of a wrist-mounted IMU. They modify the method known as improved heuristics drift elimination so that it can be implemented with step&heading algorithms. The authors

of [26] develop an inertial localization system based on smart glasses. The proposed system detects and filters out the head motions that might interfere with the estimation of the user’s position.

In general, inertial localization systems have two main challenges. The first challenge regards non-foot-mounted inertial localization systems and their need to calibrate the step length model. The second challenge is the error accumulation in the position estimation. This challenge is common for both foot-mounted and non-foot-mounted inertial localization system. The following sections review these two challenges.

2.2 Calibration of Non-Foot-Mounted Systems

Pedestrian inertial localization with non-foot-mounted IMUs relies on a step length model. The parameters of the latter need to be adapted to the user for an optimal performance of the step length model. The adaptation of the parameters is defined, in this work, as calibration.

There are two main techniques to perform the calibration: training the model parameters or manual calibration. In the former, the parameters are estimated by training them over a number of users [27]. The challenge of this alternative is to collect a data set varied enough in terms of number of users, age range, height variety, weight variety, etc. The main disadvantage of this calibration method is that the trained parameters are not optimal to the user, which leads to position errors.

In a manual calibration, the parameters of the step length model are adapted to each user [19]. A manual calibration requires the user to walk a predefined straight distance. By counting steps, an average step length can be estimated. Based on the latter, the parameters of the step length model can be adapted to match the average step length. The disadvantage of this alternative is that the manual calibration is prone to errors if the user is not familiar with the calibration method.

Manual calibration can also be implemented with maps [28]. In this case, the true distances walked by the user can be estimated through the map, and thus, the step length model can be calibrated without the need of manually measuring distances. The disadvantage of this alternative is that a map is not always available for a user to use.

The aforementioned calibration methods are possible solutions to the calibration challenge. They have, nevertheless, disadvantages that can be summarized in three points. Firstly, they may not be optimal to the user. Secondly, they may be prone to errors because they require human intervention. Finally, they may require external information, e.g. maps, which may not be available.

2.3 Drift Compensation Techniques

The attitude of an IMU can be represented in different ways, see Appendix B. One of them is the Euler angles, a triad composed of the roll, the pitch and the heading. These angles represents the successive rotations around each sensor axis to align the sensor frame with the navigation frame.

The errors in the attitude vector, also known as drift, are the main error source in inertial localization. The drift is the error accumulated in the attitude vector which is caused by the integration of the bias and the bias stability of the turn rate measurements [29].

In tri-axis IMUs, the gravity allows for the observation of two angles, roll and pitch, out of the three that represent the sensor attitude [30]. The gravity information can be integrated within the attitude tracking algorithm to correct the roll and pitch estimations [19]. However, this correction is not extensive to the heading, which remains unobserved [30].

The impossibility to observe the heading makes the position error due to the heading drift the most challenging aspect of inertial localization. In the following, we review the approaches implemented in the state of the art to address this challenge. These approaches follow one of two techniques: sensor fusion techniques and algorithm-based techniques. Each one of them has advantages and disadvantages that will also be pointed out below.

2.3.1 Drift Compensation Based on Sensor Fusion

Heading drift-reduction by sensor fusion combines the measurements of an IMU with measurements from other sensors. The latter could be from a different technology, for instance GNSS or WiFi, or the same technology, i.e. IMUs. In the following, approaches that combine IMUs with a different technology are explored in the first place. Then, approaches based on the combination of multiple IMUs are presented.

Fusion of Inertial Technology With Other Technologies

The goal of the fusion is to combine sensors whose strengths and weaknesses are complementary. In the case of inertial localization, the main weakness is the drift in the heading.

A possible sensor fusion is the combination of inertial measurements and GNSS measurements, which can be a loosely coupled fusion or a tightly coupled fusion [31]. Loosely coupled fusion refers to the fusion of GNSS position estimates with inertial position estimates. This approach is inherited from fields like vehicle localization, and it has been successfully implemented in previous inertial localization systems [28]. In this case, the inertial trajectory is corrected with the absolute position estimated through GNSS, which reduces the effect of the heading drift in the

estimated trajectory. The tight fusion is the combination of raw inertial measurements, i.e. acceleration and turn rate, with raw GNSS data [32, 33].

In indoor environments, it is possible to combine inertial localization with WiFi measurements. For instance, Chen *et al.* [34] use an IMU to track the user's position. The performance of the inertial localization system is improved by incorporating WiFi measurements. These measurements allow for the estimation of the user's initial position and walking direction.

The disadvantage of radio-frequency signals is that they are not able to estimate a position solution if there are not, at least, three access points available. In [35], the authors propose a tight coupling of inertial measurements with WiFi ranges. With this proposal, WiFi ranges support inertial localization even when not enough access points are visible to the user. Moreover, WiFi-based positioning suffers from interference between different access points [34]. Also, the variability of the signal levels makes it challenging to use WiFi signals for positioning [34].

There are further ranging-based localization techniques suitable to be combined with inertial localization. For instance, Ultra-Wide Band (UWB)-based ranging [36, 37]. However, the installation cost of the UWB nodes hinders the use of this technology [38]. In [39], Zampella *et al.* compare the performance of an inertial localization system when it is aided by UWB, Radio Frequency IDentification (RFID) and both of the latter. As expected, the system where all technologies are combined is the most accurate.

Pham *et al.* combine inertial measurements with LIDAR [40], which is a ranging-based system that uses laser to measure the distance to surrounding objects. In [40], the LIDAR is used to detect walls that are used to correct the heading estimates of an inertial localization system.

The magnetic field can also be used to improve the attitude estimation of an inertial localization system. For instance, the authors in [29] analyze the effectiveness of using magnetometers to estimate the biases of the gyroscopes. A disadvantage of magnetometers is that they are sensitive to magnetic disturbances, which are common in indoor environments. Ilyas *et al.* develop a detector of magnetic disturbances [41] in order to use only the undisturbed magnetic field measurements.

An interesting fusion of IMUs and magnets is carried out in [42]. The authors place a magnet in one foot and an inertial localization system on the other foot of the user. The goal of this set up is to improve the stance phase detection, which improves the overall system performance.

Fusion of Inertial Technology with Inertial Technology

Sensor fusion is generally understood as the combination of different technologies. Nevertheless, the fusion can also take place with sensors of the same technology. In this thesis, the systems that combine multiple IMUs are referred to as multi-IMU localization systems.

To this day, the fusion of IMUs to improve the performance of inertial localization systems has been implemented in one of two ways. The first multi-IMU approach is to combine the raw measurements of multiple IMUs in a single raw measurement. For instance, Skog *et al.* [43] propose a 16-element array made up of low-cost accelerometers. The authors prove that it is possible to reduce the overall noise figures by averaging the acceleration vector of low-cost sensors. Bancroft and Lachapelle propose different algorithms to combine up to five IMUs [44]. Each algorithm is a different way of combining the individual raw data. The authors study the benefits and shortcomings of the combination of IMUs by each algorithm.

The second multi-IMU approach combines IMUs by placing them on different parts of the body. The goal is to constraint the position estimation on the basis of the limitations of the human motion. An example is the system proposed in [45], where two IMUs are mounted on each foot respectively. The authors estimate two different position estimations of the user. Then, a constraint on the maximum separation between the aforementioned positions is applied to limit the accumulation in the position error of inertial localization systems.

The approach of integrating inertial navigation and biomechanics in an inertial localization system has also been studied. In [46], the authors propose the use of seven IMUs distributed around the legs to estimate the displacement. Then, the authors use a leg model to estimate the user's displacement. Their leg model requires the attitude of the leg limbs as input, and in order to correct the attitude errors, hard constraints are imposed on certain angles of the leg. For instance, the abduction and adduction of the knee is set to zero, i.e. the roll of the knee is forced to be null. The abduction is the motion of a limb away from body centre, whereas the adduction is the motion of the limb towards the body centre [47]. The disadvantage of this approach is that hard constraints may cause system malfunctions in some cases.

2.3.2 Drift Compensation Based on Algorithms

In the previous section, the drift of inertial localization systems was addressed by combining IMUs with other sensors of the same or different technology. There are alternatives to address the heading drift that do not require additional sensors. These alternatives are based on algorithms that exploit a specific characteristic of the environment or the human walk. Algorithm-based techniques can be classified into three main types: Simultaneous Localization And Mapping (SLAM), landmark detection and map integration. In the following, examples of these three drift-reduction techniques are given.

The first algorithm-based technique is inherited from the field of robotics [48]. This technique is commonly known as SLAM. The goal of SLAM is to localize a robot, or a user in our case, and simultaneously generate a map of the trajectory walked. The SLAM algorithm is commonly implement through particle filters [49].

In [50], the authors use the SLAM algorithm to reduce the position error of a foot

INS. The algorithm here proposed, named as FootSLAM, profits from the fact that a user revisits areas in a building, which is known as loop closure. The more the user revisits an area the more accurate the localization, and in turn, the more accurate the estimated map.

An advantage of SLAM-based algorithms is that they are a means to integrate measurements from different sources. The reason is that they are based on particle filters, which can integrate different information sources. For instance, inertial measurements and radio measurements [51] or inertial measurements with WiFi measurements [52]. The disadvantage of this algorithm is the need for loop closure, which might not always happen.

The second algorithm-based technique to reduce the heading drift is the use of landmarks. The latter are specific elements in the environment that can be detected and uniquely identified. If a landmark is detected, and the user revisits it, then it is possible to estimate the drift in the heading. That is the proposal of Munoz *et al.* [53], where the proposed landmarks are corners and stairs.

Further landmarks are investigated in [34], namely elevators, escalators, and doors in addition to corners and stairs. The authors use landmarks to correct the position estimation of the inertial localization system. In this work, it is necessary to map the location of these landmarks.

Prieto *et al.* [54] extend the concept of landmark to other elements like the body location of the sensor. In fact, the authors do not use the noun landmark. Instead, they use the term context to refer to either the motion mode of the user, the body location of the sensor or an element of the surrounding, e.g. ramps or elevators. The localization algorithm is then based on a hidden Markov model which incorporates contextual knowledge.

The disadvantage of landmark-based drift compensation is that its effectiveness depends on the accuracy with which the landmarks are detected and mapped. Moreover, the user needs to revisit the landmarks in order to compensate the drift.

The third algorithm-based technique is to incorporate maps within the inertial localization. If a map is available, it can be used to impose constraints in the trajectory estimated by the inertial localization system. A common approach when using maps is to implement the localization with a particle filter [55, 56].

When the location in question is outdoors, tools like Open Street Map (OSM)¹ are available for use. Indoor scenarios are, however, more challenging regarding the availability of maps. These maps may be nonexistent or unavailable for public use, which is one of the disadvantages of this technique.

¹www.openstreetmap.org

2.4 Summary of Unsolved Challenges of Inertial Pedestrian Localization

All in all, pedestrian localization based on IMUs has still unsolved challenges. The most important ones can be summarized in the following:

- the calibration of step length models for non-foot-mounted localization systems and,
- the drift in the heading.

These open challenges have been addressed, in the past, by following different approaches. In this work, we will combine two IMUs to propose an alternative solution to these open challenges.

Chapter 3

Fundamentals

*I have not failed, I have just found
10,000 things that won't work
—Thomas Edison*

The basic concepts and algorithms on which this thesis is built up on are presented in this chapter. We begin with a description of the method to estimate the attitude of an IMU. Following, the two alternatives for dead reckoning with IMUs are described. Finally, we introduce a well-known mathematical tool that will come in use at the end of this thesis.

3.1 Attitude Vector

Let us consider the IMU represented in Figure 3.1. This IMU has an associated coordinate frame, which will be named as the *body frame*¹. The latter is defined by the axes $\{x_b, y_b, z_b\}$ in Figure 3.1. The sensor, and therefore its associated frame, is moving in a world whose coordinate frame is fixed. The coordinate frame of the world is named the *localization frame* and it is defined by the set $\{x_n, y_n, z_n\}$, see Figure 3.1.

The attitude of a rotating body, see Figure 3.1, describes the relationship between the body frame with respect to another frame of reference, e.g. the localization frame. The attitude may be represented in three different ways [57], namely the Euler angles, the Direction Cosine Matrix (DCM) and the quaternions. In this thesis, we use the Euler angles and the DCM. The Euler angles define the three successive rotations that have to be applied around each rotation axis to align the body frame with the localization frame. We adopt the following convention regarding the Euler angles:

- the *roll* (ϕ) defines the rotation around the x-axis,
- the *pitch* (θ) defines the rotation around the y-axis and,

¹The body frame can also be referred to as the *sensor frame*.

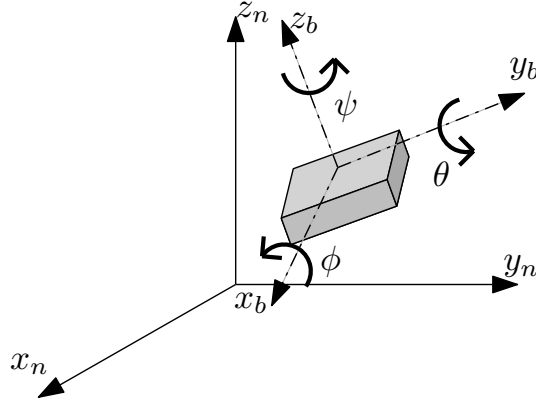


Figure 3.1: Representation of the relevant coordinate frames in inertial localization: the localization frame (n) and the body frame (b).

- the *yaw* (ψ) defines the rotation around the z -axis. In this work, we will use indistinctively the terms yaw and heading.

The direction cosine matrix, or DCM, is a 3×3 matrix that rotates a vector from one coordinate frame to another one. Given a vector whose coordinates are represented in the body frame, \mathbf{v}_b , its coordinates in the localization frame, \mathbf{v}_n , can be estimated as:

$$\mathbf{v}_n = \mathbf{C}_{nb} \cdot \mathbf{v}_b, \quad (3.1)$$

where \mathbf{C}_{nb} represents the direction cosine matrix that rotates a vector from the body frame (b) to the localization frame (n).

The Euler angles and the DCM contain the same information, i.e. the attitude of the body frame with respect to the localization frame. For further details about the relationship between the Euler angles and the DCM, the reader is referred to Appendix B.

The following sections detail the algorithm to successively track the attitude of a body with respect to a frame of reference.

3.1.1 Attitude Vector Propagation

The attitude of the IMU depicted in Figure 3.1 can be tracked iteratively through the turn rate measurements of the IMU [57]. Let us write:

$$\boldsymbol{\omega}^k = [\omega_x^k, \omega_y^k, \omega_z^k]^T, \quad (3.2)$$

where $\boldsymbol{\omega}^k$ is the 3D-turn rate measurement, at the k -th time instant, generated by the IMU. The component ω_i^k , with $i = \{x, y, z\}$, defines the turn rate around the i -axis.

The iterative tracking of the sensor attitude follows the equation:

$$\mathbf{C}_{nb}^{k+\delta^k} = \mathbf{C}_{nb}^k \cdot (\mathbf{I}_3 + a_1 \cdot \mathbf{B} + a_2 \cdot \mathbf{B}^2), \quad (3.3)$$

where \mathbf{C}_{nb}^k is the DCM at the k -th time whereas $\mathbf{C}_{nb}^{k+\delta^k}$ is the DCM δ^k seconds later. In general, δ^k denotes the sampling time of the IMU. The term \mathbf{I}_3 denotes the third-order identity matrix.

The skew matrix \mathbf{B} follows the equation:

$$\mathbf{B} = \delta^k \cdot \begin{bmatrix} 0 & -\omega_z^k & \omega_y^k \\ \omega_z^k & 0 & -\omega_x^k \\ -\omega_y^k & \omega_x^k & 0 \end{bmatrix}. \quad (3.4)$$

The scalars a_1 and a_2 are computed as:

$$a_1 = \frac{\sin(\sigma)}{\sigma}, \quad (3.5)$$

$$a_2 = \frac{1 - \cos(\sigma)}{\sigma^2}, \quad (3.6)$$

where $\sigma = \delta^k \cdot |\boldsymbol{\omega}^k|$ and $|\cdot|$ denotes the norm of the argument.

The iterative equation (3.3) requires an initial attitude matrix (\mathbf{C}_{nb}^0). In inertial localization, the process of estimating the initial matrix (\mathbf{C}_{nb}^0) is done within an initial alignment. The latter can be carried out in different ways. An alternative is by forcing the IMU to have a specific orientation. For instance, by forcing the horizontal plane of the sensor to be parallel to the horizontal plane of the localization frame, see Figure 3.1.

In practice, the accelerometers in the IMUs can be used to determine the initial attitude of the sensor. To that end, let $\boldsymbol{\alpha}^k$ be the acceleration vector measured by the IMU at the k -th time. The vector $\boldsymbol{\alpha}^k$ can then be written as:

$$\boldsymbol{\alpha}^k = [\alpha_x^k, \alpha_y^k, \alpha_z^k]^T, \quad (3.7)$$

where α_i^k denotes the acceleration measured along the i -axis, with $i = \{x, y, z\}$.

If the IMU only experiences the gravity force ($\boldsymbol{\alpha}_g$), the latter can be used to estimate the roll and pitch [30]:

$$\phi^0 = \arctan\left(\frac{\alpha_{gy}}{\alpha_{gz}}\right), \quad (3.8)$$

$$\theta^0 = \arctan\left(\frac{-\alpha_{gx}}{\sqrt{(\alpha_{gy})^2 + (\alpha_{gz})^2}}\right), \quad (3.9)$$

where $\boldsymbol{\alpha}_g = [\alpha_{gx}, \alpha_{gy}, \alpha_{gz}]^T$. To estimate the gravity force ($\boldsymbol{\alpha}_g$), the IMU should measure only the gravity force. A common practice is to keep the IMU still during the first few seconds, e.g. 5s. During that time, the acceleration vector can be averaged to estimate gravity force ($\boldsymbol{\alpha}_g$) and, then, the associated initial roll (ϕ^0) and initial pitch (θ^0) can be estimated.

The aforementioned method to estimate the attitude allows to estimate only the initial roll (ϕ^0) and pitch (θ^0). The initial yaw (ψ^0) remains unobserved [30]. This is

a limitation of inertial localization that appears when equation (3.8) and equation (3.9) are inferred. For further details regarding this limitation, the reader is referred to [30]. A common practice is to initialize the heading of inertial localization systems to zero:

$$\psi^0 = 0. \quad (3.10)$$

Equation (3.2)-equation (3.10) present the theoretical approach to track the sensor attitude. For a practical implementation, these equations need to be integrated in a probabilistic filter which is described in the following section.

3.1.2 Implementation Through UKF

The attitude tracking algorithm presented in the previous section cannot be directly implemented with measurements from medium- or low-cost IMUs. The reason is that the errors of the inertial measurements, namely the bias and bias stability, accumulate due to the integration of equation (3.3). Therefore, it is unfeasible to implement equation (3.2)-equation (3.10) standalone.

The use of Kalman filters is an alternative to reduce the effect of the inertial errors in the attitude estimation. A Kalman filter is a version of Bayesian estimators that estimate a set of states. The evolution of these states over time is modelled by the process model. Kalman filters allow to incorporate external measurements that relate to the states through the measurement model.

Regarding attitude tracking, there are two possible implementations of the Kalman filter, namely the Extended Kalman Filter (EKF) and the unscented Kalman filter (UKF). These two implementations of Kalman filter come in use when the functions of the process model or the measurement model are not linear [58]. The EKF is based on a linearization of the process model and measurement model. The disadvantage of this implementation is that it does not adapt to highly non-linear systems, e.g. a system whose process model includes sine functions, cosine functions and multiplications of the latter. In such cases, the UKF is a better fit than the EKF. Moreover, the UKF does not require any linearization, which simplifies the implementation of the filter.

Provided that the attitude tracking algorithm is highly non-linear, we implement this algorithm through an UKF [59]. The UKF is a probabilistic filter that estimates the states by averaging a set of sigma points [58]. The latter are sample points of the states distributed around the true mean and covariance of the states. The reader is referred to Appendix C for the detailed implementation of the UKF equations.

In this thesis, the states vector (\mathbf{x}) of the attitude tracking filter contains the Euler angles (Ψ) and the bias of the gyroscopes (\mathbf{b}_g). Let us write:

$$\mathbf{x} = [\Psi^T, \mathbf{b}_g^T]^T, \quad (3.11)$$

where $\Psi = [\phi, \theta, \psi]^T$, whereas $\mathbf{b}_g = [b_{gx}, b_{gy}, b_{gz}]^T$.

The UKF follows the sequence of a Kalman filter. The block diagram for an attitude tracking UKF is given in Figure 3.2. The states vector is estimated in two steps: the prediction step and the measurement update. These steps are detailed in the following.

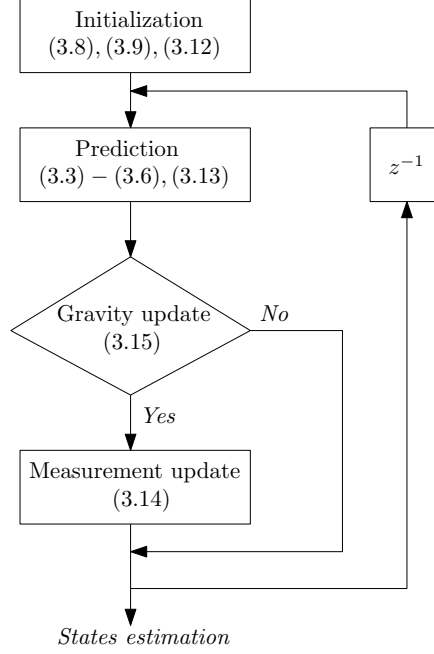


Figure 3.2: Block diagram of the UKF that iteratively tracks the attitude of an IMU.

Prediction

The states of the UKF can be initialized with equation (3.8) and equation (3.9) regarding the roll and pitch, respectively. The remaining states are usually set to zero, that is:

$$\mathbf{x}^0 = [\phi^0, \theta^0, 0, \mathbf{0}_{3 \times 1}^T]^T. \quad (3.12)$$

where $\mathbf{0}_{3 \times 1}^T$ is a zero-element vector with dimension 3×1 .

During the prediction, the attitude (Ψ) is propagated according to equation (3.3)-equation (3.6). Since the gyroscope bias is a low frequency error, its value changes slowly over time [60]. Therefore, it is reasonable to assume that its value remains constant from one time $k - 1$ to the next time k . Therefore, the process model of the bias can be formulated as:

$$\mathbf{b}_g^k = \mathbf{b}_g^{k-1}. \quad (3.13)$$

Measurement update

In the case of the attitude tracking, the measurements are the roll and pitch observed through the gravity [59]. These angles are observed when the IMU is undergoing no

external acceleration, and thus, the only force acting upon the sensor is the gravity force ($\boldsymbol{\alpha}_g$).

Under the previous condition, the roll and pitch of the IMU can be estimated by equation (3.8) and equation (3.9). Let us denote these angles by ϕ_z and θ_z respectively. Then, the measurement vector (\mathbf{z}^k) at the k -th time can be composed as:

$$\mathbf{z}^k = [\phi_z^k, \theta_z^k]^T. \quad (3.14)$$

The previous measurement vector is used during the measurement update. It takes place when the IMU is undergoing only the gravity acceleration. These times can be detected by checking the following inequality:

$$\text{abs}(|\boldsymbol{\alpha}_g| - g) \leq \delta_g, \quad (3.15)$$

where $|\cdot|$ denotes the norm of the argument and $\text{abs}(\cdot)$ denotes the absolute value of the argument. g is the value of the gravity force, which equals 9.832 m/s^2 , and δ_g is a threshold that should be set to a small value, e.g. $\delta_g = 0.8 \text{ m/s}^2$. We have chosen this value heuristically based on our experience.

3.2 Pedestrian Dead Reckoning

In dead reckoning, the position is iteratively estimated as a function of a previous estimated position and an increment in distance. A description of PDR algorithms with IMUs can be found in [59]. In the following, the two main approaches used in this thesis will be described.

3.2.1 Strapdown Algorithm

The strapdown algorithm is depicted in Figure 3.3. The first step is to estimate the attitude of the IMU in order to project the acceleration vector onto the localization frame. Then, the effect of gravity is subtracted from the projected acceleration vector. Finally, the acceleration vector is integrated once to estimate the velocity and, a second time to estimate the user's position.

The Unscented Kalman Filter

The strapdown algorithm is, like the attitude estimation, implemented in a Kalman filter. The objective is to incorporate measurements that reduce the error accumulation in the position estimation, which is the result of integrating the noise in both the acceleration vector and turn rate vector [11].

In this work, the states vector (\mathbf{x}) of the UKF that implements the strapdown algorithm is the following:

$$\mathbf{x} = [\mathbf{p}^T, \mathbf{v}^T, \boldsymbol{\Psi}^T, \mathbf{b}_g^T]^T, \quad (3.16)$$

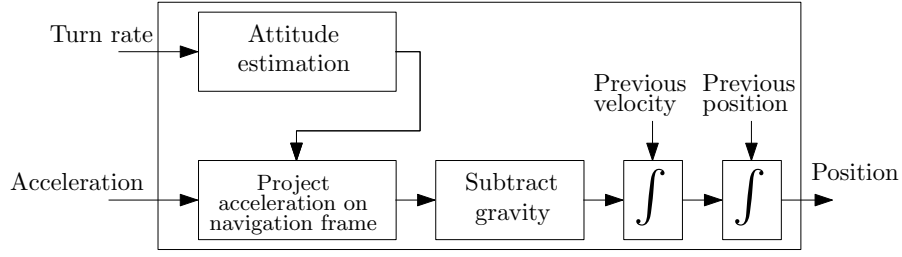


Figure 3.3: Block diagram of the strapdown algorithm, adapted from [59]. The initial velocity and position are used only in the first iteration. The initialization of the attitude is not included in this diagram.

where \mathbf{p} and \mathbf{v} are column vectors with the 3D-position and 3D-velocity of the user. $\mathbf{\Psi}$ is a column vector with the Euler angles that represent the attitude of the sensor. Finally, \mathbf{b}_g is a column vector with the bias estimation of the gyroscopes.

In the following, the UKF that implements the strapdown algorithm based only on inertial measurements is presented, see Figure 3.4.

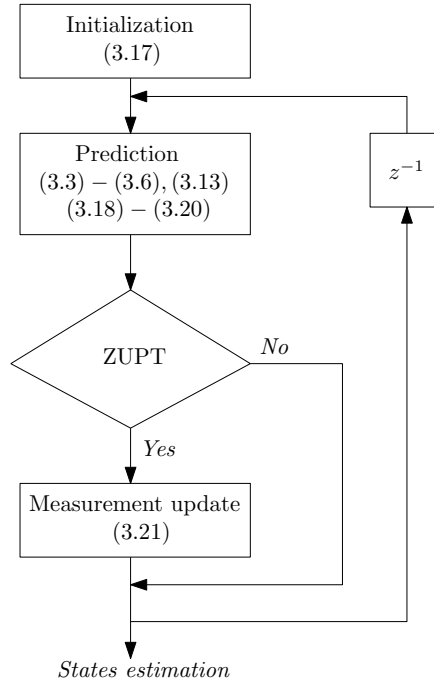


Figure 3.4: Block diagram of the UKF that iteratively tracks the position, velocity and attitude of an IMU.

Prediction

The first step of the UKF that implements the strapdown algorithm is the initialization of the states, see Figure 3.4. Whereas the attitude and gyroscope bias are initialized with equation (3.12), the user's position and velocity are usually set to

zero, that is:

$$\mathbf{x}^0 = [\mathbf{0}_{3 \times 1}^T, \mathbf{0}_{3 \times 1}^T, \phi^0, \theta^0, 0, \mathbf{0}_{3 \times 1}^T]^T, \quad (3.17)$$

where $\mathbf{0}_{3 \times 1}^T$ is a zero-element vector with dimension 3×1 .

The states prediction begins with the estimation of the sensor attitude (Ψ^k) and gyroscope bias (\mathbf{b}_g^k) at the k -th time. These estimations are described in Section 3.1.1. When the sensor attitude is known, it is possible to project the acceleration vector at the k -th time (α^k) on the localization frame (α_n^k):

$$\alpha_n^k = \mathbf{C}_{nb}^k \cdot \alpha^k, \quad (3.18)$$

where \mathbf{C}_{nb}^k is the attitude matrix, i.e. DCM, estimated through the Euler angles Ψ^k .

The velocity can be estimated recursively through:

$$\mathbf{v}^k = \mathbf{v}^{k-1} + \delta^k \cdot (\alpha_n^k - \mathbf{g}), \quad (3.19)$$

where δ^k is the sampling time, and \mathbf{g} is the gravity vector, such that $\mathbf{g} = [0, 0, 9, 832]^T \text{m/s}^2$.

Similarly, the position is recursively estimated as:

$$\mathbf{p}^k = \mathbf{p}^{k-1} + \delta^k \cdot \mathbf{v}^k. \quad (3.20)$$

For a detailed description on the equations of the UKF, the reader is referred to Appendix C.

Measurement update

In the prediction stage, the position error grows cubic over time. The trend of the position error can be reduced to linear thanks to the ZUPT update [15]. It is implemented upon detection of the stance phase, in which case, the velocity of the foot is zero:

$$\mathbf{v}_z = [0, 0, 0]^T. \quad (3.21)$$

The latter is commonly referred to as *pseudo-measurement*, which means that it is not directly measurable but that it is inferred. In this case, the inference of the pseudo-measurement value is possible by knowing that the foot does not move during the stance phase.

In short, the ZUPT is not more than a re-calibration of the velocity states when the stance phase is detected. Through the application of the ZUPT in the measurement update, the UKF Kalman filter corrects, not only the velocity estimation but also the position estimation.

It is worth highlighting that, since the stance phase is only detectable with the foot IMU, the ZUPT is applicable only when the IMU is mounted on the foot. It would be possible to implement further updates in the filter that implements the strapdown algorithm. For instance, the gravity update described in Section 3.1.1. This update is necessary if a correction of the attitude estimation is desired. In fact, the zero-velocity calibration has a minimal effect in the attitude estimation.

3.2.2 Step & Heading Algorithm

The implementation of the step&heading algorithm depends on the body location of the IMU. The block diagram for an IMU mounted on the front pocket of the trousers is given in Figure 3.5. In the following, we will refer to the location as pocket.

The *Position estimation* block, see Figure 3.5, estimates the 3D position of the user (\mathbf{p}^k) as follows:

$$p_x^k = p_x^k + s^k \cdot \cos(\psi^k), \quad (3.22)$$

$$p_y^k = p_y^k + s^k \cdot \sin(\psi^k), \quad (3.23)$$

$$p_z^k = p_z^k + v^k, \quad (3.24)$$

where p_i^k , with $i = \{x, y, z\}$, is the i -th component of the 3D position vector \mathbf{p} at the k -th time, s^k is the user's step length at the k -th time and v is the vertical displacement.

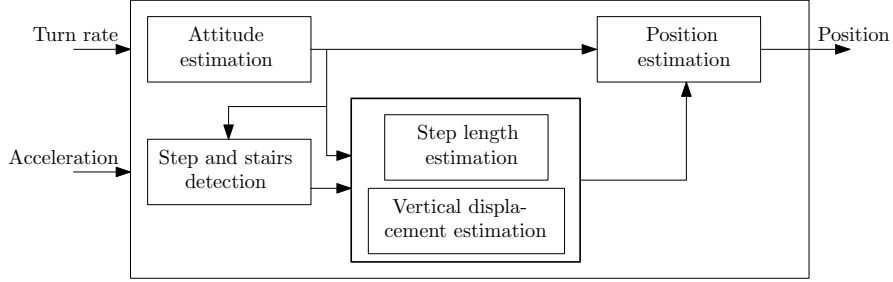


Figure 3.5: Block diagram of the step&heading algorithm for a sensor mounted on the pocket.

The implementation of equation (3.22) and equation (3.23) can be divided into two parts. The first one is the estimation of the direction of the walk (ψ^k). The second one is the estimation of the user's step length (s^k). In addition, the estimation of the step length requires a prior detection of the step events, as Figure 3.5 indicates.

Regarding the estimation of the direction of the walk (ψ^k), the reader is referred to Section 3.1.1 for details on the implementation of the attitude tracking. Regarding the step detection and step length estimation for a pocket INS, the methods are described in the following sections.

Step and Stairs Detection Algorithm

The detection of steps with a pocket IMU is implemented through the block diagram of Figure 3.6. This algorithm was first presented by Munoz *et al.* [13]. The detector analyzes two aspects of the leg pitch: the occurrence of a maximum and the amplitude of the signal. Firstly, the leg pitch must reach a local maximum. Secondly, the amplitude of the leg pitch must be larger than a pre-defined threshold (δ_p). When the second step is satisfied, a step is detected.

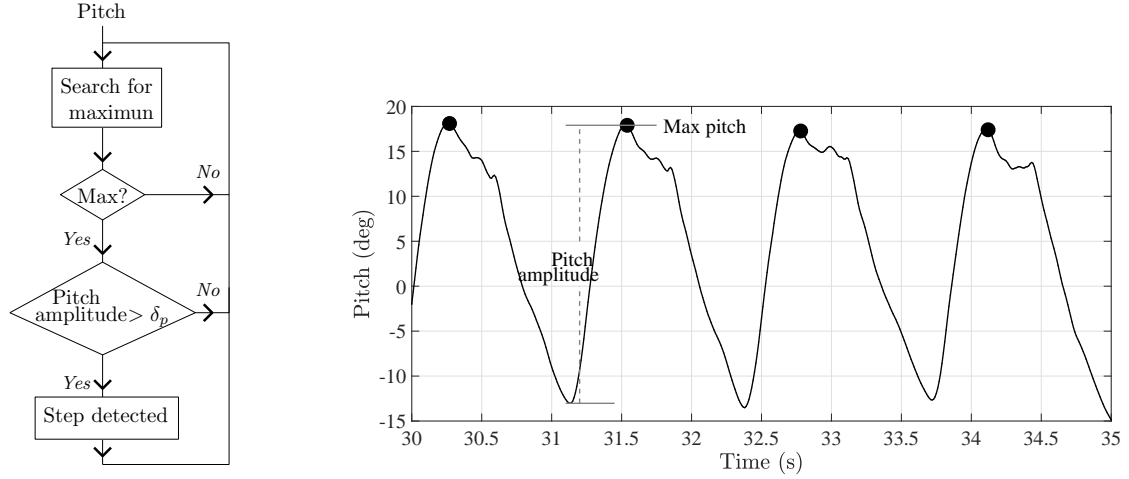


Figure 3.6: (Left) Step detector based on the pitch angle of the leg. δ_p is the minimum amplitude of the pitch of the pocket IMU that triggers the detection of a step. (Right) Pitch of the pocket IMU during four steps. The dot marks indicate the time when a step is detected.

Figure 3.6 shows an example of the leg pitch during four steps. In this example, the user was walking on a horizontal surface. Each circle mark in the figure indicates the time at which a step was detected.

If a step is detected, the algorithm may detect a stair up or stair down by analyzing again both the amplitude and the maximum of the pitch of the pocket IMU [19]. As Figure 3.7 shows, the pitch of the pocket IMU is different when the user is walking horizontally than walking the stairs. In order to distinguish walking up stairs from walking downstairs, the thresholds in Figure 3.6 need to be adjusted.

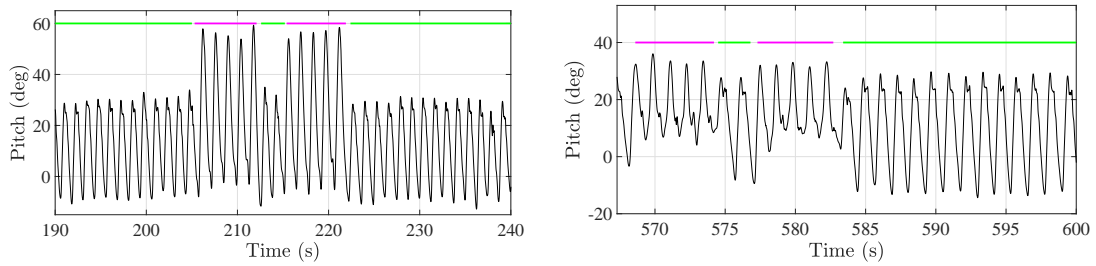


Figure 3.7: Pitch of the pocket IMU while walking horizontally (upper green line) and stairs walking (upper magenta line). (Left) Walking up stairs, (right) walking downstairs.

If a step is detected, then the step&heading algorithm proceeds to the estimation of the step length.

Step Length Estimation

Similarly to the step detection algorithm, the step length model based on the leg pitch was first presented by Munoz *et al.* [13]. The model states that the step length (s) and the amplitude of the leg pitch ($\Delta\theta$) are related by a first-order linear regression, such that:

$$s = a \cdot \Delta\theta + b, \quad (3.25)$$

where the slope a is a generic parameter which is estimated in a training phase [13]. The offset b is a user-specific parameter that has to be estimated during a calibration phase.

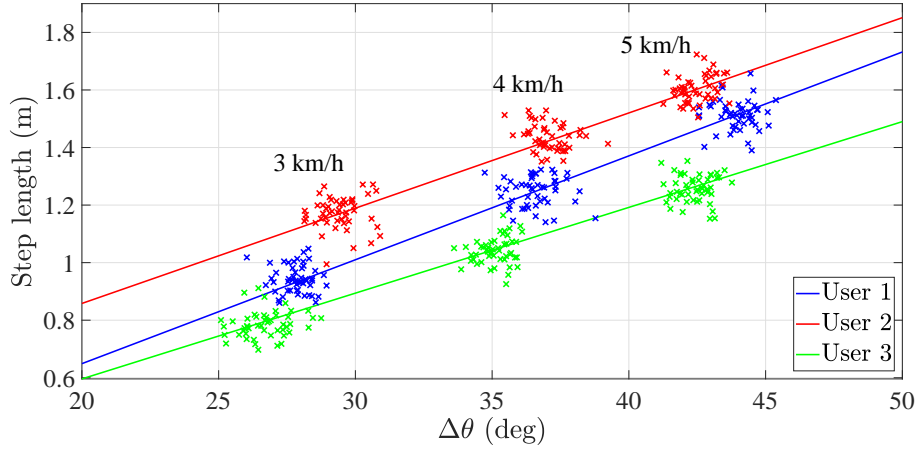


Figure 3.8: Relationship between the amplitude of the pitch of the pocket IMU and the step length for three different users. The point cloud amplitude-step length depends on the walking speed of the user.

Figure 3.8 exemplifies the relationship of equation (3.25) for three different users. The walking speed conditions the value of the pitch amplitude of the pocket IMU and the step length. In fact, the higher the walking speed, the higher these values are. From Figure 3.8, it can be seen that different users have approximately the same slope a . In contrast, the offset b differs significantly among users. The study in [13] states that the reason of the different offsets could not be related to a specific feature, e.g. the user's height. Instead, the value of the offset is associated to the user's walking style.

In the case that a stair is detected, the pocket INS estimates the vertical displacement in a deterministic way. More specifically, the vertical displacement is set to twice the standard height of the stairs [61], namely 19 cm. In addition, the horizontal displacement in the case of stairs is set to twice the standard step depth, i.e. 25.4 cm.

3.3 Robotics Fundamentals

Robotic structures like the one presented in Figure 3.9 are widely used to model the motion of robots, machines, etc. In this context, it is of interest to characterize the robotic structure, i.e. to know the absolute position of the end actuators. For that purpose, different mathematical tools that can represent a robotic structure are needed. Furthermore, it is also of interest to model the kinematics of such structures in an efficient and comprehensive way.

In this work, such tools will be used to create a model of the leg, which will be introduced in Chapter 7. The following terms and convention are used to refer to parts of the robotic structure:

- a *joint* is either the end a robotic structure or the element that connects two links, see Figure 3.9.
- a *link* is the connection between two consecutive joints, see Figure 3.9,
- a *rotation axis* is the axis around which a joint can rotate, see z_i in Figure 3.9,
- the *base frame*, which is of free choice, is the reference frame where the position of the joints is represented, see Figure 3.9,
- the coordinate frames will be defined following the right-hand rule.

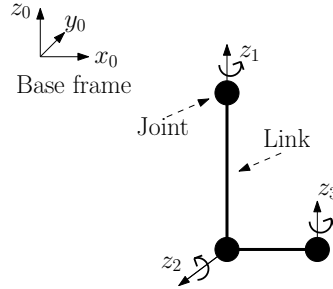


Figure 3.9: Representation of a robotic structure that consists of three joints and two links. The axis z_i indicates the axis around which a joint rotates.

The sections below present a mathematical tool to efficiently represent robotic structures. This tool can also be used to estimate the new set up of the structure when, for instance, it has experienced a rotation around one or more axes.

3.3.1 Denavit-Hartenberg Parameters

Let us consider a structure similar to the one in Figure 3.9. In order to know the structure set up, i.e. the position of the structure joints in the base frame, a mathematical tool known as the Denavit-Hartenberg parameters is used [62].

The Denavit-Hartenberg parameters are a set of four parameters that describe the position of one joint with respect to the previous one. These parameters are listed below:

- d is the link offset distance,
- θ is the link rotation angle,
- a is the link length,
- α is the link twist angle.

The Denavit-Hartenberg parameters must be estimated for each joint in the structure. The list of Denavit-Hartenberg parameters associated to Figure 3.9 is given in Table 3.1. For this case, the parameters are estimated considering that the base frame is located at the centre of the first joint, namely z_1 . A detailed explanation of how to derive the Denavit-Hartenberg parameters is given in Appendix E.

Table 3.1: Table with the associated Denavit-Hartenberg parameters of Figure 3.9. The parameters are estimated considering that the base frame is at the center of joint z_1 .

Axis	d	θ	a	α
z_1	0	0	0	0
z_2	$-l_1$	180°	0	-90°
z_3	0	180°	l_2	-90°

3.3.2 Homogenous Matrix

Let us continue with the robotic structure represented in Figure 3.9. When this structure is subject to a specific motion, namely a rotation around one or more of its rotation axes, the joint positions might change. In order to estimate the new positions of the joint, the homogenous matrix is used.

The homogenous matrix (\mathbf{H}) is, in the 3D case, a 4×4 matrix which can be written as follows:

$$\mathbf{H} = \begin{bmatrix} \begin{bmatrix} \mathbf{C}_{3 \times 3} \\ 0 & 0 & 0 \end{bmatrix} & \begin{bmatrix} \mathbf{T}_{3 \times 1} \\ 1 \end{bmatrix} \end{bmatrix}. \quad (3.26)$$

The aforementioned matrix contains the two main pieces of information:

- the relative orientation between two frames ($\mathbf{C}_{3 \times 3}$). It is important to highlight that the sub-matrix $\mathbf{C}_{3 \times 3}$ is equivalent to the rotation matrix introduced in Section 3.1,
- the relative translation between two frames ($\mathbf{T}_{3 \times 1}$). The latter is a column vector with length 3.

Let us write the homogenous matrix from frame i to frame $i - 1$ as \mathbf{H}_i^{i-1} . Given a vector \mathbf{v}_i whose coordinates are given in frame i , the coordinates of this vector in

frame $i - 1$ (\mathbf{v}_{i-1}) are estimated through the homogenous matrix \mathbf{H}_i^{i-1} as follows:

$$\mathbf{v}_{i-1} = \mathbf{H}_i^{i-1} \cdot \begin{bmatrix} \mathbf{v}_i \\ 1 \end{bmatrix}, \quad (3.27)$$

where \mathbf{v}_{i-1} and \mathbf{v}_i are three-dimensional column vectors.

The homogenous matrix can be written in terms of the Denavit-Hartenberg parameters. In this case, the goal is to estimate the coordinates of the joints in the base frame, see Figure 3.9, which has the index $i = 0$. To that end, the homogeneous matrix between two consecutive rotation axes, e.g. from z_i to z_{i-1} , can be estimated in terms of the Denavit-Hartenberg parameters as follows:

$$\mathbf{H}_i^{i-1} = \begin{bmatrix} \cos(\theta_i) & -\sin(\theta_i) \cdot \cos \alpha_i & \sin(\theta_i) \cdot \sin \alpha_i & a_i \cdot \cos(\theta_i) \\ \sin(\theta_i) & \cos(\theta_i) \cdot \cos \alpha_i & -\cos(\theta_i) \cdot \sin \alpha_i & a_i \cdot \sin(\theta_i) \\ 0 & \sin \alpha_i & \cos \alpha_i & d_i \\ 0 & 0 & 0 & 1 \end{bmatrix}. \quad (3.28)$$

The successive multiplication of homogeneous matrices leads to a single matrix, e.g. \mathbf{H}_3^0 , that estimates a vector coordinates in the frame 0 given its coordinates in frame 3. For instance, let us consider again Figure 3.9. Given the set of Denavit-Hartenberg parameters of Table 3.1, it is possible to estimate the homogenous matrix \mathbf{H}_3^0 as:

$$\mathbf{H}_3^0 = \mathbf{H}_1^0 \cdot \mathbf{H}_2^1 \cdot \mathbf{H}_3^2. \quad (3.29)$$

Then, the generalization of equation (3.29) as:

$$\mathbf{H}_n^0 = \mathbf{H}_1^0 \cdot \mathbf{H}_2^1 \cdot \dots \cdot \mathbf{H}_n^{n-1}, \quad (3.30)$$

leads to the homogenous matrix that transforms a vector from frame n to the base frame 0.

The advantage of the previous equation is that it escalates easily with the number of rotation axis of the robotic structure. That is, even if the robotic structure is complex, characterizing the relative position of consecutive axes follows the simple rules provided in Appendix E.

Chapter 4

T&E Methodology of Inertial Localization Systems

*One never notices what has been done,
one can only see what remains to be done*
– Marie Curie

One of the objectives of this thesis is to characterize the performance of the foot INS and the pocket INS. We need to understand the strengths and weaknesses of these systems and their associated body locations in order to implement a multi-IMU localization system. To characterize the performance of the systems, it is necessary to quantitatively evaluate them.

The challenge in pedestrian localization is the lack of a standardized T&E methodology that allows for such evaluation. In the following, we comment on the state of the art of the T&E methodologies implemented nowadays in localization competitions. Then, we propose a T&E methodology with which we evaluate the performance of the foot INS and the pocket INS.

The outcome of the performance evaluation is the strengths and weaknesses of each of the systems. We also identify the challenges of inertial localization systems. This identification leads us to propose a series of implementations to address these challenges, which is the second goal of this thesis.

4.1 Challenges of Test & Evaluation

The ISO/IEC 18305 standard is the first formal attempt to standardize the T&E of localization systems [63]. This work, which was published by the International Organization for Standardization (ISO) in 2016, has been barely adopted by the localization community. To the best of our knowledge, only the PerfLoc localization competition has followed the guidelines of the standard [64,65]. In fact, the standard has motivated critics where some of its shortcomings are identified [66,67]. For instance, the standard fails to provide T&E methodologies for the evaluation of the

components of a localization system. In addition, the standard does not recommend a minimum size of the experiments nor takes into account the characteristics of the users, e.g. height or age, in the definition of a scenario.

We have carried out an in-depth study of T&E methodologies in localization systems [66]. The ISO/IEC standard has been taken as a reference to assess the T&E methodologies implemented in indoor localization competitions and individual works. This analysis allows us to identify the strengths and weaknesses of not only the surveyed competitions and individual works but also the standard.

Indoor localization competitions are relevant events for the T&E of pedestrian localization systems [64, 65, 68–71]. In fact, we have identified common elements in the T&E methodologies of these events, e.g. the ground truth system or the metrics used [66]. Over the years, there have been also benchmarking initiatives which aim at defining guidelines by which researchers and developers can design T&E methodologies [72]. These initiatives are done by developers for developers, but once again their spread and acceptance is almost nonexistent [66].

The T&E methodologies implemented by researchers and developers of pedestrian localization systems have different shortcomings [66]. Among them, there is the inappropriate design of the T&E methodology, e.g. researchers and developers to not follow a structured process to design the ground truth system or the performance metrics. This shortcoming may lead to meaningless performance figures. Moreover, it is unfeasible to compare different systems, e.g. two wrist-mounted inertial localization systems, that have been characterized by independent researchers because they follow a different T&E methodology.

Another shortcoming is the inappropriate representation of the outcome of the evaluation. The representation involves both tables with performance figures and graphs. In this regard, the ISO standard may be helpful since it provides suggestions on how to represent such information.

An interesting observation of our work is that public data sets are not commonly used [66]. Generally, the pedestrian localization community does not make use of such resources. The use of public data sets is a simple solution to assess and compare different systems. We believe that it is a waste of resources not to make use of information that has been made available to us. Of course, the data sets should provide meaningful data and be comprehensive, e.g. a data set with associated ground truth and documentation, to motivate the community to use them.

The conclusion of our study is that the evaluation of pedestrian localization systems is still an open challenge. The community has not adopted yet a common T&E methodology. Nonetheless, there are similarities in the T&E methodologies of different research works, e.g. the ground truth system or the performance metrics. We have taken into account these common elements to propose our T&E methodology.

4.2 Proposed T&E Methodology

The evaluation process carried out in this work is summarized in Figure 4.1. The data base contains the sensor measurements and the associated ground truth. Both of them are collected during a set of experiments. The measurement data is processed with the inertial localization system, which generates a position estimation among other parameters such as the attitude. Next, the performance metrics are used to generate performance figures which are then represented through plots and tables.

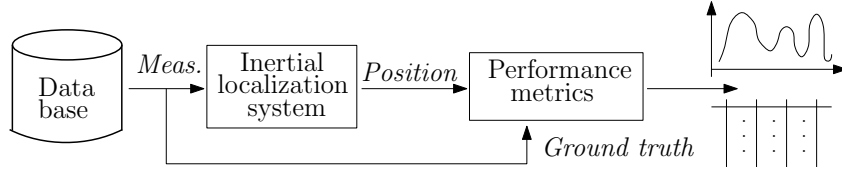


Figure 4.1: Evaluation sequence followed to generate the performance figures. *Meas.* stands for sensor measurements.

4.2.1 Ground Truth System

Our ground truth system was first presented in [73], where we used it to evaluate and compare the foot INS and the pocket INS with a set of indoor walks. Then, the assessment and comparison was extended to both the latter and a wrist-mounted inertial localization system [74]. In this work, the inertial localization systems were evaluated in an outdoor area larger than 14000 m².

The ground truth system, similar to indoor localization competitions, is based on ground truth points. The location of these points is measured in advance. Then, the user visits these points in a predefined sequence. The inertial localization system is evaluated by comparing its estimated position of a ground truth point to the true position of the ground truth point.

The location of the ground truth points is measured with a laser distance measurer. The latter gives, approximately, centimeter accuracy which is at least one order of magnitude smaller than the expected accuracy of the inertial localization systems under evaluation. This criterion is recommended by the ISO standard [63].

4.2.2 Performance Metrics

In the evaluation, we want to assess how the proposed changes affect the estimation of the horizontal distance, the heading and the height. Therefore, it is necessary to evaluate these three aspects independently.

The straightforward metric that can be implemented with ground truth points is the 3D position error. The latter is a vector magnitude whose value is influenced

by the three aspects we want to evaluate, i.e. horizontal distance, heading and height. Should we use the 3D position error, we will not be able to assess the system performance regarding the three aspects mentioned previously.

We resort to alternative metrics that quantify the system performance regarding each aspect of interest. Two of these metrics are the distance error (e_d) and the heading error (e_ψ), which are defined as follows:

$$e_d = |d_{ij}^r - d_{ij}^w|, \quad (4.1)$$

$$e_\psi = |\psi_{ij}^r - \psi_{ij}^w|, \quad (4.2)$$

where d_{ij}^r and d_{ij}^w are the true horizontal distance and the estimated horizontal distance between the i -th and the j -th ground truth points. Similarly, ψ_{ij}^r and ψ_{ij}^w are the true angle and estimated angle between the i -th and the j -th ground truth points. $|\cdot|$ denotes the absolute value of the argument. e_d and e_ψ are representative of the distance and heading error only if the trajectory between the i -th the j -th point is straight. This consideration will be taken into account in the design of the experiments.

The last metric is the height error (e_h), which is defined as follows:

$$e_h = \frac{|h_i^r - h_i^w|}{\Delta h_i^r}, \quad (4.3)$$

where h_i^r and h_i^w are the true height and the estimated height of the i -th ground truth point. $|\cdot|$ denotes the absolute value of the argument. Δh_i^r is the total height change at the i -th ground truth point, i.e.:

$$\Delta h_i^r = \sum_{j=0}^i |h_j - h_{j-1}|, \quad (4.4)$$

where h_j is the height of the j -th ground truth point. Equation (4.3) represents a height error normalized to the total change in height. For instance, a height error (e_h) equal to 0.1 m/m tells us that the inertial localization system makes an error of 40 cm in a height change of 4 m.

We estimate different statistics for each of the performance metrics. For instance, the mean and standard deviation of each of the metrics. A common practice in indoor localization competitions is to estimate the Cumulative Distribution Function (CDF) of the position error and then compare the systems with the third quartile [75, 76]. In this work, we follow a similar approach with the proposed performance metrics.

4.2.3 Data Set

The data set was collected during a set of experiments. The latter took place at the Institute of Communications and Navigation of the German Aerospace Centre (DLR). The location of the experiments is a five-storey building, see Figure 4.2.

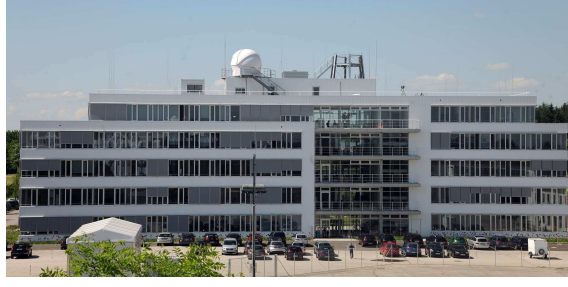


Figure 4.2: Institute of Communications and Navigation of the German Aerospace Centre (DLR).

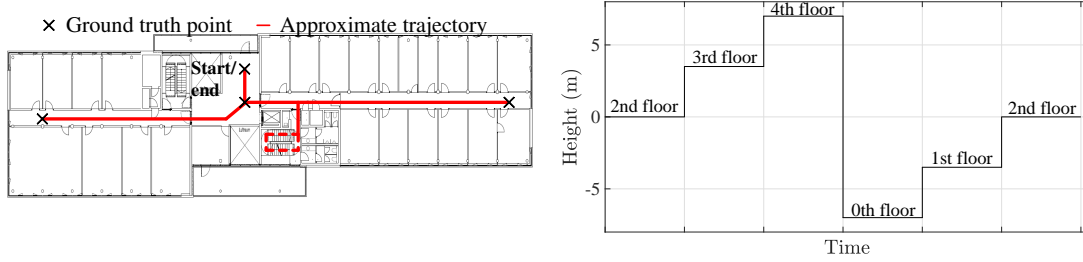


Figure 4.3: Approximate 2D trajectory (left) and height profile (right) followed by the users. The dashed lines on the floor plan indicate the stairs. The height difference between two consecutive floors is 3.5 m.

During the experiments, the users followed a predefined trajectory. They visited each of the five floors following the approximate trajectory of Figure 4.3. Moreover, they visited the floors in the sequence indicated by the height profile of Figure 4.3.

Regarding the ground truth points, the users visited three points in each floor, see Figure 4.3. The users were instructed to stop 2 s to 3 s at each ground truth point to signal that they reached one. This approach is also followed in indoor localization competitions [68]. Finally, users of different heights and different ages participated in the experiment. Each user repeated the aforementioned trajectory twice, and each trajectory lasted approximately 15 min to 20 min. The users were equipped with two IMUs mounted on the front pocket of the trousers and the front part of the foot respectively. The IMUs are measurement units from Xsens [77] whose noise characteristic are given in Appendix G.

Table 4.1: Summary of the experiments.

No. of users	Total time	No. of ground truth points
10	5 h	482

The summary of the experiments is given in Table 4.1. The outcome of the experiments is the acceleration vector and turn rate vector from both the pocket IMU and the foot IMU of each user. In addition, the ground truth points are identified by detecting when the user stopped at each ground truth point. This detection is

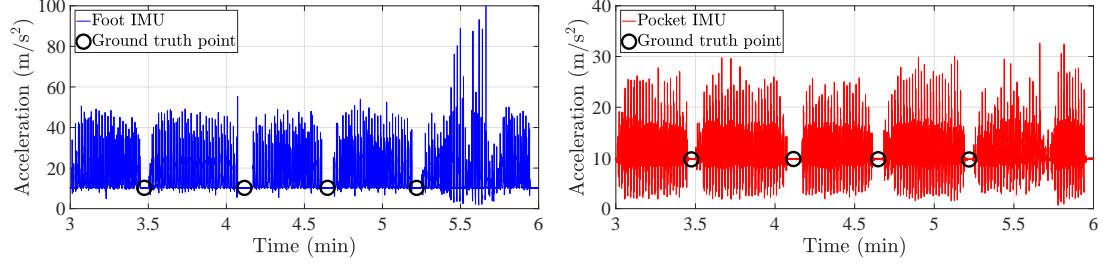


Figure 4.4: Identification of the stop at the ground truth points. The norm of the acceleration vector is presented for the foot IMU (left) and the pocket IMU (right).

done by analyzing the norm of the acceleration vector of either IMU. An example is given in Figure 4.4, where the acceleration norm of both the foot IMU and the pocket IMU is represented. We can see how the stop at the ground truth points are clearly observed by the periods of constant acceleration.

4.3 Boundary Conditions

In the following, the boundary conditions to study multi-IMU approaches are presented. These conditions refer to the number of IMUs and their placement on the user's body. The reason for setting these conditions is that the focus of this thesis is on the algorithmic part, i.e. given a set of IMUs, we want to study how to combine their measurements for an improved performance.

The number of IMUs chosen is two and the chosen body locations are the front pocket of the trousers and foot respectively. These two body locations have distinctive features while walking that can be integrated in inertial localization systems, see Section 3.2. In addition, this choice of body locations allows for the implementation of the two types of PDR algorithms, namely the strapdown algorithm and the step&heading algorithm.

The next step is to quantitatively analyze the performance of the foot INS and the pocket INS.

4.4 Characterisation of the Pocket INS and the Foot INS

The strengths and weaknesses of the foot INS and the pocket INS are determined by quantitatively evaluating the performance of two systems. The performance analysis will be used as a reference to evaluate the multi-IMU approaches. That is, we will be able to determine whether the multi-IMU localization system is more accurate than the single-IMU localization systems.

Table 4.2 summarizes the performance figures of the foot INS and the pocket INS.

We can see how the foot INS outperforms the pocket INS regarding the distance error by approximately 24%. It is important to highlight that the step length model of the pocket INS was manually calibrated to each user prior to estimating the performance figures. Thus, we can state that even if the pocket INS is calibrated to the user, the foot INS is most accurate in the distance estimation.

Table 4.2: Performance figures of the single-IMU localization systems indicated as $\mu \pm \sigma$, where μ is the mean and σ is the standard deviation.

System description	$e_d[m]$	$e_\psi[^\circ]$	$e_h[m/m]$
Pocket INS	3.8 ± 7.9	61.2 ± 48.8	0.8 ± 2.0
Foot INS	2.9 ± 8.2	66.9 ± 52.9	0.4 ± 0.4

The heading error of both single-IMU localization systems is in the same order of magnitude. In fact, the mean and standard deviation of the heading errors are similar. The heading errors in Table 4.2 may seem high for an inertial localization system. Nevertheless, we need to take into account that the duration of the walks is longer than usual for an inertial localization system. The walks take 15-20 min whereas the state of the art evaluated inertial localization systems over walks that last a few minutes, e.g. up to 5 min.

The similarity in the heading error does not allow us to make a statement on which inertial localization system is more accurate regarding the heading estimation. A highlight of the heading error is that it does not reflect the heading drift over time. In order to visualize the drift, it is necessary to plot the heading error over time. An example is given in Figure 4.5. This figure is also an example of the randomness of the heading error. On the left-hand picture, the pocket INS has a lower heading error than the foot INS and, on the right-hand picture, we observe the opposite result.

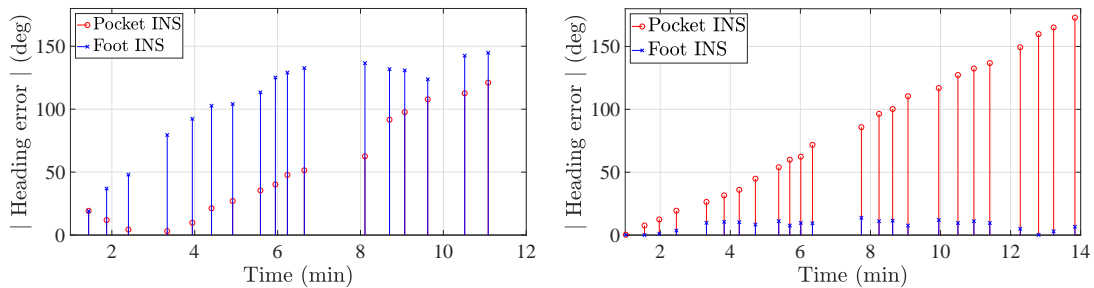


Figure 4.5: Absolute value of the heading error for the pocket INS and the foot INS. As time passes, the error accumulation increases. On the left-side picture, the pocket INS is more accurate than the foot INS. On the right-side picture, the foot INS is more accurate than the pocket INS.

Regarding the height error, Table 4.2 shows that the average height error of the pocket INS is twice the height error of the foot INS. The reason is the algorithm for stairs detection of the pocket INS. The pocket INS relies on the stairs detection

to deterministically estimate the vertical displacement, see Section 3.2.2. We have noticed that the local maxima and minima of the pitch of the pocket INS may be altered due to the bias in the turn rate measurements. In such cases, the algorithm for stairs detection may trigger both false positives and false negatives for stairs detection. The result of this behaviour is a large height error of the pocket INS with respect to the foot INS.

An example of the aforementioned shortcoming is given in Figure 4.6. The left-hand picture shows the pitch of a pocket INS disturbed by bias. In this picture, it is not possible to distinguish the periods of walking horizontally from those of walking the stairs. In contrast, the pitch in the right-hand picture is barely affected by bias. Therefore, it is possible to distinguish when the user is walking the stairs and she is walking on a horizontal surface.

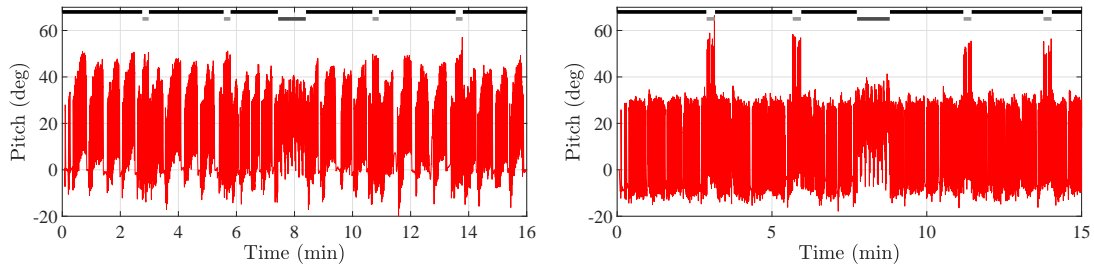


Figure 4.6: (Left) Pitch of the pocket INS with bias perturbation and (right) pitch of the pocket INS without bias perturbation. The solid black lines indicate the periods of walking horizontally. The solid grey lines indicate the periods of walking the stairs.

All in all, the outcome of the evaluation is summarized in Table 4.3. The latter contains the key aspects resulting from the evaluation of the single-IMU localization systems. There is a special focus on the comparison of both inertial localization systems. Three aspects have been considered in the evaluation, namely the gait analysis, the distance estimation and the orientation estimation.

The term gait analysis refers to the recognition of one or several events of the human walk. This category evaluates how well a single-IMU localization system identifies a specific event of the human walk. For instance, the pocket INS needs to detect steps in order to trigger the step length estimation and therefore the position estimation, see the algorithm in Figure 3.5. In contrast, the foot INS must detect the stance phase of the foot in order to correct the velocity estimation, as the algorithm in Figure 3.4 indicates. The successful detection of these events is key for the estimation of an accurate position by the respective inertial localization systems.

The evaluation of the gait analysis reveals that the foot INS misses stance phases. The mis-detection is caused by the stance phase detection method, which is based on thresholds on the norm of the acceleration vector and the norm of the turn rate vector. The foot dynamics cause the inertial measurements to exceed these thresholds, even during the stance phase, see Figure 4.7. In contrast, the step

Table 4.3: Strengths and weaknesses of the pocket INS and the foot INS.

	<i>Pocket INS</i>	<i>Foot INS</i>
Regarding gait analysis		
Strengths	<ul style="list-style-type: none"> • No missed steps • Stairs detection (2.5D) 	
Weaknesses	Noisy stairs detection	Missed stance phases
Regarding horizontal and vertical distance estimation		
Strengths		<ul style="list-style-type: none"> • Inherent 3D position • Model-free estimation
Weaknesses	Model-based estimation in 2D and 3D (calibration)	Height drift
Regarding the direction of the walk		
Weaknesses	Heading drift	Heading drift

detection method of the pocket INS is robust and it leads to no missed steps [73].

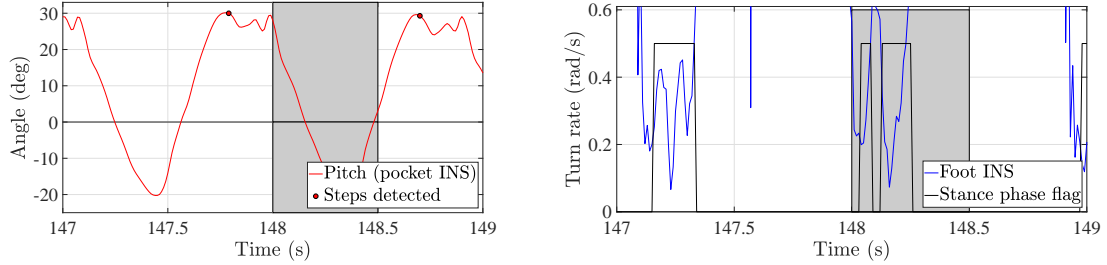


Figure 4.7: Simultaneous gait analysis of the pocket INS (left) and the foot INS (right). The shadowed area indicates the time frame where the foot INS misses a period of the stance phase.

The gait analysis shows that the pocket INS has an additional advantage: the pocket INS can observe when the user is walking the stairs [19]. This ability is thanks to the analysis of the pitch of the pocket INS, which has a different pattern when walking horizontally than when walking the stairs. Figure 4.8 is an example that illustrates the difference, in the pitch of the pocket INS, between walking horizontally and walking the stairs. During the latter, the pitch amplitude as well as the pitch maximum are larger than while walking on a flat surface.

Table 4.3 states that the pocket INS has a noisy stairs detection. This aspect refers to the fact that the stairs detection algorithm can be disturbed by the errors in the pitch signal.

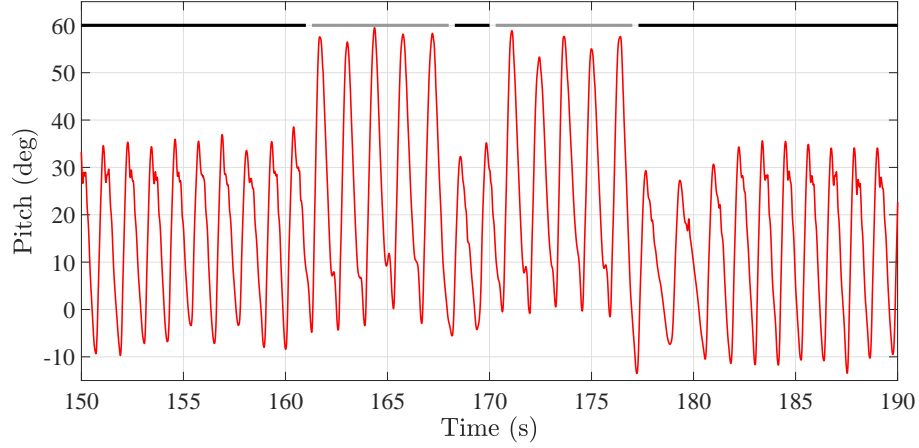


Figure 4.8: Pitch of the pocket INS while walking horizontally (upper solid black line) and walking the stairs (upper solid grey line).

The next aspect evaluated is the estimation of the horizontal distance or the vertical displacement. Table 4.3 points out that the foot INS has a model-free distance estimation. The latter refers to the fact that the foot INS does not require a model, e.g. a step length model, to estimate the step length. In contrast, the foot INS uses the strapdown algorithm to estimate the user's position, which is inherently a three-dimensional vector. Yet, the height estimation of the foot INS accumulates error over time, see Figure 4.9. This accumulation implies a height change, or height drift, even when the user is walking on a flat surface.

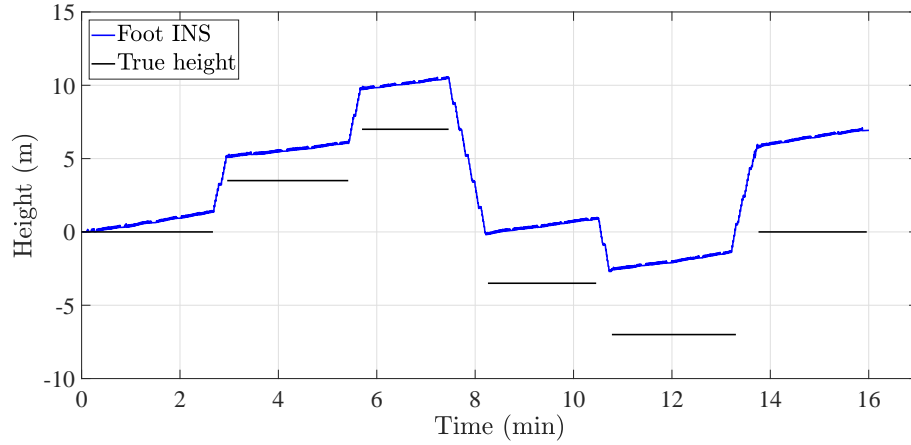


Figure 4.9: Height estimation of the foot INS.

In contrast to the foot INS, the pocket INS has to use a model to map the pitch values to step length values or to vertical displacements. Step length models have an implied disadvantage: the need for calibration. The calibration is the estimation of the model constants that allow for the optimal mapping of the pitch values to step length values.

Finally, the last aspect analyzed in Table 4.3 is the direction of the walk. The latter is related to the estimation of the user's heading, which in turn is a key element of any

inertial localization systems. As expected, the evaluation shows that both inertial localization systems have a drift in the orientation. Let us remember that drift is the term used commonly to refer to the error accumulated in the heading [29]. As Figure 4.5 depicts, the drift in the walk orientation increases over time. This behaviour is expected since an inertial localization system cannot observe the user's true heading solely with inertial measurements [30]. Therefore, it is not possible to correct the heading estimates of the Kalman filter of neither the foot INS nor the pocket INS.

The experiments show that the heading error of an inertial localization system is random. That is, the foot INS may be more accurate than the pocket INS for certain walks. Nevertheless, the situation may be the opposite in a different walk. Thus, one of the conclusions derived from this analysis is that the performance of an inertial localization system regarding its heading estimation is random.

4.5 Outline of Proposed Multi-IMU Approaches

Figure 4.10 presents the multi-IMU localization systems we develop in this thesis. These inertial localization systems address the weaknesses in Table 4.3.

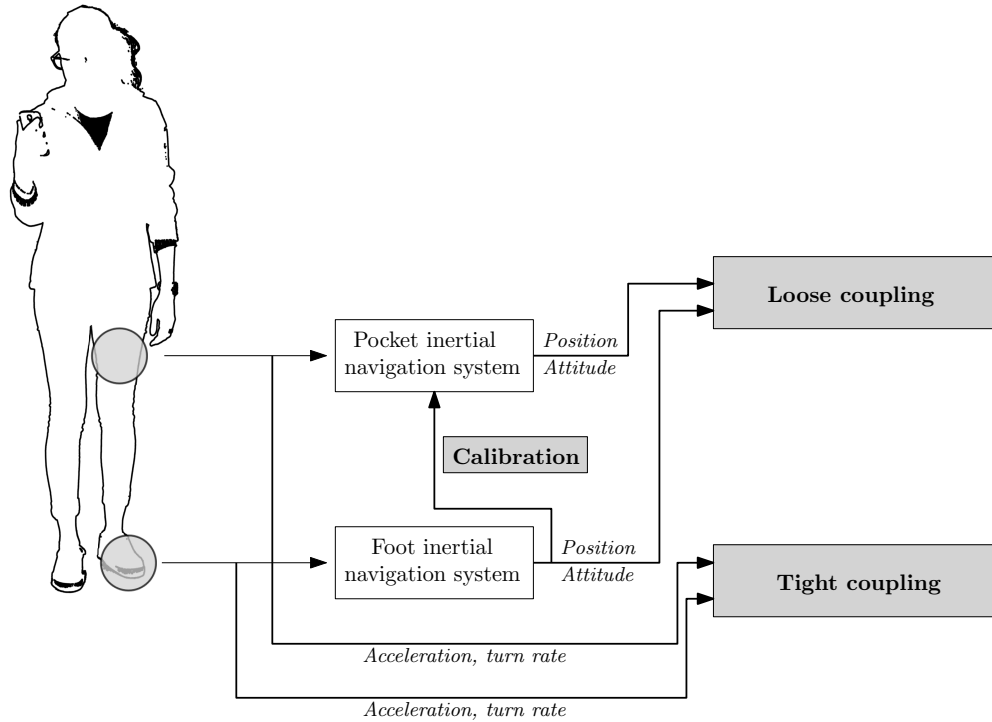


Figure 4.10: Summary of multi-IMU approaches (shadowed blocks). This figure was already presented in Section 1.3. We repeat this figure here for convenience.

The *Calibration* block in Figure 4.10 addresses the weakness of the pocket INS. This

fusion approach is extensible to any step&heading algorithm because all of them implement a step length model. The use of a foot INS to automatically calibrate the step length model based on a pocket IMU is presented in Chapter 5.

The *Loose coupling* and *Tight coupling* blocks address the limitation of the heading drift and the height drift. The goal is to study the potential of these two approaches to reduce the drift in the heading and the height with respect to single-IMU approaches. The loose coupling approach is presented in Chapter 6 whereas the tight coupling approach is presented in Chapter 7 and Chapter 8.

Both the loose coupling system and tight coupling system have advantages and disadvantages that need to be taken into account. From the research point of view, it is of interest to develop, characterize and compare both approaches. Prior to this process, we derive an initial set of advantages and disadvantages of these systems, see Table 4.4.

Table 4.4: Advantages and disadvantages of the two fusion approaches proposed.

	Loose coupling system	Tight coupling system
Advantages	<ul style="list-style-type: none"> • Modularity • Robustness 	<ul style="list-style-type: none"> • Efficiency • Can exploit correlation
Disadvantages	Duplicated functionality	Requires all sensor measurements

The loose coupling system has two advantages. For the sake of discussion, we refer to the foot INS and the pocket INS as subsystems of the loose coupling system. The first advantage of a loose coupling system is the modularity. Thanks to it, independent subsystems can work together without dependencies on the their specific implementations. Secondly, the fact that the loose coupling system relies on independent subsystems makes it robust. If one of them fails, the loose coupling system can continue operating on the other subsystem. The shortcoming of the loose coupling system is the fact of having duplicated functionality. The reason is that both subsystems estimate the same variable, namely the user's position.

The tight coupling system is, in contrast to the loose coupling system, more efficient because of the lack of duplicated functionality. Moreover, the fact that the raw measurements are processed together allows the tight coupling system to exploit possible correlations, in our particular case, between the two body locations. The disadvantage of the tight coupling system is the need of all raw measurements to be operating under normal conditions. For instance, the tight coupling system requires all sensors to be working under normal temperature conditions. If one of them is not, then the overall system may fail. This shortcoming does not occur for the loose coupling system due to the modularity.

4.6 Summary and Conclusions

The proposed T&E methodology allowed us to evaluate the performance of the single-IMU localization systems. Then, we identified their strengths and weaknesses.

In this chapter, we were able to characterize the performance of single-IMU localization systems with the proposed T&E methodology. Based on this methodology, we collected a data set with approximately 5 h of data from the foot IMU and the pocket IMU.

We successfully evaluated the performance of the foot INS and the pocket INS. That is, we estimated performance figures that quantify the performance of these inertial localization systems. Thanks to these performance figures, we compared the pocket INS and the foot INS regarding different aspects, e.g. the accuracy of the height estimation.

Finally, we were able to propose three different multi-IMU inertial localization systems to address the identified weaknesses. They address the weaknesses of the pocket INS and the foot INS. In the reminder of this thesis, we will develop the multi-IMU localization systems and evaluate their performance with the T&E methodology proposed in this chapter.

Chapter 5

Calibration of Step Length Models

*Sometimes it is the people no one can imagine anything of,
who do the things no one can imagine*
– Allan Turing

The step&heading algorithm is one of the two dead reckoning algorithms used in pedestrian localization systems, see Section 3.2. This algorithm relies on a step length model to estimate the user’s horizontal displacement during each step. The step length estimated is most accurate only if the step length model is adapted to the user.

In this work, the process of adapting the step length model to the user and the body location of the sensor is referred to as calibration. The current calibration methods are presented in the state of the art review in Section 2.2. As a summary, these approaches include manual calibration [19] and the use of predefined values [27].

The proposal of this chapter is to profit from the multi-IMU approach to develop two automatic calibration methods for a step length model of a pocket INS. We explain how the parameters of the step length model are estimated, given the step length from the foot INS and the pitch amplitude of the pocket INS. We make two proposals: the first one calibrates only one parameter of the step length model and the second one calibrates both parameters.

The results of Table 4.2 indicates that the distance accuracy of the foot INS is higher than the distance accuracy of the pocket INS. In [74], we show that the accuracy of the foot INS is approximately 20 cm per step. Provided that an adult’s foot is larger than the accuracy of the foot INS, we consider the foot INS to be accurate enough to calibrate the step length model.

5.1 Step Length Model of the Pocket INS

In pedestrian dead reckoning, there are different step length models that relate an observable signal, e.g. the norm of the acceleration, with the step length [78]. These

models can be generally expressed as:

$$s = f(p_1, p_2, \dots, p_n, c_1, c_2, \dots, c_m), \quad (5.1)$$

where s is the user's step length, p_i is an observable parameter and c_j is a predefined constant. The function $f(\cdot)$ is the step length model that relates the observable parameters (p_i) and the predefined constants (c_j) with the user's step length (s).

In this chapter, we focus on the step length model of the pocket INS. Nonetheless, the automatic calibration method based on a foot INS is extensible to the step length model of other inertial localization systems.

The step length model of the pocket INS follows equation (3.25). In the following, we will add an additional error term (e) to the step length model, such that:

$$s = a \cdot \Delta\theta + b + e, \quad (5.2)$$

where e is an unobservable random variable that represents the error in the first-order linear regression model [79]. The term $\Delta\theta$ is an observable parameter, namely the pitch amplitude of the pocket INS, and both the slope (a) and the offset (b) are the predefined constants of the model.

Let us assume that the user's step length (s_f) is known, e.g. through a foot INS, hence the sub-index f . Needless to say, the step length has an associated uncertainty. The automatic calibration method aims at estimating the predefined constants a and b that minimize the error (e) of the step length model. The constants are estimated for each user that is simultaneously wearing two IMUs, one on the foot and one on the pocket, see Figure 5.1.

5.2 Calibration Overview

Figure 5.1 presents the block diagram of the calibration method of step length models. In the diagram, only the blocks of the pocket INS that are relevant for the calibration method are shown. In a practical case, the pocket INS follows the schematic in Figure 3.5.

There are two necessary elements for the calibration method: the pitch amplitude of the pocket INS and the step length. The pocket INS estimates the pitch amplitude as the difference between the maximum and minimum of the pitch. These two angles are visualized in Figure 5.2. In the latter, we can see that the pitch amplitude of the pocket INS has an associated step length. The latter is estimated, in turn, with the output of the foot INS. To that end, the position estimation of the foot INS is sampled upon detection of the stance phase, as Figure 5.1 indicates. The reason is that the position estimation of the foot INS is most accurate during the stance phase periods. This fact is due to the ZUPT implemented in the foot INS, see Section 3.2.1.

The step length model of the pocket INS, see equation (5.2), admits two types of calibration methods. The first one is the offset (b) calibration, where only the offset

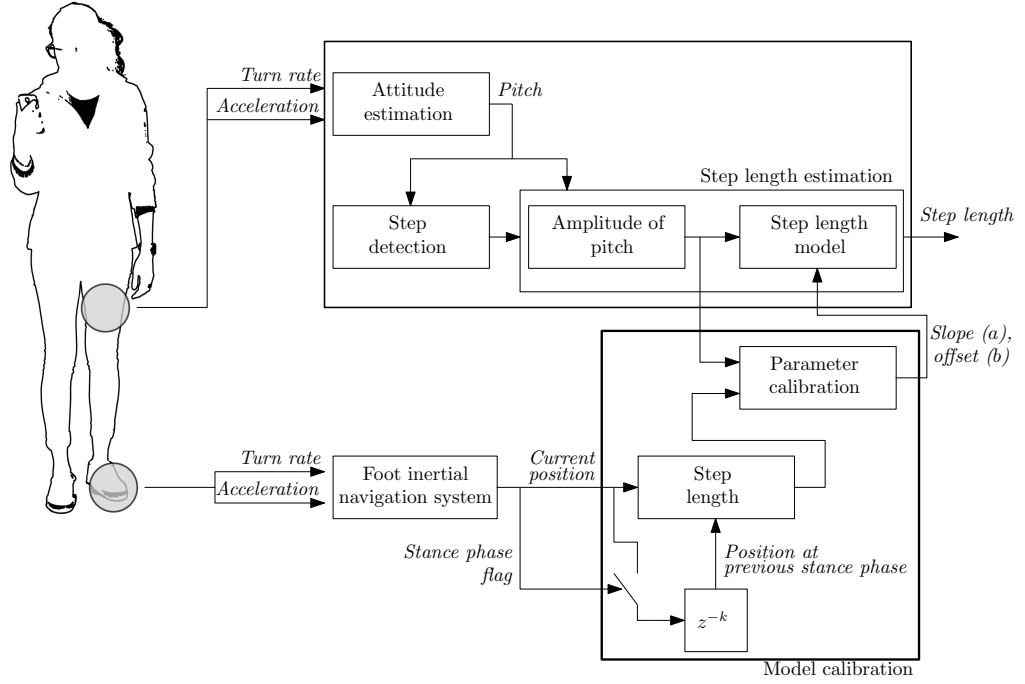


Figure 5.1: The block diagram of the calibration method is indicated by the thick solid line. The blocks of the foot INS and pocket INS that are relevant for the calibration method are shown.

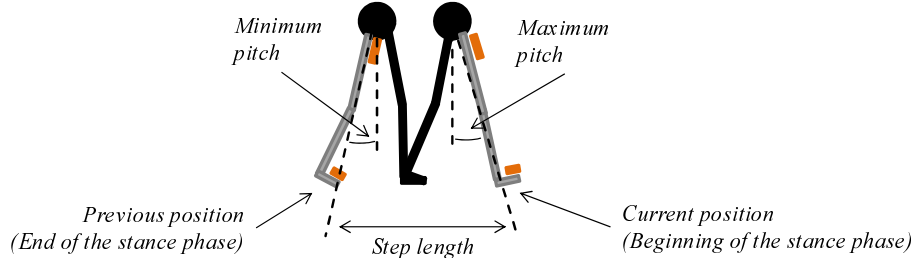


Figure 5.2: Visualization of the maximum and minimum pitch of the pitch of the pocket INS while walking. The amplitude of the pitch is related to the user's step length. The right leg is depicted in grey whereas the left leg is depicted in black.

(b) is adapted to each user. The slope (a) is trained on a set of users. We will refer to the latter as the universal value of the slope, which is $0.05 \text{ m}/^\circ$ [19]. There are specific users whose slope differs from the universal one. In these cases, a full calibration is needed, i.e. a calibration of both the slope (a) and the offset (b).

5.3 Calibration of the Offset

This section presents two alternatives to automatically calibrate the offset (b) of the step length model, see equation (3.25). These methodologies were first presented in

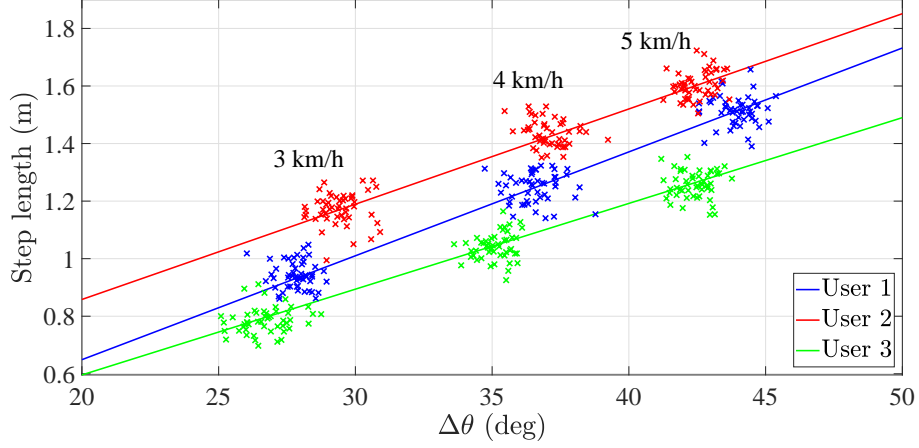


Figure 5.3: First-order linear regression models fitted to the step length and the pitch amplitude of the pocket INS of three different users.

[80]. The first alternative, namely approach 1, is inspired in the manual calibration of this step length model [19]. The second alternative, namely approach 2, aims at estimating the optimal value of the offset given the predefined slope.

Approach 1

In the absence of automatic calibration, the offset in equation (3.25) may be calibrated manually [19]. The straightforward approach is to measure a predefined distance, e.g. 10 m. The next step is to request the user to walk the previous distance while carrying the pocket INS. The last step is a post-processing stage during which the offset (b) is tuned until the estimated distance matches the predefined distance.

Although the manual calibration leads to an offset value that is customized to the user, the process is tedious and prone to errors. Fortunately, the manual calibration can be automatized using the foot INS.

The offset calibration according to approach 1 implements the following equation:

$$b = \frac{1}{n} \cdot \sum_{k=1}^n (s_f^k - a \cdot \Delta\theta^k), \quad (5.3)$$

where n is the predefined number of steps, s_f^k is the step length of the foot INS during the k -th step and $\Delta\theta^k$ is the pitch amplitude of the pocket INS during the k -th step.

The offset estimated through equation (5.3) reproduces the manual calibration. The predefined distance is set through the number of steps (n). Each step is measured both regarding its length (s_f^k) and the pitch amplitude of the pocket INS ($\Delta\theta^k$). Finally, the offset is estimated without the need of manual tuning either in real time or in a dedicated post-processing stage.

The disadvantage of this approach is that the estimated offset may depend on the predefined number of steps (n). Thus, it is not possible to state that the estimated offset is the optimal one. Let us consider again Figure 5.3. In the latter, given a specific walking speed, the pairs step length and pitch amplitude are distributed in a cloud. Therefore, mathematical optimization leads us to think that there is an offset value that optimizes the linear regression [79].

Approach 2

The following approach aims at finding the optimal offset given a predefined slope. To that end, the least squares method is used to minimize the error (e) in the step length estimation, see equation (5.2).

Let us write as $\xi(b)$ the squared error of equation (5.2) during each step. It is possible to write that:

$$\xi(b) = \sum_{k=1}^n (s_f^k - a \cdot \Delta\theta^k - b)^2, \quad (5.4)$$

where the slope (a) is fixed to the universal value, and the step length (s_f^k) and pitch amplitude of the pocket INS ($\Delta\theta^k$) are estimated for each step.

Prior to the offset optimisation, it is possible to coarsely estimate the plausible offset values. The value of the offset depends on the slope and the pitch amplitude of the pocket INS. Firstly, the slope is constrained to the universal value, namely $0.05 \text{ m}/^\circ$. Secondly, the pitch amplitude of the pocket INS is within the range 15° to 60° depending on the walking speed [19]. Finally, the human step length is within 0.5 m and 1.5 m depending on the user's walking style. Therefore, the plausible values of the offset are within -3 m and 1 m approximately.

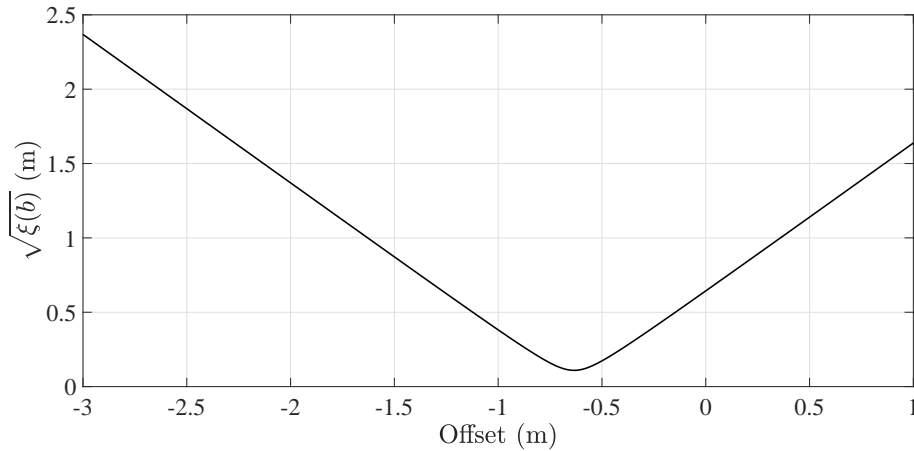


Figure 5.4: Square root of the error in the step length estimation plotted over different values of the offset. In this example, the error reaches a minimum when the offset equals -0.63 m.

Figure 5.4 shows that in the plausible value range of the offset, there is a value that minimizes the squared error. Thus, the next step is to find this offset that minimizes equation (5.4). To that end, we solve the following equation:

$$\frac{\partial \xi(b)}{\partial b} = 0. \quad (5.5)$$

The solution to the previous equation leads to:

$$b^k = \frac{1}{n} \cdot \sum_{k=1}^n (s_f^k - a \cdot \Delta \theta^k), \quad (5.6)$$

where n is the total number of steps since the beginning of the walk until the current time k .

Equation (5.6) can be interpreted as the low-pass filtered estimation of the offset over the total number of steps. The equation can be implemented recursively as follows:

$$b^k = b^{k-1} \cdot \frac{k-1}{k} + \frac{s_f^k - a \cdot \Delta \theta^k}{k}, \quad (5.7)$$

where k is the step count.

Figure 5.5 presents the offset estimation during four different walks for two different users. As expected, different users have different offset estimations. In the figure, an interesting phenomenon can be observed. The offset estimations of both users take two different values during each walk. The reason may be that the IMU was placed on the pocket, but not at the exact same location on each day.

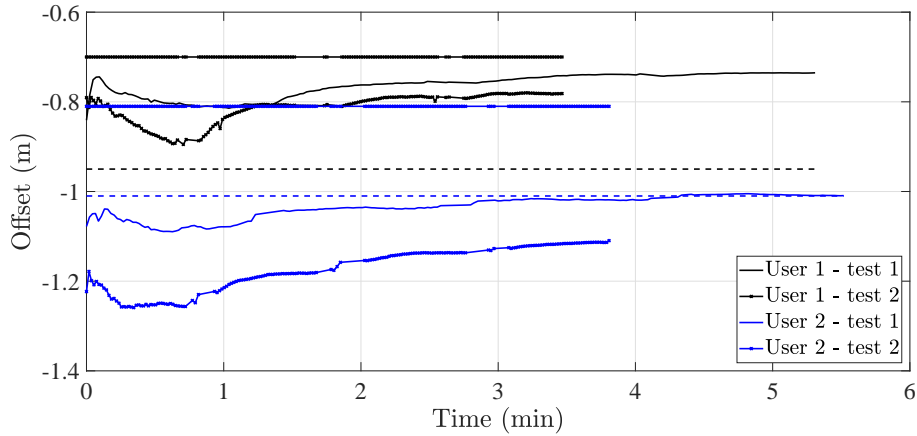


Figure 5.5: Recursive estimation of the offset following approach 1 (horizontal line) and approach 2 (variable line). The number of steps in approach 1 has been set to 10. Each pair solid horizontal-variable line corresponds to a single walk.

Comparison of the Approaches

The two approaches proposed above to automatically calibrate the step length model share a similarity. Equation (5.3) and equation (5.6) are the same in appearance.

Nevertheless, the aforementioned equations have a fundamental difference regarding the number of steps. Approach 1 fixes the number of steps to a predefined one, which conditions the value of the offset. In contrast, approach 2 does not limit the number of steps and, the offset is continuously estimated during the duration of the walk.

Let us consider the offset estimation that is shown in Figure 5.5. The estimation of approach 2 converges after 2 minutes, approximately. Therefore, the calibration requires a limited time of 2 minutes to converge to a stable offset value. The convergence suggests that the calibration method requires a limited time at the beginning of the walk. Afterwards, the calibration is finished and no additional information from the foot INS is needed. Approach 1 inherently requires only n steps to calibrate the offset. In Figure 5.5, the number of steps is set to 10. The comparison of the variable lines and the associated horizontal lines shows that both calibration methods may lead to different estimations.

If the predefined number of steps in approach 1 is increased, its offset estimation may change, see Figure 5.6. In the latter, the number of steps is set to 120, which corresponds to approximately 2 minutes under the assumption that a user walks one step per second.

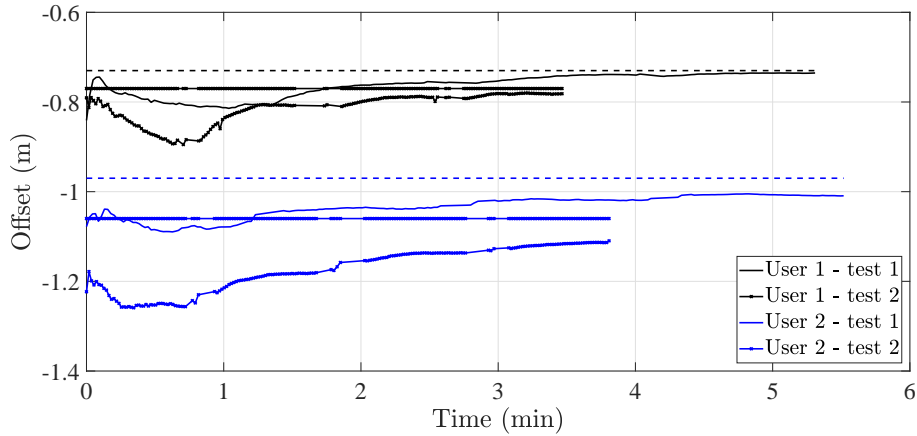


Figure 5.6: Recursive estimation of the offset following approach 1 (horizontal line) and approach 2 (variable line). The number of steps in approach 1 has been set to 120. Each pair solid horizontal-variable line corresponds to a single walk.

It can be seen that the estimations of approach 1 and approach 2 of User 1 are now more similar than in Figure 5.5. In fact, the offset of approach 2 converges to the offset of approach 1 after 2 minutes approximately in test 1. In contrast, the offset of approach 2 converges after 3 minutes approximately in test 2.

The offset estimation of User 2, see Figure 5.6 does not converge. The reason is that the slope of the step length model is not adjusted to the user. Such a case requires a full calibration, which is addressed in the next section.

5.4 Full Calibration

When the step length model of equation (5.2) was first proposed [13], Munoz *et al.* pointed out that the slope of the model remained approximately constant among users. This constant value is referred to as universal slope and it is the result of training the parameters of the step length model with data from a set of users.

The followup work in [19] shows that some users might not have a slope similar to the universal one. This fact may be caused by the user's height, the walking style or any other aspect that the author could not specify [19]. Regardless the cause, the highlight is that the slope of the step length model is not optimal to certain users and thus, it needs to be calibrated.

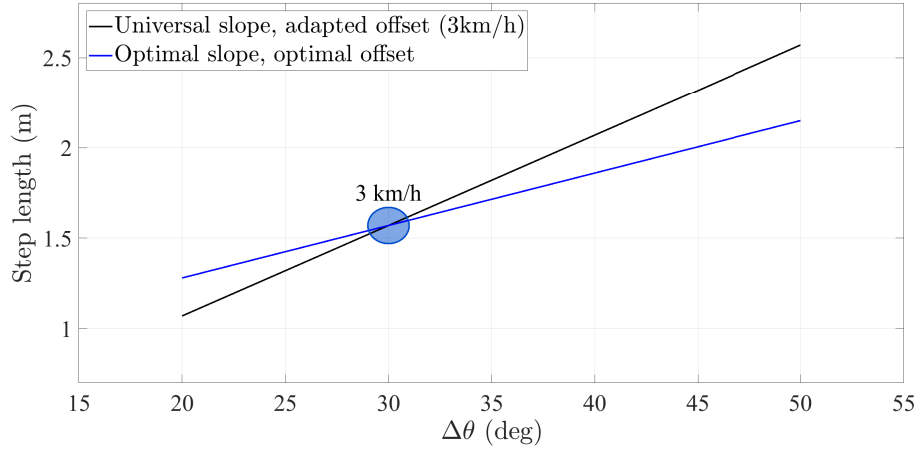


Figure 5.7: Comparison of the step length model adapted to the same user with two different set of parameters. The first set consists of the universal slope and the adapted offset when the user walks at 3 km/h. The second set is the optimal slope and the optimal offset that characterize the user.

The fact that a user's optimal slope differs from the universal slope is, in principle, not noticeable with the calibration methods proposed above. This statement holds as long as the user walks at a constant speed. Let us analyze the example in Figure 5.7. While walking at a certain speed, e.g. 3 km/h, a user has a specific leg aperture and associated step length. The latter are distributed along the circle depicted in Figure 5.7. For these given pairs $\Delta\theta$ -step length, the step length model of equation (5.2) can be adapted with different sets of parameters. For instance, the universal slope and adapted offset, black line, or the optimal slope and optimal offset, blue line.

In contrast, if the user walks faster or slower, the change in speed will be reflected in a change of the estimated offset. Figure 5.8 is an example of the different offset estimations at different walking speeds. These different estimations are an indication that the universal slope is not adapted to the user. Therefore, such a user requires a full calibration, i.e. the estimation of the optimal slope and optimal offset.

The goal of the full calibration method is, as in the previous section, to adapt

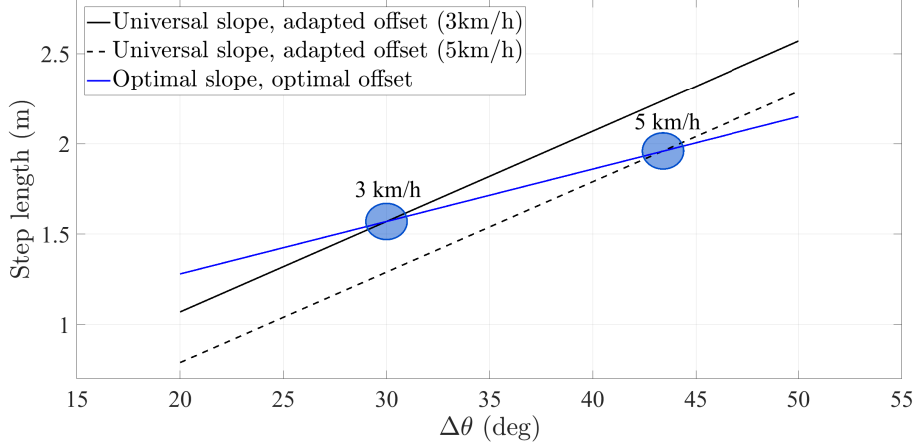


Figure 5.8: Effect of calibrating only the offset when the universal slope differs from the user's optimal slope. When the user walks at different speeds, the calibrated offset changes, e.g. the offset is 0.07 m at 3 km/h, whereas the offset equals -0.21 m at 5 km/h.

the step length model to the user so that it performs optimally. When the case indicated in Figure 5.8 occurs, a continuous offset calibration is required to account for the times when the user changes her walking speed. Thus, a continuous offset calibration would suffice to adapt the step length model to the user. Nevertheless, a continuous calibration would result in an inefficient procedure. In fact, a continuous offset calibration contradicts the conclusion of the previous section, by which the calibration is a process that takes place at the beginning of the walk and that lasts a short time, e.g. 2 minutes.

Estimation of the Optimal Model Parameters

The optimal values of the slope and offset are estimated by optimizing the following equation:

$$\xi(a, b) = \sum_{k=1}^n (s_f^k - a \cdot \Delta\theta^k - b)^2. \quad (5.8)$$

where $\xi(a, b)$ is the squared error of equation (5.2) in terms of the slope (a) and the offset (b).

Given a set of pitch amplitudes of the pocket INS ($\Delta\theta^k$) and step lengths (s_f^k) with $k = \{1, \dots, n\}$, the optimal slope (a_o) and offset (b_o) are estimated to minimize the squared error $\xi(a, b)$. To that end, the following system of equations is solved:

$$\frac{\partial \xi(a, b)}{\partial a} = 0, \quad (5.9)$$

$$\frac{\partial \xi(a, b)}{\partial b} = 0, \quad (5.10)$$

which leads to the system of equations [81]:

$$\begin{bmatrix} \sum_{k=0}^n (\Delta\theta^k)^2 & \sum_{k=0}^n \Delta\theta^k \\ \sum_{k=0}^n \Delta\theta^k & n \end{bmatrix} \cdot \begin{bmatrix} a \\ b \end{bmatrix} = \begin{bmatrix} \sum_{k=0}^n \Delta\theta^k \cdot s_f^k \\ \sum_{k=0}^n s_f^k \end{bmatrix}. \quad (5.11)$$

The solution of the system of equations yields the following expressions for the optimal slope a_o and optimal offset b_o :

$$a_o = \frac{n \cdot \sum_{k=0}^n \Delta\theta^k \cdot s_f^k - \sum_{k=0}^n \Delta\theta^k \cdot \sum_{k=0}^n s_f^k}{n \cdot \sum_{k=0}^n (\Delta\theta^k)^2 - (\sum_{k=0}^n \Delta\theta^k)^2}, \quad (5.12)$$

$$b_o = \frac{\sum_{k=0}^n (\Delta\theta^k)^2 \cdot \sum_{k=0}^n s_f^k - \sum_{k=0}^n \Delta\theta^k \cdot s_f^k \cdot \sum_{k=0}^n \Delta\theta^k}{n \cdot \sum_{k=0}^n (\Delta\theta^k)^2 - (\sum_{k=0}^n \Delta\theta^k)^2}. \quad (5.13)$$

These two equations have been used in an example to estimate the optimal parameters of a user. We compare the step length regression line with the universal slope at three different speeds: low speed, medium speed and fast speed. Taking the experiment of Munoz as a reference [19], we consider a low walking speed to be 5 km/h, a medium walking speed to be 6 km/h and a fast walking speed to be 7 km/h.

Figure 5.9 shows that, at different walking speeds, the offset calibration estimates different values. More specifically, the offset difference between the lowest speed and highest speed is 18 cm. In this example in particular, the user's optimal slope is $a_o = 0.022 \text{ m}/^\circ$, whereas the universal slope is $a_u = 0.05 \text{ m}/^\circ$.

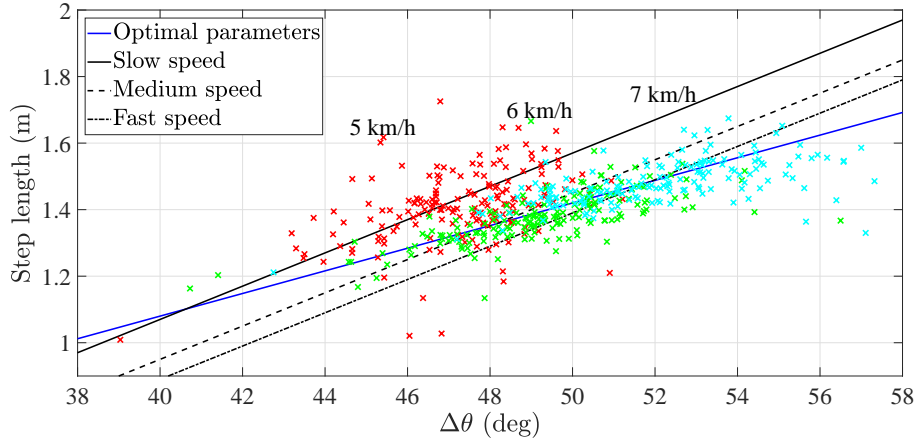


Figure 5.9: Comparison of the different step length models of a user whose optimal slope differs from the universal one. The clouds indicate the pairs step length-pitch amplitude used to train the model parameters.

Figure 5.10 is an example of the full calibration where the user's optimal slope is approximately equal to the universal slope. In particular, the difference in the offset between the lowest speed and highest speed is -5 cm which is approximately 72% smaller than the difference in Figure 5.9. Therefore, we can assume that the slope is adapted to the user.

An interesting fact to observe in Figure 5.9 and Figure 5.10 is that the point clouds are not equally distributed. The distribution is characteristic of each user and responds to the user's physiology and walking style.

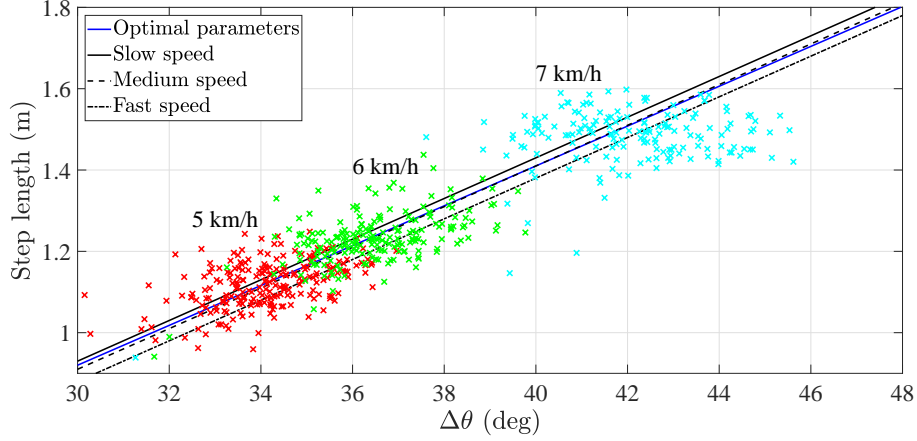


Figure 5.10: Comparison of the different step length models of a user whose optimal slope is approximately the same as the universal one. The clouds indicate the pairs step length-pitch amplitude used to train the model parameters.

Practical Implementation

This section studies the practical implementation of the full calibration method presented in the previous section. In general, the implementation of the full calibration is a two-step process. The first step is to detect the need of a full calibration of the parameters of the step length model. The second one is to carry out the full calibration as described above.

Let us begin by characterizing how the difference in offset varies with respect to two parameters: the change in walking speed and the difference between the optimal slope and the universal slope. To that end, the step length model with optimal parameters (a_o, b_o) is written as follows:

$$s = a_o \cdot \Delta\theta + b_o. \quad (5.14)$$

Similarly, the step length model can also be written with a second set of parameters:

$$s = a_u \cdot \Delta\theta + b_i, \quad (5.15)$$

where a_u denotes the universal slope and b_i denotes the calibrated offset at the walking speed ν_i . The offset calibration is assumed to be implemented with the approach proposed in Section 5.3.

At a given walking speed ν_i , the estimated step length is the same with equation (5.14) and equation (5.15). Therefore,

$$a_o \cdot \Delta\theta_i + b_o = a_u \cdot \Delta\theta_i + b_i, \quad (5.16)$$

which leads to,

$$(a_o - a_u) \cdot \Delta\theta_i = b_i - b_o, \quad (5.17)$$

where $\Delta\theta_i$ is the pitch amplitude of the pocket INS at the walking speed ν_i .

If the user walks at a different walking speed, e.g. ν_j , equation (5.17) can be written as:

$$(a_o - a_u) \cdot \Delta\theta_j = b_j - b_o. \quad (5.18)$$

Equation (5.17) and equation (5.18) can be subtracted from one another to lead to:

$$(a_o - a_u) \cdot (\Delta\theta_i - \Delta\theta_j) = (b_i - b_j). \quad (5.19)$$

This expression relates the offset difference $b_i - b_j$ to the two relevant parameters, namely:

- the difference in walking speed, represented by $\Delta\theta_i - \Delta\theta_j$ and,
- the difference between the optimal slope and the universal slope, which is represented by $a_o - a_u$.

Equation (5.19) has been used to generate the heat map in Figure 5.11. The latter depicts the dependency of the offset difference with respect to the two aforementioned parameters. Depending on the speed change, equation (5.19) can take different values. *Area 0* describes the case where the step length model is adapted to the user, i.e. $a_o \approx a_u$. In such a case, a change in walking speed causes no change in the offset estimation.

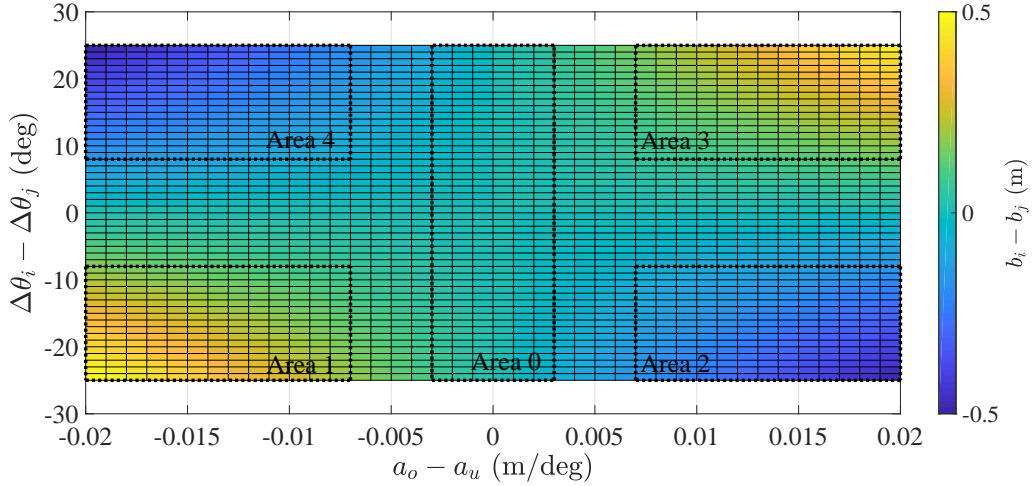


Figure 5.11: Heat map of the offset difference depending on the difference in walking speed and the difference between the universal slope and the user's optimal slope.

Area 1 and *Area 4* describe the case $a_o < a_u$. In such a case, the offset difference will be positive or negative depending on the speed sequence. The latter refers to whether the user begins walking slow and then walks faster, *Area 1*, or viceversa, *Area 4*.

Area 2 and *Area 3* depict the case $a_o > a_u$. Following the same reasoning, the offset difference depends on the speed sequence. Interestingly, the cases are reversed with respect to the previous case. For instance, a change from a slow to a fast walking speed will lead to a negative offset difference, e.g. *Area 2*.

The analysis of Figure 5.11 leads to the generalization of Figure 5.12, which indicates the trend of the offset difference with respect to the walking speed. The solid grey line corresponds to *Area 0* in Figure 5.11, i.e. if the slope is adapted to the user, then the offset remains approximately constant at different walking speeds. In the case that the slope of the step length model is not adapted, an increase in speed will lead to an increase or decrease in the offset estimation. *Area 1* and *Area 4* lead to the dashed black line, whereas *Area 2* and *Area 3* lead to the solid black line.

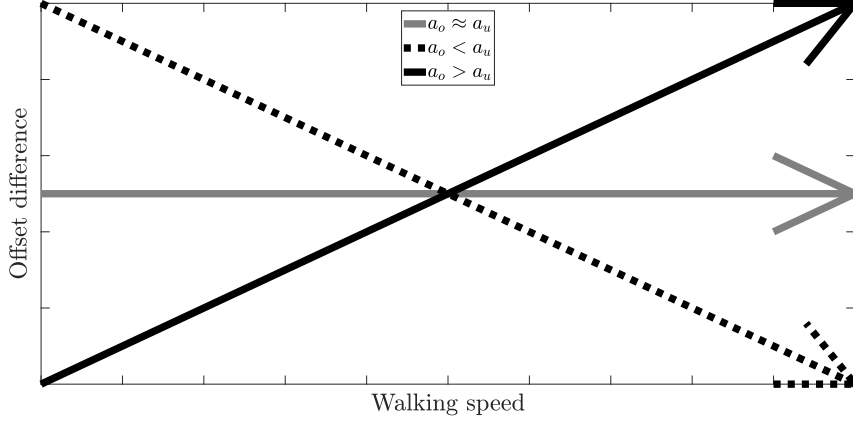


Figure 5.12: Trend of the offset difference with respect to the increase in walking speed. The trend is depicted for the three cases identified.

Provided that a change in walking speed implies a change in the offset, the next step is to analyze the variance of the offset. To that end, the offset variance (σ_b^2) is estimated with a moving average window of length n :

$$\sigma_b^2 = \frac{1}{n} \cdot \sum_{i=k-n+1}^k (b^i - \mu_b^i)^2, \quad (5.20)$$

where μ_b^i is the average of the offset in the specified window. It is important to highlight that the slope used in this analysis is the universal one.

The analysis of equation (5.20) reveals whether the model slope is adapted or not to the user. An example is shown in Figure 5.13, where User 1 has a smaller offset variance than User 2, and both users did not change their walking speed. This difference is an indication that User 1's slope is more adapted than User 2's slope because the variance of the offset change is smaller for the former than for the latter.

Let us remember that the universal slope is 0.05 m/deg . The full calibration run on User 1 and User 2 estimates the slopes below:

- User 1's optimal slope is 0.05 m/deg whereas,
- User 2's optimal slope is 0.03 m/deg .

Thus, a user whose slope is adapted has a lower offset variance than a user whose slope is not adapted. Therefore, the offset variance can be used as an indicator of the need for a full calibration.

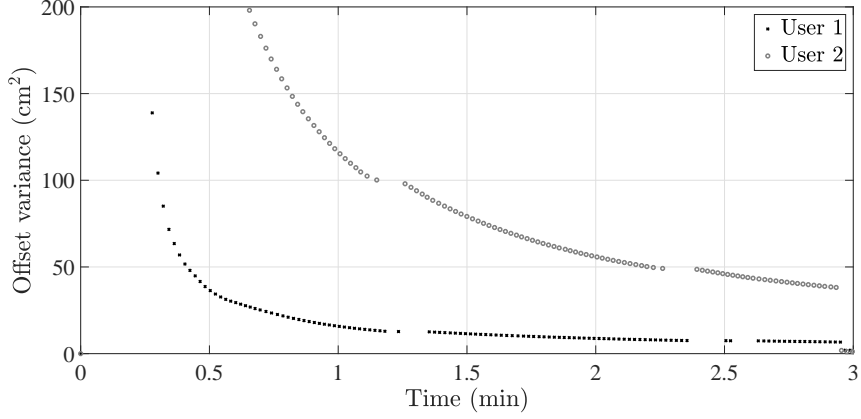


Figure 5.13: Offset variance for two different users. The offset is estimated with the offset calibration method presented in Section 5.3. User 1's slope is adapted whereas User 2's slope is not adapted.

In order to use the offset variance as an indicator, it is necessary to define two parameters, namely an elapsed time and a variance threshold. The elapsed time is the time after which the variance is analyzed. The variance threshold is the value that triggers the full calibration. The full calibration is required if the offset variance is larger than the variance threshold after the elapsed time.

The pair elapsed time-variance threshold depends on the window length n in equation (5.20). In fact, it can be seen in Figure 5.14 that the smaller the window length in is the steeper the offset variance becomes. In practice, the elapsed time needs to be long enough to allow the offset to stabilize in those cases where the slope of the step length model is adapted to the user. Therefore, and based on the results in Section 5.3, the recommended elapsed time to analyze the offset variance is 2 minutes. After 2 minutes, the offset is expected to have stabilized if either the slope is adapted or the user is walking at an approximately constant speed.

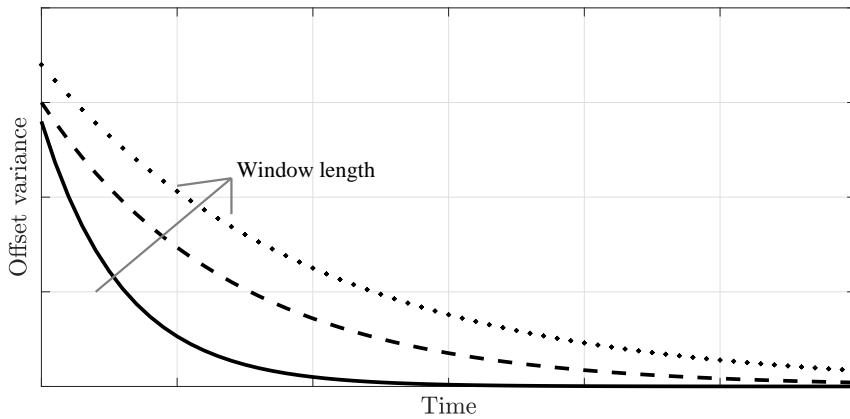


Figure 5.14: Trend of the offset variance when the window length increases. The grey arrow indicates the direction in which the window length increases.

The second parameter to be specified is the variance threshold. From the tests, we could observe that in the cases where the slope of the step length model is adapted,

the offset variance is lower than 5 cm^2 . Thus, should the offset variance be larger than 5 cm^2 after 2 minutes, the full calibration can be triggered.

The second step is the full calibration itself. The methodology to estimate the optimal slope and offset has been presented above. This methodology requires the user to walk at different speeds in order to get a rich sample set of pairs step length-pitch amplitude of the pocket INS. A rich sample set is the one that contains data from the user walking at different walking speeds, e.g. 3 km/h , 5 km/h , 7 km/h , similarly to [19]. Failure to use such a set will result in a step length model over-fitted to a certain walking speed.

To finalize, Figure 5.15 presents a block diagram of the calibration method of the step length model as presented in Section 5.3 and Section 5.4. This figure corresponds to the *Parameter calibration* block in Figure 5.1. The calibration method begins with the estimation of the optimal offset for the universal slope. If the offset variance is larger than the variance threshold after 2 minutes, then the full calibration is triggered. As indicated above, the full calibration should request the user to walk at different speeds in order to guarantee that the estimation of the optimal slope and optimal offset represent the physiology of the user.

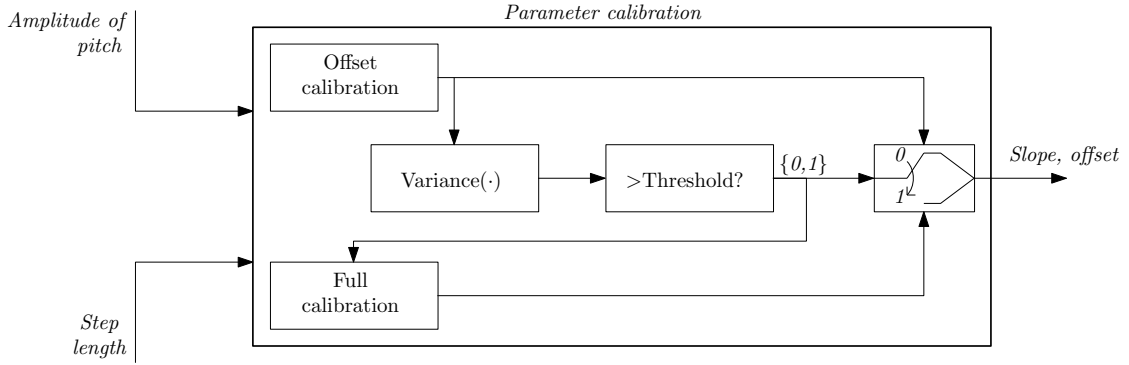


Figure 5.15: Block diagram of the *Parameter calibration* block in Figure 5.1.

5.5 Summary and Conclusions

In this chapter, we have developed two calibration methods to estimate the parameters of the step length model of the pocket INS. The calibration methods use the step length estimated by the foot INS and automatically estimate the parameters of the step length model. The first calibration method estimates only one of the parameters of the step length model, namely the offset. The second calibration method estimates both parameters of the step length model, namely the slope and the offset.

Our first conclusion is that it is feasible to automatically calibrate the parameters of a step length model by using a foot INS. We achieve the automatic calibration with two different methods that have a low computational complexity and which can be

implemented in real time. Moreover, we have noticed that the calibration is always needed prior to using the pocket INS.

Our second conclusion is that the offset calibration method needs only a limited time at the beginning of the walk to estimate the offset. In fact, we have observed that this time is approximately 2 minutes. Moreover, the offset calibration method does not need a dedicated walk to estimate the offset. Instead, we need only to run the pocket INS and the foot INS, and the offset calibration method will automatically estimate the offset. The user is not aware of the need for calibration nor the fact that the step length model of the pocket INS is being calibrated.

Our third conclusion is that the full calibration method is feasible only if the user walks at different walking speeds. In this case, feasible means that we can estimate the slope and offset of the step length model that represent the user's physiology. The full calibration method faces the risk of over-fitting when the user does not change her walking speed. Over-fitting indicates that the slope and offset are adapted only to a specific walking speed.

Chapter 6

Loose Coupling System

*If you always do what you always did,
you will always get what you always got*
– Albert Einstein

In sensor fusion, a loose coupling system refers to the combination of the output of independent systems. The latter use the raw measurements from dedicated sensors to produce an output that contains errors. The nature of these errors is different for different systems and, frequently, different systems have complementary errors, see Figure 6.1. The latter property can be exploited to combine systems in a loose coupled fashion, such that the strengths of a system compensate for the weaknesses of the other system and viceversa, as Figure 6.1 depicts.

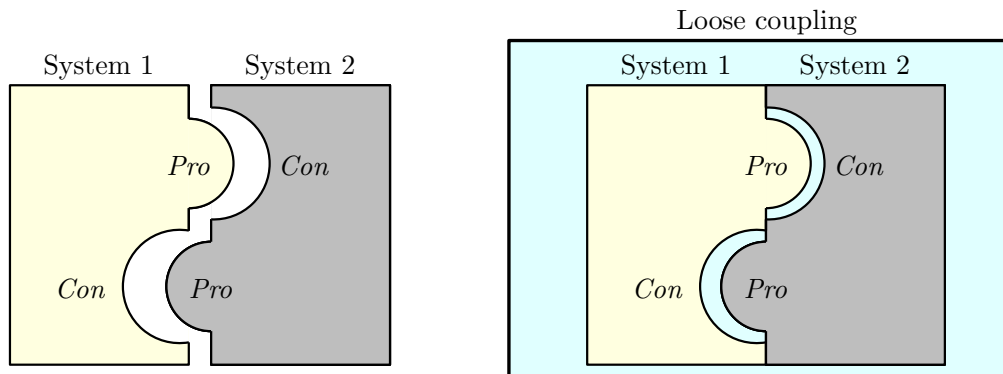


Figure 6.1: (Left) Representation of the complementary strengths (*Pro*) and weaknesses (*Con*) of two systems. (Right) Loose coupling system with combined strengths and weaknesses.

The loose coupling system has several advantages. The first one is the performance improvement of the fusion with respect to the independent systems. The second one is that a loose coupling system promotes modularity, that is, the fusion can be designed considering independent working systems that communicate with each other through predefined interfaces. Therefore, it is easier to independently design the systems that comprise the loose coupling system and then plug them together

for the final working system. Finally, robustness is another advantage of the loose coupling system. Loose coupling systems are robust because they rely on two or more systems. If one of the latter fails, the remaining independent systems take over. Robustness comes frequently at the cost of redundancy, and the robustness requirement will be dependent on the application.

In this chapter, we propose a loose coupling system that combines the outputs of the foot INS and the pocket INS. The goal is to obtain an improved position estimation with respect to the single-IMU localization systems.

6.1 System Overview

The loose coupling system was first proposed in [82] to estimate the 2D position of a user. Then, the loose coupling system is extended to 3D in [83]. After certain modifications, the final structure of the loose coupling system is the one shown in Figure 6.2. The 3D loose coupling takes the output of both the pocket INS and the foot INS to produce a single position of the user. The single-IMU localization systems keep working independently from each other.

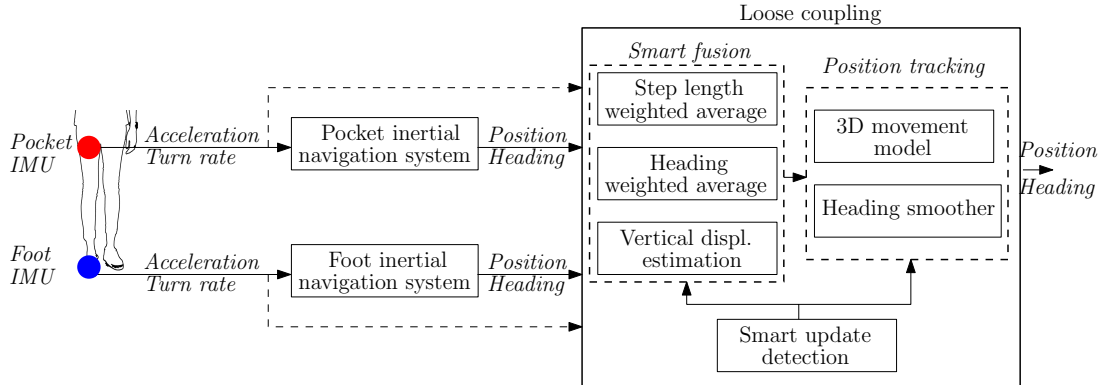


Figure 6.2: Block diagram of the 3D loose coupling. *Displ.* stands for displacement.

The proposed loose coupling system has two-steps. The first step is the smart fusion, which is divided into three parts: the step length estimation, the heading estimation and the vertical displacement estimation. Each of these parts leverages the information from the two inertial localization systems at the input.

The second step is to feed the outcome of the fusion to a position tracking system, which iteratively estimates the user's position. The *Position tracking* block estimates the 3D position in two steps. Firstly, the *Heading smoother* estimates the heading and secondly, the *3D movement model* propagates the position.

The *Heading smoother* implements a Kalman filter to smooth the heading estimate of the *Smart fusion* block. The reason for this smoothing is because the heading

estimation has ripples due to the vibrations of both the foot IMU and pocket IMU while walking. The filter state is the heading $\mathbf{x} = [\psi]$, which is propagated as $\mathbf{x}^k = \mathbf{x}^{k-1}$. The filter state is updated with the heading estimated by the *Smart fusion* block. For further details on the Kalman filter equations the reader is referred to [48].

The *3D movement model* implements the following equations to estimate the 3D position ($\mathbf{p} = [p_x, p_y, p_z]$):

$$p_x^k = p_x^{k-1} + s^k \cdot \cos(\psi^k), \quad (6.1)$$

$$p_y^k = p_y^{k-1} + s^k \cdot \sin(\psi^k), \quad (6.2)$$

$$p_z^k = p_z^{k-1} + v^k, \quad (6.3)$$

where s^k and v^k are the step length and vertical displacement respectively estimated during the *Smart fusion*. ψ^k is the output of the *Heading smoother*.

6.2 Smart Fusion

The first step of the loose coupling system is the smart fusion, i.e. the combination of the input data. In order to do that, it is necessary to identify the principles under which the information is combined. For instance, a possible solution could be the average of the position estimates of the pocket INS and the foot INS. Such an approach combines the information in a deterministic fashion, and it disregards any strengths of the inertial localization systems at the input of the loose coupling system.

Single-IMU localization systems exploit features of the human walk to improve the position tracking. These features decrease the position errors, e.g. the zero-velocity of the foot during the stance phase, see Section 3.2.1. In the proposed loose coupling system, we also take advantage of these features to identify when the estimations of the single-IMU localization systems are most accurate.

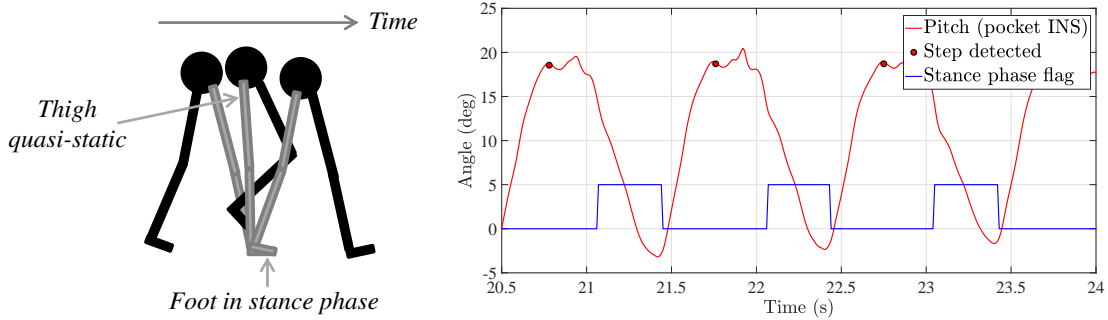


Figure 6.3: (Left) Representation, over time, of the gait phases relevant for the pocket INS and the foot INS. (Right) Behaviour of the pitch of the pocket INS and the stance phase detection flag during three steps.

The position estimation of the pocket INS is most accurate when the leg is straight and the thigh is quasi-static, see Figure 6.3. This event allows to apply the gravity

update, which updates the roll and pitch of the pocket INS, see Section 3.1. The position estimation of the foot INS is most accurate when the foot is in stance phase, see Figure 6.3. This event allows to apply the ZUPT, which updates both the velocity and position of the foot INS.

In the loose coupling system, the outputs of the pocket INS and the foot INS are sampled upon detection of the aforementioned events, that is:

- when the pitch of the pocket INS changes from its maximum to its minimum and,
- when the foot is in stance phase.

In doing so, we guarantee that the information of either inertial localization system is most accurate when it is used at the *Smart fusion* block, see Figure 6.2. In this work, this approach is referred to as smart update [82]. The concept describes the fact of exploiting the strengths of each single-IMU localization system such that the loose coupling takes the input information only when it is most accurate.

Once the input information is sampled, the next step is to combine it. To that end, it is necessary to distinguish the 2D component from the vertical one. In the following, the details of the smart fusion are presented, firstly, to estimate the 2D position and, secondly, to track the vertical displacement.

6.2.1 Fusion for 2D

The 2D position (\mathbf{p}^k) of a user can be estimated as:

$$p_x^k = p_x^{k-1} + s^k \cdot \cos(\psi^k), \quad (6.4)$$

$$p_y^k = p_y^{k-1} + s^k \cdot \sin(\psi^k), \quad (6.5)$$

where $[p_x^k, p_y^k]$ are the cartesian components of the 2D position, s^k is the step length estimation and ψ^k is the heading estimate at the k -th time, respectively. The variables s^k and ψ^k are estimated through the information of the two single-IMU systems. More specifically, we favour the most accurate input to estimate each of the variables. The criteria to estimate both the step length and the heading are presented below.

Step Length Fusion

Figure 6.2 shows that the input to the loose coupling is the position estimation of the single-IMU localization systems. Therefore, it is necessary to relate the step length with the position estimations. The step length estimated by the pocket INS (s_p^k) or the foot INS (s_f^k) is given by the Euclidean distance between two position estimations at two consecutive step detections, that is:

$$s_p^k = |\mathbf{p}_p^k - \mathbf{p}_p^{k-1}|, \quad (6.6)$$

where \mathbf{p}_p^k is the position estimate of the pocket INS at the k -th step, \mathbf{p}_p^{k-1} is the position estimate of the pocket INS at the $(k-1)$ -th step and $|\cdot|$ denotes the norm of the argument. The step length of the foot INS (s_f^k) follows the same expression as the one of equation (6.7).

The step length of the loose coupling (s^k) is a weighted average of the estimations of the pocket INS and the foot INS:

$$s^k = w_{sp} \cdot s_p^k + w_{sf} \cdot s_f^k, \quad (6.7)$$

where w_{sp} and w_{sf} are the weights of the step length estimations of the pocket INS (s_p^k) and the foot INS (s_f^k), respectively.

The weights need to reflect how much accurate the step length of the foot INS is than the step length of pocket INS, or viceversa. In order to determine that, we take into account the results of Table 4.2. More specifically, we use the standard deviation to estimate the step length weights as follows:

$$w_{sp} = \frac{\sigma_p^{-1}}{\sigma_p^{-1} + \sigma_f^{-1}}, \quad (6.8)$$

$$w_{sf} = \frac{\sigma_f^{-1}}{\sigma_p^{-1} + \sigma_f^{-1}}, \quad (6.9)$$

where σ_p and σ_f are the standard deviation of the distance estimation of the pocket INS and the foot INS, respectively. Taking into account Table 4.2, the step length weights of the pocket INS and the foot INS are 0.51 and 0.49, respectively.

It is important to highlight that the weights w_{sp} and w_{sf} are constant over time. This feature is the result of the study carried out in Chapter 4, where the evaluation shows that both inertial localization systems have approximately the same accuracy. This statement holds as long as the step length model of the pocket INS is calibrated to the user.

Heading Fusion

Similarly to the step length, the loose coupling system estimates a single heading given the heading estimations of the pocket INS and the foot INS. The approach is also similar to the step length fusion, i.e. the heading estimation is the weighted circular mean between the estimations at the input:

$$\psi = \arctan \left(\frac{w_{\psi p} \cdot \sin(\psi_p) + w_{\psi f} \cdot \sin(\psi_f)}{w_{\psi p} \cdot \cos(\psi_p) + w_{\psi f} \cdot \cos(\psi_f)} \right), \quad (6.10)$$

where $w_{\psi p}$ and $w_{\psi f}$ are the weights of the heading estimations of the pocket INS and the foot INS, respectively. We use the circular mean because it is better suited to estimate the average of circular quantities such as angles than the arithmetic mean is [84, 85].

In contrast to the case of the step length, the study in Chapter 4 revealed that the heading errors of either single-IMU localization system are random. Therefore, it is not possible to make a statement regarding the heading performance of an inertial localization system with respect to the other. In fact, every experiment is different and it is necessary to assess each case separately to determine which single-IMU localization system is generating the most accurate heading estimation at a specific time.

The weights $w_{\psi p}$ and $w_{\psi f}$ need to reflect how accurate the heading of the pocket INS is with respect to the heading of the foot INS. Provided that the heading of an inertial localization system is unobservable [30], the challenge we face in this case is how to determine, in each experiment, the relative accuracy of the heading of the pocket INS and the heading of the foot INS.

To address the challenge, we propose a method that determines, instant-wise, how accurate one heading estimation is with respect to another heading estimation. This method is explained in detail in Section 6.3. The estimated weights vary over time as the example in Figure 6.4 shows. Figure 6.4 also shows the heading estimations associated to the heading weights.

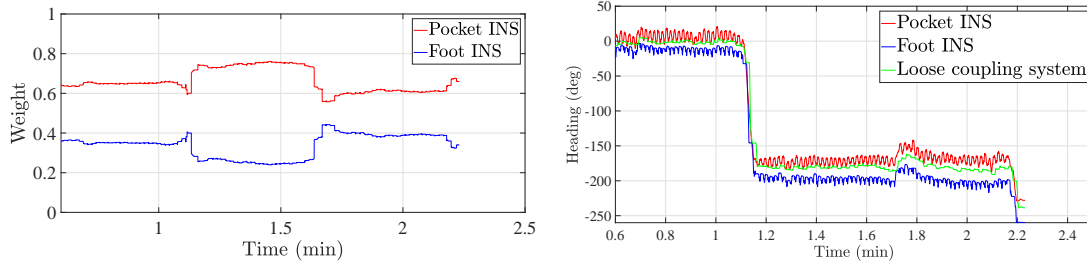


Figure 6.4: (Left) Heading weights estimated at each time instant. (Right) Heading estimation of the loose coupling after weighting the heading estimates of the pocket INS and the foot INS.

The heading weights are estimated as follows:

$$w_{\psi p} = \frac{q_p}{q_p + q_f}, \quad (6.11)$$

$$w_{\psi f} = \frac{q_f}{q_p + q_f}, \quad (6.12)$$

where q_p and q_f are the quality factor of the heading estimations of the pocket INS and the foot INS, respectively. These factors reflect how accurate one heading estimation is with respect to another one. Section 6.3 details the estimation of these factors.

6.2.2 Fusion for 3D

There are different types of 3D scenarios, like stairs, elevators, escalators, etc. In this work, only 3D scenarios with stairs are considered because they are the ones that

can be tackled with IMUs. In order to track the height in elevators or escalators, we would need to use sensors like barometers, which are out of the scope of this work. The single-IMU localization systems in Figure 6.2 provide a different type of 3D information. This fact is outlined in detail in Table 4.3. In the following, we summarize the features of each inertial localization system regarding stairs walking.

The pocket INS has the ability of accurately detecting stairs [19]. Figure 6.5 shows the pitch of the pocket INS when a user is walking horizontally and walking upstairs. Thanks to the analysis of both the pitch amplitude and the pitch maximum, it is possible to detect if the user is walking upstairs or downstairs. Nevertheless, the pocket INS requires a model to estimate the vertical displacement while stairs walking.

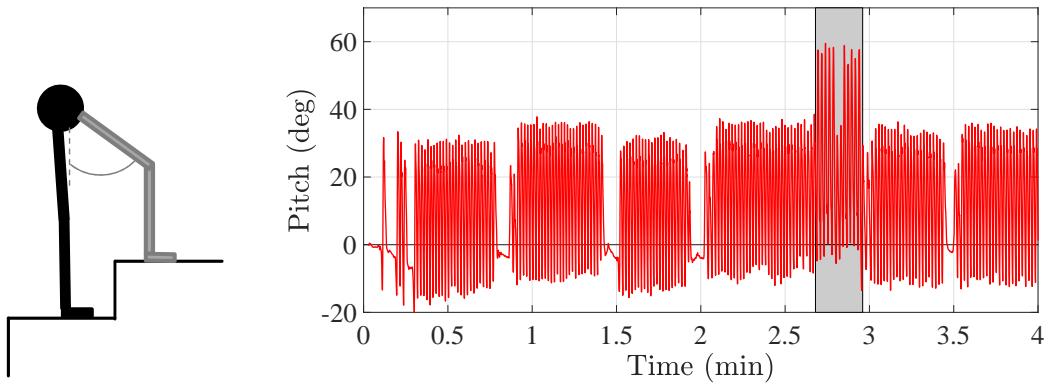


Figure 6.5: (Left) Representation of the legs while walking upstairs. The pitch of the pocket INS (grey leg) is greater than the pitch while walking horizontally. (Right) Pitch of the pocket INS during horizontal walking (non-shadowed area) and during walking upstairs (shadowed area).

The foot INS is able to provide an estimation of the z-component of the user's position, as depicted in Figure 6.6. The challenge of the foot INS is that the height error accumulates over time. The result is that even if the user walks horizontally, the height estimation is not constant, see Figure 6.6. Nonetheless, the vertical displacement over short periods of time remains more accurate than the height estimate at each time instant.

The 3D features of both the pocket INS and the foot INS can be exploited in the loose coupling. To that end, we propose the block diagram in Figure 6.7. In the latter, the height of the foot INS is sampled only upon the detection of stairs. Then, the vertical displacement (v) is estimated as:

$$v = p_z^k - p_z^{k-1}, \quad (6.13)$$

where p_z^k and p_z^{k-1} are the height estimates of the foot INS at two consecutive stairs detection. In the case of the first detected stair, the previous height (p_z^{k-1}) is the height estimation of the foot INS at the time instant of the last detected horizontal step of the pocket INS.

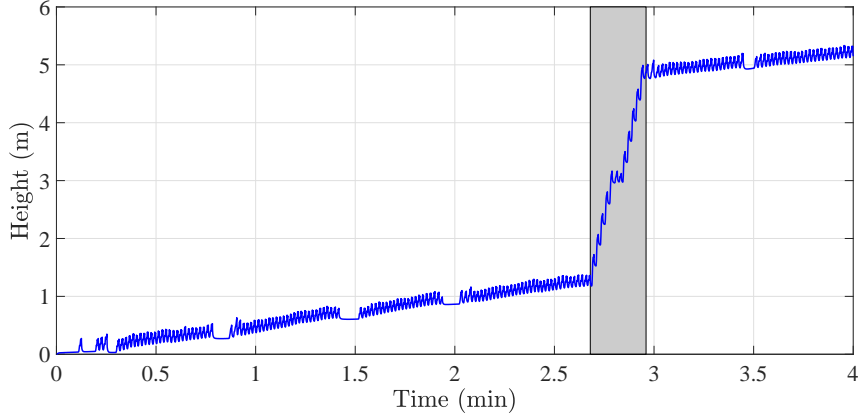


Figure 6.6: Height estimation of the foot INS for the same walk as the one depicted in Figure 6.5. The shadowed area indicates when the user was walking the stairs.

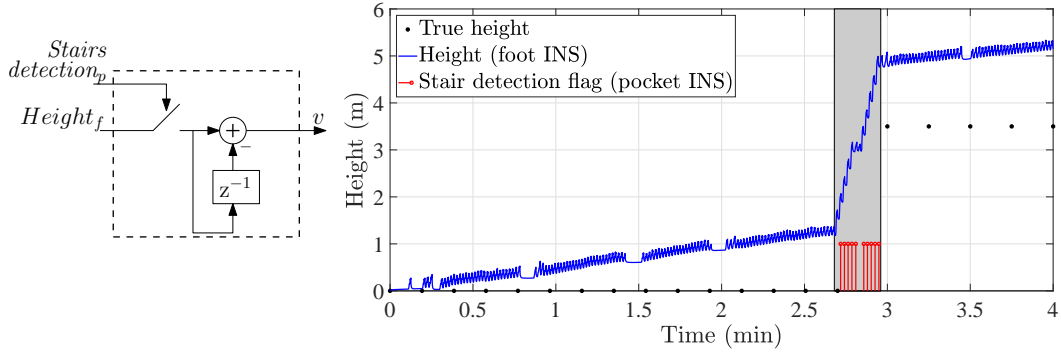


Figure 6.7: (Left) Block diagram of the *Vertical displacement estimation* block of the loose coupling system. (Right) Comparison of the height estimation of the foot INS and the stairs detection of the pocket INS. In addition, the true height during the horizontal walk is given.

6.3 Estimation of the Heading Quality

The heading fusion in equation (6.10) requires the quantification of the heading quality through the heading weights, $w_{\psi p}$ and $w_{\psi f}$. The heading depends on different factors at the specific time of performing the walk, like the random errors in the IMU such as the bias stability [11]. The random errors make it particularly challenging to determine the heading quality because, firstly, the heading is unknown and, secondly, the heading accuracy is not constant neither during one run nor from one run to the next.

Let us consider the odometries depicted in Figure 6.8. One can imagine that these are, instant-wise, the position estimations and the heading estimations input to the loose coupling system. The question that the loose coupling faces is: *how accurate is one heading estimation with respect to the other one?*

The trivial way to answer the question is to use prior information, e.g. the approximate shape of the walk. The drawback of such procedure is that the accuracy of

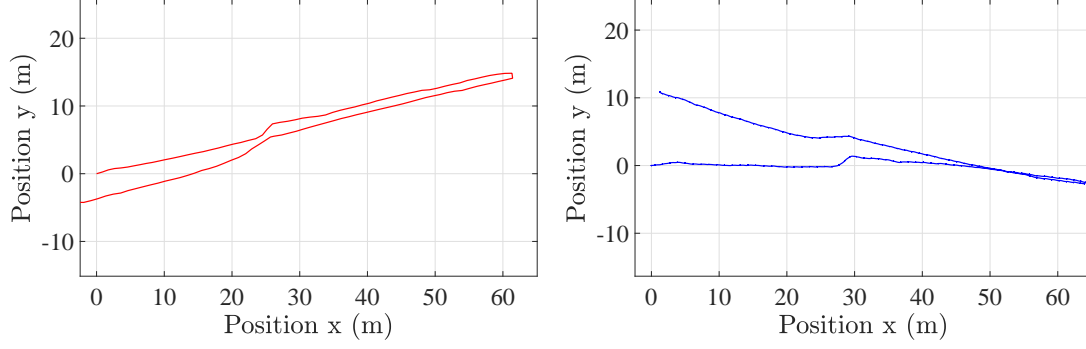


Figure 6.8: (Left) Odometry estimated by the pocket INS. (Right) Odometry estimated by the foot INS.

the heading can only be determined in postprocessing. Moreover, the accuracy is usually qualitative, and thus, deriving a performance figure becomes a challenge if no ground truth of the true path is available.

The loose coupling system in Figure 6.2 is expected to operate online. Therefore the aforementioned alternative is not applicable. In addition, we do not expect to have a ground truth system nor the human factor to produce a statement on the heading errors of each single-IMU localization system.

The method to estimate the accuracy of the heading does not require any prior knowledge or external input. Only the attitude estimation of each single-IMU localization system and the turn rate vector of the IMU are required.

6.3.1 Proposed Method

The quality factor is a figure that quantifies the accuracy of the heading estimate of an inertial localization system. The quality factor is meant to be used together with other quality factors in order to determine objectively how accurate a heading is in comparison to another one.

In order to estimate the quality factor, we make an important assumption. We consider that the roll and pitch estimates of the attitude vector are error-free. This assumption is based on the fact that an inertial localization system implements the gravity update, which decreases the errors in the roll and pitch. Therefore, the heading is the angle which is disturbed by the integration of the bias and bias stability of the turn rate vector.

The quality factor (q) of a heading is computed as depicted in Figure 6.9. The process begins with the estimated attitude vector Ψ of an inertial localization system, which contains the Euler angles roll (ϕ), pitch (θ) and heading (ψ). The latter vector will contain errors that depend on the implementation of the associated *Attitude estimation* block.

The next step is to estimate the turn rate vector ($\tilde{\omega}$) that should generate the

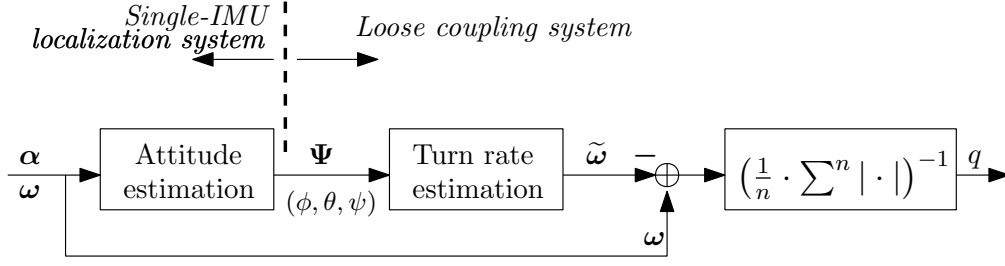


Figure 6.9: Block diagram for the estimation of the quality factor for the heading. The diagram has been adapted from [82]. α and ω are the acceleration vector and turn rate vector, respectively, measured by the IMU.

attitude vector (Ψ), which contains errors:

$$\tilde{\omega}_x = \dot{\phi} - \dot{\psi} \cdot \sin(\theta), \quad (6.14)$$

$$\tilde{\omega}_y = \dot{\theta} \cdot \cos(\phi) + \dot{\psi} \cdot \sin(\phi) \cdot \cos(\theta), \quad (6.15)$$

$$\tilde{\omega}_z = -\dot{\theta} \cdot \sin(\phi) + \dot{\psi} \cdot \cos(\phi) \cdot \cos(\theta), \quad (6.16)$$

where $\tilde{\omega}_x$, $\tilde{\omega}_y$ and $\tilde{\omega}_z$ are the components of the turn rate vector $\tilde{\omega}$ and $(\dot{\cdot})$ denotes the first derivative of the argument. For a detailed derivation of equation (6.14)-equation (6.16), the reader is referred to Appendix F. The turn rate vector ($\tilde{\omega}$) is affected by the errors in the calculation of the attitude vector (Ψ).

The next step is to compare the true turn rate vector (ω) with the estimated one ($\tilde{\omega}$). The true turn rate vector (ω) is the one measured by the IMU. Although the latter is affected by different errors [11], these errors are small in comparison to the overall error in the attitude vector (Ψ). The outcome of the comparison can be interpreted as an error vector, which is then processed in order to estimate a scalar that represents the quality factor (q), that is:

$$q = \left(\frac{1}{n} \cdot \sum_{j=k-n+1}^k |\omega^j - \tilde{\omega}^j| \right)^{-1}. \quad (6.17)$$

An example of the performance of the quality factor is shown in Figure 6.10. This example is the quality factor associated to the odometries in Figure 6.8. According to the quality factor, the heading of the pocket INS is more accurate than the heading of the foot INS. We can see that this statement is true when we compare the odometries in Figure 6.8 to the associated true walk in Figure 6.10.

The higher the value of the quality factor is, the higher the accuracy of the heading (ψ). The quality factor can be used as an indicator to compare two heading estimates and to weight them accordingly for their fusion in the loose coupling system.

6.3.2 Simulative Proof

This section describes the simulative proof carried out to validate the method proposed in Figure 6.9. The validation has two main goals. The first one is to show

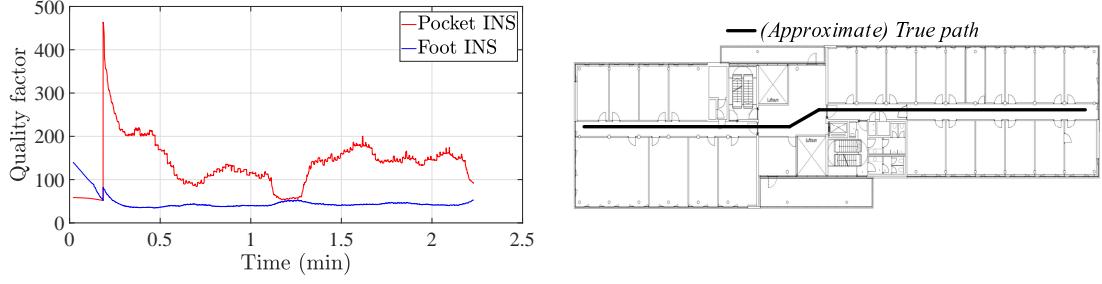


Figure 6.10: (Left) Quality factor of the odometries in Figure 6.8. (Right) Approximate ground truth of the odometries in Figure 6.8.

that the quality factor is the same for headings that have the same quality, i.e. the same errors. The latter should be valid regardless the inertial localization system that generates the heading. The second goal is to show that the higher the errors in the heading, the lower the quality factor.

The simulative proof follows the block diagram of Figure 6.11. In order to assess the quality factor values, the physical IMU is replaced by an *IMU simulator*. The simulator generates synthetic inertial measurements with a configurable level of random noise, bias and bias stability.

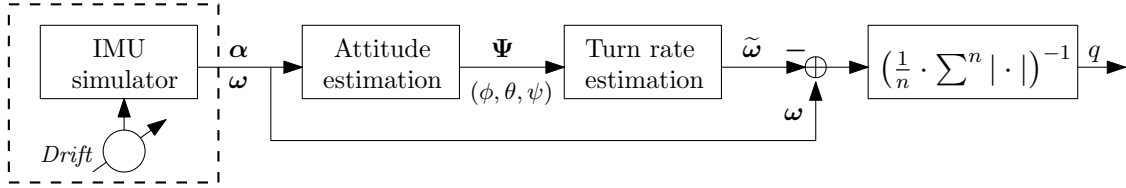


Figure 6.11: Set up of the simulative proof to validate the method to estimate the heading quality. The *Attitude estimation* is a sub-system of either the pocket INS or the foot INS. α and ω are the synthetic acceleration vector and synthetic turn rate vector, respectively.

In order to have realistic measurements, the noise levels are chosen according to those of the sensors used in this thesis. The noise levels are available in the manufacturer's user manual [77]. Nevertheless, since these values have proven to vary from the true sensors [73], we carried out an Allan variance analysis [86] to characterize the errors in the sensors. The results are given in Appendix G.

The IMU simulator is configured to generate three types of static measurements, which are summarized in Table 6.1. The synthetic inertial measurements (α , ω) allow for the comparison of the results of the configuration in Figure 6.11 in different cases, which are listed in Table 6.2. Although only some of them are mentioned below, all of them have been analyzed. The reader is referred to Appendix D for the results that are not shown in this section.

Since the synthetic inertial measurements correspond to a static IMU, the inertial localization system should produce the attitude vector $\Psi = (0, 0, 0)^T$, i.e. the attitude

Table 6.1: Configuration of the gyroscope errors of the *IMU simulator*.

Turn rate configuration	Constant bias $\left[\frac{^\circ}{s}\right]$	Bias stability $\left[\frac{^\circ}{s}/\sqrt{\text{Hz}}\right]$
Only random noise	–	–
Constant bias	(0.05, 0.05, 0.05)	–
Variable bias	(0.05, 0.05, 0.05)	(0.033, 0.033, 0.033)

Table 6.2: Error configuration of each case study.

Case study	Pocket INS	Foot INS
1	Only random noise	Only random noise
2	Constant bias	Constant bias
3	Variable bias	Variable bias
4	Constant bias	Only random noise
5	Only random noise	Constant bias
6	Variable bias	Only random noise
7	Only random noise	Variable bias
8	Constant bias	Variable bias
9	Variable bias	Constant bias

vector of a static IMU. Nonetheless, the error characteristics in Table 6.1 disturb the synthetic inertial measurements. So, *what could we expect from the pocket INS or the foot INS?* The answer would be one of the following:

- If the raw measurements are disturbed only by random noise, then the UKF should filter the noise to produce an attitude vector that is close to zero, i.e. $\Psi \approx (0, 0, 0)^T$
- If the raw measurements are disturbed by random noise and bias, regardless constant or variable, the gravity update of the filter should act to correct the roll and pitch estimates. The heading, however, remains unobservable so its error will grow over time. The nature of this growth, linear or exponential, will depend on whether the bias is constant or variable, respectively.

The case studies can be classified into two groups: raw data with same errors, case studies 1-3, or raw data with different errors, case studies 4-9. Cases studies 1-3 input raw data, to each single-IMU localization system, with the same types of errors. In such cases, one would expect that the errors in the heading are approximately the same independently of the inertial localization system. Thus, it seems intuitive to expect both inertial localization systems to have the same quality factor.

Case 1 is an interesting example where, although the raw measurements have the same errors, the quality of the output is different. Figure 6.12 shows that the heading estimated by both the pocket INS and the foot INS is the same. Therefore, any weighting factors $w_{\psi p}$ and $w_{\psi f}$ will result in the same heading estimation. Nonethe-

less, the two quality factors are different because the values input to equation (6.17) are small, namely in the order of 10^{-5} or lower. Thus, small fluctuations in the elements of equation (6.17) cause large differences in the value of the quality factor of the heading estimation of the pocket INS and the foot INS.

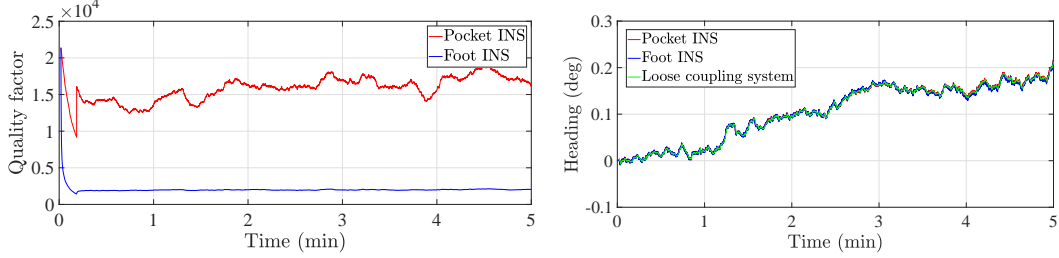


Figure 6.12: Case study 1: (Left) Quality factor estimation. (Right) Heading estimation of the pocket INS, the foot INS and the loose coupling system according to equation (6.10).

Case study 2 is represented in Figure 6.13. We can see that the heading is the same for both inertial localization systems and thus, that the quality factor is reflecting the quality of the heading. It is important to highlight that the quality factor does not inform us how accurate a single heading estimation is. Instead, the quality factor tells us how accurate one heading estimation is with respect to another one.

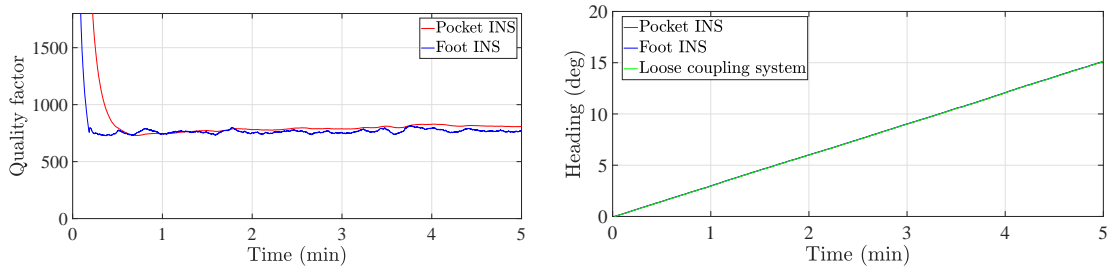


Figure 6.13: Case study 2: (Left) Quality factor estimation. (Right) Heading estimation of the pocket INS, the foot INS and the loose coupling system fusion according to equation (6.10).

Case study 4 is represented in Figure 6.14. The quality factor of the foot INS is higher than the quality factor of the pocket INS because the inertial measurements of the former are disturbed by only random noise. In contrast, the inertial measurements of the pocket INS are disturbed by both random noise and constant bias. It is interesting to highlight that the heading drift of the pocket INS grows linearly with time because of the constant bias.

The remainder case studies 8-9 are the most realistic ones because they consider signals with bias for both inertial localization systems. As expected, the heading of the loose coupling resembles the most accurate heading estimation. An example is given in Figure 6.15 for case study 8. In this example, the heading drift of the foot INS grows exponentially over time due to the bias stability.

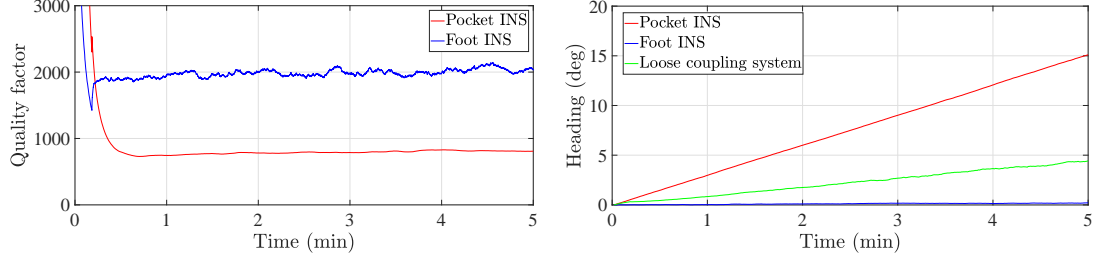


Figure 6.14: Case study 4: (Left) Quality factor estimation. (Right) Heading estimation of the pocket INS, the foot INS and the loose coupling system according to equation (6.10).

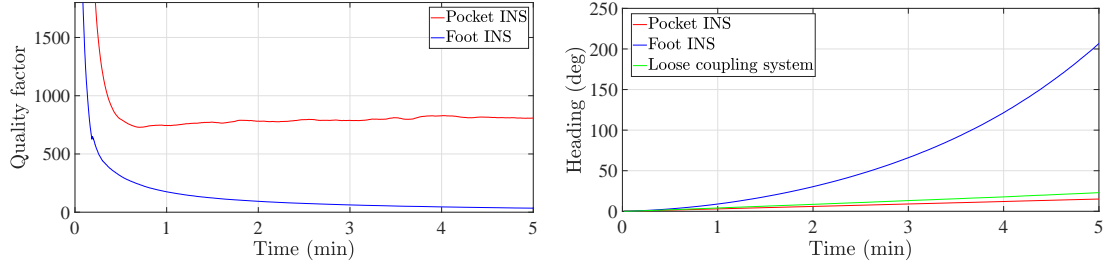


Figure 6.15: Case study 8: (Left) Quality factor estimation. (Right) Heading estimation of the pocket INS, the foot INS and the loose coupling system according to equation (6.10).

To finalize this section, let us remember the initial goals of the simulative proof to assess whether they have been met. The first goal was to assess that if the heading has the same errors, then the quality factor is the same. This goal has been proven by case studies 2-3. The second goal regards the fact that the quality factor should be lower the higher the heading error. This goal has been proven by case studies 4-9.

6.4 Summary and Conclusions

The loose coupling system combines the outputs of the pocket INS and the foot INS. The proposed loose coupling system weights the step length of the pocket INS and the foot INS with constant weights. In contrast, the proposed loose coupling system weights the heading estimation of the pocket INS and the heading of the foot INS with variable weights. They are estimated through quality factors which quantify how accurate one heading estimation is with respect to the other one. Finally, the height is estimated in two steps. First, the height of the foot INS is sampled upon the stairs detected by the pocket INS. Second, the vertical displacement of each stair is estimated and successively added to the height estimated by the loose coupling system.

The first conclusion of this chapter is regarding the combination of the step length estimations of the pocket INS and the foot INS. These two estimations have to be

weighted by constant weights because their accuracy is approximately the same. This fact holds under the assumption that the parameters of the step length model of the pocket INS are calibrated.

Table 6.3: Summary of the quality factors of each case study, where q_p and q_f are the quality factors of the heading of the pocket INS and foot INS respectively.

Case study	Pocket INS	q_p	Foot INS	q_f
1	Only random noise	15000	Only random noise	2100
2	Constant bias	800	Constant bias	800
3	Variable bias	41	Variable bias	35
4	Constant bias	807	Only random noise	2000
5	Only random noise	1600	Constant bias	768
6	Variable bias	41	Only random noise	2000
7	Only random noise	1600	Variable bias	35
8	Constant bias	800	Variable bias	35
9	Variable bias	41	Constant bias	766

The second conclusion of this chapter is regarding the combination of the heading estimations of the pocket INS and the foot INS. These estimations have to be weighted with variable weights because the heading accuracy varies not only over time but among walks. In this regard, we are able to determine the relative accuracy of the heading estimation of the pocket INS and the foot INS with the quality factor. It performs as expected whenever the signals are disturbed by both random noise, constant bias or variable bias. Table 6.3 is a summary of the case studies and the associated quality factors for each inertial localization system.

Finally, the last conclusion is related to the fusion of the height estimations of the pocket INS and the foot INS. Namely, we have succeeded in combining the complementary features of the pocket INS and the foot INS. In this case, we refer to the features regarding 3D, namely the robust stairs detection of the pocket INS and the model-free height estimation of the foot INS.

Chapter 7

Biomechanical Study of the Human Leg

*I would like to be remembered as someone who did
the best she could with the talent she had*
– J.K. Rowling

This chapter presents a new dimension of our work: the biomechanical study. Our goal is to incorporate this new dimension into an inertial localization system. We want to understand what the limitations of the human physiology of a leg are. To that end, we propose a leg model that converts Euler angles into positions of the leg limbs. Then, we validate the leg model with a set of experiments.

Thanks to the leg model, we characterize the motion of the leg in terms of the roll and pitch of each leg limb. This information can be compared to the motion of the leg derived from the roll and pitch of an inertial localization system placed on a limb. More importantly, we analyze how the errors in the roll and pitch of an inertial localization system translate into the motion of the leg.

With the aforementioned analysis, we cannot analyze the errors in the heading of an inertial localization system. Therefore, we analyze the heading of one leg limb with respect to the heading of a different leg limb. For instance, the heading of the thigh is compared to the heading of the foot. This approach allows us to observe the effect of the heading errors in the motion of the leg.

7.1 Proposed Leg Model

The analysis of the human leg will be done by modelling it as a robotic structure. The leg model will represent the leg as a set of limbs and joints. The limbs are the body members or extremities [87] whereas the joints are the connections between the limbs [88]. Figure 7.1 shows the leg model, where the chosen limbs are the thigh, the shank and the foot. The joints defined are the hip, the knee and the metatarsal.

The leg model in Figure 7.1 is used to analyze the motion of the leg regarding the rotations of the limbs, e.g. the roll and pitch of the thigh. Such an analysis can be carried out considering a user of arbitrary height [47]. For practical reasons, we fix the user's height to 180 cm. According to Glowinski *et al.* [89], the lengths of the limbs are proportional to the human height, such that:

- the thigh is 0.245 times the human height,
- the shank is 0.246 times the human height and
- the foot is 0.0577 times the human height. The length of the foot is measured from the ankle to the start of the metatarsal bone.

Thus, the limb lengths of are 44.1 cm, 44.30 cm and 10.40 cm for the thigh, the shank and the foot respectively for a user who is 180 cm tall.

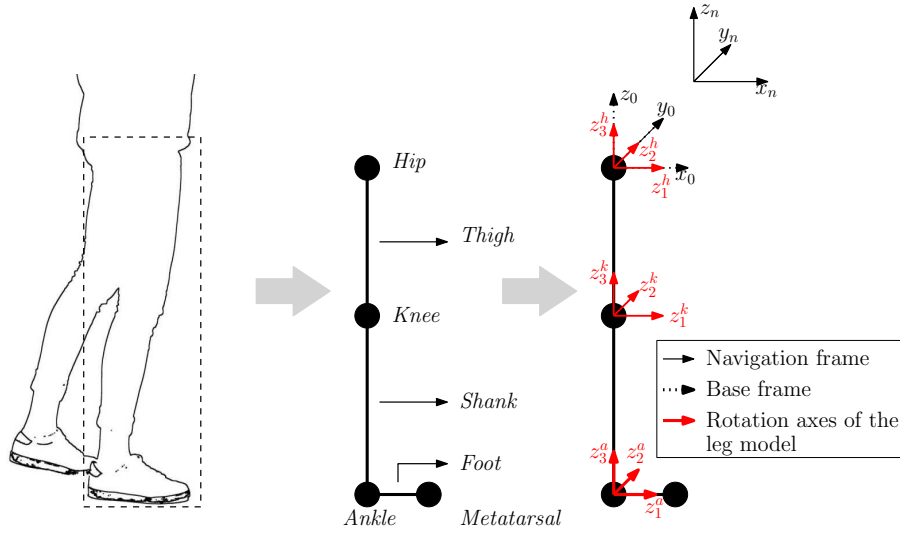


Figure 7.1: Simplification of the human leg (left) as a robotic structure (middle). The degrees-of-freedom allowed for the leg are also given (right).

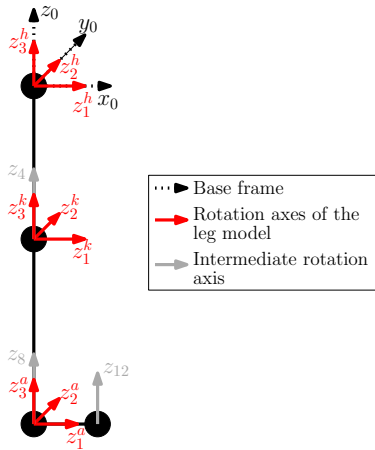
The leg model in Figure 7.1 allows the limbs to rotate around one or more rotational axes of the joints. Each rotational axis is a Degree-of-Freedom (DoF). In Figure 7.1, the leg structure has nine degrees of freedom: three around the hip (z_1^h, z_2^h, z_3^h), three around the knee (z_1^k, z_2^k, z_3^k) and three around the ankle (z_1^a, z_2^a, z_3^a). The DoF of each joint are defined to coincide with the axes of the inertial frames of the IMUs placed on each leg limb. In this way, the rotation around z_1^h represents the roll (ϕ_p), the rotation around z_2^h represent the pitch (θ_p) and the rotation around z_3^h represent the heading (ψ_p) of an IMU placed on the thigh. The same reasoning applies for an IMU placed on the shank and the foot. The IMU placed on the thigh is equivalent to the pocket IMU used so far in this thesis.

The leg model is used to analyze the structure of the leg, i.e. the position of each joint given a specific set up of the leg. To that end, we use the Denavit-Hartenberg parameters to represent the position of the leg joints in the base frame, see Section 3.3. Since the base frame is of free choice, we define it to coincide with

the navigation frame, as Figure 7.1 indicates. The difference between the base frame and the navigation frame is that the former is fixed at the centre of the user's hip. It is important to highlight that the base frame, as the navigation frame, is fixed and therefore it does not move with the leg structure. The reader is referred to Section 3.3 for more details on the definition of the Denavit-Hartenberg parameters.

The Denavit-Hartenberg parameters of the structure in Figure 7.1 are given in Table 7.1. The parameters in this table have been generated by following the steps described in Appendix E and by taking into account the degrees-of-freedom of the leg structure. It is worth highlighting that the angles θ_i are relative rotations between two consecutive frames. For instance, θ_1 is the rotation around z_1^h to align x_1^h with x_2^h . Similarly to [89], we propose a redundant leg model, i.e. a model with more degrees of freedom than the structure needs. The advantage of a redundant leg model is to simplify the kinematic process or the implementation of constraints.

Table 7.1: (Left) Leg model with all axes to allow the 9 degrees-of-freedom for the leg. (Right) Denavit-Hartenberg parameters of the leg model. The parameters ℓ_t , ℓ_s and ℓ_f refer to the length of the thigh, the shank and the foot respectively.



Axis	d	θ	a	α
z_1^h	0	-90°	0	-90°
z_2^h	0	$90^\circ + \theta_1$	0	-90°
z_3^h	0	$90^\circ + \theta_2$	0	-90°
z_4	$-\ell_t$	$180^\circ + \theta_3$	0	0
z_1^k	0	-90°	0	-90°
z_2^k	0	$90^\circ + \theta_5$	0	-90°
z_3^k	0	$90^\circ + \theta_6$	0	-90°
z_8	$-\ell_s$	$180^\circ + \theta_7$	0	0
z_1^a	0	-90°	0	-90°
z_2^a	0	$90^\circ + \theta_9$	0	-90°
z_3^a	0	$90^\circ + \theta_{10}$	0	-90°
z_{12}	ℓ_s	$180^\circ + \theta_{11}$	ℓ_f	0

Given the Denavit-Hartenberg parameters in Table 7.1, the homogenous matrix and the kinematic chain can be used to estimate the joint positions in the base frame. These positions are given by the first three elements of the last column of the homogenous matrices \mathbf{H}_4^0 , \mathbf{H}_8^0 and \mathbf{H}_{12}^0 for the knee, ankle and metatarsal joints respectively.

In the following, some examples of the application of the leg model in Table 7.1 are given. Let us begin with the joint positions of a straight leg. With the chosen user's height of 180 cm tall, the position of the user's knee joint, ankle joint and metatarsal joint are given in Table 7.2. The user's joints positions will vary provided that the user bends his leg, as indicated in Table 7.3.

Table 7.2: (Left) Representation of a straight leg. (Right) Table with the set of joint positions of a straight leg. The angles applied at each axis are also given. *Meta.* stands for metatarsal.

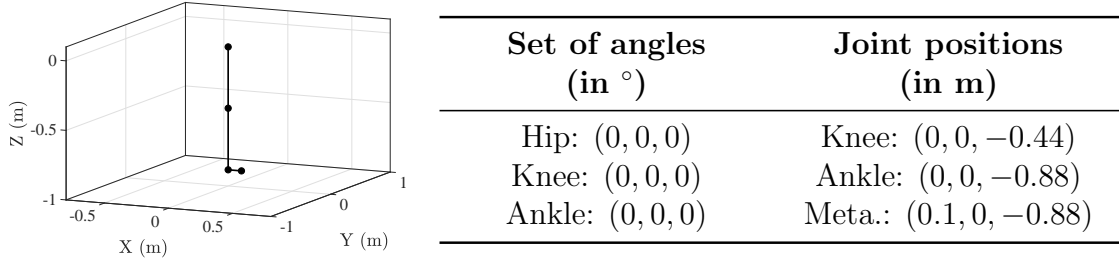
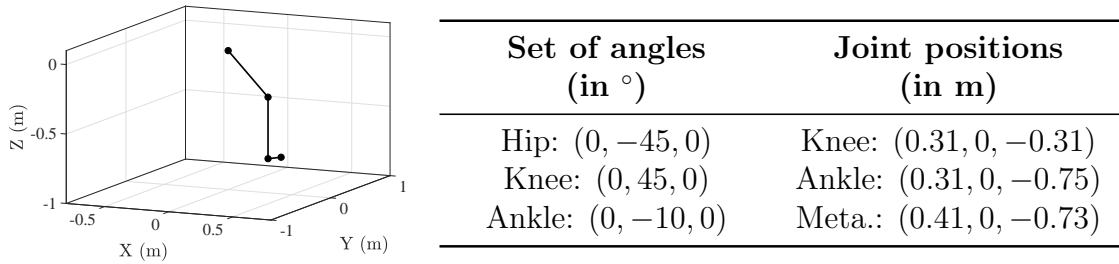


Table 7.3: (Left) Representation of a bent leg. (Right) Table with the set of joint positions of a bent leg. The angles applied at each axis are also given. *Meta.* stands for metatarsal.



7.2 Motion Tracking Experiment

We designed and carried out experiments in order to collect inertial measurements from the leg limbs together with its associated ground truth. The goal of the experiments is to firstly validate the leg model in Table 7.1. Secondly, the tests aim at providing accurate attitude data with which to analyze the biomechanics of the human leg and compare it with the attitude of the inertial localization systems.

The ground truth is generated by a camera-based motion capture system¹. The motion capture system tracks the position and attitude of an object to a precision of 0.5 mm in a 4 m×4 m area². To that end, a set of reflector markers have to be placed in a unique fashion on the object whose position and attitude have to be tracked. The ground truth is retrieved at 100 Hz.

In order to carry out the experiments, both the reflectors of the motion capture system and the IMUs had to be placed on the thigh, the shank and the foot. To that end, a set of PoliVinyl Chloride (PVC) boards were prepared to be mounted on the user's limbs. The set of reflectors and the IMUs were mounted on these PVC boards as Figure 7.2 depicts. It is important to highlight that the set up of the reflectors is unique for each board in order to identify each limb unequivocally. The advantage of these boards is that they guarantee that the sensor mounting is constant among the users that participated in the experiment.

¹<https://www.vicon.com/>

²<https://www.vicon.com/file/vicon/bonita-brochure.pdf>

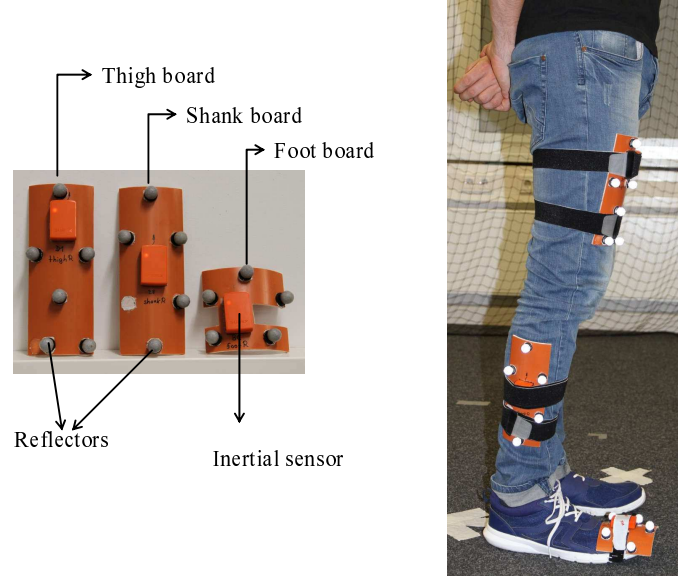


Figure 7.2: (Left) PVC boards with the unique reflector set up and the IMUs. (Right) Setup of the PVC boards on the leg limbs during the motion tracking experiments.

The experiments took place in a $8 \times 3 \text{ m}^2$ area, where the cameras of the motion capture system were set up on the ceiling. The users were requested to walk three different types of trajectories, namely a square, an eight-shape trajectory and a random trajectory. Moreover, each trajectory was repeated twice. A total of nine users participated in the experiment, see Table 7.4

Table 7.4: Summary table of the experiments to evaluate the biomechanical motion of the leg.

Number of users	9
Number of trajectories	3
Repetitions per trajectory	2
Total amount of data	3 h 37 min
Output data (motion tracking system)	3D position and attitude
Output data (IMU)	3D acceleration and 3D turn rate

The first step of the motion tracking experiment is to validate the leg model in Table 7.1. To that end, the leg model will be considered as a black box. Its input is the set of rotations around each rotation axis, which are measured by the motion capture system. Regarding notation, we will use the subindex p to refer to the thigh due to the IMU placed on the pocket. The parameters relative to the shank and foot will be denoted with the subindices s and f , respectively.

The motion capture system retrieves the quaternions from each of the limbs to the navigation frame. These quaternions can be translated into the respective direction

cosine matrices from the thigh (\mathbf{C}_{pn}), the shank (\mathbf{C}_{sn}) and the foot (\mathbf{C}_{fn}) to the navigation frame [57]. The leg model, in contrast, requires the inverse angles, i.e. from the base frame to each limb. Therefore, we preprocess the ground truth prior to input it to the leg model.

The preprocessing consists of estimating the inverse of the aforementioned matrices, namely \mathbf{C}_{pn} , \mathbf{C}_{sn} and \mathbf{C}_{fn} , and estimating their associated Euler angles. They are the ones input to the leg model, such that:

$$\begin{aligned} \theta_1 &= \phi'_p, & \theta_5 &= \phi'_s, & \theta_9 &= \phi'_f, \\ \theta_2 &= \theta'_p, & \theta_6 &= \theta'_s, & \theta_{10} &= \theta'_f, \end{aligned} \quad (7.1)$$

where subindices p , s and f refer to the thigh, shank and foot respectively. The superindex $(\cdot)'$ denotes the inverse of the Euler angle, which is estimated as described above.

In the set of equations (7.1), the heading has been set to zero for convenience, i.e. $\theta_3 = 0$, $\theta_7 = 0$ and $\theta_{11} = 0$. The reason is that the heading of the motion capture system is disturbed by uncertainties when the cameras loose sight of the reflectors. Therefore, the validation of the leg model is done by assessing the accuracy of the angles in the set of equations (7.1).

The output of the leg model is the position of each joint. In addition, the relative attitude of the joint and the base frame is provided by the 3×3 sub-matrix of the homogenous matrix of the associated joints, see Section 3.3. The attitude vectors of these matrices, namely Ψ_4^0 , Ψ_8^0 , Ψ_{12}^0 , are equivalent to the attitude of the thigh (Ψ_p), the shank (Ψ_s) and the foot (Ψ_f) respectively that are measured by the motion capture system.

The validation consists of the comparison of the output of the leg model with the ground truth. This process is summarized in Figure 7.3. The comparison leads to the estimation of the attitude errors, \mathbf{e}_p , \mathbf{e}_s and \mathbf{e}_f , where:

$$\mathbf{e}_p = (e_{\theta 1}, e_{\theta 2}, 0), \quad (7.2)$$

$$\mathbf{e}_s = (e_{\theta 5}, e_{\theta 6}, 0), \quad (7.3)$$

$$\mathbf{e}_f = (e_{\theta 9}, e_{\theta 10}, 0), \quad (7.4)$$

where $e_{\theta j}$ is the error of the θ_j angle in Table 7.1. The third element of each attitude error is zero because the leg model has been evaluated without taking into account the rotation around the z-axis.

The errors are summarized in Table 7.5. We can observe that the average errors are, generally, below 2° . There are some exceptions, e.g. θ_6 of User 7. In this case, the reason for the errors is the uncertainties in the attitude of the motion capture system. These uncertainties appear when the cameras of the motion capture system lose line of sight with the reflectors on the user's legs. The effect of the uncertainties is the appearance of spikes in the value of the angles. In fact, these uncertainties are reflected in a higher average error, see Table 7.5.

All in all, we will consider the leg model in Table 7.1 valid to analyze the biomechanical motion of the leg. The reason is that the errors are one order of magnitude

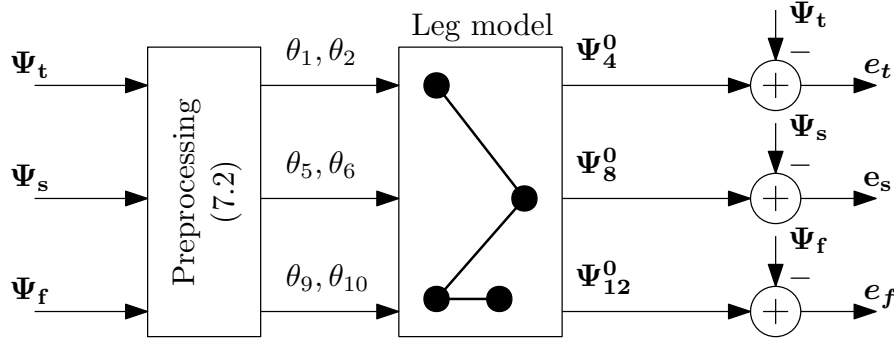


Figure 7.3: Process to validate the leg model.

Table 7.5: Results of the validation of the leg model. The error values are the average error of the associated angle over all the experiments carried out by the respective user.

User	$e_{\theta 1}$ [°]	$e_{\theta 2}$ [°]	$e_{\theta 5}$ [°]	$e_{\theta 6}$ [°]	$e_{\theta 9}$ [°]	$e_{\theta 10}$ [°]
User 1	0.1	0.1	0.3	0.1	0.3	0.1
User 2	0.7	0.5	0.3	0.1	0.2	0.1
User 3	0.7	-0.3	-0.5	-0.9	0	-0.1
User 4	0.8	-0.1	0.3	-0.1	0.2	-0.1
User 5	0.4	0.1	0.2	0.1	0.2	-0.1
User 6	0.1	-0.1	0.7	-0.4	0.7	0.3
User 7	0.2	-0.2	1.3	-3.6	0.5	-0.1
User 8	0.4	-0.1	-0.6	-1.4	0.3	0.1
User 9	1.3	-0.4	-0.7	0.2	1.1	-0.2

smaller than the usual values of the angles. In the case of the roll, namely θ_1 , θ_5 and θ_9 , the usual values are between -10° and 10° . In the case of the pitch, namely θ_2 , θ_6 and θ_{10} , the usual values are between -20° and 40° . The next step is to analyze human motion with the proposed leg model. This analysis is divided into two parts: an analysis of the tilt angles and an analysis of the relative heading. Each part is investigated in detail in the following sections.

7.3 Tilt Angles

In this section, we follow the block diagram of Figure 7.4 to analyze the tilt angles. The heading of the joints, namely θ_3 , θ_7 and θ_{11} , are set to zero.

Let us explain why the heading is excluded from the analysis of the following sections. Figure 7.5 shows the top view of the leg as well as the plausible metatarsal positions that result from rotating the leg up to 360° . Now, let us consider that the leg is subjected to a rotation ψ around the z_3^h axis. An inertial localization system may estimate an rotation $\tilde{\psi}$ with errors. Suppose now that we estimate the

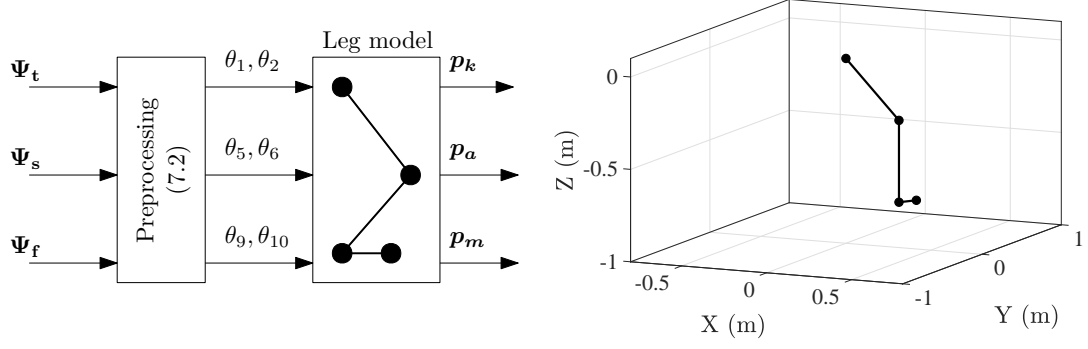


Figure 7.4: (Left) Block diagram of the analysis of human motion using the leg model: the input are the attitude vectors which are provided by the motion capture system. (Right) The output of the analysis is a set of joint positions, which can be represented in a 3D coordinate frame.

metatarsal position with both the true rotation (ψ) and the rotation ($\tilde{\psi}$). The resulting metatarsal positions, which are shown in Figure 7.5, are located on plausible metatarsal positions. That is, regardless the fact that the angle $\tilde{\psi}$ has errors, the estimated joint position that results from it is plausible. Therefore, it is not possible to observe the heading errors with the leg model.

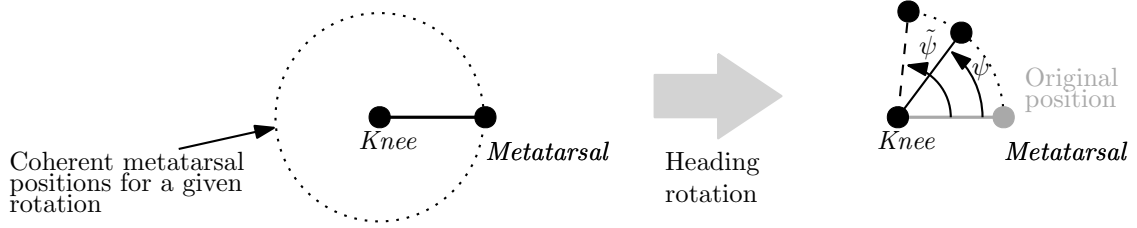


Figure 7.5: (Left) Top view of the plausible metatarsal positions for a rotation from 0° to 360° . (Right) Effect of a heading rotation with errors on the estimated joint positions.

7.3.1 Analysis with Ground Truth

Figure 7.6 shows the knee positions estimated with the data of User 1 during one of the tests. First of all, we indicate the initial standing position of the leg: the circle are the joints and the segments between them are the limbs. Each point of the red cloud is the knee position estimated with a pair of angles (θ_1, θ_2) of User 1 during that test. Let us highlight that the angles (θ_1, θ_2) are equivalent to inverse of the roll and pitch of the pocket IMU (ϕ'_p, θ'_p) . From the figure, we can see that the knee positions are constrained during the walk. The outliers of the ground truth translate into outliers of the knee position, namely the points around $(-0.3, 0.1, -0.3)$ m. The positions of the ankle and the metatarsal are also constrained, as Figure 7.7 indicates.

It is possible to state, after analyzing the data of the different users, that the motion

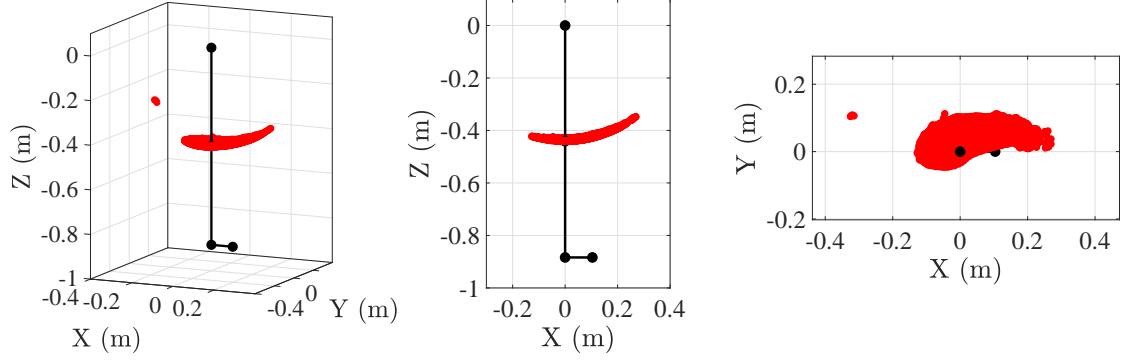


Figure 7.6: Knee positions of User 1 estimated with the leg model; from left to right: 3D view, side view and top view. The standing position of the leg is given for comparison.

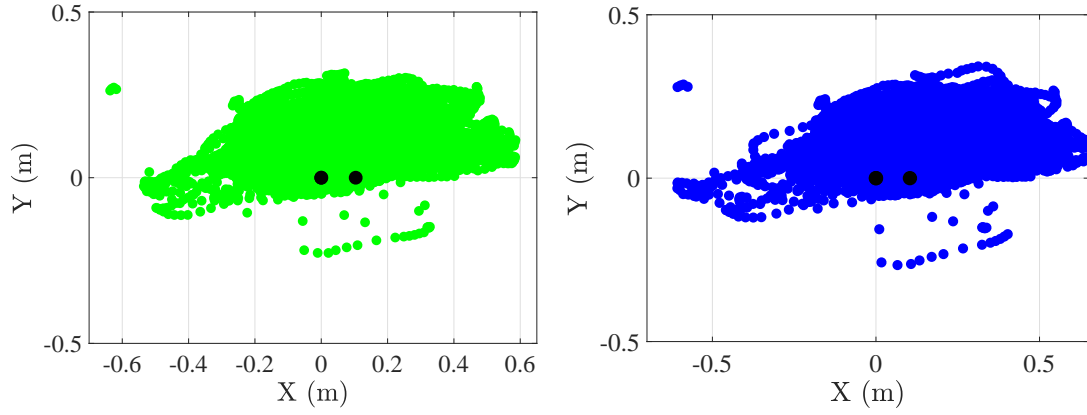


Figure 7.7: Top view of the ankle and metatarsal positions of User 1 estimated with the leg model.

of the leg joints during walking is constrained. Anatomy books [90] have already analyzed the constraints in human motion. In fact, anatomical studies report the angle ranges in for the hip, the knee and the ankle [47].

Figure 7.8 shows all the knee positions estimated with the ground truth. We also show the heat map associated to these positions. We can see that, in the heat map, the knee positions are concentrated along a specific area, which we refer to as comfort zone. This is the set of coherent positions of one of the leg joints. Similarly, the comfort zones of the ankle and the metatarsal can be represented, see Figure 7.9 and Figure 7.10.

For the sake of discussion, we will use these heat maps to extract heuristic limits of the comfort zone of each leg joint. The comfort zone of a joint defines the set of plausible positions, which we refer to as coherent positions. The heuristic limits of the comfort zone of each leg joint are given in Table 7.6. By comparing the heat map of Figure 7.8 to the heat maps of Figure 7.9 and Figure 7.10, we can see that the comfort zone of the knee is smaller than the comfort zone of either the ankle or the metatarsal. The reason is that the lower we move down the leg, the larger is the motion that the joint experiences. In fact, the ankle and the metatarsal are at the

same height and their associated comfort zones are approximately similar in size.

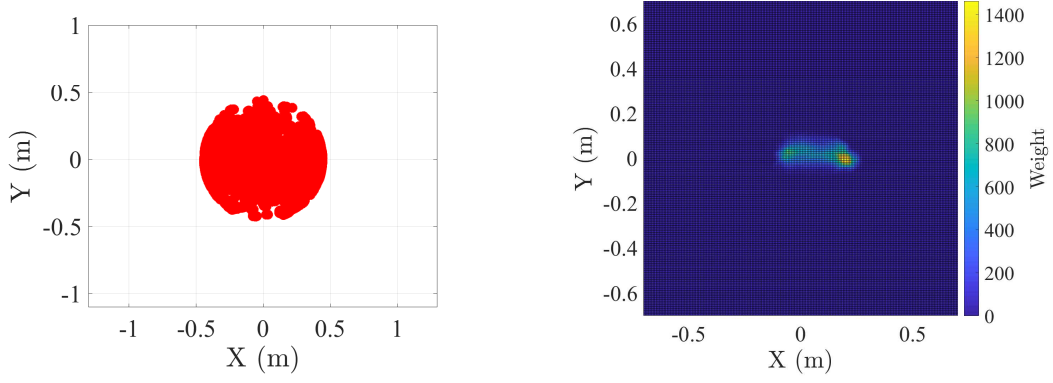


Figure 7.8: (Left) Top view of the knee positions. (Right) Heat map of the most frequent knee positions.

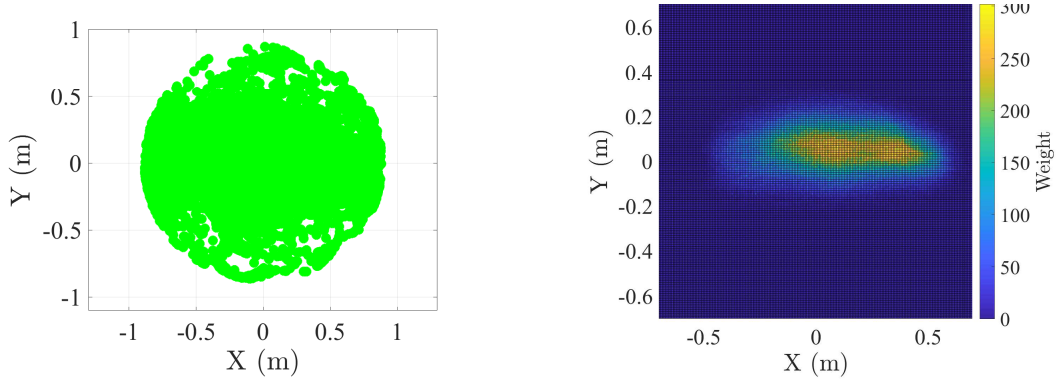


Figure 7.9: (Left) Top view of the ankle positions. (Right) Heat map of the most frequent ankle positions.

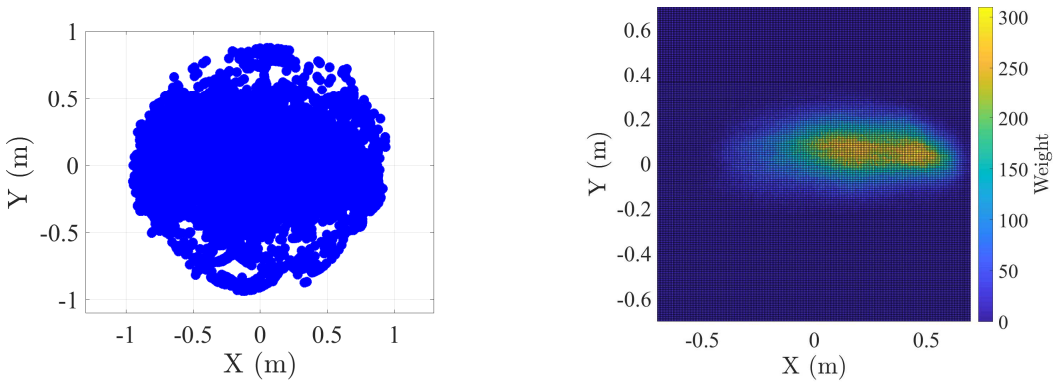


Figure 7.10: ((Left) Top view of the metatarsal positions. (Right) Heat map of the most frequent metatarsal positions.

It is important to highlight that the comfort zone of a joint is the result of using the leg model with a specific set of Euler angles. Therefore, the constraints in the joint

positions inherently imply constraints in the associated joint angles. For instance, the knee position is estimated with the hip rotations, namely θ_1 and θ_2 . Thus, the constraints on the knee positions imply also constraints on the roll and pitch of the hip, which are in turn equivalent to the roll and pitch of the pocket INS.

Table 7.6: Heuristic limits of the comfort zone of each joint given in terms of the joint position.

Joint	X limit [m]	Y limit [m]
Knee	(−0.15, 0.30)	(−0.07, 0.15)
Ankle	(−0.50, 0.63)	(−0.20, 0.33)
Metatarsal	(−0.45, 0.72)	(−0.20, 0.34)

7.3.2 Analysis with Inertial Data

As long as the angles input to the leg model are coherent, the estimated joint positions will also be coherent, i.e. within the heuristic comfort zone. This statement leads us to the question of what happens if the angles input to the leg model have errors. An example is the Euler angles estimated by an inertial localization system. We would then expect these errors to appear in a form of incoherent joint positions.

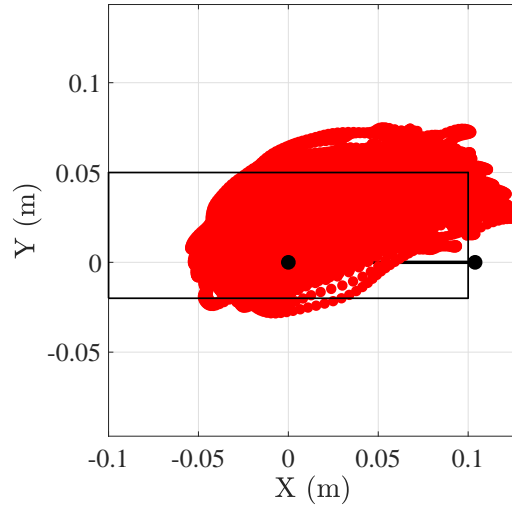


Figure 7.11: Top view of the knee positions estimated with inertial attitude. The limits of the comfort zone, which are given by the black solid line, are defined in Table 7.6.

The goal of this section is to assess the effect of the errors in the Euler angles in the estimation of the joint positions. To that end, the inertial measurements collected during the motion tracking experiment are processed with the attitude tracking algorithm described in Section 3.1. Then, we follow the schematic in Figure 7.4, where

the input to the leg model is the tilt angles estimated by the inertial localization system.

Figure 7.11 shows the knee positions estimated with the inertial Euler angles of User 1. We can see that the inertial attitude, which contains errors, leads to the estimation of incoherent knee positions. The same behaviour can be observed in Figure 7.12 for the ankle positions and the metatarsal positions.

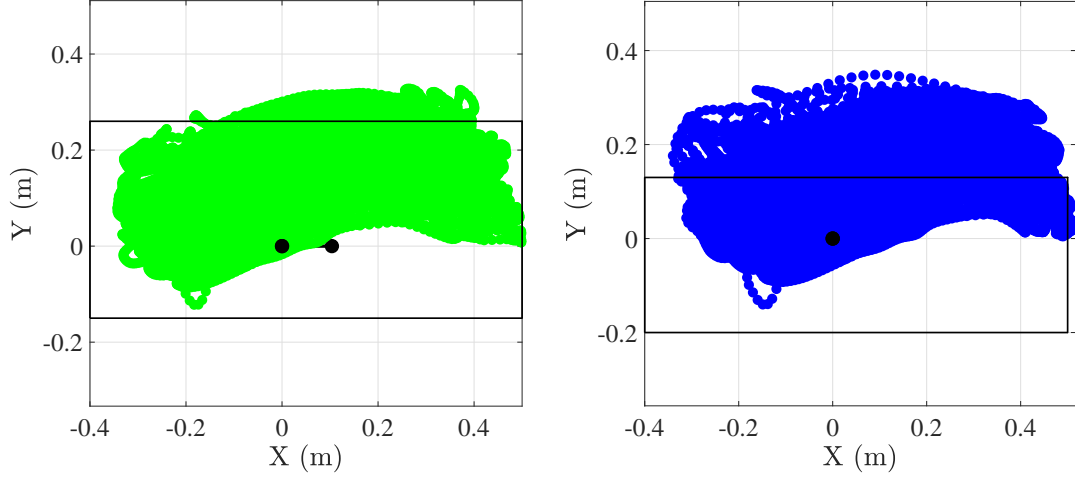


Figure 7.12: Top view of the ankle and metatarsal positions estimated with the inertial attitude. The limits of the comfort zone, which are given by the black solid line, are defined in Table 7.6.

There is an important implication associated to Figure 7.11 and Figure 7.12. It is possible to observe the errors of an inertial localization system by analysing the motion associated to its estimated tilt angles and comparing it to the expected motion of the leg limb. However, it is not possible to observe such errors if only the position estimation of the same inertial localization system is analyzed. The reason is that we would need to have a ground truth trajectory to assess the errors in the position estimation.

7.3.3 Probabilistic Model

This section describes how we derive a probabilistic model of the comfort zone to integrate it in an inertial localization system. The first step is to represent the comfort zone in terms of the tilt angles, i.e. the roll and pitch, see Figure 7.13.

We could consider the comfort zones to be associated with a certain Probability Density Function (PDF) on each of the tilt angles. Thus, our next step is to analyze the experimental PDF that would generate these comfort zones. These experimental PDFs are shown in Figure 7.14 and Figure 7.15 for the tilt angles of both the pocket IMU and the foot IMU, respectively. Similarly to Figure 7.13, these distributions have been estimated with the ground truth.

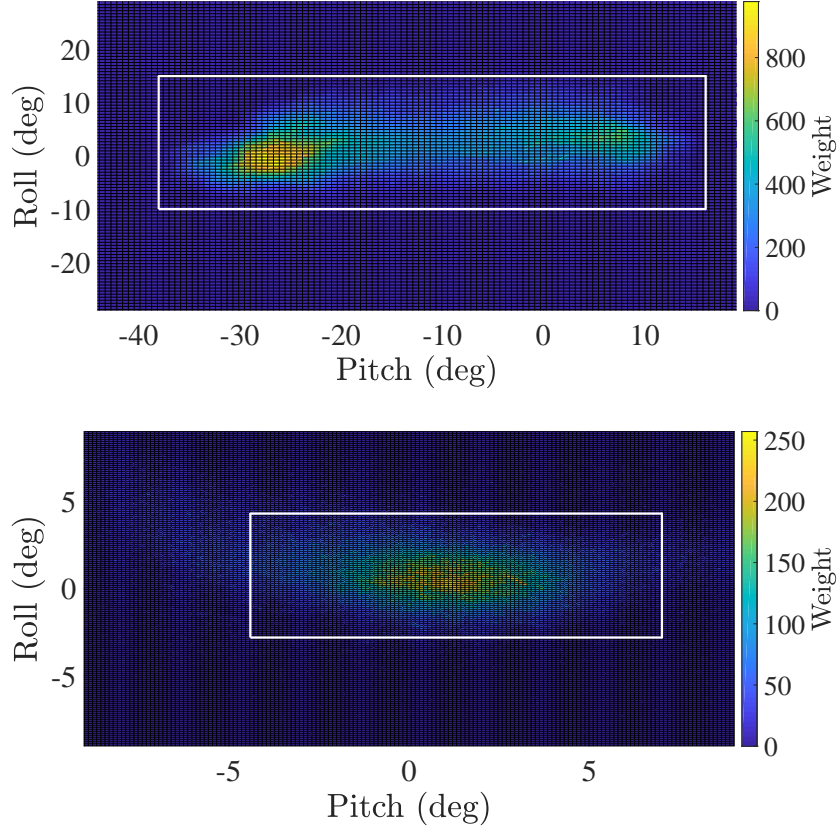


Figure 7.13: Heat map of the tilt angles of the pocket IMU (top) and the foot IMU (bottom). The rectangle represents the heuristic limits of the comfort zone.

There are different behaviours to be observed in the experimental PDFs. First of all, the roll distribution is approximately Gaussian for both the pocket IMU and the foot IMU. Still, the distribution of the roll of the foot IMU is narrower than the distribution of the roll of the pocket IMU. The reason is that the roll of the foot IMU takes values close to zero during the stance phase, see Figure 7.16. This fact causes the distribution of the roll of the foot IMU to be narrower than the distribution of the roll of the pocket IMU, despite the fact that the range of values is approximately the same for both angles.

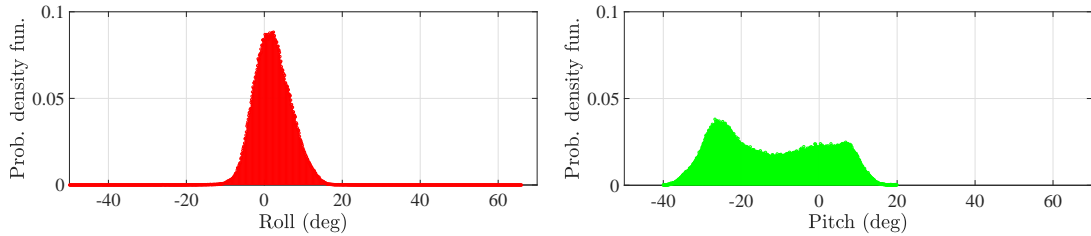


Figure 7.14: PDF of the roll (left) and the pitch (right) of the thigh. *Prob. density fun.* stands for probability density function.

Secondly, neither the PDF of the thigh pitch nor the PDF of the foot pitch are Gaussian. Either of these distributions could be modelled with a MultiVariate Normal Distribution (MVN) [91]. The non-Gaussian shape of the pitch PDF is expected

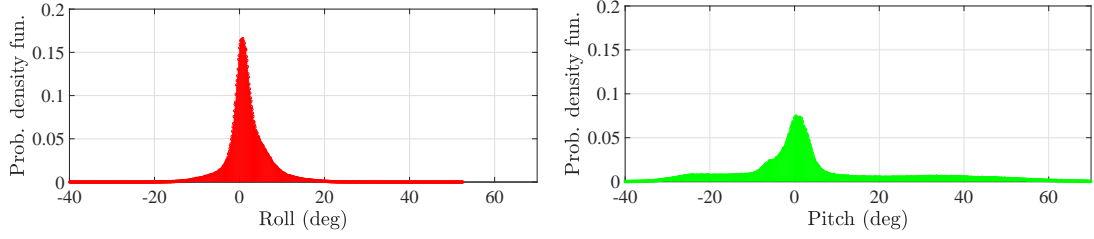


Figure 7.15: PDF of the roll (left) and the pitch (right) of the foot. *Prob. density fun.* stands for probability density function.

since the range of motion of the pitch while walking expands over a wide range of angles. An example is given in Figure 7.16, where the pitch of the pocket IMU expands from -15° to 20° approximately. In contrast, the pitch of the foot IMU expands from -30° to 50° approximately.

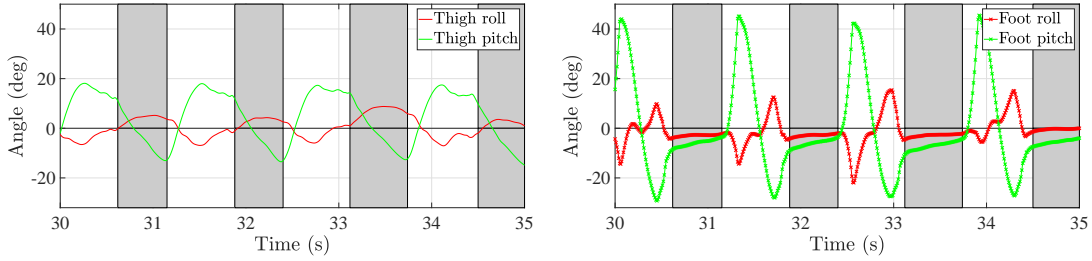


Figure 7.16: Tilt angles of the pocket IMU (left) and the foot IMU (right) over time. The shadowed areas are the stance phase periods.

The disadvantage of the pitch distribution is that it is non-Gaussian. Therefore, it cannot be integrated in a Kalman filter that estimates the attitude, see Section 3.1. Our next step is to analyze the tilt angle distribution during the stance phase. The idea is to assess the range of motion of the angles during this phase because we expect it to be smaller than in Figure 7.14 and Figure 7.15.

The result of analyzing the distribution of the tilt angles during only the stance phase is shown in Figure 7.17 and Figure 7.18. The roll distributions of either the pocket IMU or the foot IMU remain Gaussian, whereas the pitch of the foot IMU changes its distribution from a MVN to an approximately Gaussian distribution. The pitch of the pocket IMU is the angle that remains non-Gaussian. Nonetheless, the new distribution of the pitch of the pocket IMU can be better approximated by a Gaussian than the distribution in Figure 7.14.

Provided that Kalman filters perform optimally with Gaussian distributions, we will focus now on the results of Figure 7.17 and Figure 7.18. We need to characterize the Gaussian distributions, i.e. the mean and the standard deviation, that best fit the experimental PDFs in Figure 7.17 and Figure 7.18. To that end, we use the Maximum Likelihood Estimation (MLE) [91] to derive the mean and variance of each distribution.

According to the MLE, the mean (μ) and variance (σ^2) that best fit a set of n

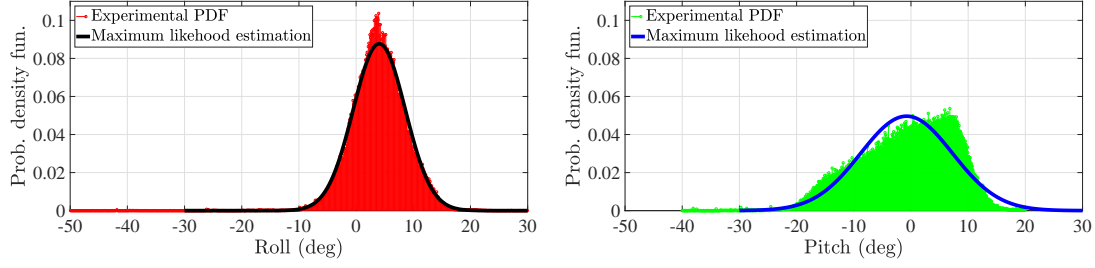


Figure 7.17: PDF of the roll (left) and the pitch (right) of the thigh during the stance phase. *Prob. density fun.* stands for probability density function.

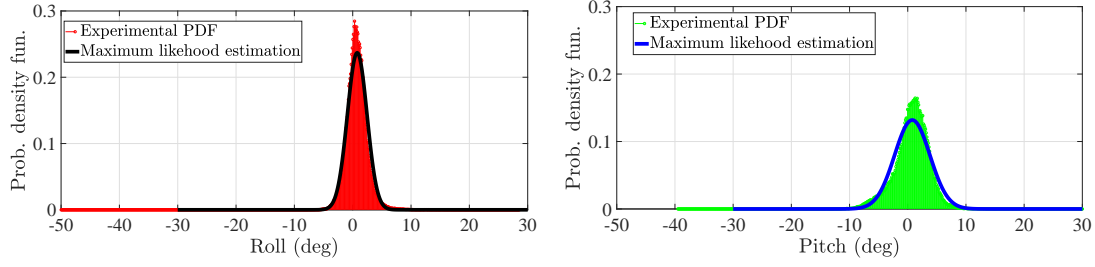


Figure 7.18: PDF of the roll (left) and the pitch (right) of the foot during the stance phase. *Prob. density fun.* stands for probability density function.

observations x_i with $i = \{1, 2, \dots, n\}$ is the following:

$$\mu = \frac{1}{n} \cdot \sum_{i=1}^n x_i, \quad (7.5)$$

$$\sigma^2 = \frac{1}{n} \cdot \sum_{i=1}^n (x_i - \mu)^2, \quad (7.6)$$

where the observations x_i are the roll or pitch of either the pocket IMU or the foot IMU.

Table 7.7 summarizes the parameters of the MLE Gaussian distributions of the tilt angles of the foot and thigh. We can see that the tilt angles of the foot are characterized by Gaussian distributions centered, approximately, around zero. Since the foot is in contact with the ground during the stance phase, its roll and pitch are limited to small values, i.e. around 0° . The MLE Gaussian distribution of the pitch of the thigh has a mean similar to the ones of the tilt angles of the foot. The difference is that the pitch distribution of the thigh is wider than for the tilt angles of the foot. Interestingly, the roll of the thigh is not centered around zero during the stance phase.

The Gaussian distributions derived with the parameters of Table 7.7 are shown in Figure 7.17 and Figure 7.18. There are two main highlights to point out. Firstly, the MLE Gaussian seems to capture the behaviour of the roll signals. However, the peak of the latter is not captured by the MLE Gaussian distributions. A similar behaviour can be observed in the pitch of the foot. Secondly, the MLE Gaussian of the pitch of the thigh fails to capture the sides of the experimental PDF. This result is expected since the pitch of the thigh does not behave as a Gaussian distribution.

Table 7.7: Parameters of the MLE Gaussian distributions of each tilt angle of the thigh and the foot.

Variable	Mean μ [°]	Standard deviation σ [°]
Thigh roll	4	4.5
Thigh pitch	-0.8	8
Foot roll	0.8	1.7
Foot pitch	0.8	3

7.4 Relative Heading

The previous section has shown us that it is not possible to observe incoherences in the individual heading estimates of each leg joint. Therefore, we propose to study the relationship between the heading estimates of the body limbs. More specifically, we focus on the relationship between the heading of the thigh and the heading of the foot.

The first step of the study is to derive the expression that relates the heading of the thigh (ψ_p) to the heading of the foot (ψ_f). It is possible to characterize this relationship by estimating the direction cosine matrix between these two limbs (\mathbf{C}_{fp}). The characterization of \mathbf{C}_{fp} follows the procedure described in Section 3.1. However, the complexity of the attitude tracking algorithm increases when the two frames involved are moving, as it is the case of the thigh and the foot while walking.

Interestingly, the DCM allows for a workaround by successively multiplying matrices. Let us denote by \mathbf{C}_{pn} and \mathbf{C}_{fn} the direction cosine matrices that represent the attitude of the thigh and the foot, respectively, with respect to the navigation frame. It is possible to use the latter as a ground truth to estimate the relative orientation of the thigh and the foot, namely:

$$\mathbf{C}_{fp} = \mathbf{C}_{pn}^T \cdot \mathbf{C}_{fn}. \quad (7.7)$$

The previous equation uses, simply explained, the navigation frame as a pivot to find the DCM between the thigh attitude and the pocket attitude. Given the matrix \mathbf{C}_{fp} , it is possible to extract the associated Euler angles (Ψ_{fp}). The latter will be referred to as the relative roll (ϕ_r), relative pitch (θ_r) and relative heading (ψ_r) between the thigh and the foot.

The use of equation (7.7) to estimate the relative heading is tedious. Therefore, prior to analyze the relative heading, we will assess if it is possible to simplify equation (7.7). To that end, we will compare the relative heading (ψ_r) estimated with equation (7.7) with the relative heading:

$$\tilde{\psi}_r = \psi_f - \psi_p, \quad (7.8)$$

where $\tilde{\psi}_r$ is the heading that results from subtracting the thigh heading (ψ_p) from the foot heading (ψ_f).

For the sake of discussion, let us refer to equation (7.7) as the matrix-based estimation of the relative heading. The heading estimated with equation (7.8) will be referred to as the approximate heading. Figure 7.19 compares the relative heading estimated with both methods, the matrix-based one and the approximate one. We can see that the differences between both estimations are minor. In fact, the average error in the indicated figure is 1.4° . Therefore, in the reminder of this section, we will follow equation (7.8) to estimate the relative heading of the thigh and the foot.

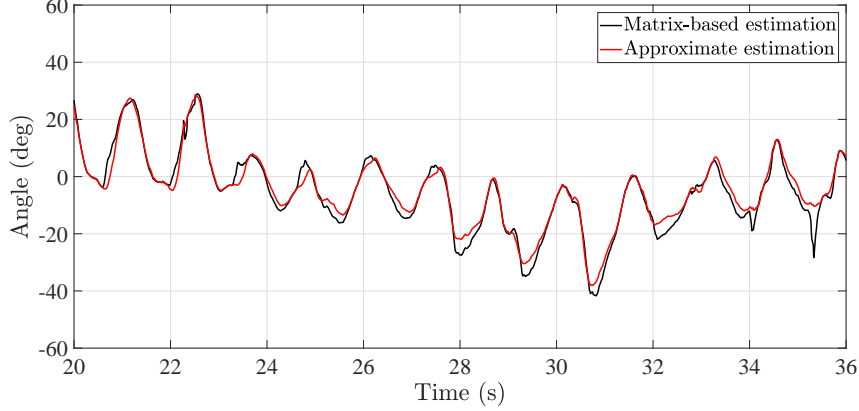


Figure 7.19: Comparison of the relative heading estimated through the matrix-based method, see equation (7.7), and the approximate method, see equation (7.8).

Figure 7.20 shows the relative heading between the foot and the thigh of one user. There are two main things to highlight in the figure. Firstly, the relative heading has an underlying offset. We believe that it is the result of the mounting of the sensor or the boards on the user's limbs. Secondly, the relative heading varies over time, which is the result of the movement of the thigh and the foot while walking. The amplitude of the variation is, as Figure 7.20, not constant since the variations in the relative heading depend on the vibrations of the thigh and foot while walking.

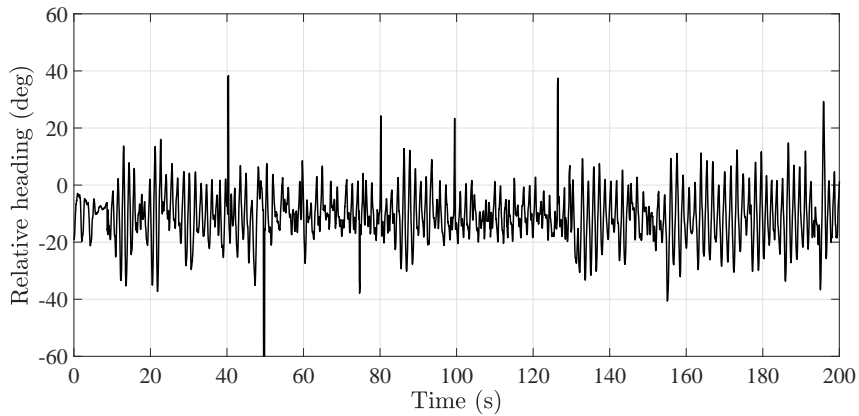


Figure 7.20: Relative heading between the thigh and the foot of a user.

Based on Figure 7.20, we model the relative heading of the thigh and the foot (ψ_r)

as Figure 7.21 depicts. In such a case, the relative heading (ψ_r) can be written as:

$$\psi_r = \psi_m + \psi_v, \quad (7.9)$$

where ψ_m is the offset of the relative heading resulting from the mounting of the sensors on the users's limbs. The term ψ_v is the varying component of the relative heading resulting from the vibrations of both the thigh and the foot while walking.

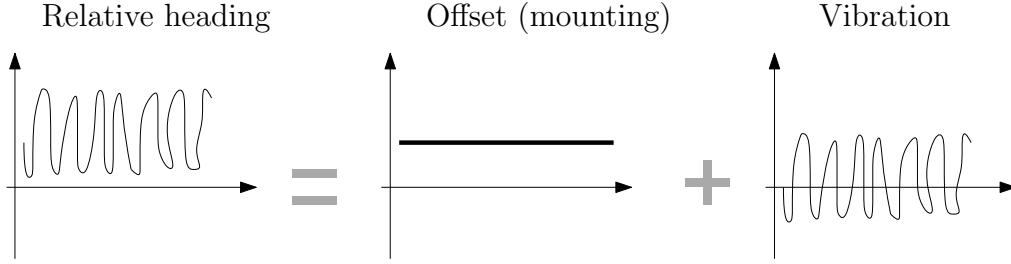


Figure 7.21: Generalization of the relative heading between the thigh and the foot.

Now, we compare the relative heading estimated with the inertial heading to the relative heading estimated with the ground truth. In Figure 7.22, we can see that the inertial relative heading has also variations due to the relative motion of the thigh and the foot. However, the key highlight of the inertial relative heading is that the low frequency component of the signal is not constant but linear over time.

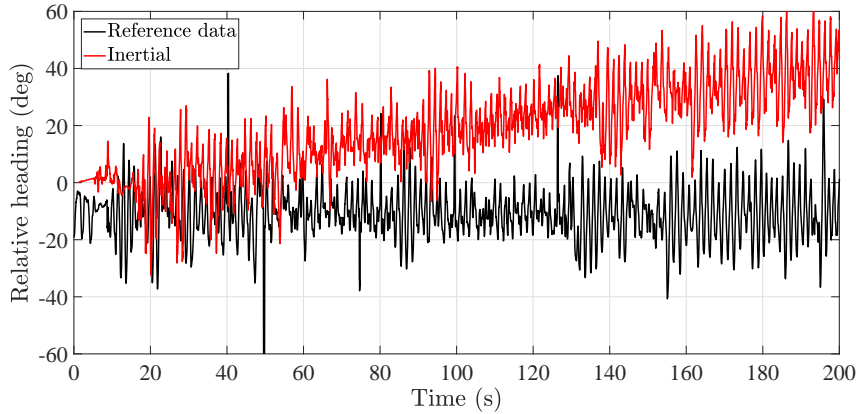


Figure 7.22: Relative heading of the thigh and foot estimated with the inertial attitude.

In order to understand the inertial relative heading (ψ_{ri}), let us write it as:

$$\psi_{ri} = \psi_m + \psi_v + \psi_e, \quad (7.10)$$

where ψ_m and ψ_v are the same contributions as in equation (7.9). The element ψ_e is the relative error in the heading estimations of the thigh and the foot. This error component grows over time as the error in the individual heading estimations

accumulates over time as well. Now, let us write the thigh heading (ψ_p) and the foot heading (ψ_f) as follows:

$$\psi_p = \psi_t + \psi_{pm} + \psi_{pv} + \psi_{pe}, \quad (7.11)$$

$$\psi_f = \psi_t + \psi_{fm} + \psi_{fv} + \psi_{fe}, \quad (7.12)$$

where ψ_t is the true heading of the user in the navigation frame. Let the subindex $j = \{p, f\}$ refer to the thigh and foot respectively. The angle ψ_{jm} is the initial offset due to the sensor mounting, the angle ψ_{jv} is the contribution due to the vibration of the limb and the angle ψ_{je} is the error in the heading estimation.

The relative heading will be affected by the difference between the heading error of the pocket (ψ_{pe}) and the heading error of the foot (ψ_{fe}). In the unlikely case that $\psi_{pe} = \psi_{fe}$, it would not be possible to observe the incoherences in the relative heading. Fortunately, the drift in the individual heading estimations is, in most cases, different and the drift in the relative heading can be clearly observed.

Similarly to Figure 7.21, the generalization of the inertial relative heading is represented in Figure 7.23. The latter shows that the inertial relative heading is decomposed in three components. The first two are equivalent to those in Figure 7.21. It is interesting to highlight that the component due to the mounting (ψ_m) is not noticeable. The reason is that the heading estimates of both the thigh and the foot start in zero.

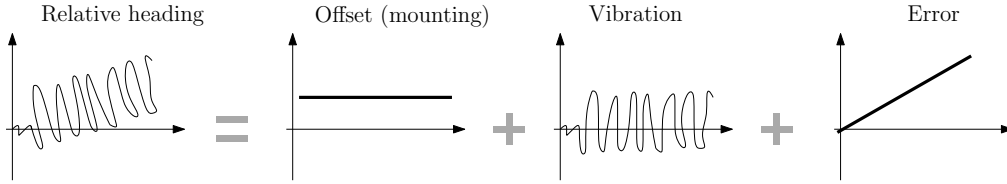


Figure 7.23: Model of the inertial relative heading as the sum of two components: a vibration due to the limb motion and a low-frequency growing error.

The relative error of the inertial relative heading has an important implication in the biomechanical behaviour of the human leg. Should this error be true, it would mean that a user's thigh and foot are constantly rotating with respect to each other. This behaviour is, in fact, not true as Figure 7.20 exemplifies. That is, the growing trend of the inertial heading is an incoherence from the biomechanical point of view. Unfortunately, it is not possible to quantify the contribution of the individual heading errors to the relative heading.

7.5 Summary and Conclusions

In this chapter, we have developed a model of the human leg. Our leg model is valid for the activity “walking” and represents the motion of the leg as a set of coherent movements. These movements are defined by a range of values of the roll and pitch

of each leg limb. The heading of the thigh limb has been analyzed with respect to the heading of the foot limb. These two heading estimations are equivalent to the heading of the pocket INS and the foot INS, respectively.

The first conclusion of this chapter is that we have been able to observe that the leg motion while walking is constrained. These constraints can be formulated in terms of coherent joint positions, which we collectively refer to as comfort zone. Thanks to the leg model, it is possible to observe that coherent joint positions are equivalent to coherent tilt angles.

During our study, we have found out that the PDF distributions of the roll of both the pocket IMU and the foot IMU are approximately Gaussian during the gait cycle. In contrast, the pitch of both the pocket IMU and the foot IMU are not Gaussian-distributed. Nevertheless, the pitch of the foot IMU can be approximated by a Gaussian distribution during the stance phase, whereas the pitch of the pocket IMU remains non-Gaussian even during the stance phase.

The second conclusion regards the estimation of the roll and pitch of an inertial localization system. We are able to observe errors in the roll and pitch angles estimated by the pocket INS and the foot INS. These incoherences are motivated by the error accumulation that disturbs the attitude estimation of any inertial localization system.

Finally, the conclusion regarding the heading estimation of an inertial localization system. The incoherences in this angle cannot be directly observed. Instead, we could observe errors in the relative heading between the thigh limb and the foot limb, i.e. between the heading of the pocket INS and the heading of the foot INS.

Chapter 8

Tight Coupling System

*If you are going to fail,
then fail gloriously
– Cate Blanchett*

The last approach investigated in this work is the tight coupling of the inertial measurements of the pocket IMU and the foot IMU. The tight coupling implements, in addition to the dead reckoning algorithm, the outcome of the biomechanical study carried out in Chapter 7.

In this chapter, the goal is to integrate the biomechanical constraints in the position estimation process. We want to avoid the use of hard constraints that do not model the reality of the human walk. It is important to highlight that since the pocket IMU is placed on the thigh, the study carried out in the previous chapter is applicable in this chapter without any modifications.

8.1 System Overview

The block diagram of the tight coupling system is shown in Figure 8.1. There are two main steps: the attitude tracking and the position tracking.

The *Attitude tracker* estimates the attitude of both the pocket IMU and the foot IMU, the biases of the respective IMUs and the user's heading. This block integrates the biomechanical constraints derived in the previous chapter.

The *3D position tracking* block estimates the 3D user's position with the user's heading estimated in the previous block. Regarding the horizontal and vertical displacement, this block exploits the features of the foot and the pocket. The detailed description of the *Attitude tracker* and the *3D position tracking* is presented below.

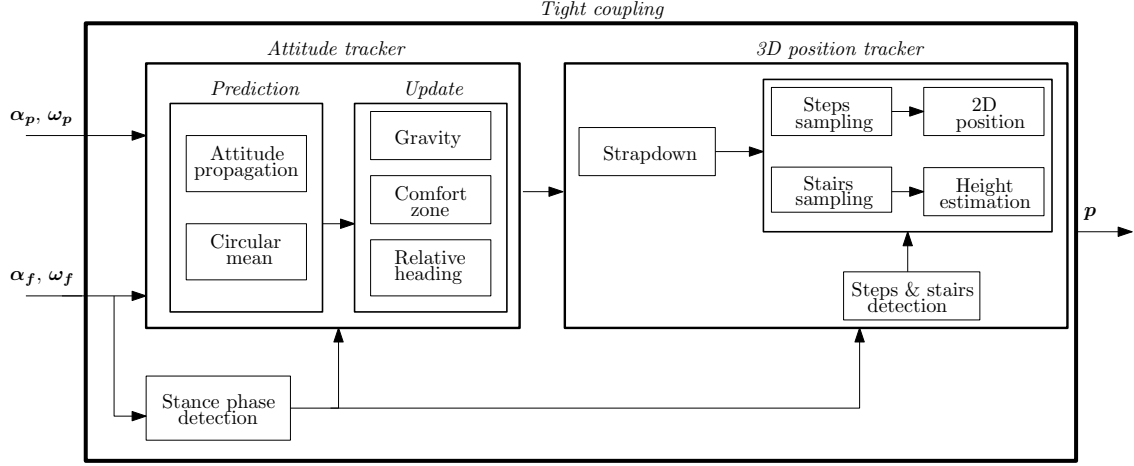


Figure 8.1: Block diagram of the tight coupling. The inputs are the acceleration vector (α) and turn rate vector (ω) of both the foot IMU (f) and the pocket IMU (p). The output is the 3D position (p) of the user.

8.2 Attitude Tracker

The attitude tracker is implemented by an unscented Kalman filter, or UKF, where the states vector (x) is:

$$x = [\Psi_p^T, b_{gp}^T, \Psi_f^T, b_{gf}^T, \psi_u]^T, \quad (8.1)$$

where Ψ_p and Ψ_f are column vectors with the Euler angles of the pocket IMU and foot IMU respectively. b_{gp} and b_{gf} are column vectors with the gyroscope bias of the pocket IMU and foot IMU respectively. The attitude (Ψ_p, Ψ_f) and the bias (b_{gp}, b_{gf}) vectors are propagated, in the prediction stage, as described in Section 3.1.

ψ_u is the user's heading, which is a scalar magnitude. The user's heading is the circular mean between the heading of the foot IMU (ψ_f) and the heading of the pocket IMU (ψ_p), that is:

$$\psi_u = \arctan \left(\frac{\sin(\psi_p) + \sin(\psi_f)}{\cos(\psi_p) + \cos(\psi_f)} \right). \quad (8.2)$$

The measurement update stage of the UKF implements different types of updates. The gravity update is detailed in Section 3.1, thus the reader is referred to that section for further details on the implementation. The remaining updates are the result of the biomechanical study carried out in Chapter 7 and their respective integrations in the filter are detailed in the following sections.

8.3 Comfort Zone Update

The goal of the comfort zone update is to assure that the tilt angles are coherent with respect of human motion. As we appreciate in Figure 8.2, the tilt angles estimated

by the pocket INS are incoherent because they are not centered around zero.

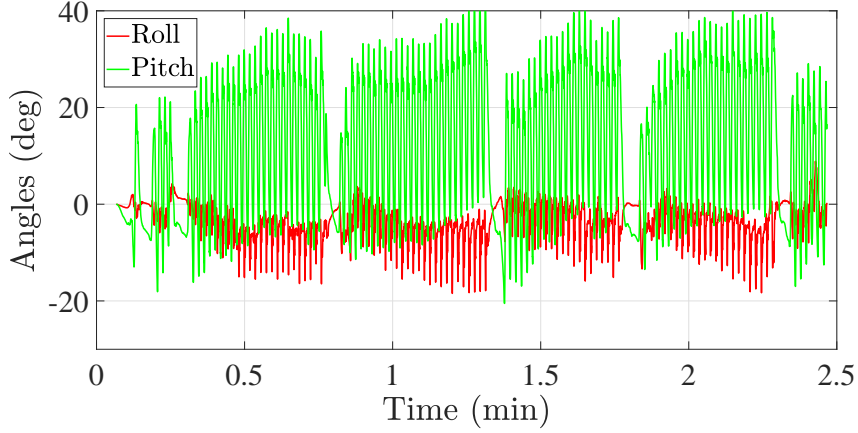


Figure 8.2: Example of the tilt angles of the pocket INS.

The *Attitude tracker* integrates the comfort zone of the tilt angles as a soft constraint on the respective filter states. Simon [92] points out that soft constraints on the filter states can be implemented through the measurement update. In our case, the measurement vector is extended with the mean of each tilt angle of both the pocket IMU and the foot IMU, i.e.:

$$\mathbf{z}_c = [\phi_p^z, \theta_p^z, \phi_f^z, \theta_f^z], \quad (8.3)$$

where \mathbf{z}_c is the measurement vector of the comfort zone. ϕ^z, θ^z are the mean values taken from Table 7.7 for the pocket (p) and the foot (f). The measurement vector requires a variance of the measurements, which are the associated values in Table 7.7.

Figure 8.3 is an example of application of the comfort zone update on the tilt angles of the pocket IMU. We can see how the comfort zone update eliminates the low frequency component that modulates the angles on the left-hand plot.

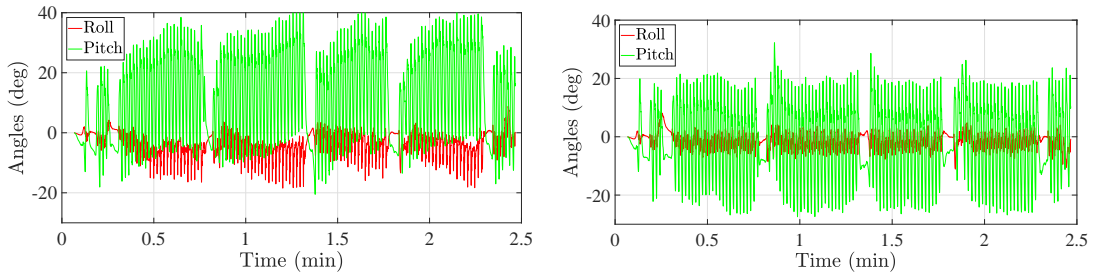


Figure 8.3: Example before (left) and after (right) the comfort zone update on the tilt angles of the pocket IMU.

8.4 Relative-Heading Update

Until now, we know that the relative heading between the pocket and the foot should be constant over time, see Section 7.4. However, the heading error in inertial localization systems makes the inertial relative heading grow over time, as Figure 8.4 exemplifies. In order to address this misbehaviour, the relative-heading update is implemented in the *Attitude tracker* of Figure 8.1.

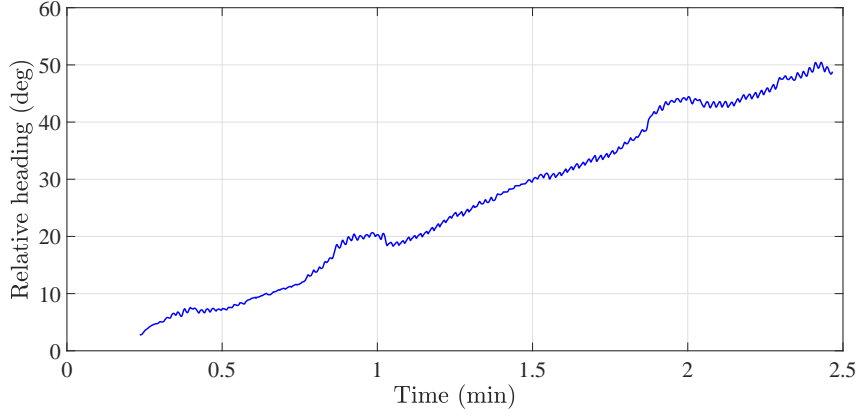


Figure 8.4: Example of the relative heading between the heading of the pocket INS and the heading of the foot INS.

The relative heading update incorporates to the filter the fact that the difference of the heading of the pocket IMU and the foot IMU should remain approximately constant over time. To that end, let us model the relative heading (ψ_r) in Figure 8.4 as a first-order linear regression model, such that:

$$\psi_r = a_r \cdot t + b_r, \quad (8.4)$$

where t is the time variable, and (a_r, b_r) are the parameters of the first order model.

The variable responsible for the increase of the relative heading is the slope (a_r). In theory, this variable should be zero. That is, we have a pseudo-measurement (\mathbf{z}_r) such that:

$$\mathbf{z}_r = a_r = 0. \quad (8.5)$$

The measurement \mathbf{z}_r is referred to as pseudo-measurement because it not measured through sensors. The same concept is used by Foxlin for the definition of the ZUPT [15].

To implement the relative heading update, we need to estimate the pseudo-measurement which is the slope of the relative heading. The estimate of the pseudo-measurement is a weighted average of the sigma points (Υ_i^k), see Appendix C. The sigma points (Υ_i^k), with $i = \{1, 2, \dots, 2n + 1\}$, is the predicted slope ($a_{i,r}^k$) of the relative heading of each sigma point, that is:

$$\Upsilon_i^k = \frac{\psi_{i,r}^k - \psi_{i,r}^{k-t_e}}{t_e}, \quad (8.6)$$

where $\psi_{i,r}^k$ and $\psi_{i,r}^{k-t_e}$ are the relative heading of the i -th sigma point at the k -th time and t_e seconds before, respectively. The parameter t_e is the elapsed time between consecutive relative heading updates. The concept behind equation (8.6) is to estimate the slope as exemplified in Figure 8.5.

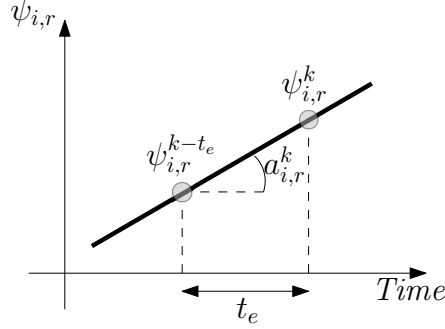


Figure 8.5: Exemplification of the relative heading update.

Each relative heading ($\psi_{i,r}^k$) is the average over the last t_w seconds of the difference between the heading of the pocket IMU ($\psi_{i,p}^j$) and the heading of the foot IMU ($\psi_{i,f}^j$), that is:

$$\psi_{i,r}^k = \frac{1}{t_w} \sum_{j=k-t_w}^k (\psi_{i,f}^j - \psi_{i,p}^j), \quad (8.7)$$

where $\psi_{i,p}^j$ and $\psi_{i,f}^j$ are the heading estimations of the i -th sigma point at the j -th time.

We need to define the elapsed time (t_e) and the window length (t_w). In the following, these two values are heuristically set to 1s and 10s respectively. That is, the *Attitude tracker* performs the relative heading update every 1s. During this update, the relative heading is estimated as the average over the last 10s of the difference between the heading of the pocket IMU and the heading of the foot IMU.

One more parameter should be defined, namely the covariance of the measurement in equation (8.6). In this update, the pseudo-measurement is perfect, which means that there is no uncertainty about it. According to Simon, perfect measurements take a covariance value of 0 [92]. Nevertheless, it is necessary to be careful when setting the covariance to 0 since there have been reported problems in setting the covariance to such a value [93]. Thus, we set it to a small value (4°), which we define heuristically.

Figure 8.6 is an example of the effect of the relative heading update. In a time period of 2.5 min, the relative heading has been reduced in approximately 73%.

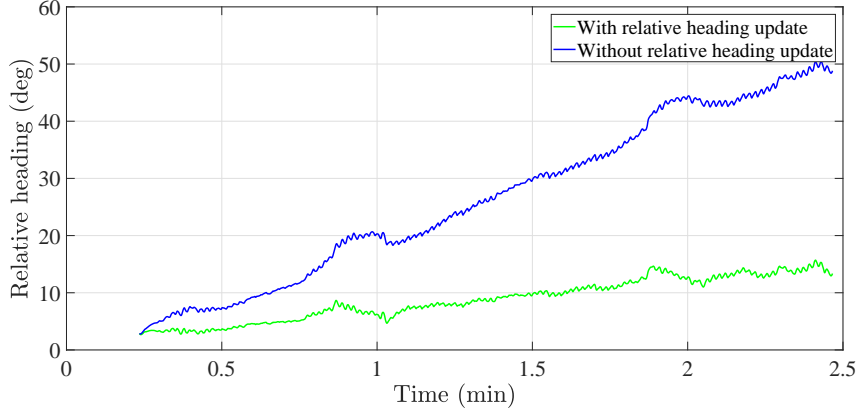


Figure 8.6: Comparison of the relative heading before and after the relative heading update.

8.5 Distance Estimation

The *3D position tracker* in Figure 8.1 relies on two main elements: the strapdown algorithm and the steps-and-stairs detection. These two elements are implementable thanks to the foot IMU and the pocket IMU, respectively. The advantages of each of them are already analyzed in Section 4.4, but they will be briefly commented below for completeness.

The strapdown algorithm has the advantage of a model-free distance estimation. However, the position error accumulates over time due to the double integration of the acceleration vector. In contrast, the steps-and-stairs detection is robust thanks to the characteristic of the pitch of the pocket IMU during the walk, but it cannot estimate distances, neither horizontal nor vertical, without a model.

The *3D position tracker* exploits the aforementioned advantages. To that end, it estimates the user's position within the *Strapdown* block. The latter implements an UKF whose states are the 3D-position (\mathbf{p}) and 3D-velocity (\mathbf{v}) of the user, i.e.:

$$\mathbf{x} = [\mathbf{p}^T, \mathbf{v}^T]^T, \quad (8.8)$$

where both \mathbf{p} and \mathbf{v} are column vectors. The implementation of such a filter is detailed in Section 3.2.1. The reader is referred to this section and references therein for further details.

The second step is to detect both steps and stairs in the *Steps & stairs detection* block of Figure 8.1. The implementation of this block is detailed in Section 3.2.2. Upon the detected steps or stairs, the *Step sampling* block samples the 2D-position estimated by the *Strapdown*. Then, the step length (s^k) between consecutive steps is computed as:

$$s^k = \|\mathbf{p}_{s,xy}^k - \mathbf{p}_{s,xy}^{k-1}\|, \quad (8.9)$$

where $\mathbf{p}_{s,xy}^k$ and $\mathbf{p}_{s,xy}^{k-1}$ are the horizontal components of the position estimates at the current detected step (k) and the previous detected step ($k-1$), respectively. $\|\cdot\|$ denotes the norm of the argument.

The step length (s^k) is then passed to the *2D position* block, where the well-known equations:

$$p_x^k = p_x^{k-1} + s^k \cdot \cos(\psi_u^k), \quad (8.10)$$

$$p_y^k = p_y^{k-1} + s^k \cdot \sin(\psi_u^k), \quad (8.11)$$

$$(8.12)$$

estimate the horizontal components (p_x^k, p_y^k) of the user's position. ψ_u^k is the user's heading estimated by the *Attitude tracker* block.

Similarly, the z-component of the position vector is iteratively estimated by sampling the *Strapdown* height when a stair is detected. This approach is equivalent to the one followed by the loose coupling system, see Section 6.2.2. The vertical displacement (v^k) is estimated as:

$$v^k = p_{s,z}^k - p_{s,z}^{k-1}, \quad (8.13)$$

where $p_{s,z}^k$ and $p_{s,z}^{k-1}$ are the z-component of the position estimated by the *Strapdown* at the current stair (k) and the previous stair ($k-1$), respectively. In addition, we also add a condition to assure that the height increment is greater than 15 cm in order to trigger the detection of a step. The z-component of the position vector at the k -th step (p_z^k) is computed as:

$$p_z^k = p_z^{k-1} + v^k, \quad (8.14)$$

The goal behind the implementation of the *3D position tracker* is to reduce the accumulation of the position error of the strapdown algorithm. Nonetheless, our proposed approach will still accumulate errors in the position estimation. Yet, we expect the error accumulation to be smaller than the one resulting from only the *Strapdown* block. The evaluation of the tight coupling system, as well as the evaluation of the inertial localization systems previously introduced in this thesis, is carried out in the next chapter.

8.6 Summary and Conclusions

This chapter proposed a tight coupling system where the raw measurements of a pocket IMU and a foot IMU are combined to estimate the position of a user. The proposed tight coupling system implements the concept of comfort zone on the roll and pitch of the thigh and foot limbs, which are equivalent to the roll and pitch of the pocket IMU and the foot IMU, respectively. This concept is implemented by a soft constraint on these angles during the measurement update of the UKF that tracks the attitude of both limbs. Regarding the heading, we implement a pseudo-measurement update on the relative heading of the thigh limb and the foot limb. Finally, the position is estimated by sampling the output of the strapdown algorithm upon the detection of steps and stairs.

There are two main conclusion regarding the tight coupling system. Firstly, the implementation of soft constraints on the roll and pitch keep the behaviour of these

angles coherent with respect to human motion. Secondly, we improve the relative heading of the thigh limb and the foot limb thanks to the pseudo-measurement update on the relative heading. In the example shown, the slope of the relative heading decreases in 73% with respect to its original value.

Chapter 9

Evaluation

*My mission in life is not merely to survive, but to thrive;
and to do so with some passion, some compassion,
some humor and some style*
– Maya Angelou

The evaluation of an inertial localization system is the process by which we generate metrics that quantitatively characterize the system performance. A quantitative evaluation is the only means to assess whether the proposed implementations improve or worsen the original single-IMU localization systems. Therefore, the evaluation is a key part of our research work.

In this chapter, we follow the T&E methodology proposed in Section 4.2. This methodology is similar to those implemented in indoor localization competitions. Then, we assess the performance of the inertial localization systems presented in Chapter 5-Chapter 8 and we compare them to the single-IMU localization systems. For the assessment, we use the data set presented in Section 4.2.3.

For the sake of completeness, we will briefly list again the metrics we use to quantify the performance of an inertial localization system. The reader is referred to Section 4.2.3 for a detailed explanation on the performance metrics. The metrics are the following:

- the distance error, $e_d = |d_{ij}^r - d_{ij}^w|$, quantifies the performance regarding the distance estimation (d_{ij}^r, d_{ij}^w) between consecutive ground truth points.
- the heading error, $e_\psi = |\psi_{ij}^r - \psi_{ij}^w|$, quantifies the performance regarding the relative heading $(\psi_{ij}^r, \psi_{ij}^w)$ between consecutive ground truth points.
- the height error, $e_h = \frac{|h_i^r - h_i^w|}{\Delta h_i^r}$, quantifies the performance regarding the height estimation $(|h_i^r - h_i^w|)$ with respect to the total height change at a certain ground truth point (Δh_i^r) .

The approximate trajectory walked by the users is presented in Figure 4.3. In Figure 9.1, we indicate the sequence in which the users visited the ground truth points. In total, we have 5 h of data collected from 10 different users.

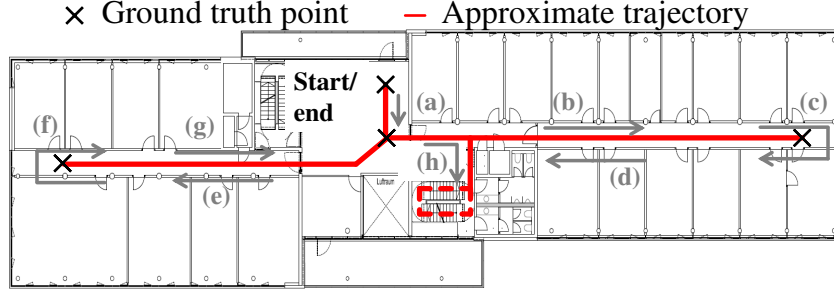


Figure 9.1: Approximate true trajectory. The walk sequence, (a)-(h), is indicated by the arrows. After (h), the users walk the stairs to the next floor.

To interpret the results below, it is not enough to analyze the performance figures on their own. It is necessary to take into account that the users walked, in average, 15 min to 20 min during each walk. Since the errors of inertial localization system are cumulative, the longer the system operates the larger its errors will be.

9.1 Evaluation of the Calibration

The proposed calibration method automatically estimates the parameters of the step length model of the pocket INS. Let us remind that the step length model follows the equation $s = a \cdot \Delta\theta + b$, where the slope (a) and the offset (b) are the model parameters to be estimated. We distinguish two cases: offset calibration or full calibration. The first one estimates only the offset of the step length model. The second case estimates both the slope and the offset of the step length model. The output of the foot INS is used to implement a least squares method that estimates the parameters of interest. For further details, the reader is referred to Chapter 5.

The pocket INS has been assessed under different configurations. On the one hand, we consider two reference implementations of the pocket INS. In the first reference implementation, the step length model uses the universal parameters [19]. In the second reference implementation, the step length model is manually calibrated to each user.

On the other hand, we consider three pocket INSs with automatic calibration. The first one implements the offset calibration over a fixed window of 2 min. Let us remember that the latter is the convergence time identified in Section 5.3. The second one implements the offset calibration with the least squares method. The third alternative implements the full calibration

As Table 9.1 shows, the pocket INS with either of the proposed calibration methods has the same heading error as the pocket INS with manual calibration or pocket INS with universal parameters. This result is expected since the calibration method effects only the step length estimation of the step&heading algorithm. The same applies to the height error, where the vertical displacement is not influenced by the step length model, see Section 3.2.2. That is, the effect of the proposed calibration

Table 9.1: Evaluation of the pocket INS with different calibration configurations. The performance figures are given as mean \pm standard deviation of the error metrics.

System description	$e_d[m]$	$e_\psi[^\circ]$	$e_h[m/m]$
Universal parameters	12.7 ± 8.8	56.7 ± 50.7	0.8 ± 2.0
Manual calibration	3.8 ± 7.9	61.2 ± 48.8	0.8 ± 2.0
Offset calibration (120 steps)	5.7 ± 9.5	56.6 ± 50.7	0.8 ± 2.0
Offset calibration (least squares)	5.9 ± 9.8	56.7 ± 50.7	0.8 ± 2.0
Full calibration	5.5 ± 9.3	57.7 ± 50.7	0.8 ± 2.0

methods on the heading error and height error are consistent with the expectations.

The key metric in this section is the distance error. The calibration with universal parameters has the highest distance error because it is the one that worst models the physiology of an user. Table 9.1 shows that the pocket INS with each of the proposed calibration methods achieves, approximately, the same average distance error. This result is supported by the CDFs in Figure 9.2.

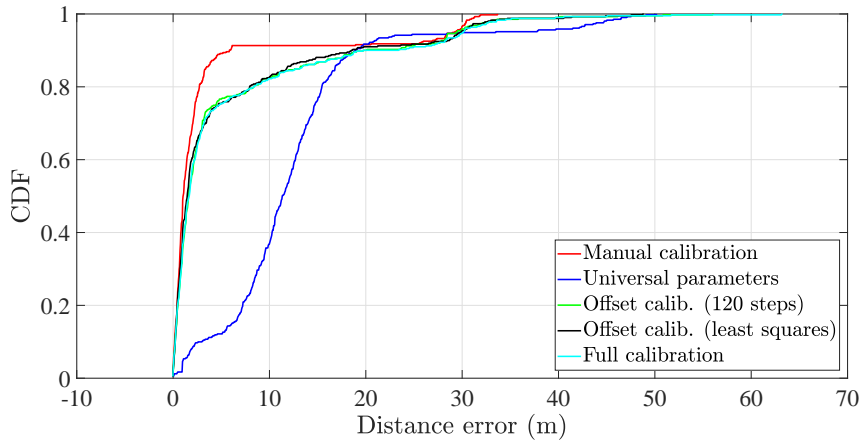


Figure 9.2: CDF of the distance error of the pocket INS with different configurations. *Calib.* stands for calibration.

Interestingly, none of the pocket INSs that implement the proposed calibration methods outperforms the manual calibration. The reason is that we calibrate the step length model with the foot INS, which has errors¹ as well. Thus, there is a lower bound to how well the step length model may perform, i.e. the estimation of the step length model cannot outperform the distance estimation of the foot INS. In addition, the step length model has errors due to the model itself. The combination of the latter two error sources explains why the distance error of the proposed pocket INSs with automatic calibration does not outperform the pocket INS with manual calibration in Table 9.1.

¹ Let us note that the distance error of the foot INS is, at least, four times smaller than the distance error of the pocket INS with universal parameters.

A surprising result is that the full calibration performs as good as the offset calibration. We obtain this result despite the fact that the users were not requested to change their walking speed during the experiments. The users walked at a comfortable pace, which remained approximately constant during the experiment. Thus, we expect the parameters estimated by the full calibration method to be over-fitted to the user’s walking pace in each walk.

An example is given in Figure 9.3, where the slope estimated by the full calibration method is approximately one order of magnitude smaller than the universal one. This result is not coherent with the expected slope of an adult. For instance, according to the step length model, a typical pitch amplitude is 40° . Provided that a user’s slope is $0.005 \text{ m}/^\circ$, the multiplication of the slope by the pitch amplitude would lead to a step length of 20 cm, which is one order of magnitude smaller than the expected value.

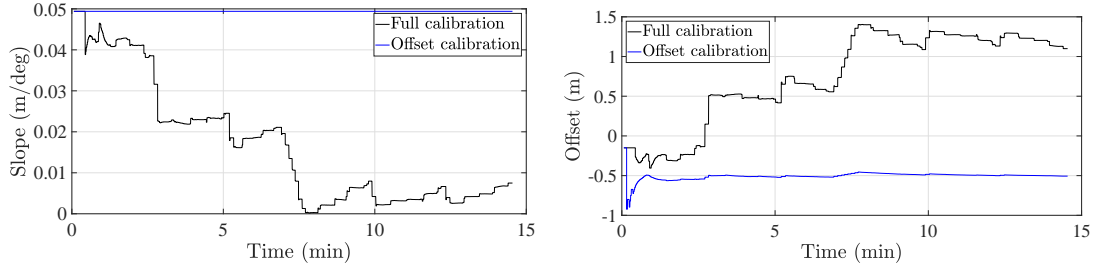


Figure 9.3: Comparison of the model parameters estimated by the full calibration method and the offset calibration method. The offset calibration is implemented with the least squares.

We finalize this section with an example of the odometry to show the effect of the calibration method. Figure 9.4 shows one stretch of a user’s trajectory: from the start to the end of the corridor. The duration of this stretch is approximately 60 s. The odometry estimated by the pocket INS with universal parameters clearly estimates longer distances than any other version of the pocket INS. We appreciate this fact by comparing the true ground truth point at the end of the corridor with the estimated one. The distance overestimation is due to the use of the universal parameters in the step length model. In this example, the parameters do not model the physiology of the user, thus leading to the overestimation of the step length, which leads to an overestimation of the distance.

The remaining versions of the pocket INS are more accurate than the pocket INS with universal parameters. Yet, we see that the most accurate inertial localization system regarding distance estimation is the pocket INS with offset calibration, which has a 0.2 m distance error at the end of the corridor. As expected, the two offset calibration methods have the same distance error.

The results of the pocket INS with full calibration need to be interpreted appropriately. The pocket INS with full calibration is less accurate than the other alternatives because, within the duration of the stretch, the full calibration did not have time to converge in the estimation of the parameters of the step length model.

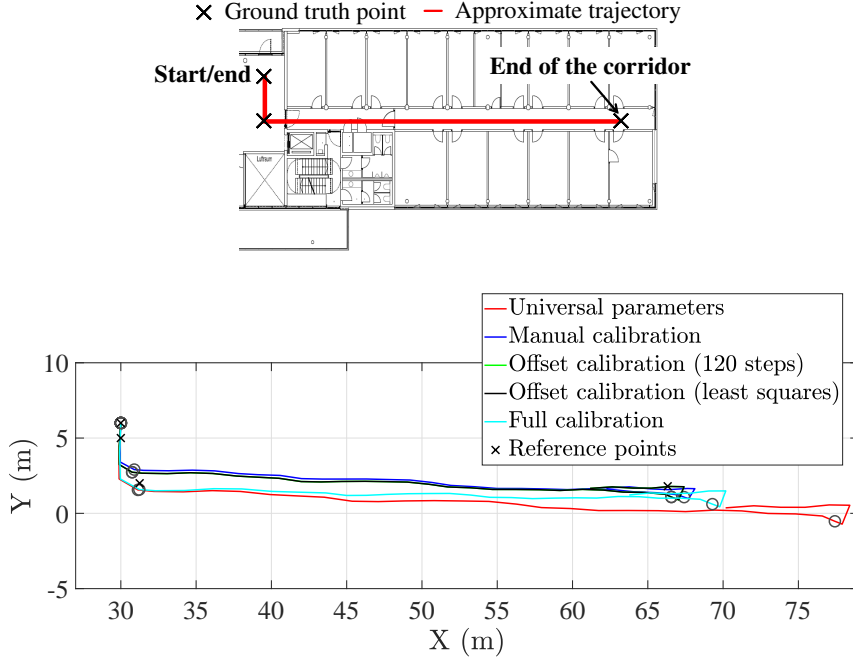


Figure 9.4: (Top) Approximate true trajectory. (Bottom) Example odometry of the pocket INS with different calibration methods. The circle marks are the estimated positions of the ground truth points.

9.2 Evaluation of the Loose Coupling System

The loose coupling system combines the outputs of the foot INS and the pocket INS to estimate a single position of the user. Also, the pocket INS implements the offset calibration during 120 steps, see Section 5.3. In the loose coupling system, the step length of the foot INS and the pocket INS are weighted with fixed weights, whereas the heading estimates are weighted with adaptive weights. The height is tracked by sampling the height of the foot INS when the pocket INS detects stairs.

Table 9.2: Evaluation of the loose coupling system. The performance figures of the single-IMU localization systems are given for comparison. The values are given as mean \pm standard deviation.

System description	$e_d[m]$	$e_\psi[^\circ]$	$e_h[m/m]$
Pocket INS with offset calibration	5.7 ± 9.5	56.6 ± 50.7	0.8 ± 2.0
Foot INS	2.9 ± 8.2	66.9 ± 52.9	0.4 ± 0.4
Loose coupling system	4.5 ± 8.2	62.2 ± 49.0	0.1 ± 0.2

The evaluation of the loose coupling system is summarized in Table 9.2. It provides not only the performance figures of the loose coupling but also the metrics of the single-IMU localization systems. The latter are considered as the reference systems.

The average distance error of the loose coupling system outperforms the pocket INS

with offset calibration but not the foot INS. The reason is that the step length of the loose coupling system is estimated with fixed weights for the respective step lengths of the single-IMU localization systems. In doing so, the loose coupling is able to perform in-between the inertial localization systems at its input. The in-between performance of the loose coupling system is supported by the CDFs of the distance error in Figure 9.5.

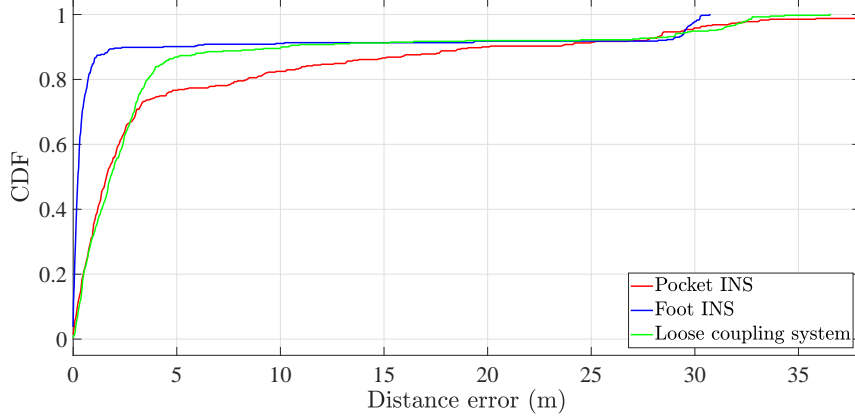


Figure 9.5: CDF of the distance error of the single-IMU localization systems and the loose coupling system.

In Table 9.2, we can see that the loose coupling system outperforms the foot INS regarding the heading error. However, it does not reach the same heading error as the pocket INS. This fact is supported by the CDF in Figure 9.6, where the loose coupling system performs between the two single-IMU localization systems.

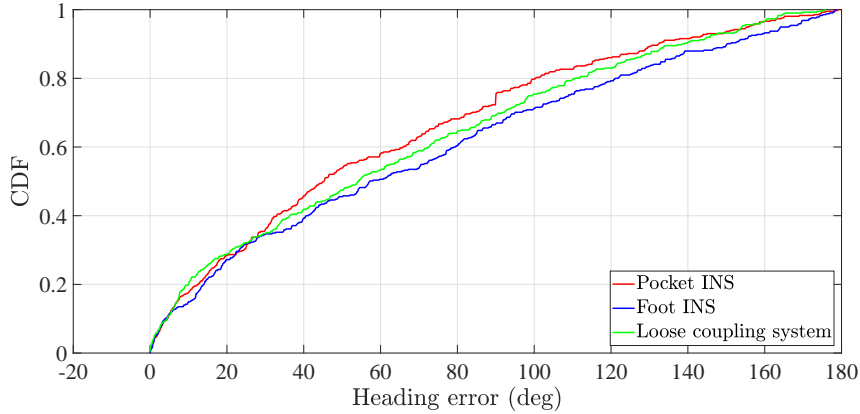


Figure 9.6: CDF of the heading error of the single-IMU localization systems and the loose coupling system.

The loose coupling system is not able to outperform the pocket INS in Figure 9.6 due to the weighting process of the heading. Although the weights favour the most accurate heading, they do not completely reject the least accurate one. Thus, the heading estimation of the loose coupling may contain more errors than the most

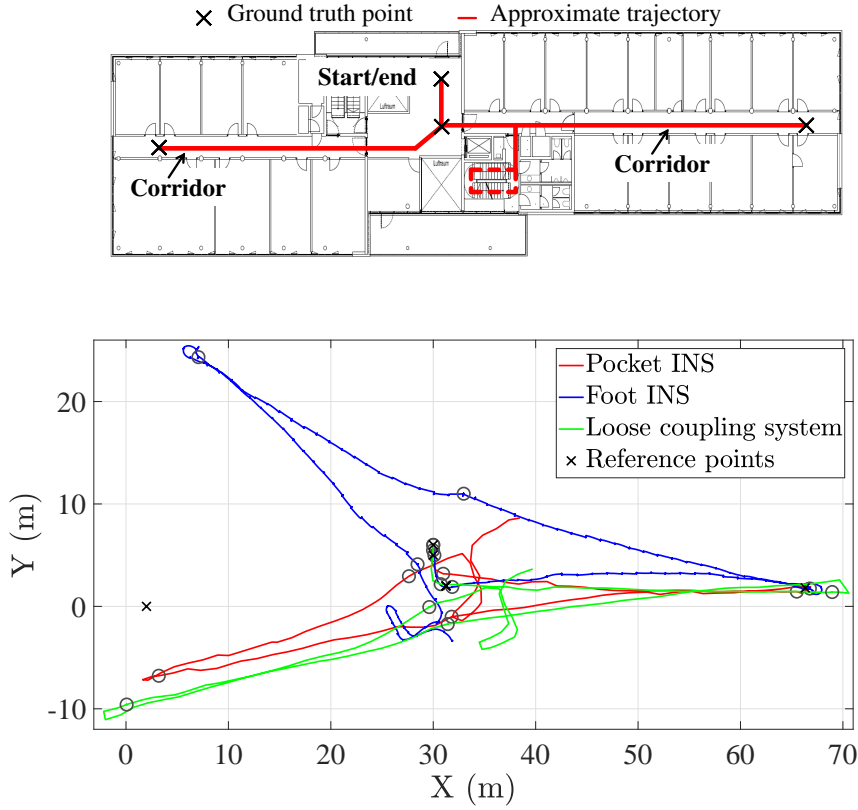


Figure 9.7: (Top) Approximate true trajectory. (Bottom) Odometry estimated by the pocket INS, the foot INS and the loose coupling. The circle marks are the estimated positions of the ground truth points.

accurate heading estimation at the input. Such a case occurs when the heading of the foot INS and the heading of the pocket INS drift in the same direction.

Figure 9.7 is an example of a walk processed with the pocket INS, the foot INS and the loose coupling system. For illustration purposes, this figure shows only part of the 15 min walk. We can see that the foot INS has the least accurate heading estimation. In contrast, the pocket INS is more accurate regarding the heading estimation, a fact that is reflected in the associated heading weights, see Figure 9.8. In this example, the weights remain approximately constant over time. This behaviour is expected since the heading of the foot INS is less accurate than the heading of the pocket INS during the complete walk, as Figure 9.7 shows.

Figure 9.9 shows the heading errors associated to the odometries of Figure 9.7. This figure shows that the heading of the foot INS is less accurate than the heading of the pocket INS.

The odometry of the loose coupling system has a heading estimation that is more similar to the pocket INS than the foot INS. Nevertheless, we see that the trajectory along the corridors overlaps for the loose coupling system but not for the pocket INS. The reason is the heading weight of the foot INS, which does not completely reject the heading of the foot INS. Since it drifts in the opposite direction of the heading of the pocket INS, its contribution makes the trajectory of the loose coupling system

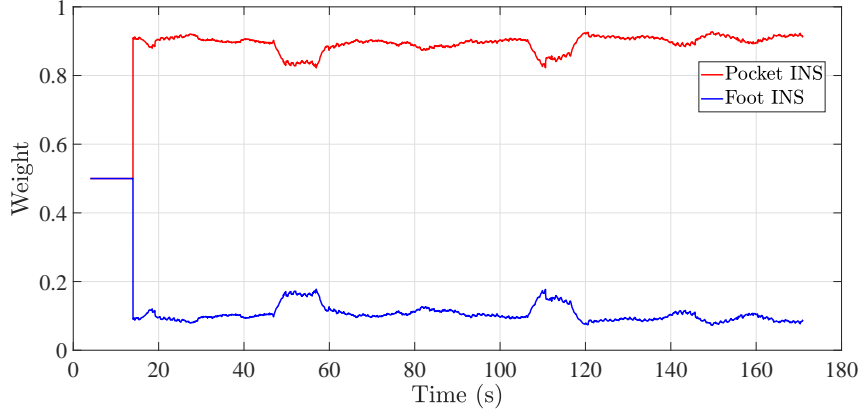


Figure 9.8: Heading weights of the foot INS and the pocket INS of Figure 9.7.

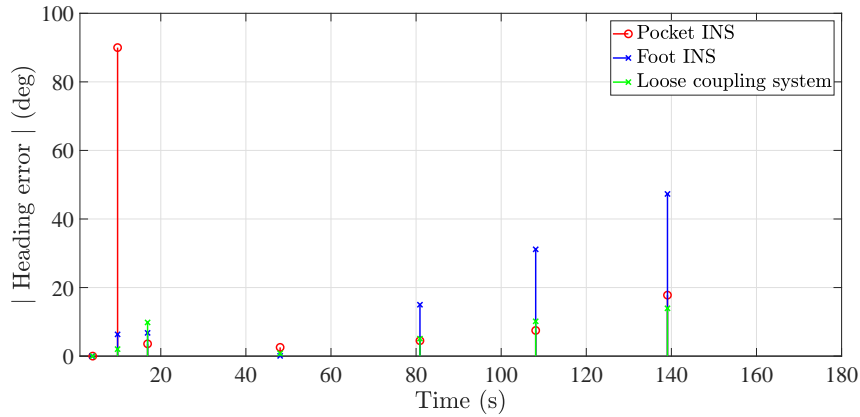


Figure 9.9: Heading error of the odometries shown in Figure 9.7.

to overlap at the corridor parts. Since the heading of the foot INS and the heading of the pocket INS drift in opposite directions, their combination through the weights of Figure 9.8 allows the loose coupling system to have a more accurate heading at the corridors.

The previous feature of the loose coupling, i.e. the fact that the trajectories may overlap more than in the single-IMU localization systems, may be beneficial for certain applications. An example are SLAM-based inertial localization systems, which exploit loop closures.

At the second ground truth point in Figure 9.9, the heading error of the pocket INS becomes larger because of the design of the walk. This ground truth point is close to the first one. Thus, some users did not have enough space to do the steps with their usual length. Instead, they had to adjust their step length to be able to step on the ground truth point. As a result, some of the steps were not long enough to trigger a step detection, leading to an odometry with a large heading error at this specific ground truth point.

The heading of the loose coupling system is, at the ground truth points, as accurate as the heading of the pocket INS. We observe this fact in Figure 9.9, yet Figure 9.7 shows that the odometry of the loose coupling at the corridors has a heading more

accurate than the heading of the pocket INS has. Unfortunately, this behaviour cannot be captured with the current ground truth system because we did not collect ground truth points at the corridors.

The height error of the loose coupling outperforms both single-IMU localization systems. In Table 9.2, a normalized height error of 0.1 m/m means that the loose coupling system has an average height error of 35 cm when the user goes up or down one floor. We make this calculation considering that the floor difference is 3.5 m, see Figure 4.3. In contrast, the foot INS makes an average height error of 1.4 m, whereas the pocket INS makes an average height error of 2.8 m.

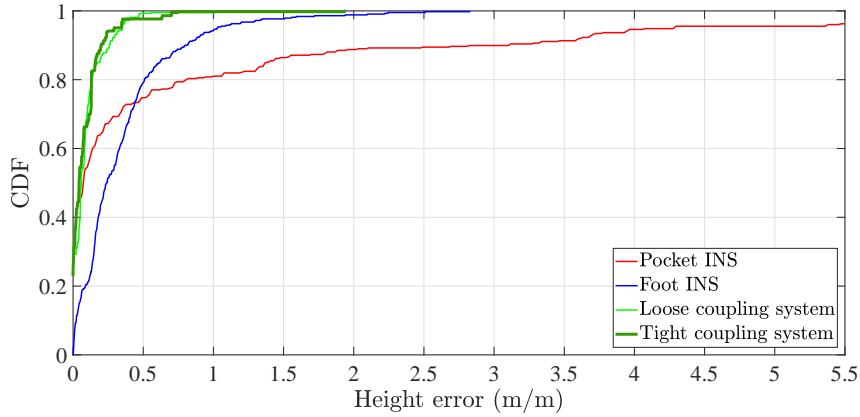


Figure 9.10: CDF of the height error of the single-IMU localization systems, the loose coupling system and the tight coupling system. The third quartile of the loose and tight coupling systems is 0.12 m, whereas the third quartile of the foot INS and the pocket INS is 0.46 m and 0.52 m respectively.

The performance increase in the height error of the loose coupling is also noticeable in the CDF of Figure 9.10. In the latter, we appreciate that the third quartile of the height error of the loose coupling system is already 74% more accurate than the third quartile of the height error of the foot INS. Regarding the pocket INS, the loose coupling system improves the third quartile of the height error in 77%.

The reason for the low height error of the loose coupling is its height estimation algorithm. The latter is based on exploiting complementary features of the pocket INS and the foot INS. This approach allows the loose coupling system to outperform both single-IMU systems instead of performing in-between them.

Figure 9.11 shows the height estimation of the foot INS, the pocket INS and the loose coupling system corresponding to Figure 9.7. This figure summarizes all the effects that we have mentioned above regarding the height performance of each of the inertial localization systems. First of all, the height estimation of the foot INS drifts over time. Second, the height estimation of the pocket INS is disturbed by outliers. For each outlier, the increment in height is constant and equals the predefined height of a step. Finally, the height of the loose coupling system outperforms the height of the single-IMU localization systems.

The vertical displacement is only estimated upon stairs detection, see the time frame

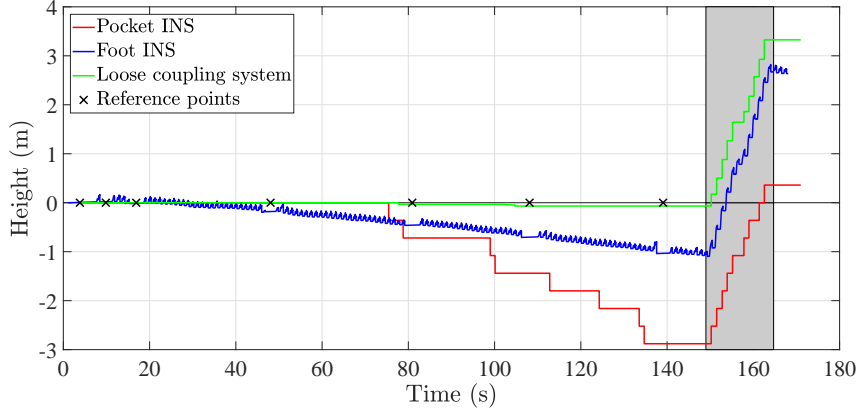


Figure 9.11: Height estimation of the inertial localization systems in Figure 9.7. The shadowed area indicates the time period when the user walks the stairs.

150s-170s in Figure 9.11. Even in the event of outliers, the height of the loose coupling system remains approximately constant because the vertical displacement is estimated through the height estimation of the foot INS, and not as a predefined value, see the time frame 80s-140s in Figure 9.11.

Considering the overall performance of the loose coupling, we believe that its most important contribution is the decrease of the average height error with respect to the single-IMU localization systems. The advantage of the loose coupling system with respect to the pocket INS is that the height is not estimated deterministically. Instead, the loose coupling samples the height estimation of the foot INS whenever stairs are detected by the pocket INS. Thus, even in the event of false positives, the vertical displacement estimated by the loose coupling is small, e.g. 1 cm, whereas the pocket INS estimates a vertical displacement of 38 cm, see Section 3.2.2.

The limitation of the loose coupling system is that it cannot, in average, outperform the most accurate single-IMU localization system in either distance error or heading error. Despite this limitation, the loose coupling system provides more robustness than a single-IMU localization system. For instance, the foot INS may perform unexpectedly, e.g. high heading error due to external conditions like temperature. An approach like the loose coupling, which relies on two independent inertial localization systems, can address such situations better than the approach of a single-IMU localization system. Once more, the cost of the loose coupling system is the increased complexity with respect to a single-IMU localization system.

9.3 Evaluation of the Biomechanical Constraints

The biomechanical study of Chapter 7 results in two types of constraints: the comfort zone and the relative heading. The former can be applied in any single-IMU localization system, e.g. the pocket INS or the foot INS. The latter can be applied in multi-IMU localization systems, e.g. the tight coupling system.

In this section, we are interested in evaluating the effect of the comfort zone update in the pocket INS and the foot INS. To that end, we incorporate the comfort zone update in the respective single-IMU localization systems following the soft constraint approach presented in Section 8.3.

Table 9.3: Evaluation of the pocket INS and the foot INS with the comfort zone update. The performance figures of the single-IMU localization systems are given for comparison. The performance figures are given as mean \pm standard deviation. *C.z.* stands for comfort zone.

System description	$e_d[m]$	$e_\psi[^\circ]$	$e_h[m/m]$
Pocket INS	3.8 ± 7.9	61.2 ± 48.8	0.8 ± 2.0
Foot INS	2.9 ± 8.2	66.9 ± 52.9	0.4 ± 0.4
Pocket INS with c.z.	3.5 ± 8.1	57.4 ± 48.5	0.1 ± 0.1
Foot INS with c.z.	2.9 ± 8.2	69.1 ± 53.3	0.4 ± 0.4

Table 9.3 summarizes the performance of the pocket INS and the foot INS without and with the comfort zone update. It is clear that the comfort zone update does not modify the distance error of the foot INS. In contrast, the average distance error of the pocket INS is reduced in almost 16% thanks to the comfort zone update. The improvement in the pocket INS with the comfort zone update is also observed in the CDF of the distance error, see Figure 9.12. The reason is that the comfort zone update modifies the value of the pitch of the pocket INS, which is used to estimate the step length.

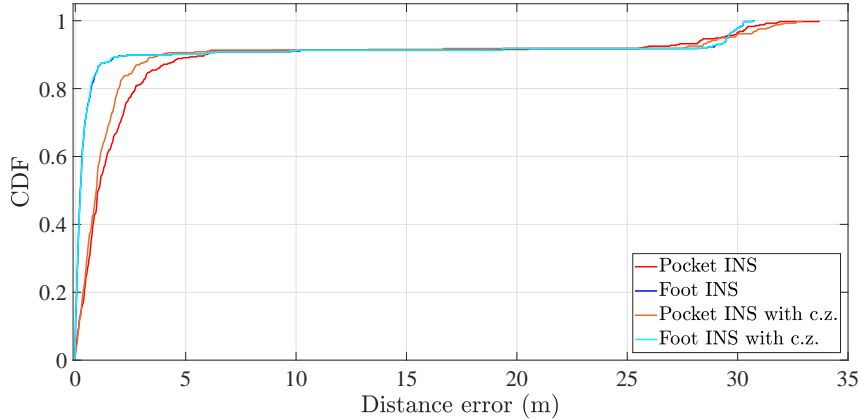


Figure 9.12: CDF of the distance error of the single-IMU localization systems without and with the comfort zone update. *C.z.* stands for comfort zone.

The comfort zone update has no effect on the heading error of an inertial localization system. For instance, the heading error of the pocket INS with the comfort zone update is improved in only 6%. In contrast, the heading error of the foot INS with the comfort zone update is worsened in only 3%.

We appreciate the most significant effect of the comfort zone in the height error of the pocket INS. The average height error of the pocket INS is reduced in approximately

88% thanks to the comfort zone update. The reason is that the comfort zone update improves the coherence of the pitch of the pocket INS. This angle conditions the detection of stairs of the pocket INS. By improving the coherence of the pitch of the pocket INS, the height error of this inertial localization system decreases.

Figure 9.13 shows that the pocket INS with the comfort zone update outperforms the other inertial localization systems. We also observe that the comfort zone update does not modify the CDF of the foot INS. The reason is that the height error of the foot INS does not depend on the coherence of either the roll or the pitch.

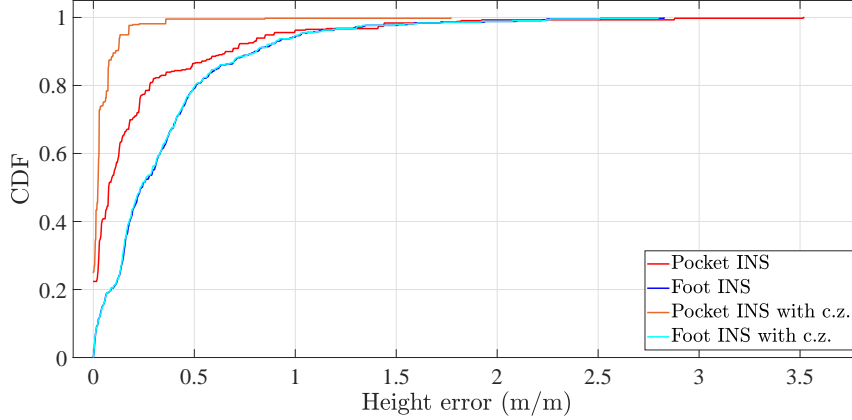


Figure 9.13: CDF of the height error of the single-IMU localization systems without and with the comfort zone update. *C.z.* stands for comfort zone.

In the following, we assess the effect of the comfort zone update on the attitude of the pocket IMU or the attitude of the foot IMU. We use a metric that will statistically compare the tilt angles without and with biomechanical constraints to the ground truth angles.

One of the metrics used in statistics to measure the discrepancy between a data set and a model is the residual sum of squares (r_{ss}) [94]:

$$r_{ss} = \sum_{i=1}^n (y_i - f(x_i))^2, \quad (9.1)$$

where y_i is the i -th sample of a data set with n samples, x_i is the observation and $f(x_i)$ is the model that estimates y_i . In general, the lower the value of the residual sum of squares, the tighter a model fits a data set.

In our evaluation, we will use the residual sum of squares to assess how the CDFs of the inertial tilt angles fit the CDFs of the ground truth tilt angles. The ground truth tilt angles are those measured by the motion capture system described in Section 7.2. We consider the tilt angles of the pocket INS and the foot INS without and with the comfort zone update.

For this assessment, we will consider the tilt angles during only the stance phase. The reason is that the comfort zone update is applied during this gait phase. Figure 9.14

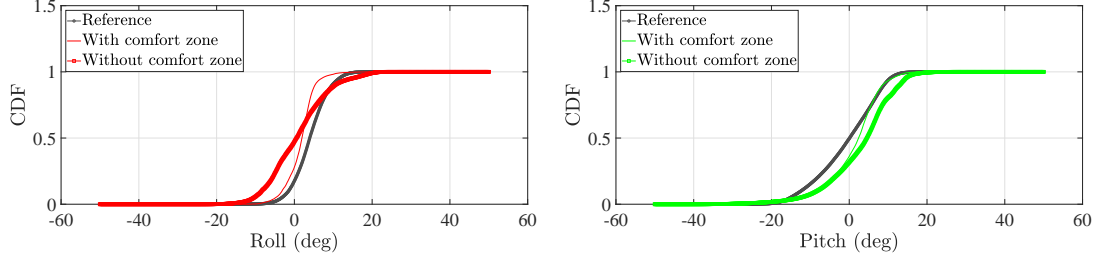


Figure 9.14: CDF of the tilt angles of the pocket IMU during the stance phase.

and Figure 9.15 present the cumulative distribution functions of the ground truth tilt angles and the inertial tilt angles of the pocket IMU and the foot IMU, respectively.

At a first glance, we can see that the distribution of the roll of the pocket IMU is further from the ground truth distribution when there is no comfort zone update, see Figure 9.14. The same occurs with the pitch distribution: the CDF of the pocket INS without the comfort zone update is shifted with respect to the ground truth CDF. In contrast, when we apply the biomechanical constraints, the resulting distribution of both tilt angles are closer to the ground truth distributions.

Regarding the foot IMU, we observe a slightly different behaviour of the distributions of the inertial tilt angles. Namely, the tilt angles without constraints fit the ground truth distributions around 0° , see Figure 9.15. However, the distributions of the angles without constraints are far from the ground truth distribution at the elbows of it. This difference is especially visible when we compare the distribution of the pitch of the foot IMU with and without constraints to the ground truth distribution.

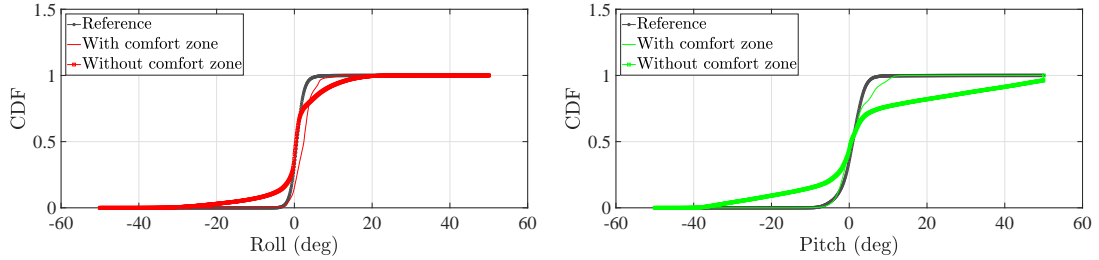


Figure 9.15: CDF of the tilt angles of the foot IMU during the stance phase.

We quantitatively quantify the closeness of the inertial distributions to the ground truth ones through the residual sum of squares. Regarding equation (9.1), the CDF of the ground truth tilt angles will be the sample data set, y_i . The CDF of the inertial tilt angles will play the role of the model, $f(x_i)$.

For all the distributions in Figure 9.14 and Figure 9.15, the associated values of the residual sum of squares are given in Table 9.4. In it, we can see how the implementation of the comfort zone update in the single-IMU localization systems achieves the best fit of the tilt angles distributions. The roll of the pocket IMU and the pitch of the foot IMU are the angles where the distribution without the comfort zone update are furthest from their ground truth distributions. This result is reflected

Table 9.4: Residual sum of squares of the tilt angles distribution of the pocket IMU and the foot IMU. The angles are taken only during the stance phase. The values of this table have no units since they represent a difference between probabilities.

System description	Pocket		Foot	
	Roll	Pitch	Roll	Pitch
Without comfort zone	8.1	5.5	3.0	16.4
With comfort zone	4.5	2.1	3.9	0.8

by a higher residual sum of squares than, for instance, the pitch of the pocket IMU or the roll of the foot IMU.

An interesting fact is that the roll of the foot IMU with biomechanical constraints does not outperform the distribution of the roll of the foot IMU without constraints. The reason may be the fact that the roll of the foot IMU without constraints fits the ground truth distribution around 0° to a degree that the non-fitness around the elbows is cancelled out.

In light of the results of Table 9.4, we repeat the analysis but taking into account the tilt angles during the complete gait cycle. The result values of the residual sum of squares are given in Table 9.5. We can see how the general behaviour remains: the implementation of the comfort zone update in the single-IMU localization systems leads to tilt angles that are a better fit than the angles estimated without the comfort zone update. We consider this result particularly encouraging: we can improve the performance of the tilt angles during the whole gait cycle by applying the comfort zone update during only the stance phase.

Table 9.5: Residual sum of squares of the tilt angles distribution of the pocket IMU and the foot IMU. The angles are taken during the complete gait cycle. The values of this table have no units since they represent a difference between probabilities.

System description	Pocket		Foot	
	Roll	Pitch	Roll	Pitch
Without comfort zone	4.1	1.9	1.6	0.2
With comfort zone	0.8	0.6	1.2	0.3

There is also an interesting result to observe in Table 9.5. The improvement in the values of the residual sum of squares is larger for the pocket IMU than for the foot IMU. That is, the comfort zone update on the pocket IMU improves the residual sum of squares in 80.5% and 68.4% for the roll and pitch respectively. In contrast, the roll of the foot IMU improves only in 25%, whereas the pitch of the foot IMU worsens from 0.2 to 0.3, which we consider a minimal effect. Overall, the fact that the comfort zone update has more effect on tilt angles of the pocket IMU than the tilt angles of the foot IMU has an important implication. Namely, that the tilt angles

of the foot IMU are more coherent than those of the pocket IMU. The reason is the dynamics of the foot while walking, which profit more from certain updates than the pocket IMU, e.g. the gravity update. This result has already been identified and documented in previous works [95].

9.4 Evaluation of the Tight Coupling System

The tight coupling system tracks the user’s position by processing simultaneously the raw data of the pocket IMU and the foot IMU. The two constraints of human motion are integrated in the tight coupling system. The first constraint is based on the comfort zone of the roll and the pitch of both the pocket IMU and the foot IMU. The second constraint is based on the relative heading between the pocket IMU and the foot IMU.

Table 9.6: Evaluation of the tight coupling system. The performance figures of the single-IMU localization systems are given for comparison. The performance figures are given as mean \pm standard deviation.

System description	$e_d[m]$	$e_\psi[^\circ]$	$e_h[m/m]$
Pocket INS	3.8 ± 7.9	61.2 ± 48.8	0.8 ± 2.0
Foot INS	2.9 ± 8.2	66.9 ± 52.9	0.4 ± 0.4
Tight coupling system	3.7 ± 8.0	18.6 ± 28.4	0.1 ± 0.2

Table 9.6 summarizes the performance of the tight coupling as well as the performance of the single-IMU localization systems. Similarly to the previous sections, the reference systems to which we compare the tight coupling system are the foot INS and the pocket INS.

The average distance error of the tight coupling system is comparable to the distance error of both the pocket INS and the foot INS. In fact, the CDF in Figure 9.16 shows that the tight coupling system performs similarly to the pocket INS. However, the foot INS still outperforms our proposed tight coupling system.

As identified in Section 4.4, the main source of errors in inertial localization is the drift in the heading. The results show that the tight coupling system reduces the average heading error in 70% with respect to the pocket INS and 72% with respect to the foot INS. Of especial interest are the CDFs of the heading error shown in Figure 9.17. In the latter, we can observe the increase in performance that the tight coupling system brings with respect to either the pocket INS or the foot INS.

The tight coupling system achieves the performance in Figure 9.17 thanks to the relative heading update. We can state that the tight coupling system reduces the heading error despite the fact that the user’s heading is not directly observed. Instead, we have analyzed and characterized the natural relationship between the heading of the thigh limb and foot limb of a user.

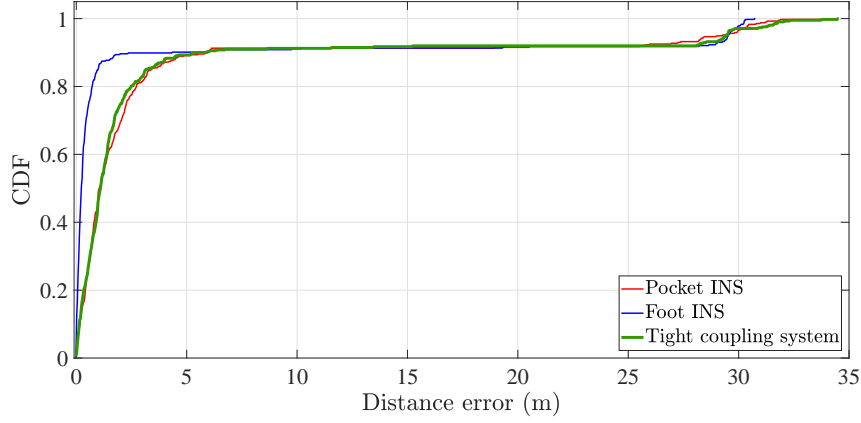


Figure 9.16: CDF of the distance error of the single-IMU localization systems and the tight coupling system.

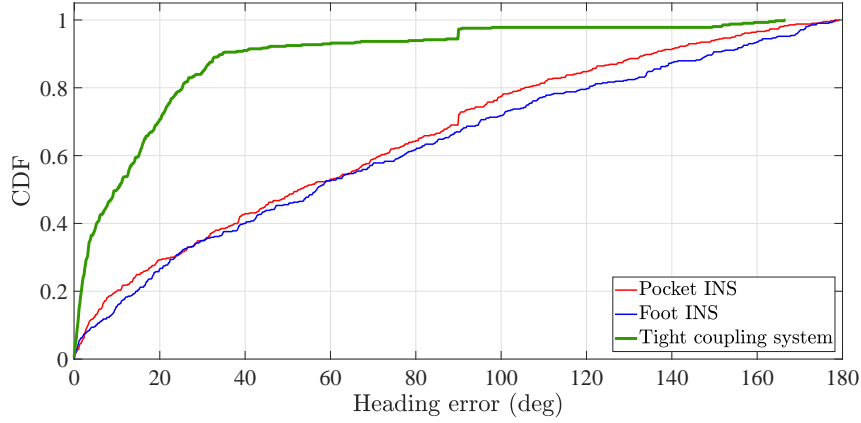


Figure 9.17: CDF of the heading error of the single-IMU localization systems and the tight coupling system.

Figure 9.18 shows the first 5 min of a walk processed with the foot INS, the pocket INS and the tight coupling system. When we qualitatively compare each trajectory to the expected one, see the top picture of Figure 9.18, we can clearly state that the tight coupling system achieves the best result.

The raw data input to each of the inertial localization systems is the same. Hence, the tight coupling system manages to improve the performance of the pocket INS and the foot INS by incorporating the knowledge of human biomechanics and its limitations. Such improvement becomes even more relevant when we compare the heading error of the foot INS and the tight coupling system, see Figure 9.19. In this case, the heading error of the tight coupling system remains approximately constant over time. In contrast, both single-IMU localization systems experience an increase in their respective heading errors. After approximately 5 min, the heading error of the foot INS is 130° , whereas the tight coupling system has a heading error of 1° approximately.

There are aspects of the tight coupling system that need improvement. An example is the distance error. In Figure 9.18, we can see that the tight coupling system has a

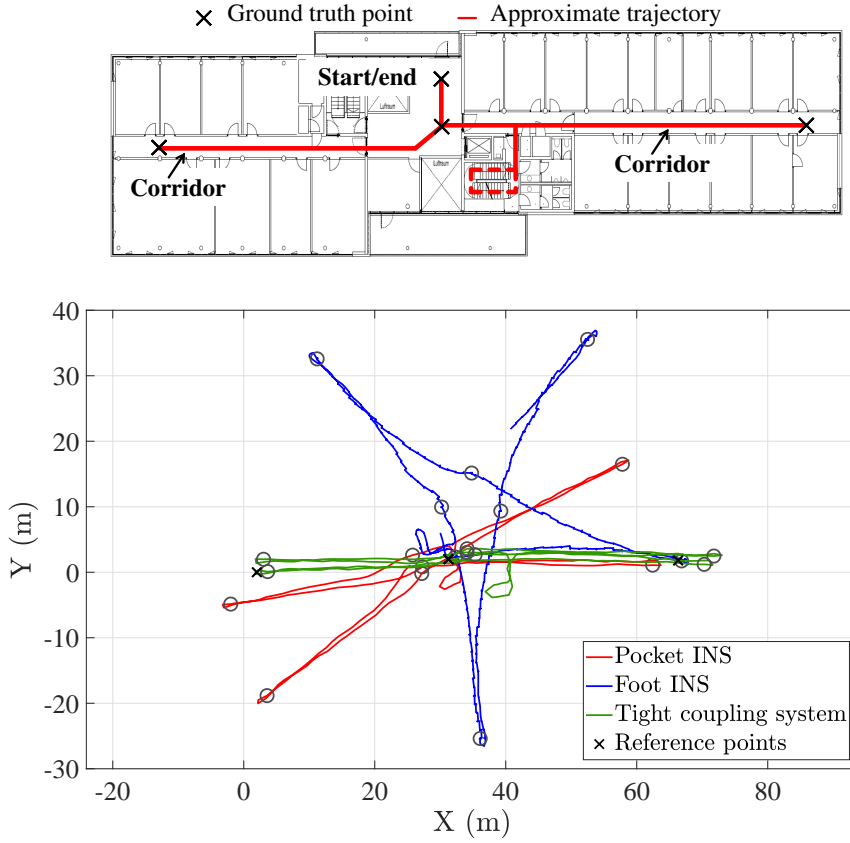


Figure 9.18: (Top) Approximate true trajectory. (Bottom) Odometry estimated by the pocket INS, the foot INS and the tight coupling system. The circle marks are the estimated positions of the ground truth points.

distance error at the right-side of the corridor. More specifically, the tight coupling exceeds the length of the corridor in 4 m approximately.

We believe the reason for the distance error of the tight coupling in Figure 9.18 is the implementation of the *3D position tracker* of the tight coupling, see Figure 8.1. This subsystem of the tight coupling system tracks the position with the strapdown algorithm, similarly to what the foot INS does. However, the foot INS tracks the attitude and the position in the same UKF, whereas the tight coupling system tracks the attitude in a separate filter. This difference in implementation may have caused the tight coupling system to have larger distance errors than the foot INS has.

Similarly to the loose coupling system, the tight coupling system outperforms the single-IMU localization systems in the height error. This result is expected since the tight coupling system tracks the height with an approach similar to one of the loose coupling system. In fact, the CDF of the height error of the tight coupling system is similar to the one of the loose coupling system, see Figure 9.10.

Figure 9.20 shows the height profile associated to Figure 9.18. In this figure, we see the expected behaviour of the single-IMU localization systems. That is, the height of the foot INS increases over time whereas the height of the pocket INS is disturbed by outliers, e.g. around 150 s.

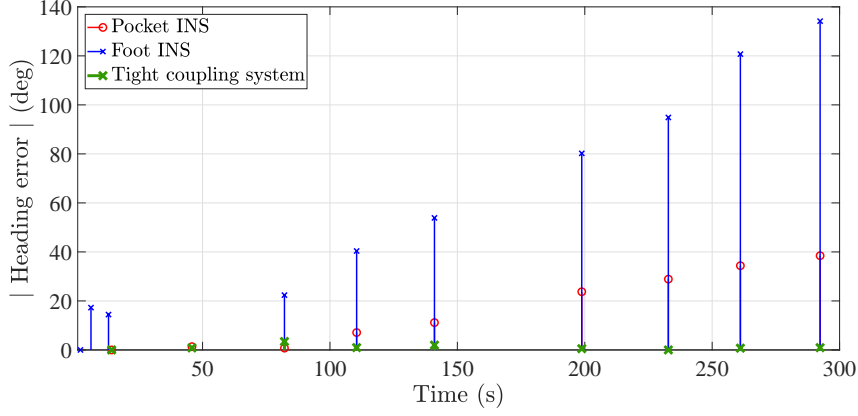


Figure 9.19: Heading error of the odometries shown in Figure 9.18.

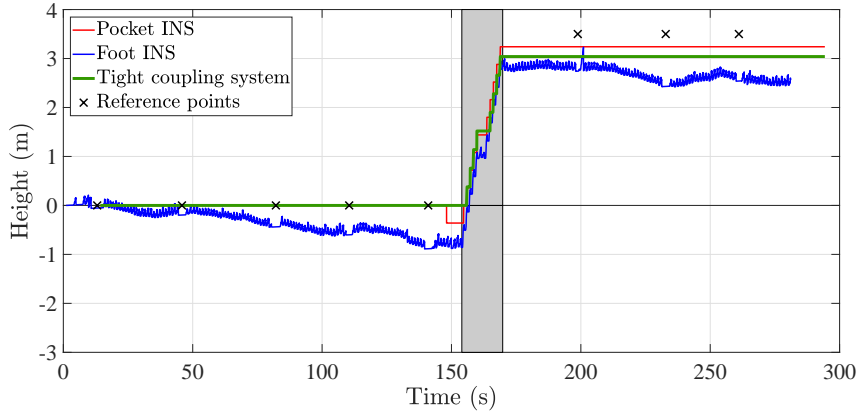


Figure 9.20: Height estimation of the inertial localization systems in Figure 9.18. The shadowed area indicates the time period when the user walks the stairs.

Regarding the height estimation, the tight coupling system has both advantages and disadvantages. On the one hand, the tight coupling system shares the advantages of the loose coupling system. For instance, it does not accumulate height errors in the same way as the foot INS does. Also, the height estimation of the tight coupling system is not as disturbed by outliers in the stairs detection as the pocket INS is.

On the other hand, the tight coupling system has a disadvantage due to its conditions to trigger a step detection flag, see Section 8.5. More specifically, there are two undetected steps 154.7s and 163.7s. The reason is the stairs detection algorithm of the tight coupling system, which is more strict than the algorithm of the pocket INS [19].

With the aforementioned stairs detection algorithm, we avoid the disadvantages regarding the outliers in the stairs detection identified in previous works [83]. Nevertheless, should the vertical displacement not exceed the threshold in the event of a stair, then the algorithm does not detect the change in height. In Figure 9.20, the two missed stairs are the first ones after walking horizontally. The vertical displacement estimated by the tight coupling does not exceed the threshold of 15 cm. Thus, the tight coupling fails to detect them.

Although the tight coupling system performs similarly to the loose coupling system, see Figure 9.10, the former system has an advantage with respect to the latter one. Namely, the comfort zone update implemented in the tight coupling system assures that the tilt angles are coherent with respect to human behaviour. Thanks to this update, the tight coupling system is less sensitive to the outliers during the stairs detection that arise due to the errors in the tilt angles. An example is shown in Figure 9.21, where the pitch angle of the pocket IMU estimated with the pocket INS and the tight coupling system is plotted while walking horizontally and downstairs. We can see that the pocket INS has undetected stairs whereas the tight coupling system detects the ten stairs that the user walked during the shadowed periods of time.

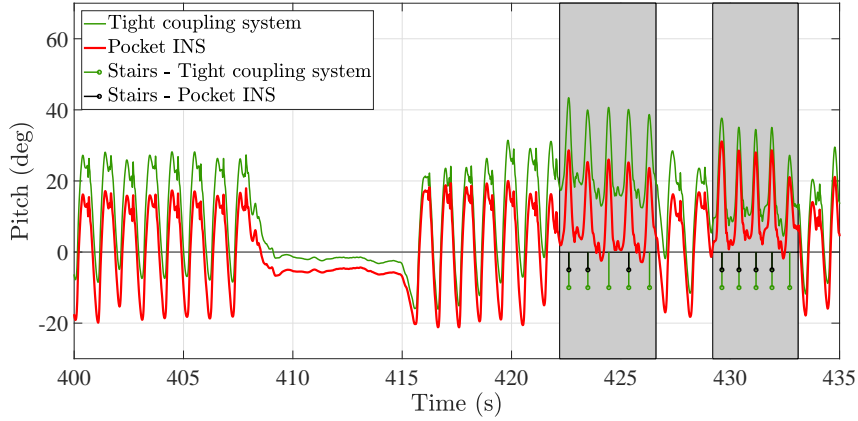


Figure 9.21: Pitch of the pocket IMU estimated by the tight coupling system and the pocket INS. The shadowed areas indicate the time when the user was walking downstairs.

Next, we want to assess the effect of the relative heading update on the relative heading between the pocket IMU and the foot IMU. Let us recall that the relative heading increases overtime following an approximately linear trend, see Figure 8.5 and Figure 8.6. In such a case, the inertial relative heading can be modelled with a first-order linear regression. We have estimated the parameters of the first-order linear regression, using the least squares method [81], of all the walks in the data set of Section 4.2.3. Then, we have used these parameters to plot the regression lines that model the relative heading over time.

The results of assessing the effect of the relative heading update are shown in Figure 9.22. For this assessment, we have considered two relative headings: without and with the effect of the relative heading update. The figure shows how the relative headings without the relative heading update grow faster over time. In contrast, the relative heading update constraints the growth of the relative heading over time. In fact, the results are less noisy than the case where the relative heading update is not applied.

In the assessment of the relative heading update, the most relevant parameter is the slope of the linear regressions of Figure 9.22. These slopes indicate how fast the relative heading grows over time. In our particular case, the average slope without

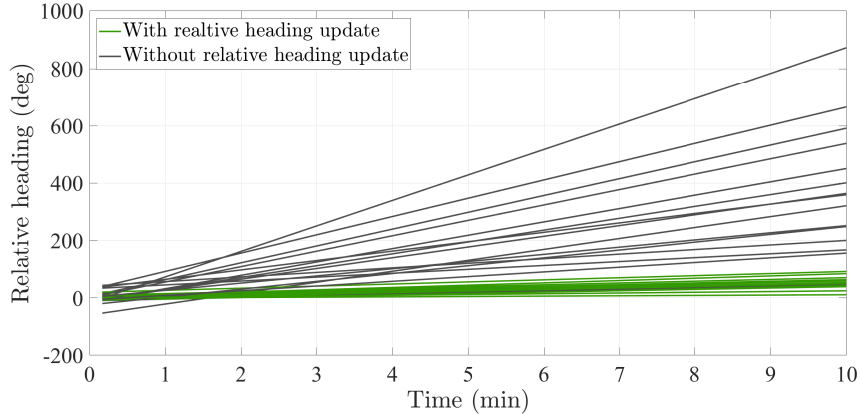


Figure 9.22: First-order linear regressions that model the relative heading without and with relative heading update.

the relative heading update is $0.63^\circ/\text{s}$. When we apply the update, the slope is reduced to $0.09^\circ/\text{s}$. That is, the relative heading update reduced the slope of the relative heading by a factor of six.

The result of this section show the advantage of the tight coupling. That is, the heading error is reduced by the implementation of the relative heading update between the heading of the pocket IMU and the foot IMU.

One of the limitations of our approach is that there is a component of the heading error that we cannot observe. The reason lies on the fact that the relative heading is the subtraction of the heading of the pocket IMU from the heading of the foot IMU. Another limitation is regarding the comfort zone update. In this work, we have implemented this concept only for walking on horizontal surfaces. We have observed that this concept is, so far, not extensible to walking upstairs or downstairs. The cause for that is the different behaviour of the tilt angles, especially the pitch, while walking the stairs.

9.5 Summary and Conclusions

This section brings together the key results of this chapter. The idea is to compare the proposed inertial localization systems not only to the single-IMU localization systems but also to each other. As we pointed out above, the third quartile is commonly used in indoor localization competitions to quantitatively evaluate and compare the competing localization systems [75, 76]. Therefore, the third quartile is the metric we use in this section to compare the inertial localization systems.

Table 9.7 lists the third quartile of the error metrics of each inertial localization system. Regarding the distance error, the foot INS is the one that outperforms the rest. We believe the reason is the robust implementation of the strapdown algorithm. The runner-up is the pocket INS with the comfort zone update, which exemplifies the beneficial effect of integrating biomechanical constraints in an inertial localization

system.

Table 9.7: Third quartile of the distance error, the heading error and the height error. *Calib.* stands for calibration. *C.z.* stands for comfort zone.

System description	$Q_3(e_d)[m]$	$Q_3(e_\psi)[^\circ]$	$Q_3(e_h)[m/m]$
Pocket INS (manual calib.)	2.3	90.6	0.5
Foot INS	0.57	109	0.5
Pocket INS with offset calibration (120 steps)	4.5	90.6	0.5
Pocket INS with offset calibration (least squares)	5.1	90.6	0.5
Pocket INS with full calibration	5.3	90.6	0.5
Pocket INS with c.z.	1.8	90.0	0.1
Foot INS with c.z.	0.57	111.5	0.5
Loose coupling system	3.2	99.7	0.1
Tight coupling system	2.1	22.0	0.1

Figure 9.23 shows that the inertial localization systems perform similarly regarding the average distance error. This result contrasts the performance figures in Table 9.7, where the foot INS is clearly the most accurate in distance estimation.

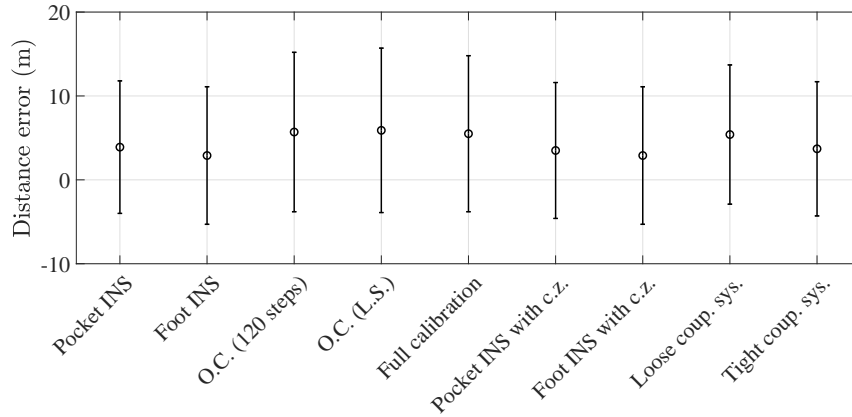


Figure 9.23: Error bar of the distance error of all the inertial localization systems studied in this work. *O.C.* stands for pocket INS with offset calibration. *Full calibration* refers to the pocket INS with full calibration. *C.z.* stands for comfort zone. *Coup. sys.* stands for coupling system.

Regarding the heading error, Table 9.7 shows a clear winner: the tight coupling system. This result reassures the conclusion of Section 9.4. The implementation of biomechanical constraints in inertial localization can reduce the heading error if we combine two IMUs. The third quartile of the heading error of the tight coupling system improves the pocket INS in 77% and the foot INS in 81%. It is obvious that the tight coupling system still presents heading errors. Nevertheless, the results

we obtain are encouraging and they open up a new alternative to further develop inertial localization systems.

Figure 9.24 backs up the previous result. All inertial localization systems except the tight coupling system perform approximately the same regarding the average heading error. The tight coupling system stands out with the lowest heading error. In fact, in the worst case, the heading error of the tight coupling system is the same as the average heading error of all the other inertial localization systems.

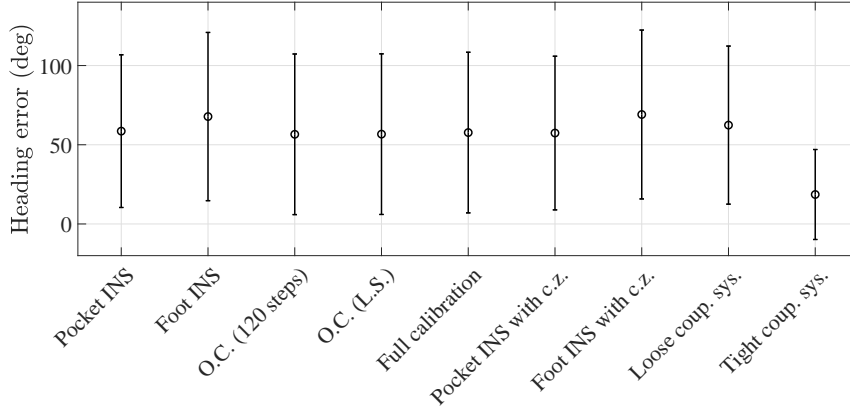


Figure 9.24: Error bar of the heading error of all the inertial localization systems studied in this work. *O.C.* stands for pocket INS with offset calibration. *Full calibration* refers to the pocket INS with full calibration. *C.z.* stands for comfort zone. *Coup. sys.* stands for coupling system.

As expected from the previous sections, the third quartile of the height error indicates that the loose coupling system, the pocket INS with the comfort zone update and the tight coupling system are the most accurate. More specifically, the third quartile of the height error of the pocket INS and the foot INS is reduced in 80% thanks to either the loose coupling system or the comfort zone update.

We can see that the pocket INS and foot INS share the same third quartile of the height error, namely 0.5 m/m . This similarity is unexpected when we take into account the difference in the CDFs of the pocket INS and the foot INS, see Figure 9.10. Thus, we realize that it is necessary to consider different metrics if we are to compare inertial localization systems. For instance, if we would have to choose between the foot INS and the pocket INS based solely on the height error of Table 9.7, we would believe that both inertial localization systems perform similarly. However, the decision between the foot INS and the pocket INS would be different if we consider Figure 9.25.

In summary, in order to evaluate an inertial localization system, we need to find all the metrics that characterize the performance of the system from different points of view. In addition, we need to consider multiple metrics simultaneously in order to objectively assess the performance of an inertial localization system.

Another example is the third quartile of the distance error of the pocket INS with different calibration methods in Table 9.7. Based on these three values, the reader

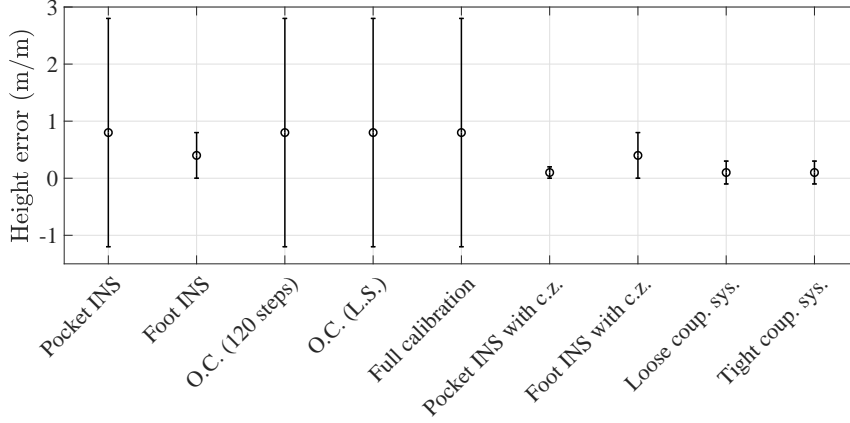


Figure 9.25: Error bar of the height error of all the inertial localization systems studied in this work. *O.C.* stands for pocket INS with offset calibration. *Full calibration* refers to the pocket INS with full calibration. *C.z.* stands for comfort zone. *Coup. sys.* stands for coupling system.

may be inclined to choose the pocket INS with offset calibration over a fixed number of steps. The reason behind this choice may be that the distance error is lower for this implementation of the pocket INS than the other two implementations of the pocket INS. Nevertheless, Figure 9.23 shows that in average, the proposed calibration methods perform similarly. Thus, the reason for choosing the calibration over a fixed period of time should be not only because its third quartile is the lowest, but also because it is the most efficient one.

Another factor to take into account to assess the performance of an inertial localization system is the duration of the walks. The time factor will condition the value of the performance figures because inertial localization system accumulate errors, e.g. heading errors, over time. Therefore, the errors of an inertial localization system will increase with the duration of the walks.

We finalize this chapter with a summary of the strengths and weaknesses of all the inertial localization systems addressed in this work. In general, the proposed fusion methods inherit the strengths of the single-IMU localization systems. An example is the robust steps and stairs detection of the pocket INS, which is inherited by all the proposed inertial localization systems, see Table 9.8. Nevertheless, there is a cost to overcome the weaknesses in Table 9.8: an increased complexity of the inertial localization systems.

One of the weaknesses of the pocket INS is its reliance on the calibration of the step length model to achieve optimal performance, see Table 9.8. As opposed to the pocket INS, none of the proposed inertial localization systems has inherited this weakness thanks to either the automatic calibration or the coupling approaches.

The implementation of the comfort zone update in single-IMU localization systems allows for the estimation of tilt angles that are coherent with respect to human behaviour. By improving the coherence of the tilt angles, we can improve the performance metrics that directly depend on the coherence of the tilt angles, e.g. the

Table 9.8: Summary of the strengths and weaknesses of all the inertial localization systems considered in this work. *w/ calib.* stands for with calibration and *w/ c. z.* stands for with comfort zone.

Description	Inertial localization system						Loose coupling system	Tight coupling system
	Pocket INS	Foot INS	Pocket INS w/ calib.	Pocket INS w/ c. z.	Foot INS w/ c. z.			
Strengths								
Robust step detection	×		×		×		×	×
Robust stairs detection	×		×		×		×	×
Model-free distance estimation		×					×	×
Inherent 3D tracking		×					×	×
Coherent tilt angles					×			×
Coherent relative heading								×
Weaknesses								
Manual calibration	×							
Height drift		×					×	
Heading drift	×	×	×	×	×	×	×	×

height error of the pocket INS.

Regarding height estimation, there are two main features we have exploited in both the loose coupling and the tight coupling. We have profited from the 3D tracking of the foot INS. In order to reduce the height drift, the height of the foot INS is sampled upon the stair detection of the pocket INS. In this way, the loose coupling system and tight coupling system are able to overcome this disadvantage of the foot INS, see Table 9.8.

The attitude tracking is one of the most critical subsystems of an inertial localization system. In fact, the heading drift affects all inertial localization systems, as Table 9.8 indicates. In this work, we have addressed this weakness with two different approaches: the loose coupling system and the tight coupling system.

The loose coupling system has the advantage that it is robust, i.e. if one of the single-IMU localization system fails it can carry on the position tracking with the inertial localization system. Nevertheless, the loose coupling system has the disadvantage that it cannot outperform the most accurate single-IMU localization system, see Table 9.7.

As opposed to the loose coupling system, the tight coupling system relies on the normal operation of both IMUs. An example is regarding temperature, and more specifically, that the IMUs are operating under normal temperature conditions. In that case, the tight coupling system is able to outperform the single-IMU localization systems. The reason is the relative heading update, which guarantees that the performance of the inertial localization system is coherent with respect to the expected motion of the leg. Nonetheless, the tight coupling system is still affected by the drift in the heading, although in a smaller scale than the foot INS or the pocket INS, see Figure 9.17.

The last two strengths in Table 9.8 have been identified during the study carried out in Chapter 7. These strengths regard the coherence of the attitude angles of an inertial localization system. The advantage of the concept of coherent tilt angles is that it can implement both in single-IMU localization systems and multi-IMU localization systems. In contrast, the concept of a coherent relative heading can only be exploited in multi-IMU localization systems.

All in all, this chapter has quantitatively evaluated all the inertial localization systems proposed in Chapter 5-Chapter 8. The quantitative evaluation has allowed us to compare the proposed inertial localization systems to the reference ones, namely the foot INS and the pocket INS. Moreover, we have compared the proposed inertial localization systems among each other and we have identified their strengths and weaknesses.

Chapter 10

Conclusions and Future Work

*If you can dream it,
you can do it
– Walt Disney*

This chapter closes this work. First of all, we summarize the main contributions of this thesis. Second, we conclude our work by identifying its main learnings. Third, we suggest topics for future work that we believe may be of interest to our line of research. Finally, we list our publications which document the main contributions of this thesis.

10.1 Summary of the Main Contributions

The overall objective of this work is to improve pedestrian inertial localization. In this thesis, we extend the state-of-the-art approach of using only one inertial measurement unit (IMU) to simultaneously using two IMUs. The first goal is to identify the challenges of inertial localization systems. The second goal is to develop solutions to these challenges. The proposed solutions profit from the simultaneous use of a foot IMU and a pocket IMU. In the following, we summarize the four main contributions we have made to achieve these goals.

Our first contribution is related to the test and evaluation (T&E) of inertial localization systems and has two parts. The first one is the development of our own T&E methodology and the second one is the identification of the open challenges of inertial localization. We have developed our own T&E methodology because, to this day, there is no standardized T&E methodology to characterize the performance of pedestrian localization system. Our T&E methodology is based on ground truth points, which make it practical to carry out repeatable experiments. Moreover, we have defined metrics that characterize the performance of an inertial localization system over the three most important aspects: distance accuracy, heading accuracy and height accuracy.

Thanks to our T&E methodology, we have assessed the performance of the foot

INS and the pocket INS and characterized the open challenges of pedestrian inertial localization. Among the identified challenges, we contribute to the following:

- the need for calibration of step length models,
- the reduction of the height drift of the strapdown algorithm,
- the reduction of the heading drift of inertial localization systems and,
- the improvement of the coherence of the attitude vector.

Our second contribution is the use of the foot INS to automatically calibrate step length models. More specifically, we propose two calibration methods. They use the output of the foot INS to automatically estimate the parameters of the step length model, which are specific to each user. The proposed methods estimate either one or both parameters of the step length model of a pocket INS. We implement these calibration methods in the pocket INS and observe that all of them have the same distance error. The automatic calibration of the step length model eases the use of the pocket INS, since the user does not need to manually calibrate the step length model.

Our third contribution is the loose coupling system, which implements a modular approach to combine the output of the pocket INS and the foot INS. Our proposed loose coupling system estimates the horizontal position by weighting the step length and heading of the pocket INS and foot INS. The heading weights are estimated based on a quality factor, which is a novel concept that we have developed in our work. The quality factor quantifies the accuracy of the heading based only on the attitude vector of an inertial localization system and the turn rate vector of the associated IMU. The height of the loose coupling system is estimated by sampling the height of the foot INS upon the stairs detected by the pocket INS.

The loose coupling system is more robust than the single-IMU localization systems because it relies on two independent systems. The most significant achievement of the loose coupling system is the reduction of the height error by 75% and 87% with respect to the foot INS and the pocket INS, respectively.

Our fourth contribution regards the integration of the biomechanical constraints of the human walk in inertial localization systems. We identify three main parts of this contribution. Firstly, we have characterized the coherent motion of the human walk in terms of the roll and pitch of each leg limb and the relative heading between leg limbs. Secondly, we have formulated constraints on the roll, pitch and heading based on the previous characterization. Finally, we have integrated the constraints in a tight coupling system which simultaneously processes the raw measurements of a pocket IMU and a foot IMU.

Thanks to the relative heading update, the tight coupling system reduces the heading error by 70% and 72% with respect to the pocket INS and the foot INS, respectively. The tight coupling system also outperforms the pocket INS and the foot INS regarding the height error, which is reduced by 87% and 75% with respect to the height error of the pocket INS and the foot INS, respectively.

10.2 Conclusions

In the following, we present the four main conclusions of this work. The first conclusion is related to the T&E of inertial localization systems. Thanks to our proposed T&E methodology, we have been able to quantitatively and objectively compare the performance of the different inertial localization systems. We hope that the community adopts such a T&E methodology, which has also proven useful in indoor localization competitions.

Our second conclusion is related to the calibration of step length models. From our work, we can conclude that it is possible to use a foot INS to automatically calibrate the parameters of a step length model. In this way, the user becomes unaware of the need for calibration, which makes the use of the inertial localization system more appealing than when the calibration is done manually. We have also observed that the calibration is always needed for the pocket INS. Therefore, our proposed automatic calibration method is a key enabler for using the pocket INS. The calibration method needs only approximately 2 min at the beginning of the walk to calibrate the step length model to the user.

The third conclusion of our work regards the loose coupling system. We have learned to determine how accurate the heading estimation one inertial localization system is with respect to the heading estimation of another inertial localization system without a reference attitude. Furthermore, the loose coupling system has shown us that we can exploit complementary features of the foot INS and the pocket INS to improve the accuracy of the height estimation.

The fourth conclusion of our work is drawn from the integration of biomechanical constraints in inertial localization systems. We have learned that we can observe the errors in inertial localization systems by analyzing the human motion associated to their attitude estimation. In this way, we do not need to compare the position estimation to a reference position to state that the position estimation has errors. Moreover, we can reduce both the heading and height error in inertial localization systems by integrating motion constraints.

We close our work by stating that multi-IMU localization systems are more accurate than single-IMU localization systems. This accuracy is reflected in a considerable improvement of the heading error and the height error. Therefore, we recommend the use of multiple IMUs placed on different parts of the body to improve the accuracy of an inertial localization system.

10.3 Future Work

Along the course of this thesis, we have identified possible topics that are of interest for future work. First of all, we think it is necessary to develop T&E methodologies that allow to characterize the performance of the different components of pedestrian localization systems.

The automatic calibration method assumes that the IMU does not slip during the walk. Once the IMUs are integrated within the clothes, they may slip during the walk. An extension of the automatic calibration is to assess whether it is necessary to recalibrate the parameters of the step length model if the IMU slips. If the answer is affirmative, it would be necessary to develop a method to detect that the IMU has slipped.

Another extension of this work is the adaptation of the comfort zone concept to 3D cases, e.g. stairs or ramps. Moreover, the concept of the comfort zone can be applied to further activities than walking, e.g. running or duck walking. The estimation of the user's position during such activities is still a challenge.

There is one aspect of human biomechanics that has not been exploited in this work: rigid body kinematics. Rigid body kinematics are able to relate acceleration and turn rate of consecutive links of a rigid body. This approach has been followed in human motion monitoring and we believe it will be of interest to assess its applicability in inertial localization.

The scope of this work considers only inertial measurements in the localization system. In the future, magnetic field measurements from different body locations could be integrated in an inertial localization system to estimate the position. In fact, magnetometers are frequently integrated together with IMUs. Therefore, it seems natural to integrate them in the position estimation process as well. Similarly, an extension of our work is the integration of landmark detection and SLAM to further reduce the drift in inertial localization systems.

10.4 List of Publications

Table 10.1 lists all the publications related to the work we have presented in this thesis. The publications are classified by authorship, namely as first author or as co-author.

Table 10.1: List of publications classified by authorship. *Publ.* stands for publication.

<i>As first author</i>		
Topic	Publ. type	Title
T&E	Conference	D. Bousdar Ahmed, E. Munoz Diaz, and S. Kaiser, "Performance comparison of foot- and pocket-mounted inertial navigation systems", in <i>2016 International Conference on Indoor Positioning and Indoor Navigation (IPIN)</i> , 2016.

Continued on next page

Table 10.1 – *Continued from previous page*

Topic	Publ. type	Title
T&E	Conference	D. Bousdar Ahmed, L. E. Díez Blanco, and E. Munoz Diaz, “Performance comparison of wearable-based pedestrian navigation systems in large area”, in <i>2017 International Conference on Indoor Positioning and Indoor Navigation (IPIN)</i> , 2017.
T&E	Journal	D. Bousdar Ahmed and L. E. Díez and E. Munoz Diaz and Juan Jesús García Domínguez, “A survey on test and evaluation methodologies of pedestrian localization systems”, in <i>IEEE Sensors Journal</i> , 2019.
Calibration	Conference	D. Bousdar Ahmed, E. Munoz Diaz, and J. A. Conejo Minguez, “Exploiting wearable devices for the calibration of inertial navigation systems”, in <i>2017 International Conference on Indoor Positioning and Indoor Navigation (IPIN)</i> , 2017.
Calibration	Patent	Calibration of empirical model for step length estimation by means of an inertial measurement unit mounted on the foot wear (under review). DE file number: 10 2017 103 607.5
Loose coupling	Patent	Standalone and automatic quality evaluation of the heading estimation of inertial navigation systems by means of inertial measurements. DE file number: 10 2017 122 465.3
Loose coupling	Journal	D. Bousdar Ahmed and E. Munoz Diaz, “Loose coupling of wearable-based INSs with automatic heading evaluation”, in <i>Sensors</i> , vol. 17, no. 11, p. 2534, 2017.
Loose coupling	Conference	D. Bousdar Ahmed and E. Munoz Diaz, “3D loose-coupled fusion of inertial sensors for pedestrian localization”, in <i>2018 International Conference on Indoor Positioning and Indoor Navigation (IPIN)</i> , 2018.
Tight coupling	Patent	Drift reduction in orientation estimation through application of biomechanical models (under review). DE file number: 10 2017 124 173.6
Tight coupling	Conference	D. Bousdar Ahmed and K. Metzger, “Wearable-based pedestrian inertial navigation with constraints based on biomechanical models”, in <i>2018 IEEE/ION Position, Location and Navigation Symposium (PLANS)</i> , 2018.
Tight coupling	Conference	D. Bousdar Ahmed, “Inertial pedestrian localization with soft constraints based on biomechanical models”, in <i>2019 International Conference on Indoor Positioning and Indoor Navigation (IPIN)</i> , 2019.
<i>As co-author</i>		
Sensor fusion	Journal	A. Correa, E. Munoz Diaz, D. Bousdar Ahmed, A. Morell, and J. L. Vicario, “Advanced pedestrian positioning system to smartphones and smartwatches”, in <i>Sensors</i> , vol. 16, no. 11, p. 1903, 2016.
Foot INS	Journal	E. Munoz. Diaz, S. Kaiser, and D. Bousdar Ahmed, “Height error correction for shoe-mounted inertial sensors exploiting foot dynamics”, in <i>Sensors</i> , vol. 18, no. 3, p. 888, 2018.

Continued on next page

Table 10.1 – *Continued from previous page*

Topic	Publ. type	Title
Inertial localization	Book chapter	E. Munoz Diaz, D. Bousdar Ahmed and S. Kaiser “A review of indoor localization methods based on inertial sensors”, in <i>Eds., Geographical and fingerprinting data for positioning and navigation systems: Challenges, experiences and technology roadmap (Intelligent data-centric systems: Sensor collected intelligence)</i> , 1st ed. Academic Press, 2018.
Leg model	Conference	S. García de Villa, E. Munoz Diaz, D. Bousdar Ahmed, J. J. García and A. Jiménez, “IMU-based characterization of the leg for the implementation of biomechanical models” in <i>2019 International Conference on Indoor Positioning and Indoor Navigation (IPIN)</i> , 2019.

Appendix A

Human Gait

*The journey of a thousand miles
begins with one step*
—Lao Tzu

The human gait can be decomposed in the phases of Figure A.1 [96]. Three main events of the human gait are relevant in this thesis: the stance phase, the step and the stride.

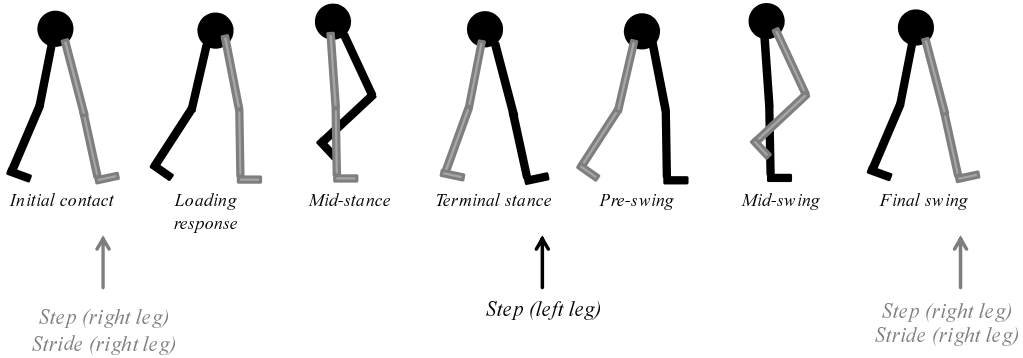


Figure A.1: Phases of the gait cycle. The right leg is depicted in grey whereas the left leg is depicted in black.

The stance phase is defined as the time when the foot is contact with the ground. In Figure A.1, the first foot to be in stance phase is the right one. During the stance phase, the foot is characterized by its stillness, therefore the foot is not moving during the stance phase.

The stance phase lasts approximately 33% of the gait cycle. This phase is exploited in inertial localization together with the strapdown algorithm [15]. This gait phase is used to implement the ZUPT update which exploits the fact that the foot is not moving, i.e. that its velocity is zero, once every gait cycle.

The strides of the gait cycle define when one foot hits the ground. In one gait cycle, each foot hits the ground once and thus there is one stride of the right leg and one stride of the right leg. Figure A.1 begins with the stride of the right foot.

In contrast, the steps define when either foot hits the ground. That is, there are two steps during one gait cycle, as indicated in Figure A.1. The first step in Figure A.1 coincides with the stride of the right leg. The following step occurs when the left leg hits the ground, and so on.

The detection of steps and strides is used in inertial localization together with the step&heading algorithm. In fact, the detection of a step or a stride depends on the body location of the IMU. If the device is mounted on the lower body, i.e. either leg, shank or foot, then the events detected are strides. In contrast, if the device is mounted on the upper body, then the events detected are steps.

Despite the fact that the stride and step events are different, these two terms are frequently used interchangeably in inertial localization. However, it is important to know that these events are different and that their detection depends on the body location of the IMU.

It is straightforward to see that in one gait cycle the number of steps is double the number of strides. Additionally, the lengths of the steps and strides are also different. Figure A.2 shows that the stride length is larger than the step length.

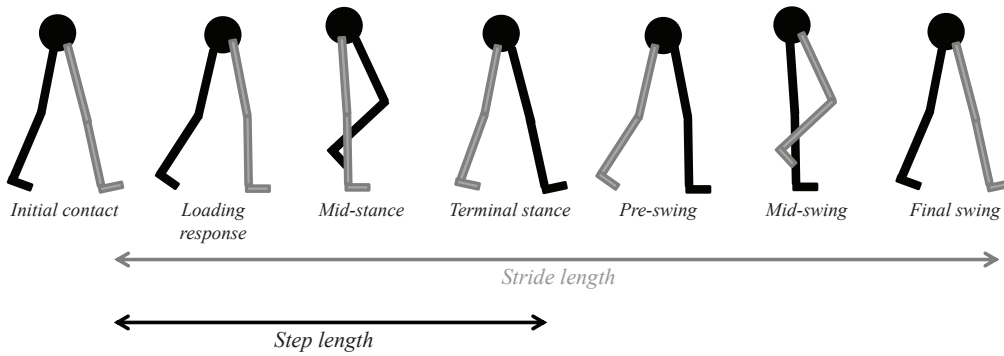


Figure A.2: Stride and step length during the gait cycle.

Appendix B

Attitude Representation

*Attitude is a little thing
that makes a big difference*
—Winston Churchill

In this chapter, the relevant mathematical representations of the attitude of a body will be described. Beforehand, it is necessary the recall the following concepts:

- the *navigation frame* defines the coordinate frame of the world, and therefore this frame is fixed. There will exist elements, e.g. a sensor, whose attitude or position might change in the navigation frame, see Figure B.1. Generally, this frame is defined according to the right-handed rule, with the z-axis pointed to the local vertical [57].
- the *body frame* defines the coordinate frame of the body that rotates and moves in a fixed frame. The body frame may refer, for instance, to the coordinate frame of the sensor. Given that the body can rotate within the navigation frame, the body frame rotates along with it, see Figure B.1.

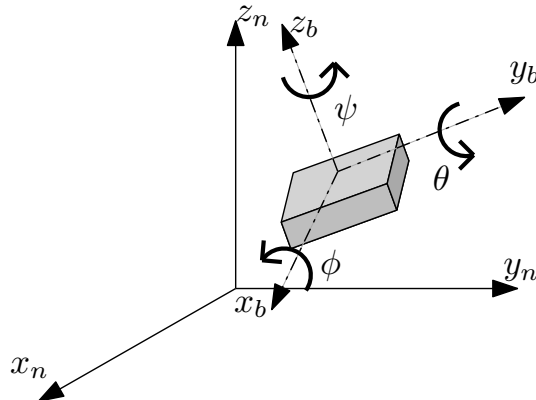


Figure B.1: Navigation frame (n) and body frame (b). Each axis of the body frame can be presented in the navigation frame through the attitude of the body frame.

The attitude of any rotating body, e.g. $\{x_b, y_b, z_b\}$ in Figure B.1, can be expressed

with respect to another frame, e.g. $\{x_n, y_n, z_n\}$ in Figure B.1. There are three mathematical representations for that: the Euler angles, the DCM and the quaternions.

In this appendix, we focus on the Euler angles and the DCM since they are the two alternatives used throughout this thesis. The DCM can be expressed in terms of the Euler angles and viceversa. For instance, the DCM (\mathbf{C}_{nb}) can be written as the successive multiplications of the three matrices that represent the rotation around the x-axis (ϕ), y-axis (θ) and z-axis (ψ), which leads to:

$$\mathbf{C}_{nb} = \begin{bmatrix} \cos(\theta) \cdot \cos(\psi) & -\cos(\phi) \cdot \sin(\psi) + \sin(\phi) \cdot \sin(\psi) & \sin(\phi) \cdot \sin(\psi) \\ \cos(\theta) \cdot \sin(\psi) & \sin(\phi) \cdot \sin(\theta) \cdot \cos(\psi) + \cos(\phi) \cdot \sin(\theta) \cdot \cos(\psi) & \cos(\phi) \cdot \sin(\theta) \cdot \cos(\psi) \\ -\sin(\theta) & \sin(\phi) \cdot \sin(\theta) \cdot \sin(\psi) + \cos(\phi) \cdot \sin(\theta) \cdot \sin(\psi) & \cos(\phi) \cdot \sin(\theta) \cdot \sin(\psi) \\ \sin(\phi) \cdot \cos(\theta) & \cos(\phi) \cdot \cos(\theta) & \cos(\phi) \cdot \cos(\theta) \end{bmatrix}, \quad (\text{B.1})$$

Similarly, given the DCM (\mathbf{C}_{nb}):

$$\mathbf{C}_{nb} = \begin{bmatrix} c_{11} & c_{12} & c_{13} \\ c_{21} & c_{22} & c_{23} \\ c_{31} & c_{32} & c_{33} \end{bmatrix}, \quad (\text{B.2})$$

the Euler angles ($[\phi, \theta, \psi]$) can be estimated as follows:

$$\phi = \arctan\left(\frac{c_{32}}{c_{33}}\right), \quad (\text{B.3})$$

$$\theta = \arcsin(-c_{31}), \quad (\text{B.4})$$

$$\psi = \arctan\left(\frac{c_{21}}{c_{11}}\right), \quad (\text{B.5})$$

where ϕ , θ and ψ are commonly known as the roll, pitch and yaw respectively. The yaw may also be referred to as the heading.

Appendix C

Unscented Kalman Filter

*A wise girl knows her limits,
a smart girl knows she has none
—Marilyn Monroe*

In the following, the equations to implement an UKF are presented. The detailed explanation of the UKF can be found in [58].

We begin by defining the states vector, i.e. the vector with the variables that we want to estimate. Let \mathbf{x}^k denote the states vector at the k -time. Furthermore, we consider \mathbf{x}^k to be a column vector. The states vector has an associated covariance matrix \mathbf{P}_x^k .

The time evolution of the states is determined by the process model ($\mathbf{F}(\cdot)$):

$$\mathbf{x}^k = \mathbf{F}(\mathbf{x}^{k-1}, \mathbf{u}^{k-1}, \mathbf{v}^k), \quad (\text{C.1})$$

where \mathbf{u}^{k-1} is a the control vector at time $k - 1$ and \mathbf{v}^k represents the noise in the process model. The noise of the process model is commonly assumed to be a zero-mean Gaussian random vector with covariance matrix \mathbf{Q} , which is a matrix with dimensions $n \times n$.

The UKF may incorporate external measurements (\mathbf{z}^k) through the measurement model (\mathbf{H}). The vector \mathbf{z} is a column vector, with m elements, that relates to the states as follows:

$$\mathbf{z}^k = \mathbf{H}(\mathbf{x}^k, \mathbf{w}^k), \quad (\text{C.2})$$

where \mathbf{w}^k is the noise of the measurement model. This noise is commonly assumed to be a zero-mean Gaussian random vector with covariance matrix \mathbf{R} . The dimensions of the covariance matrix (\mathbf{R}) are $m \times m$.

The UKF estimates the states in two stages: the prediction stage and the measurement update. That is, the UKF follows the structure of a standard Kalman filter. The difference with respect to the Kalman filter lies in how the states are predicted and how the predicted measurement vector is estimated.

In this thesis, we will use the following notation for Kalman filters:

- The subindex $-$ will denote the variables estimated during the prediction. For instance, the predicted states at time k are written as \mathbf{x}_-^k . These variables can also be referred to as prior.
- The subindex $+$ will denote the variables output by the filter. For instance, \mathbf{x}_+^k is the states vector after the k -th iteration of the UKF. These states can also be referred to as posterior. Note that, the posterior states might be the result of either a prediction stage and an update stage or only the prediction stage. Either case will depend on whether the measurement update of the UKF is applicable or not.

States Prediction

The prediction of the states is done through the sigma points (χ). The sigma points are a set of points chosen to be spread around the true mean and covariance of the states (\mathbf{x}). χ is a matrix with dimensions $n \times (2n+1)$, where each column represents a sigma point. Thus, the UKF has a total of $2n+1$ sigma points, and each one is a sample of the states vector.

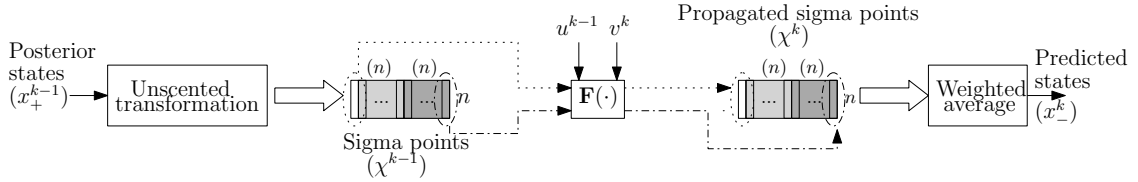


Figure C.1: Block diagram of the states prediction of an UKF.

Figure C.1 presents the block diagram of the states prediction. The prediction of the UKF begins by estimating the points χ^{k-1} through the posterior states at time $k-1$, i.e. \mathbf{x}_+^{k-1} . This estimation is known as unscented transformation and follows the equation:

$$\chi^{k-1} = \left[\mathbf{x}_+^{k-1}, \mathbf{x}_+^{k-1} + \gamma \cdot \sqrt{\mathbf{P}_{\mathbf{x}_+}^{k-1}}, \mathbf{x}_+^{k-1} - \gamma \cdot \sqrt{\mathbf{P}_{\mathbf{x}_+}^{k-1}} \right], \quad (\text{C.3})$$

where:

$$\begin{aligned} \gamma &= \sqrt{n + \lambda}, \\ \lambda &= \alpha^2 \cdot (n + \kappa) - n. \end{aligned}$$

The variable α is set to a small positive value, e.g. $10^{-4} \leq \alpha \leq 1$. The variable κ is a secondary scaling parameter. The reader is referred to [58] for more details on the design of the values of α and κ .

The next step is to propagate the sigma points with the process model of equation (C.1). That is, we compute a new set of $2n+1$ sigma points as follows:

$$\chi_i^k = \mathbf{F}(\chi_i^{k-1}, \mathbf{u}^{k-1}, \mathbf{v}^k), \quad (\text{C.4})$$

where i denotes the i -th column of the sigma point matrix of equation (C.3).

The matrix $\boldsymbol{\chi}^k$ contains the propagated sigma points, which are used to estimate the predicted states:

$$\mathbf{x}_-^k = \sum_{i=0}^{2n} w_i^{(m)} \cdot \boldsymbol{\chi}_i^k, \quad (\text{C.5})$$

where $w_i^{(m)}$ is the weight of the i -th sigma point, which takes the following values:

$$w_0^{(m)} = \frac{\lambda}{n + \lambda}, \quad (\text{C.6})$$

$$w_i^{(m)} = \frac{1}{2(n + \lambda)}, \quad i = 1, \dots, 2n. \quad (\text{C.7})$$

The covariance matrix of the predicted states $\mathbf{P}_{\mathbf{x}_-}^k$ is estimated as:

$$\mathbf{P}_{\mathbf{x}_-}^k = \left(\sum_{i=0}^{2n} w_i^{(c)} \cdot (\boldsymbol{\chi}_i^k - \mathbf{x}_-^k) \cdot (\boldsymbol{\chi}_i^k - \mathbf{x}_-^k)^T \right) + \mathbf{Q}, \quad (\text{C.8})$$

where the weights $w_i^{(c)}$ are computed as follows:

$$w_0^{(c)} = \frac{\lambda}{n + \lambda} + 1 - \alpha^2 + \beta, \quad (\text{C.9})$$

$$w_i^{(c)} = \frac{1}{2(n + \lambda)}, \quad i = 1, \dots, 2n. \quad (\text{C.10})$$

The parameter β incorporates prior information about the states distribution. For Gaussian distributions, β is set to 2 [58].

Measurement Update

The measurement update in an UKF begins by estimating the matrix of measured sigma points ($\boldsymbol{\Upsilon}^k$), which is a $m \times 2n + 1$ matrix, whose columns are computed as:

$$\boldsymbol{\Upsilon}_i^k = \mathbf{H}(\boldsymbol{\chi}_i^k, \mathbf{w}^k). \quad (\text{C.11})$$

The matrix of measured sigma points ($\boldsymbol{\Upsilon}^k$) is then used to estimate the predicted measurement vector (\mathbf{z}_-^k):

$$\mathbf{z}_-^k = \sum_{i=0}^{2n} w_i^{(m)} \cdot \boldsymbol{\Upsilon}_i^k. \quad (\text{C.12})$$

The covariance matrix of the measurement vector ($\mathbf{P}_{\mathbf{z}}^k$) and the cross-covariance matrix ($\mathbf{P}_{\mathbf{xz}}^k$) follow the equations:

$$\mathbf{P}_{\mathbf{z}}^k = \left(\sum_{i=0}^{2n} w_i^{(c)} \cdot (\boldsymbol{\Upsilon}_i^k - \mathbf{z}_-^k) \cdot (\boldsymbol{\Upsilon}_i^k - \mathbf{z}_-^k)^T \right) + \mathbf{R}, \quad (\text{C.13})$$

$$\mathbf{P}_{\mathbf{xz}}^k = \left(\sum_{i=0}^{2n} w_i^{(c)} \cdot (\boldsymbol{\chi}_i^k - \mathbf{x}_-^k) \cdot (\boldsymbol{\Upsilon}_i^k - \mathbf{z}_-^k)^T \right). \quad (\text{C.14})$$

Finally, the measurement update of the states follows the standard equations of a Kalman filter. That is, the Kalman gain (\mathbf{K}^k) is estimated as:

$$\mathbf{K}^k = \mathbf{P}_{xz}^k \cdot (\mathbf{P}_z^k)^{-1}. \quad (\text{C.15})$$

Then, the updated states (\mathbf{x}_+^k) and updated covariance matrix (\mathbf{P}_{x+}^k) are computed as:

$$\mathbf{x}_+^k = \mathbf{x}_-^k + \mathbf{K}^k \cdot (\mathbf{z}^k - \mathbf{z}_-^k), \quad (\text{C.16})$$

$$\mathbf{P}_{x+}^k = \mathbf{P}_{x-}^k - \mathbf{K} \cdot \mathbf{P}_z^k \cdot \mathbf{K}^T. \quad (\text{C.17})$$

Appendix D

Simulative Proof Results (Extension)

*My idea of sexy is that less is more
The less you reveal, the more people can wonder
– Emma Watson*

As a reminder, the summary table with the cases studies of the simulative proof is presented again. The cases marked with a star are the ones included in this appendix.

Table D.1: Error configuration of each case study.

Case study	Pocket INS	Foot INS
1	Only random noise	Only random noise
2	Constant bias	Constant bias
3*	Variable bias	Variable bias
4	Constant bias	Only random noise
5*	Only random noise	Constant bias
6*	Variable bias	Only random noise
7*	Only random noise	Variable bias
8	Constant bias	Variable bias
9*	Variable bias	Constant bias

Figure D.1 reflects case study 3, where the raw measurements are disturbed by variable bias. From the figure, we appreciate that the quality factor of the heading of the pocket INS is slightly higher than the quality factor of the heading of the foot INS. This is supported by the plot where the heading is represented. In the latter, the heading of the pocket INS has a smaller error than the heading of the foot INS.

Figure D.2-Figure D.4 present the examples where one inertial localization system has close-to perfect measurements, i.e. only random noise, and the second inertial localization system is disturbed by both noise and bias.

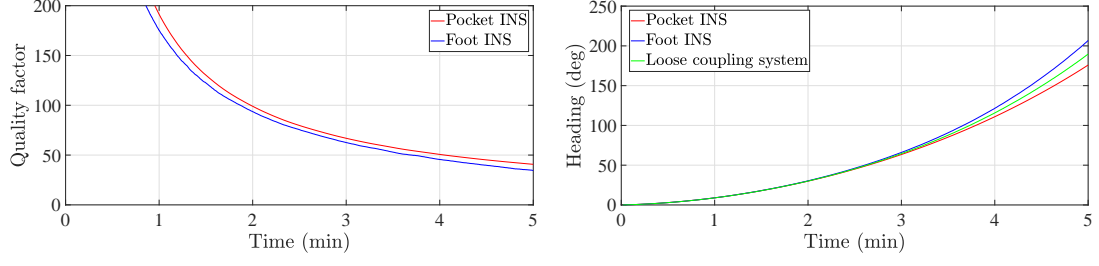


Figure D.1: Case study 3: (Left) Quality factor estimation. (Right) Heading estimation of the pocket INS, the foot INS and the loose coupling system fusion according to equation (6.10).

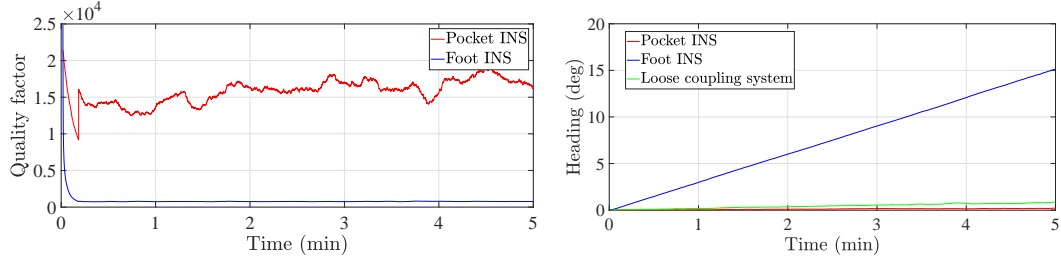


Figure D.2: Case study 5: (Left) Quality factor estimation. (Right) Heading estimation of the pocket INS, the foot INS and the loose coupling system fusion according to equation (6.10).

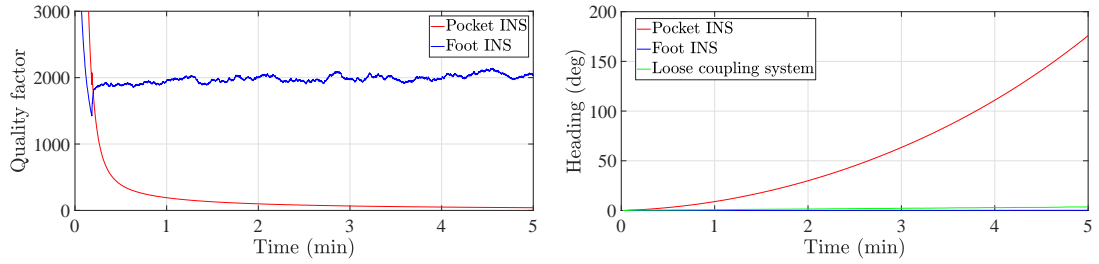


Figure D.3: Case study 6: (Left) Quality factor estimation. (Right) Heading estimation of the pocket INS, the foot INS and the loose coupling system fusion according to equation (6.10).

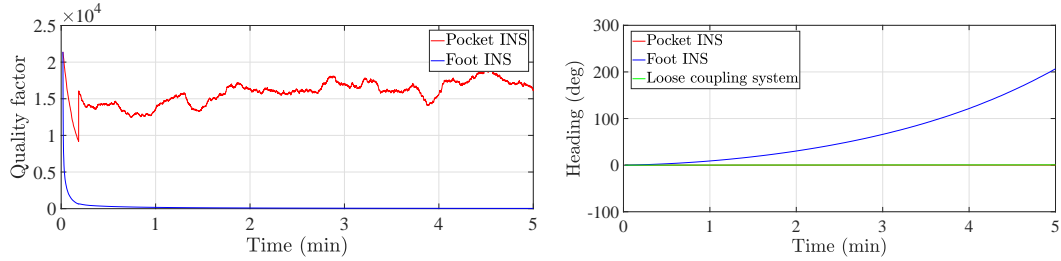


Figure D.4: Case study 7: (Left) Quality factor estimation. (Right) Heading estimation of the pocket INS, the foot INS and the loose coupling system fusion according to equation (6.10).

Figure D.5 presents case study 9. The behaviour of the quality factor and the heading is approximately the same as that of case study 8.

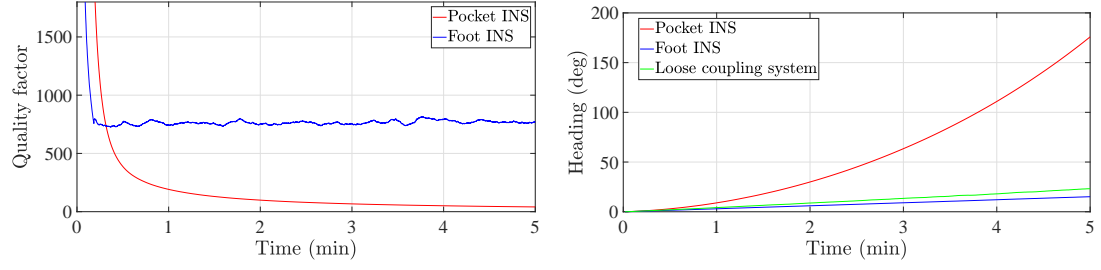


Figure D.5: Case study 9: (Left) Quality factor estimation. (Right) Heading estimation of the pocket INS, the foot INS and the loose coupling system fusion according to equation (6.10).

Appendix E

Derivation of the Denavit-Hartenberg Parameters

*A person with a new idea is a crank
until the idea succeeds
—Mark Twain*

The derivation of the Denavit-Hartenberg parameters of a robotic structure can be done following the steps below. In this chapter, these parameters are derived for the structure of Figure E.1.

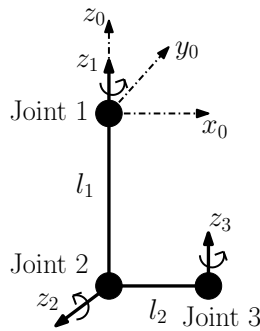


Figure E.1: Representation of a robotic structure with three joints. Each joint has only one rotation axis, z_i . The base frame is represented by the triad $\{x_0, y_0, z_0\}$.

It is important to highlight that the derivation of the Denavit-Hartenberg parameters must be done by following consistent rules. In this thesis, the right-hand rule is used to define the coordinate frames. Furthermore, the positive direction of rotation around an axis is defined according to the right-hand rule. These positive directions of rotation are indicated in Figure E.1.

Prior to the derivation of the Denavit-Hartenberg parameters, it is necessary to define the base frame. In this example, the base frame is defined to be in the centre of the first joint, see Figure E.1.

Once the reference frame is defined, the sequence of steps that allows for the derivation of the Denavit-Hartenberg parameters is the following:

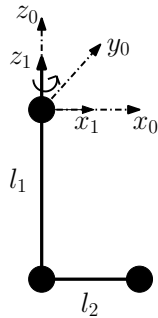
1. define the z -axis pointing along the axis of rotation, let this axis be z_i ,
2. find the common normal between the current z -axis, i.e. z_i , and the previous one, i.e. z_{i-1} . The common normal is the normal line to both axes and it is the shortest line between them. If z_i and z_{i-1} are parallel, then the common normal is of free choice,
3. define the new x -axis, i.e. x_i . It is co-linear with the common normal, i.e.

$$x_i = z_i \times z_{i-1}, \quad (\text{E.1})$$

where \times denotes the vector product operation.

4. define the new origin as the intersection between z_i and x_i ,
5. find the link offset (d_i). It is the depth along z_{i-1} from the origin of z_{i-1} to the normal.
6. find the link rotation angle (θ_i). It is the angle around z_{i-1} to align x_{i-1} with x_i ,
7. find the link length (a_i). It is the distance around the rotated x_{i-1} , from z_{i-1} to the origin of the new joint,
8. find the twist angle (α_i). It is the rotation around x_i to align z_{i-1} with z_i ,
9. repeat steps 1-8 until the parameters for all rotation axes are derived.

Let us begin with the definition of the Denavit-Hartenberg parameters of axis z_1 . Since the latter is the first joint, we define the axis x_1 as indicated in the figure of Table E.1. Given that the axes are fully aligned, the Denavit-Hartenberg parameters are all zero, see Table E.1.

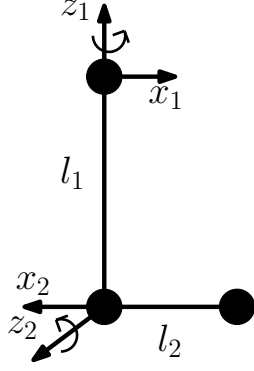


Axis	d	θ	a	α
z_1	0	0	0	0

Table E.1: (Left) Definition of the new x -axis, i.e. x_1 . (Right) Denavit-Hartenberg parameters associated to the axis z_1 .

The next set of Denavit-Hartenberg parameters are those associated to the axis z_2 . Since the axis z_2 is given, the next step is to define the common normal, i.e. the line perpendicular to both z_1 and z_2 . It can be found by using the right hand rule, see

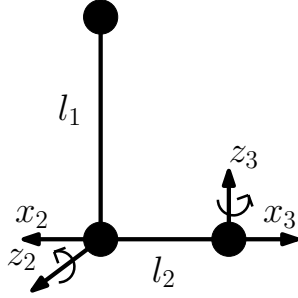
equation (E.1), which in turn leads to the next step, namely the definition of the axis x_2 . The resulting x_2 points in the direction indicated in Figure E.2. The new origin, according to step 4, would be in the centre of the second joint of Figure E.1. With all the axes of joints 1 and 2 defined, the derivation of the Denavit-Hartenberg parameters is straightforward. Steps 5-8 lead to the parameters given in Table E.2.



Axis	d	θ	a	α
z_1	0	0	0	0
z_2	$-l_1$	180°	0	-90°

Table E.2: (Left) Definition of the new x -axis, i.e. x_2 . (Right) Denavit-Hartenberg parameters associated to the axis z_2 .

The last set of parameters to be defined are those associated to joint 3. Once more, steps 2-3 lead to the x_3 axis indicated in the figure of Table E.3. Then, steps 5-8 lead to the Denavit-Hartenberg parameters listed in Table E.3.



Axis	d	θ	a	α
z_1	0	0	0	0
z_2	$-l_1$	180°	0	-90°
z_3	0	180°	l_2	-90°

Table E.3: (Left) Definition of the new x -axis, i.e. x_3 . (Right) Denavit-Hartenberg parameters associated to the axis z_3 .

Appendix F

Derivation of the Turn Rate Equations

*Success is a science,
if you have the conditions you get the result
– Oscar Wilde*

In this chapter, the methodology to derive the equations of the turn rate vector given a set of Euler angles is presented. The derivation of the turn rate vector requires the knowledge of the rotation sequence that was followed to derive the attitude in the first place. In fact, different rotation sequences around the cartesian axes will lead to different Euler angles [57].

Annotations on Rotation Matrices

The Euler angles indicate the rotation around each one of the cartesian axis. More specifically, the roll (ϕ), the pitch (θ) and the heading (ψ) are the rotation around the x-axis, y-axis and z-axis, respectively, that must be carried out to align the body frame with the navigation frame, see Appendix B.

Each of the aforementioned rotations can be represented by a matrix. Let us denote by $\mathbf{R}_x(\phi)$ the rotation matrix that rotates a vector around the x-axis an angle equal to ϕ . This matrix can be written as follows:

$$\mathbf{R}_x(\phi) = \begin{bmatrix} 1 & 0 & 0 \\ 0 & \cos(\phi) & -\sin(\phi) \\ 0 & \sin(\phi) & \cos(\phi) \end{bmatrix}. \quad (\text{F.1})$$

Similarly, $\mathbf{R}_y(\theta)$ is the rotation matrix that rotates a vector around the y-axis an angle equal to θ . In this case, the matrix follows the equation:

$$\mathbf{R}_y(\theta) = \begin{bmatrix} \cos(\theta) & 0 & \sin(\theta) \\ 0 & 1 & 0 \\ -\sin(\theta) & 0 & \cos(\theta) \end{bmatrix}. \quad (\text{F.2})$$

Finally, $\mathbf{R}(\psi)$ denotes the rotation matrix that rotates a vector around the z-axis an angle equal to ψ :

$$\mathbf{R}_z(\psi) = \begin{bmatrix} \cos(\psi) & -\sin(\psi) & 0 \\ \sin(\psi) & \cos(\psi) & 0 \\ 0 & 0 & 1 \end{bmatrix}. \quad (\text{F.3})$$

The successive rotation around the axis can be represented by successively multiplying the aforementioned matrices. For instance, the three successive rotations around, first, the x-axis, second, the y-axis and third, the z-axis, is represented by:

$$\mathbf{C}_{nb} = \mathbf{R}_z(\psi) \cdot \mathbf{R}_y(\theta) \cdot \mathbf{R}_x(\phi). \quad (\text{F.4})$$

In fact, the previous equation is the derivation of the matrix \mathbf{C}_{nb} given in Appendix B.

Problem Statement

The problem statement can be formulated as follows: derive the set of equations to estimate the turn rate vector in the body frame ($\boldsymbol{\omega}_b$). To that end, the known variables are the following:

- the Euler angles that rotate a vector from the body frame to the navigation frame, namely the roll (ϕ), the pitch (θ) and the yaw (ψ),
- the derivative of the previous angles, namely the derivative of the roll ($\dot{\phi}$), the derivative of the pitch ($\dot{\theta}$) and the derivative of the yaw ($\dot{\psi}$).

In addition, it is known that the Euler angles are obtained by rotating first around the x-axis, second around the y-axis and third around the z-axis.

Method to Estimate the Turn Rate Vector

Prior to describing the method, let us define three variables that will come in handy for the derivation of the equations of the turn rate vector. These variables are:

$$\boldsymbol{\omega}_{\dot{\phi}} = (\dot{\phi}, 0, 0)^T, \quad (\text{F.5})$$

$$\boldsymbol{\omega}_{\dot{\theta}} = (0, \dot{\theta}, 0)^T, \quad (\text{F.6})$$

$$\boldsymbol{\omega}_{\dot{\psi}} = (0, 0, \dot{\psi})^T. \quad (\text{F.7})$$

The latter are the turn rate vector resulting from the roll, pitch and yaw rotations respectively. Moreover, these vector are given in the frame where they are first applied.

The turn rate vector in the body frame ($\boldsymbol{\omega}_b$) can be computed as the sum of the individual contributions of each of the rate of change of the Euler angles, that is:

$$\boldsymbol{\omega}_b = \boldsymbol{\omega}_{\dot{\phi}b} + \boldsymbol{\omega}_{\dot{\theta}b} + \boldsymbol{\omega}_{\dot{\psi}b}, \quad (\text{F.8})$$

where each of the three addends are estimated as:

$$\boldsymbol{\omega}_{\dot{\phi}b} = \mathbf{R}_1 \cdot \boldsymbol{\omega}_{\dot{\phi}}, \quad (\text{F.9})$$

$$\boldsymbol{\omega}_{\dot{\theta}b} = \mathbf{R}_2 \cdot \boldsymbol{\omega}_{\dot{\theta}}, \quad (\text{F.10})$$

$$\boldsymbol{\omega}_{\dot{\psi}b} = \mathbf{R}_3 \cdot \boldsymbol{\omega}_{\dot{\psi}}, \quad (\text{F.11})$$

where \mathbf{R}_i is the rotation matrix from the i -th frame to the body frame. These matrices are a product of a subset of $\{\mathbf{R}_x(\phi), \mathbf{R}_y(\theta), \mathbf{R}_z(\psi)\}$.

Let us now derive the addends in equation (F.8). To that end, we will determine the contributions of each one of the addends separately.

Contribution of $\boldsymbol{\omega}_{\dot{\phi}b}$

We begin with $\boldsymbol{\omega}_{\dot{\phi}b}$, for which Figure F.1-(a) is given. In this case, the original frame is the body frame $\{x_b, y_b, z_b\}$, to which a rotation ϕ is applied. The latter rotation leads to the frame $\{x', y', z'\}$. It can be seen in Figure F.1-(a) that $x' = x_b$.

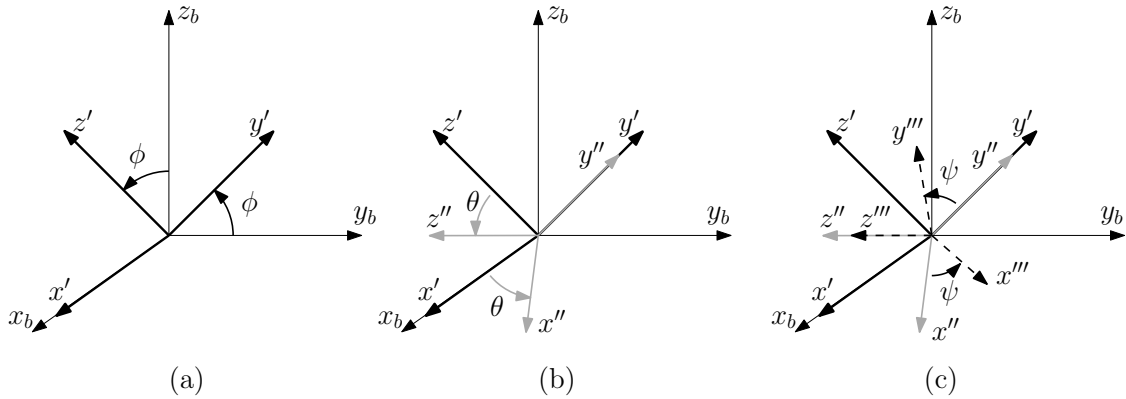


Figure F.1: Three successive rotations represented by the Euler angles. (a) Rotation around the x-axis. (b) Rotation around the resulting y-axis, namely y' . (c) Rotation around the resulting z-axis, namely z'' .

In order to determine the rotation matrix (\mathbf{R}_1), it necessary to determine the frame where the rotation ϕ is applied. From Figure F.1-(a), it can be seen that the frame where the rotation is applied is the body frame itself. Thus:

$$\mathbf{R}_1 = \begin{bmatrix} 1 & 0 & 0 \\ 0 & 1 & 0 \\ 0 & 0 & 1 \end{bmatrix}. \quad (\text{F.12})$$

The contribution of $\boldsymbol{\omega}_{\dot{\phi}b}$ can now be estimated:

$$\boldsymbol{\omega}_{\dot{\phi}b} = \mathbf{R}_1 \cdot \boldsymbol{\omega}_{\dot{\phi}} = \boldsymbol{\omega}_{\dot{\phi}} = [\dot{\phi}, 0, 0]^T. \quad (\text{F.13})$$

Contribution of $\omega_{\dot{\theta}b}$

The next addend to be determined is $\omega_{\dot{\theta}b}$. For the latter, Figure F.1-(b) is provided. In this case, the turn rate vector $\omega_{\dot{\theta}b}$ is the result of rotating last frame $\{x', y', z'\}$ a total of θ around the y' -axis. Such rotation results in the new frame $\{x'', y'', z''\}$. Similarly to the previous rotation, it is now sufficed that $y'' = y'$.

Now, we determine the rotation matrix \mathbf{R}_2 . In this case, the rotation θ around the y -axis is applied in the frame $\{x', y', z'\}$, which is represented by the matrix $\mathbf{R}_x(\phi)$. The latter is the matrix from the body frame to the $\{x', y', z'\}$, whereas \mathbf{R}_2 is the inverse matrix, i.e. from the $\{x', y', z'\}$ frame to the body frame. In the case of rotation matrices, the inverse of a matrix coincides with the transpose of the same matrix. Thus, it can be written that:

$$\mathbf{R}_2 = \mathbf{R}_x(\phi)^T. \quad (\text{F.14})$$

The contribution of $\omega_{\dot{\theta}b}$ can now be estimated:

$$\omega_{\dot{\theta}b} = \mathbf{R}_2 \cdot \omega_{\dot{\theta}} = \begin{bmatrix} 0, \dot{\theta} \cdot \cos(\phi), -\dot{\theta} \cdot \sin(\phi) \end{bmatrix}^T. \quad (\text{F.15})$$

Contribution of $\omega_{\dot{\psi}b}$

Finally, the last addend to be determined is $\omega_{\dot{\psi}b}$. The vector $\omega_{\dot{\psi}b}$ results from rotating the frame $\{x'', y'', z''\}$ a total of ψ around the z'' -axis. Such rotation leads to the frame $\{x''', y''', z'''\}$ depicted in Figure F.1-(c).

The last rotation matrix \mathbf{R}_3 is determined like \mathbf{R}_1 or \mathbf{R}_2 . In this case, the frame where the rotation ψ is applied is the frame $\{x'', y'', z''\}$ which is represented by:

$$\mathbf{R}'' = \mathbf{R}_y(\theta) \cdot \mathbf{R}_x(\phi), \quad (\text{F.16})$$

where \mathbf{R}'' is the rotation matrix from the body frame to the $\{x'', y'', z''\}$ frame. The matrix \mathbf{R}_3 represents the inverse rotation to \mathbf{R}'' , i.e. the rotation from the $\{x'', y'', z''\}$ frame to the body frame, thus:

$$\mathbf{R}_3 = (\mathbf{R}_y(\theta) \cdot \mathbf{R}_x(\phi))^T = \mathbf{R}_x(\phi)^T \cdot \mathbf{R}_y(\theta)^T. \quad (\text{F.17})$$

The contribution of $\omega_{\dot{\psi}b}$ can now be estimated:

$$\begin{aligned} \omega_{\dot{\psi}b} = \mathbf{R}_3 \cdot \omega_{\dot{\psi}} = & [-\dot{\psi} \cdot \sin(\theta), \\ & \dot{\psi} \cdot \sin(\phi) \cdot \cos(\theta), \\ & \dot{\psi} \cdot \cos(\phi) \cdot \cos(\theta)]^T. \end{aligned} \quad (\text{F.18})$$

Turn Rate Vector Estimation

Given the equations above, the turn rate vector in the body frame ($\boldsymbol{\omega}_b$) can be estimated through the Euler angles following equation (F.8), that is:

$$\begin{aligned}\boldsymbol{\omega}_b = & [\dot{\phi} - \dot{\psi} \cdot \sin(\theta), \\ & \dot{\theta} \cdot \cos(\phi) + \dot{\psi} \cdot \sin(\phi) \cdot \cos(\theta), \\ & -\dot{\theta} \cdot \sin(\phi) + \dot{\psi} \cdot \cos(\phi) \cdot \cos(\theta)]^T.\end{aligned}\tag{F.19}$$

Appendix G

Noise Parameters of the Inertial Sensors

*I am extraordinarily patient,
provided that I get my own way in the end
– Margaret Thatcher*

Table G.1 and Table G.2 summarize the random walk (σ_{rw}) and bias stability (σ_{bs}) of the each IMU. The parameters have been estimated with the Allan variance analysis [86].

Table G.1: Random walk and bias stability of the accelerometers.

	σ_{rw} [$\text{m/s}^2/\sqrt{\text{Hz}}$]		σ_{bs} [m/s^2]	
	Foot IMU	Pocket IMU	Foot IMU	Pocket IMU
X axis	$2.6 \cdot 10^{-3}$	$2.3 \cdot 10^{-3}$	$6.9 \cdot 10^{-6}$	$2.1 \cdot 10^{-5}$
Y axis	$2.4 \cdot 10^{-3}$	$2.5 \cdot 10^{-3}$	$5.5 \cdot 10^{-6}$	$6.7 \cdot 10^{-6}$
Z axis	$6.2 \cdot 10^{-3}$	$5.5 \cdot 10^{-3}$	$5.2 \cdot 10^{-5}$	$7.7 \cdot 10^{-5}$

Table G.2: Random walk and bias stability of the gyroscopes.

	σ_{rw} [$\text{rad/s}/\sqrt{\text{Hz}}$]		σ_{bs} [rad/s]	
	Foot IMU	Pocket IMU	Foot IMU	Pocket IMU
X axis	$5.0 \cdot 10^{-4}$	$4.9 \cdot 10^{-4}$	$4.6 \cdot 10^{-7}$	$8.9 \cdot 10^{-7}$
Y axis	$4.8 \cdot 10^{-4}$	$5.0 \cdot 10^{-4}$	$7.1 \cdot 10^{-7}$	$4.5 \cdot 10^{-7}$
Z axis	$5.2 \cdot 10^{-4}$	$4.9 \cdot 10^{-4}$	$5.2 \cdot 10^{-7}$	$4.8 \cdot 10^{-7}$

Bibliography

- [1] S. Y. Labib, “Capitalism in medieval Islam,” *The Journal of Economic History*, vol. 29, no. 1, pp. 79–96, 1969.
- [2] Zephyr, “Biopatch HP user guide.” <https://www.zephyranywhere.com/media/download/biopatch-device-user-manual.pdf>. Accessed: 2018-05-23.
- [3] “Footlogger.” http://footlogger.com:8080/hp_new/footlogger/. Accessed: 2018-05-23.
- [4] “What is a wearable device?.” <http://www.wearabledevices.com/what-is-a-wearable-device/>. Accessed: 2018-05-23.
- [5] “Wearable momentum continues.” <http://www.ccsinsight.com/press/company-news/2516-wearables-momentum-continues>. Accessed: 2018-05-23.
- [6] A. Basiri, T. Moore, C. Hill, and P. Bhatia, “Challenges of LBS market analysis: Current market description.” http://lbs2014.lbsconference.org/sites/default/files/u3/7_2_ppt.pdf.
- [7] A. Clegg, J. Young, S. Iliffe, M. O. Rikkert, and K. Rockwood, “Frailty in elderly people,” *The Lancet*, vol. 381, pp. 752–762, Mar. 2013.
- [8] Statistisches Bundesamt, “Unfallentwicklung auf Deutschen Strassen 2015.” https://www.destatis.de/DE/PresseService/Presse/Pressekonferenzen/2016/Unfallentwicklung_2015/unfallentwicklung_uebersicht.html, 2016. Accessed: 2018-05-23.
- [9] H. Senaratne, M. Mueller, M. Behrisch, F. Lalanne, J. Bustos-Jimenez, J. Schneidewind, D. Keim, and T. Schreck, “Urban mobility analysis with mobile network data: A visual analytics approach,” *IEEE Transactions on Intelligent Transportation Systems*, vol. 19, pp. 1537–1546, May 2018.
- [10] Y. Pu, J. Luo, Y. Wang, C. Hu, Y. Huo, and J. Zhang, “Privacy preserving scheme for location based services using cryptographic approach,” in *IEEE Symposium on Privacy-Aware Computing (PAC)*, IEEE, sep 2018.
- [11] O. J. Woodman, “An introduction to inertial navigation,” tech. rep., Computer Laboratory, University of Cambridge, Aug. 2007.

- [12] E. Munoz Diaz, A. L. Mendiguchia Gonzalez, and F. De Ponte Müller, “Standalone inertial pocket navigation system,” in *ION/PLANS*, March 2014.
- [13] E. Munoz Díaz and A. L. Mendiguchía González, “Step detector and step length estimator for an inertial pocket navigation system,” in *Proceedings of the IEEE/ION Position Location and Navigation Symposium (PLANS)*, South Korea, October 2014.
- [14] Y. J. Chen, “Advantages of MEMS and its distinct new applications,” *Advanced Materials Research*, vol. 813, pp. 205–209, sep 2013.
- [15] E. Foxlin, “Pedestrian tracking with shoe-mounted inertial sensors,” *IEEE Computer Graphics and Applications*, vol. 25, no. 6, pp. 38–46, 2005.
- [16] I. Skog, P. Handel, J. O. Nilsson, and J. Rantakokko, “Zero-velocity detection - An algorithm evaluation,” *IEEE Transactions on Biomedical Engineering*, vol. 57, pp. 2657–2666, Nov. 2010.
- [17] J. Ruppelt, N. Kronenwett, G. Scholz, and G. F. Trommer, “High-precision and robust indoor localization based on foot-mounted inertial sensors,” in *2016 IEEE/ION Position, Location and Navigation Symposium (PLANS)*, pp. 67–75, April 2016.
- [18] J. Kim, H. Jang, D. Hwang, and C. Park, “A step, stride and heading determination for the pedestrian navigation system,” *Positioning*, vol. 1, no. 8, 2004.
- [19] E. Munoz Diaz, “Inertial pocket navigation system: Unaided 3D positioning,” *Sensors*, vol. 15, pp. 9156–9178, Apr. 2015.
- [20] Z.-A. Deng, G. Wang, Y. Hu, and D. Wu, “Heading estimation for indoor pedestrian navigation using a smartphone in the pocket,” *Sensors*, vol. 15, pp. 21518–21536, Aug. 2015.
- [21] V. Renaudin, M. Susi, and G. Lachapelle, “Step length estimation using handheld inertial sensors,” *Sensors*, vol. 12, pp. 8507–8525, June 2012.
- [22] Z.-A. Deng, G. Wang, Y. Hu, and Y. Cui, “Carrying position independent user heading estimation for indoor pedestrian navigation with smartphones,” *Sensors*, vol. 16, p. 677, May 2016.
- [23] M. Elhoushi, J. Georgy, A. Noureldin, and M. J. Korenberg, “Motion mode recognition for indoor pedestrian navigation using portable devices,” *IEEE Transactions on Instrumentation and Measurement*, vol. 65, pp. 208–221, Jan. 2016.
- [24] H. Zhang, W. Yuan, Q. Shen, T. Li, and H. Chang, “A handheld inertial pedestrian navigation system with accurate step modes and device poses recognition,” *IEEE Sensors Journal*, vol. 15, pp. 1421–1429, Mar. 2015.
- [25] L. E. Diez, A. Bahillo, S. Bataineh, A. D. Masegosa, and A. Perallos, “Enhancing improved heuristic drift elimination for wrist-worn PDR systems in

- buildings,” in *2016 IEEE 84th Vehicular Technology Conference (VTC-Fall)*, IEEE, Sept. 2016.
- [26] J. Windau and L. Itti, “Walking compass with head-mounted IMU sensor,” in *2016 IEEE International Conference on Robotics and Automation (ICRA)*, IEEE, May 2016.
 - [27] T. Moder, K. Wisiol, P. Hafner, and M. Wieser, “Smartphone-based indoor positioning utilizing motion recognition,” in *Indoor Positioning and Indoor Navigation (IPIN), 2015 International Conference on*, pp. 1–8, Oct 2015.
 - [28] F. T. Alaoui, D. Betaille, and V. Renaudin, “A multi-hypothesis particle filtering approach for pedestrian dead reckoning,” in *2016 International Conference on Indoor Positioning and Indoor Navigation (IPIN)*, pp. 1–8, Oct 2016.
 - [29] E. Munoz Diaz, F. de Ponte Müller, and J. G. Domínguez, “Use of the magnetic field for improving gyroscopes’ biases estimation,” *Sensors*, vol. 17, p. 832, apr 2017.
 - [30] Freescale Semiconductor, “Tilt sensing using a three-axis accelerometer. AN3461,” tech. rep., Freescale Xtrinsic, 2013.
 - [31] M. S. Grewal, L. R. Weill, and A. P. Andrews, *Global positioning systems, inertial navigation, and integration*. John Wiley & Sons, Inc., dec 2000. pp: 335, 384.
 - [32] B. Cui, X. Chen, and X. Tang, “Improved curvature Kalman filter for GNSS/INS based on transformation of posterior sigma-points error,” *IEEE Transactions on Signal Processing*, vol. 65, pp. 2975–2987, jun 2017.
 - [33] J. Le Scornec, M. Ortiz, and V. Renaudin, “Foot-mounted pedestrian navigation reference with tightly coupled GNSS carrier phases, inertial and magnetic data,” in *2017 International Conference on Indoor Positioning and Indoor Navigation (IPIN)*, IEEE, sep 2017.
 - [34] Z. Chen, H. Zou, H. Jiang, Q. Zhu, Y. C. Soh, and L. Xie, “Fusion of WiFi, smartphone sensors and landmarks using the Kalman filter for indoor localization,” *Sensors*, vol. 15, no. 1, pp. 715–732, 2015.
 - [35] Y. Zhuang and N. El-Sheimy, “Tightly-coupled integration of WiFi and MEMS sensors on handheld devices for indoor pedestrian navigation,” *IEEE Sensors Journal*, vol. 16, pp. 224–234, Jan. 2016.
 - [36] P. K. Yoon, S. Zihajehzadeh, B.-S. Kang, and E. J. Park, “Robust biomechanical model-based 3D indoor localization and tracking method using UWB and IMU,” *IEEE Sensors Journal*, vol. 17, pp. 1084–1096, feb 2017.
 - [37] P. Chen, Y. Kuang, and X. Chen, “A UWB/improved PDR integration algorithm applied to dynamic indoor positioning for pedestrians,” *Sensors*, vol. 17, p. 2065, Sept. 2017.

- [38] A. Alarifi, A. Al-Salman, M. Alsaleh, A. Alnafessah, S. Al-Hadhrami, M. Al-Ammar, and H. Al-Khalifa, "Ultra wideband indoor positioning technologies: Analysis and recent advances," *Sensors*, vol. 16, p. 707, may 2016.
- [39] F. Zampella, A. R. Jimenez, and F. Seco, "Robust indoor positioning fusing PDR and RF technologies: The RFID and UWB case," in *International Conference on Indoor Positioning and Indoor Navigation*, IEEE, Oct. 2013.
- [40] D. Pham and Y. Suh, "Pedestrian navigation using foot-mounted inertial sensor and LIDAR," *Sensors*, vol. 16, p. 120, January 2016.
- [41] M. Ilyas, K. Cho, S.-H. Baeg, and S. Park, "Drift reduction in pedestrian navigation system by exploiting motion constraints and magnetic field," *Sensors*, vol. 16, p. 1455, Sept. 2016.
- [42] A. Norrdine, Z. Kasmi, and J. Blankenbach, "Step detection for ZUPT-aided inertial pedestrian navigation system using foot-mounted permanent magnet," *IEEE Sensors Journal*, vol. 16, pp. 6766–6773, Sept. 2016.
- [43] I. Skog, J. O. Nilsson, P. Hndel, and A. Nehorai, "Inertial sensor arrays, maximum likelihood, and Cramer-Rao bound," *IEEE Transactions on Signal Processing*, vol. 64, pp. 4218–4227, Aug. 2016.
- [44] J. B. Bancroft and G. Lachapelle, "Data fusion algorithms for multiple inertial measurement units," *Sensors*, vol. 11, pp. 6771–6798, June 2011.
- [45] I. Skog, J. O. Nilsson, D. Zachariah, and P. Hndel, "Fusing the information from two navigation systems using an upper bound on their maximum spatial separation," in *2012 International Conference on Indoor Positioning and Indoor Navigation (IPIN)*, pp. 1–5, Nov. 2012.
- [46] X. L. Meng, Z. Q. Zhang, S. Y. Sun, J. K. Wu, and W. C. Wong, "Biomechanical model-based displacement estimation in micro-sensor motion capture," *Measurement Science and Technology*, vol. 23, Mar. 2012.
- [47] J. Sabotta, *Sabotta interaktiv: Bewegungsapparat*. Elsevier, 2007.
- [48] S. Thrun, W. Burgard, and D. Fox, *Probabilistic robotics (Intelligent robotics and autonomous agents)*. The MIT Press, 2005.
- [49] M. Arulampalam, S. Maskell, N. Gordon, and T. Clapp, "A tutorial on particle filters for online nonlinear/non-Gaussian Bayesian tracking," *IEEE Transactions on Signal Processing*, vol. 50, no. 2, pp. 174–188, 2002.
- [50] M. G. Puyol, D. Bobkov, P. Robertson, and T. Jost, "Pedestrian simultaneous localization and mapping in multistory buildings using inertial sensors," *IEEE Transactions on Intelligent Transportation Systems*, vol. 15, pp. 1714–1727, Aug. 2014.
- [51] S. Lee, B. Kim, H. Kim, R. Ha, and H. Cha, "Inertial sensor-based indoor pedestrian localization with minimum 802.15.4a configuration," *IEEE Transactions on Industrial Informatics*, vol. 7, pp. 455–466, aug 2011.

- [52] H. Shin, Y. Chon, and H. Cha, “Unsupervised construction of an indoor floor plan using a smartphone,” *IEEE Transactions on Systems, Man, and Cybernetics, Part C (Applications and Reviews)*, vol. 42, pp. 889–898, nov 2012.
- [53] E. Munoz Diaz, M. Caamano, and F. Sánchez, “Landmark-based drift compensation algorithm for inertial pedestrian navigation,” *Sensors*, vol. 17, p. 1555, July 2017.
- [54] J. Prieto, S. Mazuelas, and M. Z. Win, “Context-aided inertial navigation via new belief condensation,” *IEEE Transactions on Signal Processing*, vol. 64, pp. 3250–3261, June 2016.
- [55] J. L. Carrera, Z. Zhao, T. Braun, and Z. Li, “A real-time indoor tracking system by fusing inertial sensor, radio signal and floor plan,” in *International Conference on Indoor Positioning and Indoor Navigation (IPIN)*, IEEE, Oct. 2016.
- [56] A. Perttula, H. Leppakoski, M. Kirkko-Jaakkola, P. Davidson, J. Collin, and J. Takala, “Distributed indoor positioning system with inertial measurements and map matching,” *IEEE Transactions on Instrumentation and Measurement*, vol. 63, pp. 2682–2695, nov 2014.
- [57] J. W. David Titterton, *Strapdown inertial navigation technology*. Institution of Engineering and Technology, 2004.
- [58] S. Haykin, ed., *Kalman filtering and neural networks*. John Wiley & Sons, Inc., Oct. 2001.
- [59] J. Conesa and R. M. Antoni Pérez-Navarro, Joaquin Torres-Sospedra, eds., *Geographical and fingerprinting data for positioning and navigation systems: Challenges, experiences and technology roadmap (Intelligent data-centric systems: Sensor collected intelligence)*. Academic Press, 1st ed., Sept. 2018. Chapter 16.
- [60] E. Munoz Diaz, O. Heirich, M. Khider, and P. Robertson, “Optimal sampling frequency and bias error modeling for foot-mounted IMUs,” in *Indoor Positioning and Indoor Navigation (IPIN), International Conference on*, no. October, pp. 28–31, 2013.
- [61] Stairway Manufacturers Association, “Visual interpretation of the international residential code.” <https://www.brockportny.org/files/building-code/Stair-construction-visual-2006-Code.pdf>, 2006. International Code Council: Falls Church, VA, USA.
- [62] P. Corke, “A robotics toolbox for MATLAB,” *IEEE Robotics & Automation Magazine*, vol. 3, pp. 24–32, 3 1996.
- [63] “ISO/IEC 18305: Information technology – Real time locating systems – Test and evaluation of localization and tracking systems,” 2016.
- [64] N. Moayeri, M. O. Ergin, F. Lemic, V. Handziski, and A. Wolisz, “PerfLoc (part 1): An extensive data repository for development of smartphone indoor localiza-

- tion apps,” in *2016 IEEE 27th Annual International Symposium on Personal, Indoor, and Mobile Radio Communications (PIMRC)*, IEEE, sep 2016.
- [65] N. Moayeri, C. Li, and L. Shi, “PerfLoc (Part 2): Performance evaluation of the smartphone indoor localization apps,” in *International Conference on Indoor Positioning and Indoor Navigation (IPIN)*, 2018.
 - [66] D. Bousdar Ahmed, L. E. Díez, E. Munoz Diaz, and J. J. García Domínguez, “A survey on test and evaluation methodologies of pedestrian localization systems,” *IEEE Sensors Journal*, 2019. (Under review).
 - [67] F. Potorti, A. Crivello, P. Barsocchi, and F. Palumbo, “Evaluation of indoor localisation systems: Comments on the ISO/IEC 18305 standard,” in *International Conference on Indoor Positioning and Indoor Navigation (IPIN)*, IEEE, Sept. 2018.
 - [68] “Ipin competition.” http://ipin2018.ifsttar.fr/fileadmin/contributeurs/IPIN2018/COMPETITION/IPIN2018_CallForCompetition_v2.1.pdf, 2018. Data set 1: <http://ipin-conference.org/2018/ipincompetition/> Data set 2: http://ipin2018.ifsttar.fr/fileadmin/contributeurs/IPIN2018/COMPETITION/IPIN2018_CallForCompetition_v2.1.pdf.
 - [69] “IPIN Competition.” <http://indoorloc.uji.es/ipin2017track3/>, 2017.
 - [70] D. Lymberopoulos, J. Liu, X. Yang, A. Naguib, A. Rowe, N. Trigoni, and N. Moayeri, “Microsoft indoor localization competition - IPSN,” 2015. Seattle, WA, USA.
 - [71] D. Lymberopoulos, J. Liu, Y. Zhang, P. Dutta, X. Yang, A. Rowe, and V. Sequeira, “Microsoft indoor localization competition - IPSN,” 2016. Vienna, Austria.
 - [72] T. Van Haute, E. De Poorter, J. Rossey, I. Moerman, V. Handziski, A. Behboodi, F. Lemic, A. Wolisz, N. Wistrm, T. Voigt, P. Crombez, P. Verhoeve, and J. Javier De Las Heras, “The EVARILOS benchmarking handbook: Evaluation of RF-based indoor localization solutions,” in *2nd International Workshop on Measurement-based Experimental Research, Methodology and Tools*, May 2013.
 - [73] D. Bousdar Ahmed, E. Munoz Diaz, and S. Kaiser, “Performance comparison of foot- and pocket-mounted inertial navigation systems,” in *2016 International Conference on Indoor Positioning and Indoor Navigation (IPIN)*, IEEE, Oct. 2016.
 - [74] D. Bousdar Ahmed, L. E. Díez Blanco, and E. Munoz Diaz, “Performance comparison of wearable-based pedestrian navigation systems in large areas,” in *2017 International Conference on Indoor Positioning and Indoor Navigation (IPIN)*, IEEE, Sept. 2017.
 - [75] F. Potortì, S. Park, A. J. Ruiz, P. Barsocchi, M. Girolami, A. Crivello, S. Lee, J. Lim, J. Torres-Sospedra, F. Seco, R. Montoliu, G. Mendoza-Silva, M. P.

- Rubio, C. Losada-Gutiérrez, F. Espinosa, and J. Macias-Guarasa, “Comparing the performance of indoor localization systems through the EvAAL framework,” *Sensors*, vol. 17, p. 2327, Oct. 2017.
- [76] D. Lymberopoulos, J. Liu, X. Yang, R. R. Choudhury, V. Handziski, and S. Sen, “A realistic evaluation and comparison of indoor location technologies: Experiences and lessons learned,” in *Proceedings of the 14th International Conference on Information Processing in Sensor Networks*, IPSN ’15, (New York, USA), pp. 178–189, ACM, Apr. 2015.
- [77] X. Technologies, “MTw user manual.” pp. 14-18, 61.
- [78] L. E. Diez, A. Bahillo, J. Otegui, and T. Otim, “Step length estimation methods based on inertial sensors: A review,” *IEEE Sensors Journal*, vol. 18, pp. 6908–6926, Sept. 2018.
- [79] S. Haykin, *Adaptive filter theory (3rd ed.)*. Upper Saddle River, NJ, USA: Prentice-Hall, Inc., 1996.
- [80] D. Bousdar Ahmed, E. Munoz Diaz, and J. A. Conejo Minguez, “Exploiting wearable devices for the calibration of inertial navigation systems,” in *2017 International Conference on Indoor Positioning and Indoor Navigation (IPIN)*, IEEE, Sept. 2017.
- [81] S. J. Miller, “The method of least squares.” https://web.williams.edu/Mathematics/sjmiller/public_html/BrownClasses/54/handouts/MethodLeastSquares.pdf.
- [82] D. Bousdar Ahmed and E. Munoz Diaz, “Loose coupling of wearable-based INSs with automatic heading evaluation,” *Sensors*, vol. 17, p. 2534, Nov. 2017.
- [83] D. Bousdar Ahmed and E. Munoz Diaz, “3D loose-coupled fusion of inertial sensors for pedestrian localization,” in *2018 International Conference on Indoor Positioning and Indoor Navigation (IPIN)*, IEEE, sep 2018.
- [84] NCSS Statistical Software, “Circular data analysis.” https://ncss-wpengine.netdna-ssl.com/wp-content/themes/ncss/pdf/Procedures/NCSS/Circular_Data_Analysis.pdf.
- [85] N. I. Fisher, *Statistical analysis of circular data*. Cambridge University Press, 1993.
- [86] M. Marinov and Z. Petrov, “Allan variance analysis on error characters of low-cost MEMS accelerometer MMA8451Q,” in *International Conference of Scientific Paper AFASES*, May 2014.
- [87] “Limb.” <http://medical-dictionary.thefreedictionary.com/limb>.
- [88] “Joint.” <https://medical-dictionary.thefreedictionary.com/joint>.
- [89] S. Głowiński and T. Krzyżyński, “An inverse kinematic algorithm for the human leg,” *Journal of Theoretical and Applied Mechanics*, p. 53, oct 2016.

https://www.exeley.com/exeley/journals/journal_of_theoretical_and_applied_mechanics/54/1/pdf/10.15632_jtam-pl.54.1.53.pdf.

- [90] I. A. Kapandji MD, *Physiology of the joints: Volume 2 lower limb*. Churchill Livingstone, 2010.
- [91] K. P. Murphy, *Machine learning - A probabilistic perspective*. MIT Press Ltd, 2012.
- [92] D. Simon, “Kalman filtering with state constraints: a survey of linear and nonlinear algorithms,” *IET Control Theory & Applications*, vol. 4, pp. 1303–1318, aug 2010.
- [93] P. Crocoll, L. Görcke, G. F. Trommer, and F. Holzapfel, “Unified model technique for inertial navigation aided by vehicle dynamics model,” *Navigation*, vol. 60, pp. 179–193, sep 2013.
- [94] D. A. Dickey, S. G. Pantula, and J. O. Rawlings, *Applied regression analysis*. Springer New York, 2001.
- [95] D. Bousdar Ahmed, “Inertial pedestrian localization with soft constraints based on biomechanical models,” in *2019 International Conference on Indoor Positioning and Indoor Navigation (IPIN)*, IEEE, Sept. 2019. (Under review).
- [96] J. Perry, “Observational gait analysis handbook,” *Pathokinesiology Department & the Physical Therapy Department*, p. 36, 1989.